David Holcman · Zeev Schuss

Stochastic Narrow Escape in Molecular and Cellular Biology

Analysis and Applications

Springer

Stochastic Narrow Escape in Molecular and Cellular Biology

David Holcman • Zeev Schuss

Stochastic Narrow Escape in Molecular and Cellular Biology

Analysis and Applications

Springer

David Holcman
Group of Applied Mathematics
and Computational Biology
Ecole Normale Superieure
Paris, France

Zeev Schuss
Department of Mathematics
Tel Aviv University School
of Mathematical Science
Tel Aviv, Israel

ISBN 978-1-4939-3102-6 ISBN 978-1-4939-3103-3 (eBook)
DOI 10.1007/978-1-4939-3103-3

Library of Congress Control Number: 2015947260

Springer New York Heidelberg Dordrecht London

Printed on acid-free paper

Springer Science+Business Media LLC New York is part of Springer Science+Business Media (www.springer.com)

Des petits trous, des petits trous, toujours des petits trous, S. Gainsbourg, le poinçonneur des lilas, 1958.

Preface

This monograph consists of two main parts, mathematical and biological. The mathematical part, which is quite sophisticated involving advanced asymptotic methods in partial differential equations, is aimed primarily at applied mathematicians and theoretical physicists who are interested in biological applications. The targeted readership of the second part is much wider and includes also computational biologists, theoretical chemists, biochemists, biophysicists, and physiologists. This part does not necessarily require the in-depth digesting of the tough analysis of the first part. It includes a summary of output formulas from the first part and mainly concentrates on their applications in various models of specific problems in theoretical molecular and cellular biology.

Stochastic narrow escape consists in the passage of a diffusing particle through a narrow opening in an impermeable wall or the arrival of the trajectory of a diffusion process at a small target. For example, a stochastic narrow escape occurs when an ion diffusing inside a biological cell finds a protein channel molecule embedded in the cell membrane and squeezes through it across the membrane. A similar situation occurs when a neurotransmitter molecule, such as glutamate, released from a vesicle at the pre-synaptic terminal into a synaptic cleft of a neuron, finds its way by diffusion to a receptor on the post-synaptic terminal of an excitatory synapse and binds to it. Another example is a channel, such as calcium, or a receptor, moving toward its destination in the post-synaptic density (PSD) on a cellular membrane crowded with insurmountable and impermeable obstacles, finds its destination by diffusion through the narrow openings between the obstacles.

The mathematical narrow escape problem in stochastic theory is to calculate the mean first passage time (MFPT) of a diffusion process to a small absorbing target (Dirichlet boundary) on the otherwise impermeable (Neumann) boundary of a bounded domain (see Fig. 1.1). The main mathematical effort here is to develop asymptotic methods for the approximate evaluation of the MFPT (also called the narrow escape time, NET) in the various geometries of cellular structures (see Sect. 3.3). The problem is equivalent to the construction of an asymptotic solution to the homogeneous mixed Neumann–Dirichlet boundary value problem for the Poisson equation in a bounded domain in the limit of shrinking Dirichlet part.

The NET becomes infinite in this limit, thus rendering its computation a singular perturbation problem.

We review in Chaps. 1–3 of this monograph recent developments in the non-standard asymptotics of the problem, which are based on several ingredients: a better resolution of the singularity of Neumann's function, resolution of the boundary layer near the small target by conformal mappings of domains with bottlenecks, and on the break up of composite domains into simpler compartments. The new methodology applies to two- and higher-dimensional problems.

In Chaps. 4–9, we review applications of the narrow escape problem in cell biology (see Holcman and Schuss 2013a,b). Critical biological processes, such as synaptic plasticity and transmission, activation of genes by transcription factors, or double-stranded DNA break repair, are controlled by diffusion in structures that have both large and small spatial scales. These may be small binding sites inside or on the surface of the cell, or narrow passages between subcellular compartments. The great disparity in spatial scales is the key to controlling cell function by structure. We report here recent progress on resolving analytical and numerical difficulties in extracting properties from experimental data, from biophysical models, and from Brownian dynamics simulations of diffusion in multi-scale structures.

The results of Chaps. 1–3 are applied first to the classification of the various geometries of cellular domains that control ionic and molecular fluxes. The different NETs in various cell geometries are manifested in Brownian dynamics simulations in cellular biology. Specifically, Brownian dynamics simulations can be coarse-grained to the time scale of the NET, thus revealing the dependence of cell function on cell structure.

The resolution of the synaptic transmission by solving the NET problem in the synaptic cleft and in the dendritic spine takes advantage of the particular geometries of the synaptic spine and of the synaptic cleft. The explicit asymptotic expression of the NET is applied to stochastic chemical reactions in microdomains, to regulation of calcium flux through the dendritic spine neck, to the delivery of vesicles in neurite outgrowth, to DNA repair in two-dimensional confinement, to control of reactions by hidden binding sites, to asymmetric dumbbell-shaped division in cells, to coarse-graining a stochastic model of a chemical reaction into a Markov chain model, to the coarse-graining of molecular diffusion on a membrane crowded with obstacles to an effective diffusion, as observed in supermicroscopic imaging, to physical virology with a model of the early steps of viral infection in cells, and so on.

Acknowledgements Much of the material presented in this book is based on our collaboration with many scientists and students, whose names are listed next to ours in the author index (A. Singer, J. Reingruber, N. Hoze, K. Dao Duc, N. Rouach, C. Guerrier, T. Lagache, A. Amitai, J. Cartailler, O. Shukroun, J. Yang, A. Taflia, A. Biess, S. Vakeroudis, G. Malherbe, K. Tsaneva, D. Fresche, J. Sibille, I. Kupka, and many others).

Paris, France David Holcman
Tel Aviv, Israel Zeev Schuss

Contents

List of Figures

List of Symbols

We use interchangeably $\langle\cdot\rangle$ and $\mathbb{E}(\cdot)$ to denote expectation (average) of a random variable, but $\mathbb{E}(\cdot\mid\cdot)$ and $\Pr\{\cdot\mid\cdot\}$ to denote conditional expectation and conditional probability, respectively.

$C^n(\Omega)$	Space of functions with continuous derivatives of order n in Ω
$d_E(\boldsymbol{x},\boldsymbol{y}),\ d(\boldsymbol{x},\boldsymbol{y})$	Euclidean and geodesic distance between $\boldsymbol{x}$ and $\boldsymbol{y}$
$\det(\boldsymbol{A})$	The determinant of the matrix $\boldsymbol{A}$
$dS_{\boldsymbol{x}}$	Surface area or arclength element
D	Diffusion coefficient
$\delta(\boldsymbol{x})$	Dirac's delta function (functional)
$\Delta,\ \Delta_{\boldsymbol{x}}$	Greek *Delta*, the Laplace operator (with respect to $\boldsymbol{x}$): $\dfrac{\partial^2}{\partial x_1^2}+\dfrac{\partial^2}{\partial x_2^2}+\cdots+\dfrac{\partial^2}{\partial x_d^2}$
$\Delta_M f$	The Laplace–Beltrami operator on a Riemannian manifold $\dfrac{1}{\sqrt{\det G}}\sum\limits_{i,j}\dfrac{\partial}{\partial\xi_i}\left(g^{ij}\sqrt{\det G}\dfrac{\partial f}{\partial\xi_j}\right)$
$\mathbb{E}(x),\ \langle x\rangle$	The expected value (expectation) of the random variable x
ε	Relative size of the Dirichlet boundary to $\lvert\partial\Omega\rvert$
$\mathcal{F}(N)$	Approximation to $\mathcal{H}(\boldsymbol{x}_1,\ldots,\boldsymbol{x}_N)$ for large N
$\boldsymbol{G}$	Metric on a manifold
$\boldsymbol{G}^{-1}$	The inverse of $\boldsymbol{G}$
$\mathcal{H}(\boldsymbol{x}_1,\ldots,\boldsymbol{x}_N)$	The energy $\sum\limits_{i=1}^{N}\sum\limits_{j=i+1}^{N}\Big(\frac{1}{\lvert\boldsymbol{x}_i-\boldsymbol{x}_j\rvert} - \frac{1}{2}\log\lvert\boldsymbol{x}_i-\boldsymbol{x}_j\rvert - \frac{1}{2}\log\left(2+\lvert\boldsymbol{x}_i-\boldsymbol{x}_j\rvert\right)\Big)$
$\boldsymbol{J}(t,\boldsymbol{x})$	Diffusion flux density vector
$K(\cdot)$	Complete elliptic integral of the first kind
e	The eccentricity $\sqrt{1-b^2/a^2}$ of the ellipse
L	Length of Brownian rod
$\boldsymbol{n}(\boldsymbol{x})$	Unit outer normal at a boundary point $\boldsymbol{x}$

$N(\boldsymbol{x}, \boldsymbol{\xi})$	The Neumann function
$\nabla,\ \nabla_{\boldsymbol{x}}$	Greek *nabla*, the gradient operator (with respect to $\boldsymbol{x}$): $\left(\frac{\partial}{\partial x_1}, \frac{\partial}{\partial x_2}, \dots, \frac{\partial}{\partial x_d}\right)^T$
$\nabla \cdot \boldsymbol{J}$	The divergence operator $\frac{\partial J_1(\boldsymbol{x})}{\partial x_1} + \frac{\partial J_2(\boldsymbol{x})}{\partial x_2} + \cdots + \frac{\partial J_d(\boldsymbol{x})}{\partial x_d}$
$\frac{\partial v(\boldsymbol{x})}{\partial n(\boldsymbol{x})}$	Normal derivative at $\boldsymbol{x} \in \partial\Omega$
Ω	A planar or spatial domain
$\lvert\Omega\rvert, \lvert\Omega\rvert_g$	Euclidean (Riemannian) volume (area) of Ω
$\partial\Omega$	The boundary of Ω
$\lvert\partial\Omega\rvert, \lvert\partial\Omega\rvert_g\rvert$	Euclidean (Riemannian) measure of $\partial\Omega$
$\partial\Omega_a,\ \partial\Omega_r$	Absorbing and reflecting parts of $\partial\Omega$, respectively
$\Pr\{\text{event}\}$	The probability of *event*
$p_{\boldsymbol{X}}(\boldsymbol{x})$	The probability density function of the vector $\boldsymbol{X}$
$R_c,\ r_c$	Radii of curvature
$\mathbb{R}, \mathbb{R}^d$	The real line, the d-dimensional Euclidean space
(Σ, g)	A two-dimensional Riemannian manifold with metric g
V_x	The partial derivative of V with respect to x : $\partial V \partial x$
$\operatorname{tr}(\boldsymbol{A})$	Trace of the matrix $\boldsymbol{A}$
$\operatorname{Var}(x)$	The variance of x
$\boldsymbol{w}(t),\ \boldsymbol{v}(t)$	Vectors of independent Brownian motions
$x,\ f(x)$	Scalars—lowercase letters
$\boldsymbol{x}, \boldsymbol{f}(\boldsymbol{x})$	Vectors—bold lowercase letters
x_i	The ith element of the vector $\boldsymbol{x}$
$\boldsymbol{x}(\cdot)$	Trajectory or function in function space
$\boldsymbol{x} \cdot \boldsymbol{y}$	Dot (scalar) product of the vectors $\boldsymbol{x}$ and $\boldsymbol{y}$: $\boldsymbol{x} \cdot \boldsymbol{y} = x_1 y_1 + x_2 + y_2 + \cdots + x_d y_d$
$\dot{\boldsymbol{x}}(t)$	Time derivative: $d\boldsymbol{x}(t)/dt$

List of Acronyms

AAV	Adeno-associated virus
AMPA (AMPAR)	α-Amino-3-hydroxy-5-methyl-4-isoxazolepropionic acid (receptor)
APC/C	Anaphase-promoting complex (cyclosome)
Cdc20 molecule	Cell-division cycle protein 20
DNA	Deoxyribonucleic acid
GNET	Gated narrow escape time
HA	Influenza hemagglutinin
MFPT	Mean first passage time
microRNA (miRNA)	A small non-coding RNA molecule
mRNA	Messenger RNA
MT	Microtubule
MTT	Mean time to reach a threshold
NET	Narrow escape time
NMDA	*N*-methyl-D-aspartate (receptor)
NT	Neurotransmitter
PAV	Pontryagin, Andronov, Vitt
pdf	Probability density function
PSD	Post-synaptic density
PTEN	Phosphatase and tensin homolog
RNA	Ribonucleic acid
SAC	Spindle assembly checkpoint
SDE	Stochastic differential equation

Chapter 1
Elementary Theory of Stochastic Narrow Escape

1.1 Introduction

Stochastic narrow escape, as defined in the Preface, consists in the passage of a diffusing particle through a narrow opening in an impermeable wall or the arrival of the trajectory of a diffusion process at a small target. A stochastic narrow escape is a rare event on the time scale of diffusion in the sense that the times between stochastic narrow escapes may be much longer than the times between all other diffusional events and, indeed, they become infinite as the narrow opening or target shrinks to zero. It is therefore practically impossible to explore the high-dimensional parameter space by Brownian-dynamics or other simulations. Very often these rare events are the manifestations of cellular function, such as cross-membrane ionic currents, neuronal signalling, the effective motion of a receptor between obstacles on a membrane, and so on. The time-scale of cellular events is determined by the time-scale of stochastic narrow escapes of molecular diffusion.

These rare molecular events are very sensitive to the geometrical structure of the cellular environment in which the molecule or ions diffuse. In many cases the molecular fluxes through the narrow openings or into small targets are controlled by structure, not by forces. It is therefore imperative that in any physical or mathematical model of ionic or molecular motion between cells the mean narrow escape time (NET) be computable, preferably analytically or at least by molecular or Brownian dynamics simulations. The latter, however, have the serious drawback that rare events are hard to come by in simulations, which quite often fail to produce cellular events from simulations of molecular motion. It is not clear to this day if any Brownian dynamics has been able to produce the ionic current through a protein channel of an excitable membrane.

Therefore the mathematical narrow escape problem in stochastic theory is to calculate the mean first passage time of a diffusion process to a small target on the impermeable boundary of a bounded domain (see Fig. 1.1). The mathematical problem here is equivalent to solving the mixed Dirichlet–Neumann boundary value

D. Holcman, Z. Schuss, *Stochastic Narrow Escape in Molecular and Cellular Biology*, DOI 10.1007/978-1-4939-3103-3_1

Fig. 1.1 Brownian trajectory escaping through a small absorbing window a domain with otherwise reflecting boundary

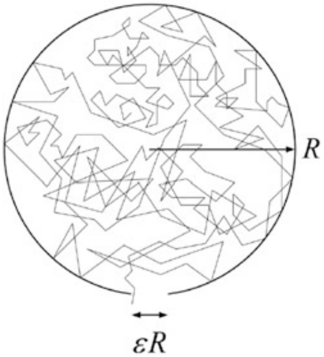

problem for the Poisson equation with small Dirichlet and large Neumann parts. This mixed boundary value problem goes back to Helmholtz (1860) and Lord Rayleigh (1945) in the context of the theory of sound. The renewed interest in the problem is due, as mentioned above, to the emergence of the NET as the key to the determination of biological cell function from its geometrical structure (Holcman and Schuss 2013a). The NET problem is closely connected to the eigenvalue problem for the mixed problem and for the Neumann problem in domains with bottlenecks. The evaluation of the NET coarse-grains the molecular time scale to the cellular level, thus clarifying the role of cell geometry in determining cell function. The NET coarse-grains Brownian dynamics simulations into coarser spatial scale that can be used for resolving the long-time behavior of simulated trajectories.

The NET diverges as the Dirichlet part of the boundary shrinks, thus rendering the computation a singular perturbation problem. In two dimensions the problem is not the same as in higher dimensions, because the singularity of the Neumann function in two dimensions is logarithmic, while that in higher dimensions is algebraic. The computation is related to the calculation of the principal eigenvalue of the mixed Dirichlet–Neumann problem for the Laplace equation in the domain, when the Dirichlet boundary is only a small patch on the otherwise Neumann boundary. Specifically, the principal eigenvalue is asymptotically the reciprocal of the NET in the limit of shrinking patch.

1.2 The Mixed Boundary Value Problem

Consider free Brownian motion in a bounded domain $D \subset \mathbb{R}^d$ $(d = 2, 3)$, whose boundary $\partial\Omega$ is sufficiently smooth (the analysis in higher dimensions is similar to that for $d = 3$). The Brownian trajectory $\boldsymbol{x}(t)$ is reflected at the boundary, except for a small hole $\partial\Omega_a$, where it is absorbed, as shown in Figs. 1.1 and 1.2 (left). The reflecting part of the boundary is $\partial\Omega_r = \partial\Omega - \partial\Omega_a$. The lifetime in Ω of a Brownian trajectory that starts at a point $\boldsymbol{x} \in \Omega$ is the first passage time τ of the trajectory to

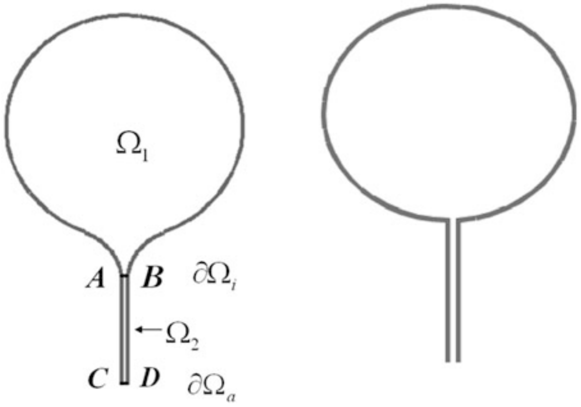

Fig. 1.2 Mathematical idealizations of the cross sections of neuronal spine morphologies as composite domains: *Left:* the bulky head Ω_1 is connected smoothly by an interface $\partial\Omega_i = AB$ to a narrow neck Ω_2. The entire boundary is $\partial\Omega_r$ (reflecting), except for a small absorbing part $\partial\Omega_a = CD$. *Right:* the head, shown separately in Fig. 1.1, is connected to the neck without a funnel

the absorbing boundary $\partial\Omega_a$. The NET

$$v(\boldsymbol{x}) = \mathbb{E}[\tau \,|\, \boldsymbol{x}(0) = \boldsymbol{x}] \tag{1.1}$$

is finite under quite general conditions (Schuss 2010b). As the size (e.g., the diameter) of the absorbing hole decreases to zero, but that of the domain remains finite, the NET increases indefinitely. A measure of smallness can be chosen as the ratio between the surface area of the absorbing boundary and that of the entire boundary, for example

$$\varepsilon = \left(\frac{|\partial\Omega_a|}{|\partial\Omega|}\right)^{1/(d-1)} \ll 1, \tag{1.2}$$

provided that the isoperimetric ratio remains bounded,

$$\frac{|\partial\Omega|^{1/(d-1)}}{|\Omega|^{1/d}} = O(1) \quad \text{for } \varepsilon \ll 1 \tag{1.3}$$

(see the pathological example below when (1.3) is violated). The NET $v(\boldsymbol{x})$ satisfies the Pontryagin–Andronov–Vitt (PAV) mixed boundary value problem for the Poisson equation (Pontryagin et al. 1933; Schuss 2010b)

$$\Delta v(\boldsymbol{x}) = -\frac{1}{D} \quad \text{for } \boldsymbol{x} \in \Omega \tag{1.4}$$

$$v(\boldsymbol{x}) = 0 \quad \text{for } \boldsymbol{x} \in \partial\Omega_a \tag{1.5}$$

$$\frac{\partial v(\boldsymbol{x})}{\partial n(\boldsymbol{x})} = 0 \quad \text{for } \boldsymbol{x} \in \partial\Omega_r, \tag{1.6}$$

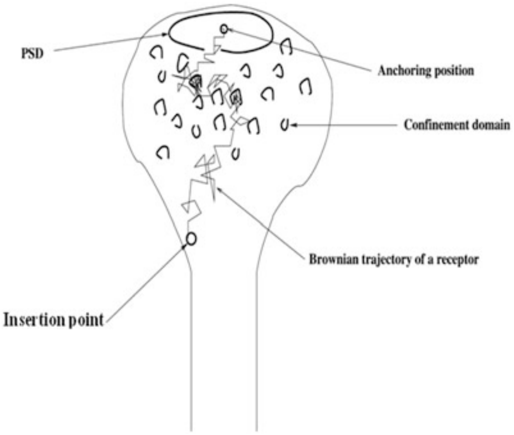

Fig. 1.3 Receptor movement on the neuronal membrane

where D is the diffusion coefficient and $\boldsymbol{n}(\boldsymbol{x})$ is the unit outer normal vector to the boundary at $\boldsymbol{x} \in \partial\Omega$. If Ω is a subset of a two-dimensional Riemannian manifold, as in Fig. 1.3, the Laplace operator is replaced with the Laplace–Beltrami operator. The compatibility condition

$$\int\limits_{\partial\Omega_a} \frac{\partial v(\boldsymbol{x})}{\partial n}\, dS_{\boldsymbol{x}} = -\frac{|\Omega|}{D} \tag{1.7}$$

is obtained by integrating (1.4) over Ω and using (1.5) and (1.6).

The solution $v(\boldsymbol{x})$ diverges to infinity as the hole shrinks to zero, e.g., as $\varepsilon \to 0$, except in a boundary layer near $\partial\Omega_a$, because the compatibility condition (1.7) fails in this limit. Our purpose here is to find an asymptotic approximation to $v(\boldsymbol{x})$ for small ε.

A Pathological Example The following pathological example shows that when (1.3) is violated the NET does not necessarily increase to infinity as the relative area of the hole decreases to zero. This is illustrated by the following example. Consider a cylinder of length L and radius a. The boundary of the cylinder is reflecting, except for one of its bases (at $z = 0$, say), which is absorbing. The NET problem becomes one dimensional and its solution is

$$v(z) = Lz - \frac{z^2}{2}. \tag{1.8}$$

Here there is neither a boundary layer nor a constant outer solution; the NET grows gradually with z. The NET, averaged against a uniform initial distribution in the cylinder, is $\mathbb{E}\tau = L^2/3$ and is independent of a, that is, the assumption that the NET becomes infinite is violated. It holds, however, if the domain is sufficiently thick, e.g., when a ball of radius independent of ε can be rolled on the reflecting boundary inside the domain.

1.3 Neumann's Function and an Helmholtz Integral Equation

First, we prove the following theorem, which is valid for two- and higher-dimensional narrow escape problems.

Theorem 1.3.1 (The Helmholtz Integral Equation). *Under the assumption that the solution $v(\boldsymbol{x})$ of (1.4)–(1.6) diverges to infinity for all $\boldsymbol{x} \in \Omega$ as $\varepsilon \to 0$, the leading order approximation to the boundary flux density*

$$g(\boldsymbol{x}) = \frac{\partial v(\boldsymbol{x})}{\partial n} \text{ for } \boldsymbol{x} \in \partial\Omega_a, \tag{1.9}$$

is the solution of the Helmholtz integral equation

$$\int_{\partial\Omega_a} N(\boldsymbol{x}, \boldsymbol{\xi}))g(\boldsymbol{x})\, dS_{\boldsymbol{x}} = -C_\varepsilon \text{ for } \boldsymbol{\xi} \in \partial\Omega_a \tag{1.10}$$

for some constant C_ε.

Proof. To calculate the NET $v(\boldsymbol{x})$, we use the Neumann function $N(\boldsymbol{x}, \boldsymbol{\xi})$, which is a solution of the boundary value problem

$$\begin{aligned} \Delta_{\boldsymbol{x}} N(\boldsymbol{x}, \boldsymbol{\xi}) &= -\delta(\boldsymbol{x} - \boldsymbol{\xi}) \quad \text{for } \boldsymbol{x}, \boldsymbol{\xi} \in \Omega, \\ \frac{\partial N(\boldsymbol{x}, \boldsymbol{\xi})}{\partial n(\boldsymbol{x})} &= -\frac{1}{|\partial\Omega|} \quad \text{for } \boldsymbol{x} \in \partial\Omega, \boldsymbol{\xi} \in \Omega, \end{aligned} \tag{1.11}$$

and is defined up to an additive constant. Green's identity gives

$$\begin{aligned} &\int_{\Omega} [N(\boldsymbol{x}, \boldsymbol{\xi})\Delta v(\boldsymbol{x}) - v(\boldsymbol{x})\Delta N(\boldsymbol{x}, \boldsymbol{\xi})]\, d\boldsymbol{x} \\ &= \int_{\partial\Omega} \left[N(\boldsymbol{x}, \boldsymbol{\xi}) \frac{\partial v(\boldsymbol{x})}{\partial n} - v(\boldsymbol{x}) \frac{\partial N(\boldsymbol{x}, \boldsymbol{\xi})}{\partial n} \right] dS_{\boldsymbol{x}} \\ &= \int_{\partial\Omega} N(\boldsymbol{x}, \boldsymbol{\xi}) \frac{\partial v(\boldsymbol{x})}{\partial n}\, dS_{\boldsymbol{x}} + \frac{1}{|\partial\Omega|} \int_{\partial\Omega} v(\boldsymbol{x})\, dS_{\boldsymbol{x}}. \end{aligned}$$

On the other hand, Eqs. (1.4) and (1.11) imply that

$$\int_{\Omega} [N(\boldsymbol{x}, \boldsymbol{\xi})\Delta v(\boldsymbol{x}) - v(\boldsymbol{x})\Delta N(\boldsymbol{x}, \boldsymbol{\xi})]\, d\boldsymbol{x} = v(\boldsymbol{\xi}) - \frac{1}{D} \int_{\Omega} N(\boldsymbol{x}, \boldsymbol{\xi})\, d\boldsymbol{x},$$

hence

$$v(\boldsymbol{\xi}) - \frac{1}{D}\int\limits_{\Omega} N(\boldsymbol{x},\boldsymbol{\xi})\,d\boldsymbol{x} = \int\limits_{\partial\Omega} N(\boldsymbol{x},\boldsymbol{\xi})\frac{\partial v(\boldsymbol{x})}{\partial n}\,dS_{\boldsymbol{x}} + \frac{1}{|\partial\Omega|}\int\limits_{\partial\Omega} v(\boldsymbol{x})\,dS_{\boldsymbol{x}}. \tag{1.12}$$

Note that the second integral on the right-hand side of (1.12) is an additive constant. The integral

$$C_\varepsilon = \frac{1}{|\partial\Omega|}\int\limits_{\partial\Omega} v(\boldsymbol{x})\,dS_{\boldsymbol{x}} \tag{1.13}$$

is the average of the NET on the boundary. Now (1.12) takes the form

$$v(\boldsymbol{\xi}) = \frac{1}{D}\int\limits_{\Omega} N(\boldsymbol{x},\boldsymbol{\xi})\,d\boldsymbol{x} + \int\limits_{\partial\Omega_a} N(\boldsymbol{x},\boldsymbol{\xi})\frac{\partial v(\boldsymbol{x})}{\partial n}\,dS_{\boldsymbol{x}} + C_\varepsilon, \tag{1.14}$$

which is an integral representation of $v(\boldsymbol{\xi})$. We use the boundary condition (1.5) and (1.9) to write (1.14) as

$$0 = \frac{1}{D}\int\limits_{\Omega} N(\boldsymbol{x},\boldsymbol{\xi})\,d\boldsymbol{x} + \int\limits_{\partial\Omega_a} N(\boldsymbol{x},\boldsymbol{\xi})g(\boldsymbol{x})\,dS_{\boldsymbol{x}} + C_\varepsilon, \tag{1.15}$$

for all $\boldsymbol{\xi} \in \partial\Omega_a$. Equation (1.15) is an integral equation for $g(\boldsymbol{x})$ and C_ε. To construct an asymptotic approximation to the solution, we note that the first integral in Eq. (1.15) is a regular function of $\boldsymbol{\xi}$ on the boundary. Indeed, due to the symmetry of the Neumann function, we have from (1.11)

$$\Delta_{\boldsymbol{\xi}}\int\limits_{\Omega} N(\boldsymbol{x},\boldsymbol{\xi})\,d\boldsymbol{x} = -1 \quad \text{for } \boldsymbol{\xi} \in \Omega \tag{1.16}$$

and

$$\frac{\partial}{\partial n(\boldsymbol{\xi})}\int\limits_{\Omega} N(\boldsymbol{x},\boldsymbol{\xi})\,d\boldsymbol{x} = -\frac{|\Omega|}{|\partial\Omega|} \quad \text{for } \boldsymbol{\xi} \in \partial\Omega. \tag{1.17}$$

Equation (1.16) and the boundary condition (1.17) are independent of the hole $\partial\Omega_a$, so they define the first integral on the right-hand side of (1.15) as a regular function of $\boldsymbol{\xi}$, up to an additive constant, also independent of $\partial\Omega_a$.

The assumption that for all $\boldsymbol{x} \in \Omega$ the NET $v(\boldsymbol{x})$ diverges to infinity as $\varepsilon \to 0$ and (1.13) implies that $C_\varepsilon \to \infty$ in this limit. This means that for $\boldsymbol{\xi} \in \partial\Omega_a$ the second integral in (1.15) must also become infinite in this limit, because the first integral is independent of $\partial\Omega_a$. Therefore, the leading order approximation to the solution $g(\boldsymbol{x})$ of the integral equation (1.15) is the solution of (1.10). □

1.4 The NET on a Two-Dimensional Riemannian Manifold

We consider a Brownian trajectory $\boldsymbol{x}(t)$ in a bounded domain Ω on a two-dimensional Riemannian manifold (Σ, g) (see relevant references in Sect. 1.4). For a domain $\Omega \subset \Sigma$ with a smooth boundary $\partial\Omega$ (at least C^1), we denote by $|\Omega|_g$ the Riemannian surface area of Ω and by $|\partial\Omega|_g$ the arclength of its boundary, computed with respect to the metric g. As in the previous section, the boundary $\partial\Omega$ is partitioned into an absorbing arc $\partial\Omega_a$ and the remaining part $\partial\Omega_r = \partial\Omega - \partial\Omega_a$ is reflecting for the Brownian trajectories. We assume that the absorbing part is small, that is, (1.2) holds in the form

$$\varepsilon = \frac{|\partial\Omega_a|_g}{|\partial\Omega|_g} \ll 1,$$

however, Σ and Ω are independent of ε; only the partition of the boundary $\partial\Omega$ into absorbing and reflecting parts varies with ε. The first passage time τ of the Brownian motion from Ω to $\partial\Omega_a$ has a finite mean $u(\boldsymbol{x}) = \mathbb{E}[\tau\,|\,\boldsymbol{x}(0) = \boldsymbol{x}]$ and the function $u(\boldsymbol{x})$ satisfies the mixed Neumann–Dirichlet boundary value problem (1.4)–(1.6), which is now written as

$$D\Delta_g u(\boldsymbol{x}) = -1 \quad \text{for}\, \boldsymbol{x} \in \Omega \tag{1.18}$$

$$\frac{\partial u(\boldsymbol{x})}{\partial n} = 0 \quad \text{for}\, \boldsymbol{x} \in \partial\Omega - \partial\Omega_a \tag{1.19}$$

$$u(\boldsymbol{x}) = 0 \quad \text{for} \quad \text{for}\, \boldsymbol{x} \in \partial\Omega_a, \tag{1.20}$$

where D is the diffusion coefficient and Δ_g is the Laplace–Beltrami operator on Σ

$$\Delta_M f = \frac{1}{\sqrt{\det G}} \sum_{i,j} \frac{\partial}{\partial \xi_i}\left(g^{ij}\sqrt{\det G}\frac{\partial f}{\partial \xi_j}\right), \tag{1.21}$$

with

$$\boldsymbol{t}_i = \frac{\partial|\boldsymbol{x}|}{\partial \xi_i}, \quad g_{ij} = \langle \boldsymbol{t}_i, \boldsymbol{t}_j \rangle, \quad G = (g_{ij}), \quad g^{ij} = (G^{-1})_{ij}. \tag{1.22}$$

Obviously, $u(\boldsymbol{x}) \to \infty$ as $\varepsilon \to 0$, except for $\boldsymbol{x}$ in a boundary layer near $\partial\Omega_a$.

Theorem 1.4.1. *Under the above assumptions the NET is given by*

$$\mathbb{E}[\tau\,|\,\boldsymbol{x}] = u(\boldsymbol{x}) = \frac{|\Omega|_g}{\pi D}\left[\log\frac{1}{\varepsilon} + O(1)\right] \quad \textit{for}\; \varepsilon \ll 1. \tag{1.23}$$

Proof. We fix the origin $\mathbf{0} \in \partial\Omega_a$ and represent the boundary curve $\partial\Omega$ in terms of arclength s as $(x(s), y(s))$ and rescale s so that

$$\partial\Omega = \{(x(s), y(s)) : -1/2 < s \le 1/2\}$$

and

$$(x(-1/2), y(-1/2)) = (x(1/2), y(1/2)).$$

We assume that the functions $x(s)$ and $y(s)$ are real analytic in the interval $2|s| < 1$ and that the absorbing part of the boundary $\partial\Omega_a$ is the arc

$$\partial\Omega_a = \{(x(s), y(s)) \, : \, |s| < \varepsilon\}.$$

The Neumann function can be written as

$$N(\boldsymbol{x}, \boldsymbol{\xi}) = -\frac{1}{2\pi} \log d(\boldsymbol{x}, \boldsymbol{\xi}) + v_N(\boldsymbol{x}, \boldsymbol{\xi}) \text{ for } \boldsymbol{x} \in B_\delta(\boldsymbol{\xi}), \tag{1.24}$$

where $B_\delta(\boldsymbol{\xi})$ is a geodesic ball of radius δ centered at $\boldsymbol{\xi}$ and $v_N(\boldsymbol{x}; \boldsymbol{\xi})$ is a regular function (Garabedian 1964; Aubin 1998; Gilbarg and Trudinger 2001). We consider a normal geodesic coordinate system (x, y) at the origin, such that one of the coordinates coincides with the tangent coordinate to $\partial\Omega_a$. We choose unit vectors $\boldsymbol{e}_1, \boldsymbol{e}_2$ as an orthogonal basis in the tangent plane at 0 so that for any vector field $\boldsymbol{X} = x_1\boldsymbol{e}_1 + x_2\boldsymbol{e}_2$, the metric tensor g can be written as

$$g_{ij} = \delta_{ij} + \varepsilon^2 \sum_{kl} a_{ij}^{kl} x_k x_l + o(\varepsilon^2), \tag{1.25}$$

where $|x_k| \leq 1$, because ε is small. It follows that for $\boldsymbol{x}, \boldsymbol{y}$ inside the geodesic ball or radius ε, centered at the origin, $d(\boldsymbol{x}, \boldsymbol{y}) = d_E(\boldsymbol{x}, \boldsymbol{y}) + O(\varepsilon^2)$, where d_E is the Euclidean metric.

To construct an asymptotic expansion of the solution of (1.10) for small ε, we recall that when both $\boldsymbol{x}$ and $\boldsymbol{\xi}$ are on the boundary, $v_N(\boldsymbol{x}, \boldsymbol{\xi})$ becomes singular [see Garabedian 1964, p. 247, (7.46)] and the singular part gains a factor of 2, due to the singularity of the "image charge." Denoting by $\tilde{v}_N$ the new regular part, (1.10) becomes

$$\int\limits_{|s'|<\varepsilon} \left[\tilde{v}_N(\boldsymbol{x}(s'); \boldsymbol{\xi}(s)) - \frac{\log d(\boldsymbol{x}(s), \boldsymbol{\xi}(s'))}{\pi} \right] f(s')\, S(ds') = C_\varepsilon, \tag{1.26}$$

where $S(ds')$ is the induced measure element on the boundary, $\boldsymbol{x} = (x(s), y(s))$, $\boldsymbol{\xi} = (\xi(s), \eta(s))$, and $f(s') = g_0(\boldsymbol{x}(s'))$. Expanding all functions in powers of ε and then in powers of s and s' for $|s|, |s'| < \varepsilon$, the integrals give at the leading order [see Holcman and Schuss (2004), Singer et al. (2006c), Schuss (2013) for details of the computation]

$$\varepsilon(\log\varepsilon - 1) f_0 + \sum_p \left(\frac{\varepsilon^{2p+1}}{2p+1} \log\varepsilon - \frac{\varepsilon^{2p+1}}{(2p+1)^2} \right) f_{2p} = \frac{\pi}{2} \int\limits_{-\varepsilon}^{\varepsilon} v_0(s')\, ds' + C_\varepsilon, \tag{1.27}$$

where f_n are the Taylor coefficients of $f(s)$ and $v_n(s)$ are the coefficients in the expansion of $v(s)$ in powers of ε. Equation (1.27) and

$$\frac{1}{2}\int_{-\varepsilon}^{\varepsilon} f(s)\,S(ds) = \sum_p \frac{\varepsilon^{2p+1}}{(2p+1)} f_{2p}$$

determine the leading order term in the expansion of C_ε. Indeed, the compatibility condition (1.7) gives

$$\int_{-\varepsilon}^{\varepsilon} f(s)\,S(ds) = -|\Omega|_g, \tag{1.28}$$

so using the fact that $\int_{-\varepsilon}^{\varepsilon} v_0(s')S(ds') = O(\varepsilon)$, we find that the leading order expansion of C_ε in (1.27) is

$$C_\varepsilon = \frac{|\Omega|_g}{\pi}\left[\log\frac{1}{\varepsilon} + O(1)\right] \quad \text{for } \varepsilon \ll 1. \tag{1.29}$$

If the diffusion coefficient is D, (1.10) gives the NET from a point $\boldsymbol{x} \in \Omega$, outside the boundary layer, as

$$\mathbb{E}[\tau \,|\, \boldsymbol{x}] = u(\boldsymbol{x}) = \frac{|\Omega|_g}{\pi D}\left[\log\frac{1}{\varepsilon} + O(1)\right] \quad \text{for } \varepsilon \ll 1. \tag{1.30}$$

□

Higher-order terms in the expansion (1.30) are given in Singer et al. (2006b).

1.4.1 Exit Near Singularities of the Boundary

If the window is at a corner of an opening angle α in the boundary (see Fig. 1.4), the NET is to leading order

$$\mathbb{E}\tau = \frac{|\Omega|}{D\alpha}\left[\log\frac{1}{\varepsilon} + O(1)\right]. \tag{1.31}$$

Indeed, putting the origin at the apex of the angle and the real axis on one of the rays of the angle, the conformal mapping $z \mapsto z^{\pi/\alpha}$ of Ω flattens the corner and leaves $\partial\Omega_a$ small. The Neumann function for the upper half plane, $\pi^{-1}\log z$, is transformed into $\alpha^{-1}\log z$, so (1.30) gives (1.31).

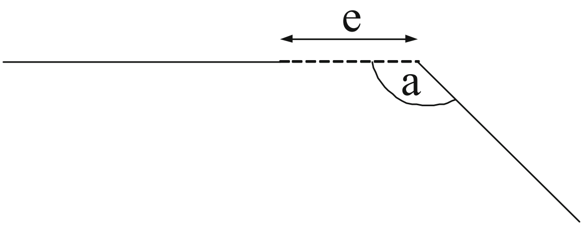

Fig. 1.4 A small opening near a corner of angle α

To see that the area factor $|\Omega|$ remains unchanged under any conformal mapping $f : (x, y) \mapsto (u(x, y), v(x, y))$, we note that this factor is a consequence of the compatibility condition (1.7), that relates the area to the integral

$$\int\limits_{\Omega} \Delta_{(x,y)} w \, dx \, dy = -\frac{|\Omega|}{D},$$

where $w(x, y) = \mathbb{E}[\tau \,|\, x(0) = x, y(0) = y]$ satisfies $\Delta_{(x,y)} w = -1/D$. According to the Cauchy–Riemann equation the Laplacian transforms as

$$\Delta_{(x,y)} w = (u_x^2 + u_y^2) \Delta_{(u,v)} w$$

and the Jacobian of the transformation is $J = u_x^2 + u_y^2$. Therefore,

$$\int\limits_{\Omega} \Delta_{(x,y)} w \, dx \, dy = \int\limits_{f(\Omega)} \Delta_{(u,v)} w \, du \, dv.$$

This means that the compatibility condition remains unchanged and gives the area of the original domain. Higher order asymptotics are given in Singer et al. (2006c).

If the absorbing arc is at a cusp of the boundary, the leading order term of the asymptotic expansion of the NET can be found by mapping the domain conformally onto the upper half plane. A cusp can be viewed as a corner with opening angle $\alpha = 0$, so a different asymptotic expansion than (1.31) should be expected. Consider, for example, Brownian motion in a domain enclosed between the circles $(x - 1/2)^2 + y^2 = 1/4$ and $(x - 1/4)^2 + y^2 = 1/16$ (see Fig. 1.5). The conformal mapping $z \mapsto \exp\{\pi i (1/z - 1)\}$ maps this domain onto the upper half plane. Therefore, the NET is to leading order

$$\mathbb{E}\tau = \frac{|\Omega|}{D} \left[\frac{1}{\varepsilon} + O(1) \right]. \tag{1.32}$$

This result can also be obtained by mapping the cusped domain to the unit circle. The absorbing boundary is then transformed to an exponentially small arc of length $\exp\{-\pi/\varepsilon\} + O(\exp\{-2\pi/\varepsilon\})$, and Eq. (1.32) is recovered.

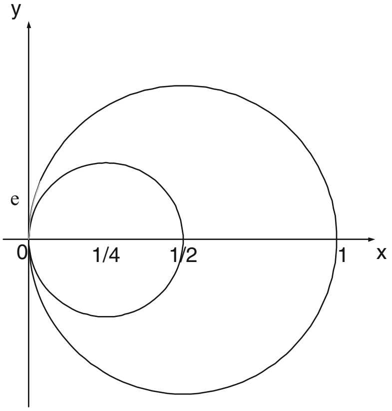

Fig. 1.5 The point (0, 0) is a cusp point of the dotted domain bounded between the two circles. The end of the small absorbing arc of length ε is the cusp point

If the ratio between the two radii, d, is less than 1, then the domain between the two circles is mapped conformally onto the upper half plane by the function $\exp\left\{\pi i(1-z)/(d^{-1}-1)z\right\}$ (for $d = 1/2$ we arrive at the previous example), so the NET is to leading order

$$\mathbb{E}\tau = \frac{|\Omega|}{(d^{-1}-1)D}\left(\frac{1}{\varepsilon} + O(1)\right). \tag{1.33}$$

The NET tends algebraically fast to infinity, much faster than the $O\left(\log \varepsilon^{-1}\right)$ behavior near smooth or corner boundaries. The NET for a cusp is much larger because it is harder for the Brownian motion to enter the cusp than to enter a corner. The NET (1.33) can be written in terms of d instead of the area. Substituting $|\Omega| = \pi R^2(1-d^2)$, we find that

$$\mathbb{E}\tau = \frac{\pi R^2 d(1+d)}{D}\left(\frac{1}{\varepsilon} + O(1)\right), \tag{1.34}$$

where R is the radius of the outer circle. Note that although the area of Ω is a monotonically decreasing function of d, the NET is a monotonically increasing function of d and tends to a finite limit as $d \to 1$. Similarly, one can consider different types of cusps and find that the leading order term for the NET is proportional to $1/\varepsilon^{\lambda}$, where λ is a parameter that describes the order of the cusp, and can be obtained by the same method of conformal mapping (Singer et al. 2006c).

1.4.2 NET on a Two-Dimensional Sphere

Another example is that of Brownian motion on the surface of a 3-sphere of radius R, described by the spherical coordinates (θ, ϕ)

$$x = R\sin\theta\cos\phi, \quad y = R\sin\theta\sin\phi, \quad z = R\cos\theta.$$

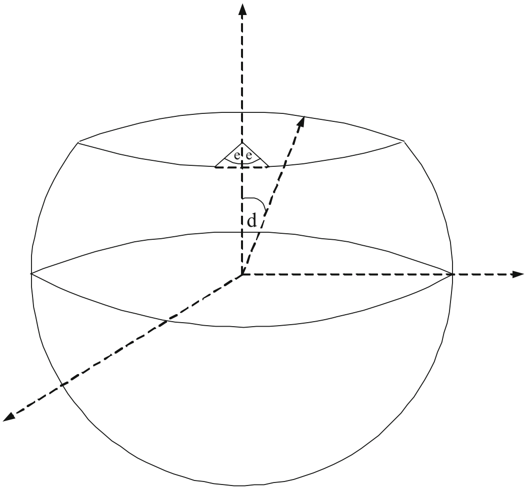

Fig. 1.6 A sphere of radius R without a spherical cap at the north pole with central angle δ. The Brownian motion is absorbed at the boundary of the cap or only at an arc of length 2ε on the boundary of the cap

In spherical coordinates Eqs. (1.21) and (1.22) give (John 1982)

$$g_{\theta\theta} = R^2, \quad g_{\phi\phi} = R^2 \sin^2\theta, \quad g_{\theta\phi} = g_{\phi\theta} = 0. \tag{1.35}$$

Therefore, for a function on the 3-sphere $w = w(\theta, \phi)$ the Laplace–Beltrami operator Δ_M is given by

$$\Delta_M f = R^{-2}\left(\frac{\partial^2 f}{\partial\theta^2} + \cot\theta\,\frac{\partial f}{\partial\theta} + \frac{1}{\sin^2\theta}\frac{\partial^2 f}{\partial\phi^2}\right).$$

If the Brownian motion is absorbed when it reaches a small spherical cap centered at the north pole $\theta = 0$ with a small opening angle δ (see Fig. 1.6), the MFPT to the cap, $v(\theta)$, satisfies the PAV boundary value problem

$$\Delta_M v = R^{-2}\left(v'' + \cot\theta\, v'\right) = -1 \tag{1.36}$$

$$v'(\pi) = 0, \quad v(\delta) = 0, \tag{1.37}$$

because due to rotational symmetry the FPT to the spherical cap is independent of the initial angle ϕ. The solution of the boundary value problem (1.36), (1.37) is given by

$$v(\theta) = 2R^2 \log \frac{\sin\frac{\theta}{2}}{\sin\frac{\delta}{2}}. \tag{1.38}$$

A different approach to the calculation of the MFPT of Brownian motion on the 3-sphere is based on the stereographic projection of the sphere onto the plane (Hille 1976). A related problem is that of entering a circular corral on the 3-sphere through a small arc. These cases are discussed in Singer et al. (2006b) and

Schuss (2013). A general approach leading to explicit asymptotic computations and valid for several holes uses matching asymptotics [see Cheviakov et al. (2010) and the next section].

1.4.3 *The Matched Asymptotics Approach*

In the matched asymptotics approach to the NET problem from a domain Ω in $\mathbb{R}^2$, a boundary layer solution is constructed near an absorbing window $\partial\Omega_a$ of size 2ε (Ward et al. 1993, 2010). First, the mixed boundary value problem (1.4)–(1.6) is converted to local coordinates (η, s), where η is the distance of a point $\boldsymbol{x} \in \Omega$ from the boundary $\partial\Omega$ and s is the arclength from the center of the window to the orthogonal projection of $\boldsymbol{x}$ on $\partial\Omega$. If $\partial\Omega$ is sufficiently smooth in a neighborhood of the window $\partial\Omega_a$, Eq. (1.4) for the MFPT $v(\boldsymbol{x})$ is converted locally to

$$w_{\eta\eta} - \frac{\kappa}{1-\kappa\eta} w_\eta + \frac{1}{1-\kappa\eta}\left(\frac{1}{1-\kappa\eta} w_s\right)_s = -\frac{1}{D}, \tag{1.39}$$

where $w(\eta, s) = v(\boldsymbol{x})$ and κ is the boundary curvature at the projection of $\boldsymbol{x}$ on $\partial\Omega$. If s is measured from the center of the arc $\partial\Omega_a$, the stretching $\eta = \varepsilon\hat{\eta}$, $s = \varepsilon\hat{s}$, $\hat{w}(\hat{\eta}, \hat{s}) = w(\eta, s)$ maps a boundary strip near $\partial\Omega_a$ into the upper half plane. Assuming, as we may, that the origin $\boldsymbol{x} = \boldsymbol{0}$ is at the center of $\partial\Omega_a$, we set $\boldsymbol{y} = \boldsymbol{x}/\varepsilon = (\hat{\eta}, \hat{s})$. An expansion in powers of ε gives the leading order boundary layer problem for (1.4)–(1.6) as

$$\hat{w}_{\mathrm{BL},\hat{\eta}\hat{\eta}} + \hat{w}_{\mathrm{BL},\hat{s}\hat{s}} = 0 \ \text{ for } 0 < \hat{\eta} < \infty,\ -\infty < \hat{s} < \infty \tag{1.40}$$

$$\hat{w}_{\mathrm{BL},\hat{\eta}}(0, \hat{s}) = 0 \ \text{ for } |\hat{s}| > 1, \quad \hat{w}_{\mathrm{BL}}(0, \hat{s}) = 0 \ \text{ for } |\hat{s}| < 1. \tag{1.41}$$

We specify the growth condition $\hat{w}_{\mathrm{BL}} \sim A \log|\boldsymbol{y}|$ as $|\boldsymbol{y}| \to \infty$, where A is as yet an undetermined constant. Setting $z = \hat{s} + i\hat{\eta}$, the transformation $\zeta = u + iv = \operatorname{Arcsin} z = -i\operatorname{Log}\left[iz + \sqrt{1-z^2}\right]$ maps the upper half plane $\hat{\eta} > 0$ onto the semi-infinite strip $\hat{\Omega} = \{-\pi/2 < u < \pi/2,\ 0 < v < \infty\}$. The mixed boundary value problem (1.40), (1.41) is transformed into

$$\hat{W}_{uu}(u, v) + \hat{W}_{vv}(u, v) = 0 \ \text{ for } (u, v) \in \hat{\Omega}$$

$$\hat{W}_u\left(\pm\frac{\pi}{2}, v\right) = 0 \ \text{ for } 0 < v < \infty,\ \ \hat{W}(u, 0) = 0 \ \text{ for } -\frac{\pi}{2} < u < \frac{\pi}{2},$$

where $\hat{W}(u, v) = \hat{w}_{\mathrm{BL}}(\hat{\eta}, \hat{s})$. The solutions $\hat{W}(u, v) = Av$ have the required logarithmic behavior for $|\boldsymbol{y}| \to \infty$, specifically,

$$\hat{w}_{\mathrm{BL}} \sim A \log|\boldsymbol{y}| + \log 2 + o(1) \ \text{ as } |\boldsymbol{y}| \to \infty. \tag{1.42}$$

The constant A is related to the boundary flux by $A = 2\pi^{-1} \int_0^1 \hat{w}_{\mathrm{BL},\hat{\eta}}(0, \hat{s})\, d\hat{s}$.

The leading term $w_{\text{OUT}}(\boldsymbol{x})$ in the outer expansion satisfies the original equation with the reduced boundary condition and the matching condition

$$\begin{aligned}
\Delta_{\boldsymbol{x}} w_{\text{OUT}}(\boldsymbol{x}) &= -\frac{1}{D} \quad \text{for } \boldsymbol{x} \in \Omega \\
\frac{\partial w_{\text{OUT}}(\boldsymbol{x})}{\partial n} &= 0 \quad \text{for } \boldsymbol{x} \in \partial\Omega - \{\boldsymbol{0}\} \\
w_{\text{OUT}}(\boldsymbol{x}) &\sim A\left[\log\left(\frac{1}{\varepsilon}\right) + \log 2 + \log|\boldsymbol{x}|\right] \quad \text{for } \boldsymbol{x} \to \boldsymbol{0}.
\end{aligned}$$

Now the compatibility condition (1.7) gives (1.30).

1.4.4 Exit Through Several Windows

The diffusion flux through a cluster of small absorbing windows in an otherwise reflecting boundary of a domain depends on the relative distance between the windows. For example, splitting an absorbing window into two equal parts and moving them apart increases the absorption flux by nearly 50 % (Holcman and Schuss 2008a). Thus, the case of several targets is not a straightforward generalization of the single target case. In fact, the MFPT of a Brownian trajectory to any one of several targets $\partial\Omega_a$ contains information about their relative distances. In particular, when the small Dirichlet windows form a cluster, the MFPT to any one of them is influenced by the others, which is not the case for well-separated windows (Holcman and Schuss 2008a,b).

First, we consider exit through two windows. For a regular domain in $\mathbb{R}^2$ with two Dirichlet arcs of lengths 2ε and 2δ (normalized by the perimeter $|\partial\Omega|$) and separated by the Euclidean distance $\Delta = \varepsilon + \Delta' + \delta$ between the centers, and in a regular domain in $\mathbb{R}^3$ with two Dirichlet circular windows of small radii a and b, separated by the Euclidean distance $\Delta = a + \Delta' + b$ between the centers (see Fig. 1.7), the NET $\bar{\tau}_\varepsilon$ is given by

$$\bar{\tau}_\varepsilon = \frac{|\Omega|}{\pi D\left(\log\frac{1}{\varepsilon} + \log\frac{1}{\delta}\right)} \frac{\log\frac{1}{\delta}\log\frac{1}{\varepsilon} - \left[\log\left|\varepsilon + \Delta' + \delta\right| + O(1)\right]^2}{1 + 2\dfrac{\log|\varepsilon + \Delta' + \delta| + O(1)}{\log\frac{1}{\delta} + \log\frac{1}{\varepsilon}}} \tag{1.43}$$

as $a, b, \varepsilon, \delta, \Delta' \to 0$ (Holcman and Schuss 2008a,b). As the windows drift apart the NET becomes the sum of the single window NETs. A new result is obtained as the windows touch (for $d = 3$) or merge (for $d = 2$).

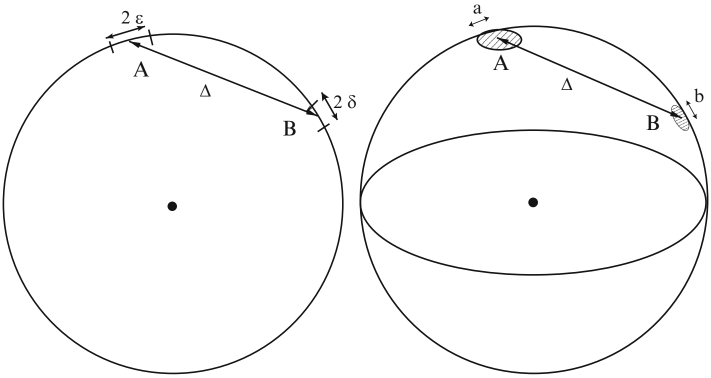

Fig. 1.7 Schematic representation of a disk and a sphere with two holes on the boundary. In the plane, the arclengths of the holes are 2δ and 2ε, respectively, at Euclidean distance Δ apart, while in 3D, the radii of the holes are, respectively, a and b

1.4.5 Derivation of the Helmholtz Integral Equation

The generalization of Theorem 1.3.1 to the case of two windows is as follows. The conditional NET of a Brownian trajectory $\boldsymbol{x}(t)$ that starts at $\boldsymbol{x} \in \Omega$ is $u(\boldsymbol{x}) = E[\tau \,|\, \boldsymbol{x}(0) = \boldsymbol{x}]$, which is the solution of the mixed boundary value problem (1.4)–(1.6), through each hole is

$$\Phi_A = -\int\limits_A g(\boldsymbol{x})\, dS_{\boldsymbol{x}}, \quad \Phi_B = -\int\limits_B g(\boldsymbol{x})\, dS_{\boldsymbol{x}},$$

where for $\boldsymbol{x} \in \partial\Omega_a$, $g(\boldsymbol{x}) = D\partial u(\boldsymbol{x})/\partial n$ is the absorption flux density. To compute the fluxes, we first integrate Eq. (1.4) over the domain and get

$$\Phi_A + \Phi_B = |\Omega|. \tag{1.44}$$

The solution of (1.4)–(1.6) is represented as

$$u(\boldsymbol{\xi}) = \int\limits_{\Omega} N(\boldsymbol{x}, \boldsymbol{\xi})\, d\boldsymbol{x} + \int\limits_{\partial\Omega_a} N(\boldsymbol{x}, \boldsymbol{\xi}) \frac{\partial u(\boldsymbol{x})}{\partial n}\, dS_{\boldsymbol{x}} + C,$$

where $C = |\partial\Omega|^{-1} \oint_{\partial\Omega} u(\boldsymbol{x})\, dS_{\boldsymbol{x}}$ is a constant to be determined from the boundary condition (1.5) and $dS_{\boldsymbol{x}}$ is a surface area element on $\partial\Omega_a$. To estimate C, we choose, respectively, $\boldsymbol{\xi} \in A$ and $\boldsymbol{\xi} \in B$, and using the boundary condition (1.5), we obtain the two equations

$$F(\boldsymbol{\xi}) = \int\limits_A N(\boldsymbol{x}, \boldsymbol{\xi}) g_A(\boldsymbol{x})\, dS_{\boldsymbol{x}} + \int\limits_B N(\boldsymbol{x}, \boldsymbol{\xi}) g_B(\boldsymbol{x})\, dS_{\boldsymbol{x}} \text{ for } \boldsymbol{\xi} \in A \bigcup B, \tag{1.45}$$

where

$$F(\boldsymbol{\xi}) = -\left(\int\limits_{\Omega} N(\boldsymbol{x}, \boldsymbol{\xi})\, d\boldsymbol{x} + C\right) \approx -C. \tag{1.46}$$

Equation (1.45) is called the Helmholtz integral equation (Helmholtz 1860). We denote the centers of the absorbing disks (arcs) A and B by $\mathbf{0}_A$ and $\mathbf{0}_B$, respectively. The variables r and r' are the signed arclengths in A and B, measured from their centers. The equations for the fluxes g_A and g_B in the windows A and B form an approximate solution of (1.45) for well-separated A and B and constants $\tilde{g}_A,\ \tilde{g}_B$. They are only approximations, because the integral $\int_B N(\boldsymbol{x}, \boldsymbol{\xi}) g_B(\boldsymbol{x})\, dS_{\boldsymbol{x}}$ is not constant for $\boldsymbol{\xi} \in A$, though it is much smaller than $\int_A N(\boldsymbol{x}, \boldsymbol{\xi}) g_A(\boldsymbol{x})\, dS_{\boldsymbol{x}}$ there. If, however, A and B are not well separated, the flux expressions are not even an approximate solution, because the integrals are of comparable orders of magnitude.

The fluxes calculated in *loc. cit.* are

$$g_A(\boldsymbol{x}) \sim \frac{\tilde{g}_A f\left(\dfrac{r}{\varepsilon}\right)}{\sqrt{1 - \dfrac{r^2}{\varepsilon^2}}} \quad \text{for } \boldsymbol{x} \in A,\ d = 2 \tag{1.47}$$

and a similar expression for $\boldsymbol{x} \in B$, where $f(\alpha)$ is a positive smooth function for $|\alpha| \le 1$ such that $f(0) = 1$.

1.4.6 Asymptotic Solution of the Helmholtz Equation

It was shown in Singer et al. (2006a) that the flux density through a single hole of size 2ε is given by (1.47), where $f(x)$ is a smooth positive even function for $-1 \le x \le 1$ and $f(0) = 1$, where $\tilde{g}_A$ and $\tilde{g}_B$ are constants. The computations of Holcman and Schuss (2004) and Singer et al. (2006b, Part II) show that the solution of (1.45) has the form

$$g_A(r) = \frac{\tilde{g}_A f\left(\dfrac{r}{\varepsilon}\right)}{\sqrt{1 - \dfrac{r^2}{\varepsilon^2}}} \quad \text{for } -\varepsilon \le r \le \varepsilon,$$

$$g_B(r) = \frac{\tilde{g}_B f\left(\dfrac{r}{\varepsilon}\right)}{\sqrt{1 - \dfrac{r^2}{\varepsilon^2}}} \quad \text{for } \varepsilon + \Delta' \le r \le 3\varepsilon + \Delta'.$$

Now f is a positive smooth function for $-1 \le x \le 1$ and for $1 + \Delta'/\varepsilon \le x \le 3 + \Delta'/\varepsilon$, such that $f(0) = f\left(2 + \Delta'/\varepsilon\right) = 1$. $f_\Delta(0) = f_\Delta\left(2 + \Delta'/\varepsilon\right) = 1$. For small ε and all $\xi \ge \varepsilon$, we approximate

$$\int_A N(\boldsymbol{x},\xi)g_A(\boldsymbol{x})\,dS_{\boldsymbol{x}} = \varepsilon\alpha\tilde{g}_A[N(\mathbf{0}_A,\mathbf{0}_B)+O(1)], \tag{1.48}$$

where

$$\alpha = \int_{-1}^{1} \frac{f(x)\,dx}{\sqrt{1-x^2}}. \tag{1.49}$$

and the Neumann function for the variables $\boldsymbol{x}$ and $\boldsymbol{\xi}$ at the centers of the two windows, respectively, is given by

$$N(\mathbf{0}_A,\mathbf{0}_B) = -\frac{1}{\pi}\log(\varepsilon+\delta+\Delta') + O(1).$$

The detailed analysis of the approximation is given in Holcman and Schuss (2008a). Using (1.48) and the computations of Singer et al. (2006a), we get that

$$\int_A N(\boldsymbol{x},\boldsymbol{\xi})g_A(\boldsymbol{x})\,dS_{\boldsymbol{x}} \approx \begin{cases} \dfrac{\alpha\varepsilon[-\log\varepsilon+\pi v_S(0,\varepsilon)]\tilde{g}_A}{D\pi} & \text{for } \boldsymbol{\xi}\in A \\ -\varepsilon\alpha\tilde{g}_A N(\mathbf{0}_A,\mathbf{0}_B)+O(1) & \text{for } \boldsymbol{\xi}\in B. \end{cases}$$

An analogous expression is obtained for $\boldsymbol{x}\in B$ and $\boldsymbol{\xi}\in A$ (with β instead of α). Using the boundary conditions (1.45) and the approximation (1.60), we obtain that

$$\begin{aligned} &\frac{\alpha\varepsilon(\log\varepsilon)\tilde{g}_A[1+o(1)]}{\pi} + \frac{\delta\beta\tilde{g}_B\,[\log(\varepsilon+\delta+\Delta')+O(1)]}{\pi} \\ &= \frac{\varepsilon\alpha\tilde{g}_A\,[\log(\varepsilon+\delta+\Delta')+O(1)]}{\pi} + \frac{\beta\delta(\log\delta)\tilde{g}_B[1+o(1)]}{\pi} = C. \end{aligned}$$

The flux condition (1.44) gives for small ε that

$$\int_A g_A(\boldsymbol{x})\,dS_{\boldsymbol{x}} = \int_{-\varepsilon}^{\varepsilon} \frac{\tilde{g}_A f\left(\dfrac{r}{\varepsilon}\right)}{\sqrt{1-\dfrac{r^2}{\varepsilon^2}}}\,dr\,(1+o(1)) = \alpha\varepsilon\tilde{g}_A(1+o(1)),$$

hence, for $d=2$, Eq. (1.44) gives

$$\alpha\varepsilon\tilde{g}_A + \beta\delta\tilde{g}_B = -|\Omega|[1+o(1)]. \tag{1.50}$$

Therefore, we get for the constant $C=\bar{\tau}_{A\cup B}$, which is the MFPT to any one of the two windows,

$$C = \frac{|\Omega|[1+o(1)]}{\pi\left(\log\dfrac{1}{\varepsilon}+\log\dfrac{1}{\delta}\right)} \frac{\log\dfrac{1}{\delta}\log\dfrac{1}{\varepsilon} - [\log(\varepsilon+\Delta'+\delta)+O(1)]^2}{1-2\dfrac{[\log(\varepsilon+\Delta'+\delta)+O(1)]}{\log\dfrac{1}{\delta}+\log\dfrac{1}{\varepsilon}}}. \tag{1.51}$$

Equation (1.51) reduces to the single window formula (1.30) in the limit $\delta \to 0$. The condition (1.44) gives

$$\alpha\varepsilon\tilde{g}_A + \beta\delta\tilde{g}_B = -|\Omega|(1 + o(1)). \tag{1.52}$$

Note that the derivation of (1.51) requires a generalization of the method of Holcman and Schuss (2004) and Singer et al. (2006a), which consists in deriving and solving a Helmholtz integral equation on several windows. The solution depends on the separation between the windows in a strongly nonlinear way. The effect of varying the distance between the windows is shown in Fig. 1.8. Recently, using matched asymptotics (Ward et al. 2010), the following estimate for two windows was obtained,

$$\bar{v} \sim \frac{|\Omega|}{D\pi}\left[-\frac{1}{2}\log\left(\frac{\varepsilon l}{4}\right) - \frac{\pi}{2}\log|x_2 - x_1| + \pi R_*\right] \text{ for } O(\varepsilon) \ll |x_2 - x_1| \ll O(1),$$

where $R_* \equiv R(x_1^*, x_1^*)$ is the regular part of the Neumann function at $x_1^* \in \partial\Omega$. In general,

$$\bar{v} \sim \begin{cases} \dfrac{|\Omega|}{D\pi}\left[-\log(\varepsilon d_1) + \pi R_*\right] \\ \text{for a two-window cluster} \\ \\ \dfrac{|\Omega|}{D\pi}\left[-\dfrac{1}{2}\log\left(\dfrac{\varepsilon l}{4}\right) + \dfrac{\pi}{4}\left(R(x_1;x_1) + R(x_2;x_2) + 2G(x_1;x_2)\right)\right] \\ \text{for well-separated windows.} \end{cases}$$

Here $x_1^* \in \partial\Omega$ is the center of the two-window cluster, $R_* \equiv R(x_1^*, x_1^*)$ is the regular part of the Neumann function at x_1^*, and

$$d_1 = \frac{l}{2}\left[1 + \frac{2a}{l}\right]^{1/2}, \tag{1.53}$$

where $2a$ is the distance along the boundary between the two windows. For the special case of the unit disk $\mathcal{D}(1)$, where the regular part R has the uniform value $R = 1/(8\pi)$. Indeed, the Neumann function $G(x;\xi)$ with $\int_\Omega G(x;\xi)\,dx = 0$ and $\xi \in \partial\mathcal{D}(1)$ is given by Ward et al. (2010)

$$G(x;\xi) = -\frac{1}{\pi}\log|x - \xi| + \frac{|x|^2}{4\pi} - \frac{1}{8\pi}, \qquad R(\xi;\xi) = \frac{1}{8\pi}. \tag{1.54}$$

The average MFPT with respect to the initial position to any one of N equal absorbing arcs of length 2ε, centered at $x_1, \ldots, x_N$ on the boundary of the unit disk, is

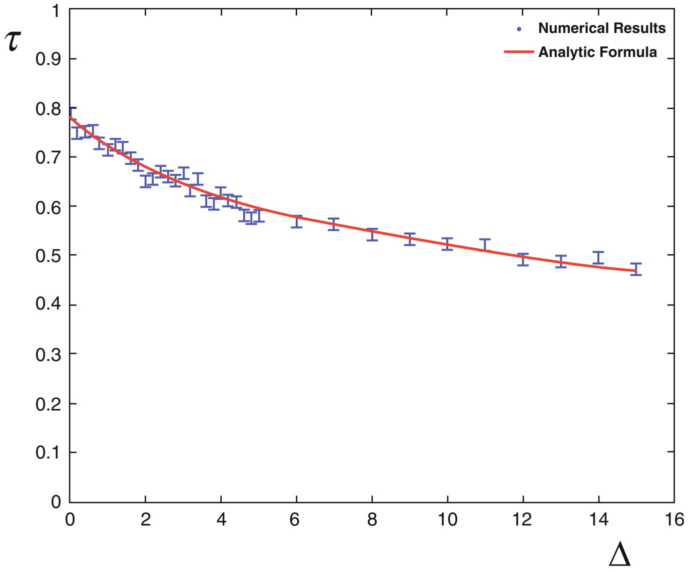

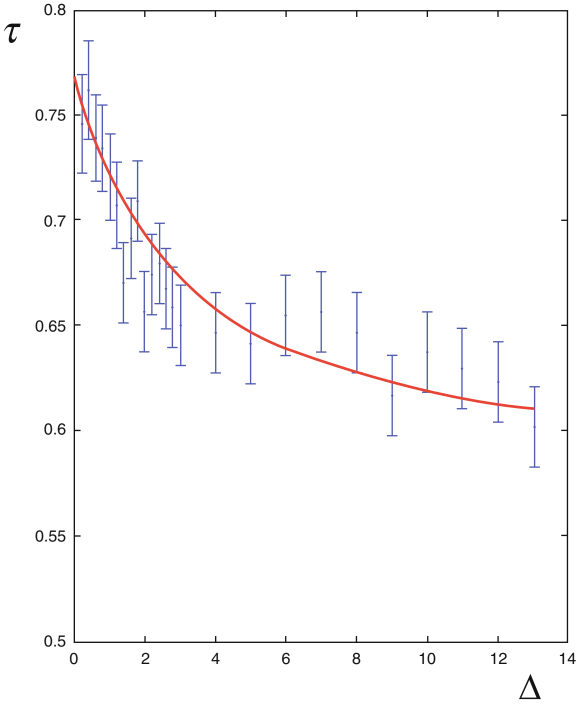

Fig. 1.8 The MFPT τ, normalized by τ_1 (the NET for a single window), as a function of the distance Δ between two holes, normalized by ε. *Top*: the MFPT for $d = 2, \varepsilon = \delta = 0.02$, $D = 1$. The cell radius is $R = 2$. The contribution of the regular part of the Green function is estimated as 1.3 by a numerical fit. *Bottom*: the values of the parameters are $d = 3$, $a = \varepsilon = \delta = 0.3$, $R = 2$, $D = 1$

$$\bar{v} \sim \frac{1}{DN}\left[-\log\left(\frac{\varepsilon}{2}\right)+\frac{N}{8}-\frac{1}{N}\sum_{i=1}^{N}\sum_{j\neq i}^{N}\log|x_i-x_j|\right]. \tag{1.55}$$

The sum in (1.55) is minimized when $x_j = e^{2\pi ij/N}$ are the equally spaced Nth roots of unity,

$$\begin{aligned} v(x) &\sim \frac{1}{DN}\left[-\log\left(\frac{\varepsilon N}{2}\right)+\frac{N}{8}-\pi\sum_{j=1}^{N}G(x;x_j)\right] \\ \bar{\tau} &\sim \frac{1}{DN}\left[-\log\left(\frac{\varepsilon N}{2}\right)+\frac{N}{8}\right]. \end{aligned} \tag{1.56}$$

1.4.7 Annotations

The narrow escape problem in diffusion theory was considered first by Lord Rayleigh in (1945) and elaborated in Fabrikant (1989, 1991); the terminology NET was introduced in Singer et al. (2006a). A recent review of early results on the NET problem with many biological applications is given in Bressloff and Newby (2013) and in Holcman and Schuss (2013a).

In the matched asymptotics approach to the NET problem from a domain Ω in $\mathbb{R}^2$, a boundary layer solution is constructed near an absorbing window $\partial\Omega_a$ of size 2ε (Ward et al. 1993, 2010). The method has been developed in Ward and Keller (1993), Ward et al. (1993), Ward and Van De Velde (1992), Kolokolnikov et al. (2005), and Cheviakov et al. (2010). In three dimensions the method was used in Ward and Keller (1993), where the boundary layer problem is the classical electrified disk problem (Jackson 1975). Further refinements of (1.30) are given in Ward and Keller (1993), Ward et al. (1993), Ward and Van De Velde (1992), Kolokolnikov et al. (2005), Cheviakov et al. (2010), Singer et al. (2006b), and Schuss et al. (2007).

The NET calculated in Chap. 1 was calculated for small absorbing windows in a smooth reflecting boundary in Ward and Keller (1993), Ward et al. (1993), Ward and Van De Velde (1992), Kolokolnikov et al. (2005), Cheviakov et al. (2010), Coombs et al. (2009), Grigoriev et al. (2002), Holcman and Schuss (2004), Singer et al. (2006a,b,c), Singer and Schuss (2006), Bénichou and Voituriez (2008), Schuss et al. (2007), Gandolfi et al. (1985), and others. Several more complex cases, such as the NET through a window at a corner or at a cusp in the boundary and the NET on Riemannian manifolds, were considered in Singer et al. (2006a,b,c). Exit through many holes is discussed in Holcman and Schuss (2008a,b, 2012a), and Cheviakov et al. (2010) and the references therein.

1.5 NET in Bounded Domains in $\mathbb{R}^3$

The NET problem in three dimensions is more complicated than that in two dimensions, primarily because the singularity of Neumann's function for a regular domain is more complicated than (1.2).

1.5.1 *The Neumann Function in Regular Domains in* $\mathbb{R}^3$

The Neumann function $N(\boldsymbol{x},\boldsymbol{y})$ for a bounded domain $\Omega \subset \mathbb{R}^3$ with a sufficiently smooth boundary $\partial\Omega$ is the solution of the boundary value problem

$$\Delta_{\boldsymbol{x}} N(\boldsymbol{x},\boldsymbol{y}) = -\delta(\boldsymbol{x}-\boldsymbol{y}) + \tfrac{1}{|\Omega|}, \quad \text{for } \boldsymbol{x},\boldsymbol{y} \in \Omega \tag{1.57}$$

$$\frac{\partial N(\boldsymbol{x},\boldsymbol{y})}{\partial \nu_{\boldsymbol{x}}} = 0, \quad \text{for } \boldsymbol{x} \in \partial\Omega,\ \boldsymbol{y} \in \Omega, \tag{1.58}$$

where $\boldsymbol{\nu}(\boldsymbol{x})$ is the outer unit normal to the boundary $\partial\Omega$. If $\boldsymbol{x}$ or $\boldsymbol{y}$ (or both) are in $\partial\Omega$, then only a half of any sufficiently small ball about a boundary point is contained in Ω, which means that the singularity of Neumann's function is $(2\pi|\boldsymbol{x}-\boldsymbol{y}|)^{-1}$. Therefore Neumann's function for $\boldsymbol{y} \in \partial\Omega$ can be written as

$$N(\boldsymbol{x},\boldsymbol{y}) = \frac{1}{2\pi|\boldsymbol{x}-\boldsymbol{y}|} + v(\boldsymbol{x},\boldsymbol{y}), \tag{1.59}$$

where $v(\boldsymbol{x},\boldsymbol{y})$ satisfies

$$\Delta_{\boldsymbol{x}} v(\boldsymbol{x},\boldsymbol{y}) = \frac{1}{|\Omega|} \quad \text{for } \boldsymbol{x} \in \Omega,\ \boldsymbol{y} \in \partial\Omega \tag{1.60}$$

In general, the Neumann function has the form (Garabedian 1964)

$$N(\boldsymbol{x},\boldsymbol{\xi}) = \frac{1}{4\pi|\boldsymbol{x}-\boldsymbol{\xi}|} + v_S(\boldsymbol{x},\boldsymbol{\xi}), \tag{1.61}$$

where $v_S(\boldsymbol{x},\boldsymbol{\xi})$ has a weaker singularity at $\boldsymbol{x}=\boldsymbol{\xi}$ when $\boldsymbol{x} \in \partial\Omega$ and $\boldsymbol{\xi} \in \Omega \cup \partial\Omega$ (see Theorem 1.5.1 below). It follows that only the singular part of the Neumann function contributes to the leading order approximation to the solution of the integral equation (1.10). Thus we obtain for the leading order approximation to the absorption flux density $g_0(\boldsymbol{x})$ on $\partial\Omega_a$ and to the leading order approximation C_0 of the MFPT C the Helmholtz integral equation (1.10)

$$\frac{1}{2\pi}\int\limits_{\partial\Omega_a} \frac{g_0(\boldsymbol{x})}{|\boldsymbol{x}-\boldsymbol{\xi}|}\, dS_{\boldsymbol{x}} = -C_0. \tag{1.62}$$

Here C_0 is a constant, which represents the first approximation to the MFPT. It is also the electrostatic capacity of the window (Jackson 1975).

The structure of Neumann's function for a regular domain in $\mathbb{R}^3$ is described in the following theorem (Popov 1992).

Theorem 1.5.1 (Popov). *Assume $\Omega \in \mathbb{R}^3$ is a bounded domain whose boundary $\partial\Omega$ has continuous partial derivatives up to order three. Then for $z \in \partial\Omega$, $\boldsymbol{y} \in \Omega \cup \partial\Omega$, the structure of the Neumann function (in dimensionless variables) is*

$$N(\boldsymbol{y}, z) = \frac{1}{2\pi|\boldsymbol{y} - z|} - \frac{1}{8\pi}\left[L(z) + N(z)\right] \ln|\boldsymbol{y} - z| + v_S(\boldsymbol{y}, z), \tag{1.63}$$

where $L(z)$ and $N(z)$ are the principal curvatures of $\partial\Omega$ at z and $v_S(\boldsymbol{y}, z)$ is a bounded function of $\boldsymbol{x}, \boldsymbol{y}$ in Ω.

Thus Neumann's function for a ball in $\mathbb{R}^3$ is found from the canonical representation of a hemisphere of (dimensionless) radius R at the south pole, $x_3 = R - \sqrt{R^2 - (x_1^2 + x_2^2)}$. We find that $L(z) = N(z) = \dfrac{1}{R}$, so for $|z| = R$ we have

$$N(\boldsymbol{y}, z) = \frac{1}{2\pi|\boldsymbol{y} - z|} + \frac{1}{4\pi R} \ln \frac{1}{|\boldsymbol{y} - z|} + O(1). \tag{1.64}$$

Further analysis of the $O(1)$ term is given in Silbergleit et al. (2003). The structure of Neumann's function for a ball is given in Kellog (1954, p. 247, Exercise 4).

1.5.2 Elliptic Absorbing Window

An explicit solution to the Helmholtz equation (1.62) can be found when the hole $\partial\Omega_a$ is an ellipse (Rayleigh 1945; Lurie 1964). Consequently, the MFPT from a large cavity of volume $|\Omega|$ to a small elliptic absorbing window on an otherwise reflecting boundary $\partial\Omega$ can be calculated explicitly to leading order.

Theorem 1.5.2. *Assume the boundary $\partial\Omega$ of a bounded domain $\Omega \subset \mathbb{R}^3$ is sufficiently regular and the absorbing boundary $\partial\Omega_a$ is the ellipse*

$$\frac{x^2}{a^2} + \frac{y^2}{b^2} \leq 1, \quad z = 0, \quad (b \leq a). \tag{1.65}$$

If

$$\varepsilon = \left(\frac{|\partial\Omega_a|}{|\partial\Omega|}\right)^{1/2} \ll 1,$$

and

$$\frac{|\Omega|^{2/3}}{|\partial\Omega|}, \frac{|\partial\Omega|}{|\Omega|^{2/3}} = O(1) \;\; \textit{for } \varepsilon \ll 1,$$

then the MFPT from a Ω *to* $\partial\Omega_a$ *is to leading order*

$$\mathbb{E}\tau(a,b) \sim \frac{|\Omega|}{2\pi Da} K(e), \tag{1.66}$$

where $K(\cdot)$ *is the complete elliptic integral of the first kind and* $e = \sqrt{1 - b^2/a^2}$ *is the eccentricity of the ellipse.*

If the hole is circular, $e = 0$ and $K(0) = \pi/2$, so that

$$\mathbb{E}\tau(a,a) \sim \frac{|\Omega|}{4Da} = O\left(\frac{1}{\varepsilon}\right). \tag{1.67}$$

If the hole is an elongated ellipse with $b \ll a$, the eccentricity is $e = \sqrt{1 - b^2/a^2} \simeq 1$, which gives the asymptotic expansion for the elliptic integral (Abramowitz and Stegun 1972, p. 591)

$$K(e) \approx \frac{1}{2} \log\left(\frac{16}{1-e}\right). \tag{1.68}$$

Now (1.66) becomes

$$\mathbb{E}\tau(a,b) \sim \frac{|\Omega|}{2\pi Da} \log\left(\frac{4a}{b}\right), \tag{1.69}$$

showing that for $b \ll 1$ and $b \ll a$, the NET depends logarithmically on the short axis b.

A related problem is that of reaching a narrow spine-like absorbing or partially absorbing protrusion of the boundary into the domain. For the case of an ellipsoidal protrusion with transversal semi-axes $a_2 \geq a_1$ and height a_3 the eccentricity is $e = \sqrt{1 - a_1^2/a_2^2}$ with $f = a_3/a_1$. With the elliptic integral

$$K(e,f) = \frac{2}{\pi} \int_0^{\pi/2} \frac{d\theta}{\sqrt{(1 - e^2 \sin^2\theta)(1 + f^2 \tan^2\theta)}}, \tag{1.70}$$

the NET is given by Reingruber et al. (2009)

$$\bar{\tau} = \frac{|V|}{4a_1 D} K(e,f). \tag{1.71}$$

For $a_1 = a_2$ and $f = a_3/a_1$, the NET is

$$\bar{\tau} = \frac{|V|}{2\pi a_1 D} \begin{cases} \dfrac{\arccos f}{\sqrt{1-f^2}}, & f \le 1 \\ \\ \dfrac{\operatorname{arccosh} f}{\sqrt{f^2-1}}, & f \ge 1. \end{cases} \tag{1.72}$$

In the limit $f \gg 1$, we obtain the approximation

$$\bar{\tau} \approx \frac{|V|}{2\pi a_1 D} \frac{\ln(2f)}{f}.$$

If the narrow protrusion is reflecting, except for N absorbing circular disks of radius s on its surface, the NET is given approximately by Reingruber et al. (2009)

$$\tau_{\text{part-spine}} = \frac{|V|}{4a_1 D} \frac{K(e,f)Ns + (1-\sigma)a_1}{Ns}. \tag{1.73}$$

The proof of Theorem 1.5.2 is based on the following lemma (see Lurie 1964).

Lemma 1.5.1 (Helmholtz (1860)). *Assume $\partial\Omega_a$ is the ellipse*

$$\frac{x^2}{a^2} + \frac{y^2}{b^2} \le 1, \quad z = 0, \quad (b \le a).$$

Then the solution of the Helmholtz equation (1.62) is

$$g_0(\boldsymbol{x}) = \frac{\tilde{g}_0}{\sqrt{1 - \dfrac{x^2}{a^2} - \dfrac{y^2}{b^2}}}, \tag{1.74}$$

where $\tilde{g}_0$ is a constant.

Proof (of Theorem 1.5.2). The MFPT is to leading order the constant C_0 in (1.74), therefore we need to determine the value of the constant $\tilde{g}_0$ in (1.74). To this end, we use the value

$$\int\limits_{\partial\Omega_a} g_0(\boldsymbol{x})\, dS_x = \int\limits_{-a}^{a} dx \int\limits_{-b\sqrt{1-\frac{x^2}{a^2}}}^{b\sqrt{1-\frac{x^2}{a^2}}} \frac{\tilde{g}_0\, dy}{\sqrt{1 - \dfrac{x^2}{a^2} - \dfrac{y^2}{b^2}}} = 2\pi ab\tilde{g}_0$$

and apply the compatibility condition (1.7) to obtain

$$\tilde{g}_0 = -\frac{|\Omega|}{2\pi Dab}.$$

Hence

$$C_0 = -\frac{1}{2\pi} \int\limits_{\partial\Omega_a} \frac{g_0(\boldsymbol{x})}{|\boldsymbol{x}-\boldsymbol{y}|}\, dS_x = \frac{|\Omega|}{2\pi Da} K(e). \tag{1.75}$$

It follows that

$$\mathbb{E}\tau \sim \frac{|\Omega|}{2\pi Da} K(e).$$

□

The explicit solution of the Helmholtz equation for a general shaped window, such as a rectangle, is yet unknown.

1.6 Second Order Asymptotics for a Circular Window

To obtain higher order asymptotics of the MFPT, we use Popov's Theorem 1.5.1 and Helmholtz's Lemma 1.5.1 in (1.10). We get the following theorem.

Theorem 1.6.1. *Under the assumptions of Theorems 1.5.1 and 1.5.2 for a circular window of radius* $a \ll |\partial\Omega|^{1/2}$

$$\mathbb{E}\tau = \frac{|\Omega|}{4aD\left[1 + \dfrac{L(\mathbf{0}) + N(\mathbf{0})}{2\pi}\, a \log a + o(a \log a)\right]} \quad \textit{for } a \ll |\partial\Omega|^{1/2}. \tag{1.76}$$

Proof. To obtain higher order asymptotics of the MFPT, we us Popov's Theorem 1.5.1 and Helmholtz's Lemma 1.5.1 in (1.10), which, in view of (1.63), now becomes the generalized Helmholtz equation

$$\int\limits_{\partial\Omega_a} g(\boldsymbol{x}) \left[\tfrac{1}{2\pi|\boldsymbol{x}-\boldsymbol{y}|} + H(\boldsymbol{x},\boldsymbol{y}) \log|\boldsymbol{x}-\boldsymbol{y}| + O(1)\right] dS_{\boldsymbol{x}} = -C \quad \text{for } \boldsymbol{y} \in \partial\Omega_a \tag{1.77}$$

$$H(\boldsymbol{x},\boldsymbol{y}) = -\tfrac{1}{8\pi}[L(\boldsymbol{y}) + N(\boldsymbol{y})] \sim -\tfrac{1}{8\pi}[L(\mathbf{0}) + N(\mathbf{0})], \quad \text{for } \boldsymbol{x},\boldsymbol{y} \in \partial\Omega_a,\ \varepsilon \ll 1,$$

where $L(\mathbf{0}), N(\mathbf{0})$ are the principal curvatures at the center $\mathbf{0}$ of $\partial\Omega_a$. To solve (1.77), we expand $g(\boldsymbol{x}) = g_0(\boldsymbol{x}) + g_1(\boldsymbol{x}) + g_2(\boldsymbol{x}) + \cdots$, where $g_{i+1}(\boldsymbol{x}) \ll g_i(\boldsymbol{x})$ for $\varepsilon \ll 1$ and choose

$$g_0(\boldsymbol{x}) = \frac{-2C}{a\pi\sqrt{1 - \dfrac{|\boldsymbol{x}|^2}{a^2}}}. \tag{1.78}$$

According to Lemma 1.5.1, if $\partial\Omega_a$ is a circular disk of radius a, then

$$\frac{1}{2\pi}\int\limits_{\partial\Omega_a}\frac{g_0(\boldsymbol{x})}{|\boldsymbol{x}-\boldsymbol{y}|}\,dS_{\boldsymbol{x}}=C\quad\text{for all}\quad \boldsymbol{y}\in\partial\Omega_a. \tag{1.79}$$

It follows that $g_1(\boldsymbol{x})$ satisfies the integral equation

$$\frac{1}{2\pi}\int\limits_{\partial\Omega_a}\frac{g_1(\boldsymbol{x})}{|\boldsymbol{x}-\boldsymbol{y}|}\,dS_{\boldsymbol{x}}=\frac{2C}{a\pi}\int\limits_{\partial\Omega_a}\frac{H(\boldsymbol{x},\boldsymbol{y})\log|\boldsymbol{x}-\boldsymbol{y}|}{\sqrt{1-\dfrac{|\boldsymbol{x}|^2}{a^2}}}\,dS_{\boldsymbol{x}}. \tag{1.80}$$

Setting $y=a\boldsymbol{\eta}$, $\boldsymbol{x}=a\boldsymbol{\xi}$, and changing to polar coordinates in the integral on the right-hand side of (1.80), we obtain

$$\frac{1}{2\pi}\int\limits_{\partial\Omega_a}\frac{g_1(\boldsymbol{x})}{|\boldsymbol{x}-\boldsymbol{y}|}\,dS_{\boldsymbol{x}}=\frac{2Ca^2}{a\pi}\int\limits_0^{2\pi}d\theta\int\limits_0^1\frac{H(a\boldsymbol{\xi},a\boldsymbol{\eta})\,[\log a+\log|\boldsymbol{\xi}-\boldsymbol{\eta}|]}{\sqrt{1-r^2}}\,r\,dr, \tag{1.81}$$

which gives in the limit $\varepsilon\to0$ (e.g., keeping $|\Omega|$ fixed and $a\to0$) that

$$\frac{1}{2\pi}\int\limits_{\partial\Omega_a}\frac{g_1(\boldsymbol{x})}{|\boldsymbol{x}-\boldsymbol{y}|}\,dS_{\boldsymbol{x}}=-\frac{C[L(\boldsymbol{0})+N(\boldsymbol{0})]}{2\pi}\,a\log a+o(a\log a). \tag{1.82}$$

As in the pair (1.78), (1.79), we obtain that

$$g_1(\boldsymbol{x})=\frac{-C[L(\boldsymbol{0})+N(\boldsymbol{0})]}{\pi^2\sqrt{1-\dfrac{|\boldsymbol{x}|^2}{a^2}}}\,\log a+o(\log a). \tag{1.83}$$

To determine the asymptotic value of the constant C, we recall that $g(\boldsymbol{x})=\partial u(\boldsymbol{x})/\partial\nu$ and use in (1.7) the approximation

$$g(\boldsymbol{x})\sim g_0(\boldsymbol{x})+g_1(\boldsymbol{x})\sim\frac{-2C}{a\pi\sqrt{1-\dfrac{|\boldsymbol{x}|^2}{a^2}}}\left[1+\frac{L(\boldsymbol{0})+N(\boldsymbol{0})}{2\pi}\,a\log a\right].$$

We obtain the NET (in dimensionless variables) as

$$\mathbb{E}\tau=\frac{|\Omega|}{4aD\left[1+\dfrac{L(\boldsymbol{0})+N(\boldsymbol{0})}{2\pi}\,a\log a+o(a\log a)\right]},$$

which is (1.76). □

Higher order asymptotics of the principal eigenvalue of the Laplace equation in Ω with the mixed Dirichlet–Neumann boundary conditions (1.5), (1.6) are derived from the asymptotic representation $\lambda_1(a) \sim (\mathbb{E}\tau)^{-1}$ for $a \ll |\partial\Omega|^{1/2}$, which gives

$$\lambda_1(a) = \frac{4aD}{|\Omega|}\left[1 + \frac{L(\mathbf{0}) + N(\mathbf{0})}{2\pi}\, a \log a + o(a \log a)\right]. \tag{1.84}$$

If Ω is a ball of radius R, then $L(\mathbf{0}) + N(\mathbf{0}) = 2/R$ and the NET $\mathbb{E}\tau = C$ is given (in dimensional variables) by

$$\begin{aligned}\mathbb{E}\tau &= \frac{|\Omega|}{4aD\left[1 - \dfrac{a}{\pi R}\log\dfrac{R}{a} + o\left(\dfrac{a}{R}\log\dfrac{R}{a}\right)\right]}\\ &= \frac{|\Omega|}{4aD}\left[1 + \frac{a}{\pi R}\log\frac{R}{a} + o\left(\frac{a}{R}\log\frac{R}{a}\right)\right].\end{aligned} \tag{1.85}$$

Higher order asymptotics for a ball can be obtained from Silbergleit et al. (2003) and Kellog (1954, p. 247, Exercise 4).

1.6.1 Higher Order Asymptotics in the Unit Ball

If Neumann's function is defined as the solution of

$$\Delta G_s = \frac{1}{|\Omega|} \text{ for } \boldsymbol{x} \in \Omega, \quad \partial_r G_s = \delta(\cos\theta - \cos\theta_j)\delta(\phi - \phi_j) \text{ for } \boldsymbol{x} \in \partial\Omega, \tag{1.86}$$

$$\int_\Omega G_s\, d\boldsymbol{x} = 0,$$

then the following lemma holds (Cheviakov et al. 2010).

Lemma 1.6.1 (Cheviakov, Ward, Straube). *Neumann's function on the unit ball in $\mathbb{R}^3$, satisfying (1.86), is given by*

$$\begin{aligned}G_s(\boldsymbol{x}; \boldsymbol{x}_j) &= \frac{1}{2\pi\left|\boldsymbol{x} - \boldsymbol{x}_j\right|} + \frac{1}{8\pi}\left(|\boldsymbol{x}|^2 + 1\right)\\ &\quad + \frac{1}{4\pi}\log\left(\frac{2}{1 - |\boldsymbol{x}|\cos\gamma + \left|\boldsymbol{x} - \boldsymbol{x}_j\right|}\right) - \frac{7}{10\pi},\end{aligned} \tag{1.87}$$

where γ is the angle between $\boldsymbol{x}$ and $\boldsymbol{x}_j$, given by $\cos\gamma = \cos\theta\cos\theta_j + \sin\theta\sin\theta_j\cos(\phi - \phi_j)$.

1.7 The NET Through Multiple Absorbing Windows

Next, we generalize the matched asymptotics expansion presented in Sect. 1.4.3 for two-dimensional domains to the three-dimensional unit ball with N small disjoint absorbing windows, $\partial\Omega_{\varepsilon_j}$ ($j = 1, \dots, N$) each of area $|\partial\Omega_{\varepsilon_j}| = O(\varepsilon^2)$, in the limit $\varepsilon \to 0$. We need to construct a uniform asymptotic expansion of the solution to the mixed problem

$$\Delta v \equiv v_{rr} + \frac{2}{r}v_r + \frac{1}{r^2\sin^2\theta}v_{\phi\phi} + \frac{\cot\theta}{r^2}v_\theta + \frac{1}{r^2}v_{\theta\theta} = -\frac{1}{D} \quad \text{for } r = |\boldsymbol{x}| \le 1 \tag{1.88}$$

$$v = 0 \quad \text{for } \boldsymbol{x} \in \partial\Omega_a = \cup_{j=1}^{N} \partial\Omega_{\varepsilon_j},\ j = 1, \dots, N, \quad \partial_r v = 0 \text{ for } \boldsymbol{x} \in \partial\Omega \backslash \partial\Omega_a. \tag{1.89}$$

The outer solution, valid away from $\partial\Omega_{\varepsilon_j}$, is given in the form of the expansion suggested by Lemma 1.6.1,

$$v(\boldsymbol{x}) \sim \varepsilon^{-1}v_0 + \log\left(\frac{\varepsilon}{2}\right)\chi_0 + v_1(\boldsymbol{x}) + \varepsilon\log\left(\frac{\varepsilon}{2}\right)v_2(\boldsymbol{x}) + \varepsilon v_3(\boldsymbol{x}) + \cdots, \tag{1.90}$$

where the coefficients v_0, χ_0 are unknown constants, while $v_1(\boldsymbol{x})$, $v_2(\boldsymbol{x})$, $v_3(\boldsymbol{x})$, and higher order coefficients are unknown functions, to be determined.

In the inner region, near the jth absorbing window, we introduce the local curvilinear coordinates (η, s_1, s_2), where $\eta \equiv \varepsilon^{-1}(1-r)$, $s_1 \equiv \varepsilon^{-1}\sin(\theta_j)\left(\phi - \phi_j\right)$, $s_2 \equiv \varepsilon^{-1}(\theta - \theta_j)$, the inner expansion is

$$v \sim \varepsilon^{-1}w_0 + \log\left(\frac{\varepsilon}{2}\right)w_1 + w_2 + \cdots. \tag{1.91}$$

Using (1.91) in (1.88) leads to

$$w_0 = v_0\left(1 - w_c\right), \tag{1.92}$$

where v_0 is a constant to be determined and w_c is the solution of the boundary layer equation

$$\mathcal{L}w_c \equiv w_{c\eta\eta} + w_{cs_1s_1} + w_{cs_2s_2} = 0 \quad \text{for } \eta \ge 0,\ -\infty < s_1, s_2 < \infty \tag{1.93}$$

$$\partial_\eta w_c = 0 \quad \text{for } \eta = 0,\ s_1^2 + s_2^2 \ge a_j^2, \qquad w_c = 1 \quad \text{for } \eta = 0,\ s_1^2 + s_2^2 \le a_j^2 \tag{1.94}$$

$$w_c \to 0 \quad \text{for } \rho = \varepsilon^{-1}|\boldsymbol{x} - \boldsymbol{x}_j| \to \infty. \tag{1.95}$$

The boundary value problem (1.93), (1.94) with the matching condition (1.95) is the well-known electrified disk problem in electrostatics (cf. Jackson 1975), whose solution is

$$w_c = \frac{2}{\pi}\int_0^\infty \frac{\sin\mu}{\mu}\, e^{-\mu\eta/a_j} J_0\left(\frac{\mu\sigma}{a_j}\right) d\mu = \frac{2}{\pi}\sin^{-1}\left(\frac{a_j}{L}\right), \tag{1.96}$$

where $\sigma \equiv (s_1^2 + s_2^2)^{1/2}$, $J_0(z)$ is the Bessel function of the first kind of order zero, and $L = L(\eta, \sigma)$ is defined by

$$L(\eta, \sigma) \equiv \frac{1}{2}\left(\left[(\sigma + a_j)^2 + \eta^2\right]^{1/2} + \left[(\sigma - a_j)^2 + \eta^2\right]^{1/2}\right). \tag{1.97}$$

The far-field behavior of w_c in (1.96) is given by

$$w_c \sim \frac{2a_j}{\pi}\left[\frac{1}{\rho} + \frac{a_j^2}{6}\left(\frac{1}{\rho^3} - \frac{3\eta^2}{\rho^5}\right) + \cdots\right] \quad \text{as} \quad \rho \to \infty, \tag{1.98}$$

which is uniformly valid in η, s_1, and s_2. Thus (1.92) and (1.98) give the far-field expansion of w_0 as

$$w_0 \sim v_0\left(1 - \frac{c_j}{\rho} + O(\rho^{-3})\right) \text{ for } \rho \to \infty,\ c_j \equiv \frac{2a_j}{\pi}, \tag{1.99}$$

where c_j is the electrostatic capacitance of the circular disk of radius a_j.

Writing the matching condition that the near-field behavior of the outer expansion (1.90) must agree with the far-field behavior of the inner expansion (1.91),we obtain the uniform expansion

$$\begin{aligned} v &\sim \frac{v_0}{\varepsilon} + v_1 + \varepsilon \log\left(\frac{\varepsilon}{2}\right) v_2 + \varepsilon v_3 + \cdots \\ &\sim \frac{v_0}{\varepsilon}\left(1 - \frac{c_j}{\rho}\cdots\right) + \log\left(\frac{\varepsilon}{2}\right) w_1 + w_2 + \cdots . \end{aligned} \tag{1.100}$$

The definition $\rho \sim \varepsilon^{-1}|\boldsymbol{x} - \boldsymbol{x}_j|$ gives in (1.100) the expansion $v_1 \sim -v_0 c_j/|\boldsymbol{x} - \boldsymbol{x}_j|$ as $\boldsymbol{x} \to \boldsymbol{x}_j$ for $j = 1, \ldots, N$ so that v_1 is solution of the distributional equation

$$\Delta v_1 = -\frac{1}{D} \text{ for } |\boldsymbol{x}| < 1,\ \partial_r v_1 = -2\pi v_0 \sum_{j=1}^N \frac{c_j}{\sin\theta_j}\delta(\theta - \theta_j)\delta(\phi - \phi_j) \text{ for } |\boldsymbol{x}| = 1. \tag{1.101}$$

The solvability condition for (1.101) gives

$$v_0 = \frac{|\Omega|}{2\pi D N \bar{c}}, \qquad \bar{c} \equiv \frac{1}{N}\sum_{j=1}^N c_j, \qquad c_j = \frac{2a_j}{\pi}. \tag{1.102}$$

Thus, the solvability condition for the problem for v_1 determines the unknown leading-order constant v_0 in the outer expansion. The solution to (1.101), represented in terms of the Neumann functions (1.87), up to an unknown additive constant χ, is given by

$$v_1 = -2\pi v_0 \sum_{i=1}^{N} c_i G_s(x;x_i) + \chi, \qquad \chi \equiv |\Omega|^{-1} \int_{\Omega} v_1 \, dx. \tag{1.103}$$

Iterating this procedure by expanding v_1 in the limit $\boldsymbol{x} \to \boldsymbol{x}_j$ and by using the near-field expansion of $G_s(\boldsymbol{x};\boldsymbol{x}_j)$ gives

$$\chi = \log\left(\frac{\varepsilon}{2}\right) \chi_0 + \chi_1, \tag{1.104}$$

hence

$$w_1 = \left(\frac{v_0 c_j}{2} + \chi_0\right)(1 - w_c), \tag{1.105}$$

and

$$v_2 = -2\pi \sum_{i=1}^{N} c_i \left(\frac{v_0 c_i}{2} + \chi_0\right) G_s(x;x_i) + \chi_2. \tag{1.106}$$

Repeated iterations of this procedure determine all the function v_k and w_k (Cheviakov et al. 2010).

1.7.1 Third-Order Asymptotics

Specialization of the above asymptotics to a three-term expansion for N windows with a common radius $\varepsilon \ll 1$, centered at $\boldsymbol{x}_j$ with $|\boldsymbol{x}_i - \boldsymbol{x}_j| = O(1)$ for $i \neq j$, gives the average NET up to third order (see Sect. 1.6.1) (Cheviakov et al. 2010)

$$\bar{v} = \frac{|\Omega|}{4\varepsilon D N} \left\{ 1 + \frac{\varepsilon}{\pi} \log\left(\frac{2}{\varepsilon}\right) \right.$$
$$\left. + \frac{\varepsilon}{\pi}\left[-\frac{9N}{5} + 2(N-2)\log 2 + \frac{3}{2} + \frac{4}{N}\mathcal{H}(\boldsymbol{x}_1, \ldots, \boldsymbol{x}_N) \right] + O\left(\varepsilon^2 \log\left(\frac{1}{\varepsilon}\right)\right) \right\},$$

where the discrete energy-like function $\mathcal{H}(\boldsymbol{x}_1, \ldots, \boldsymbol{x}_N)$ is defined by

$$\mathcal{H}(\boldsymbol{x}_1, \ldots, \boldsymbol{x}_N) = \sum_{i=1}^{N} \sum_{j=i+1}^{N} \left(\frac{1}{|\boldsymbol{x}_i - \boldsymbol{x}_j|} - \frac{1}{2}\log|\boldsymbol{x}_i - \boldsymbol{x}_j| - \frac{1}{2}\log\left(2 + |\boldsymbol{x}_i - \boldsymbol{x}_j|\right) \right).$$

The spatial arrangement that minimizes the energy $\mathcal{H}(\boldsymbol{x}_1,\dots,\boldsymbol{x}_N)$ is given as follows. For $N = 2$, the traps are antipodal, for $N = 3$ they are the vertices of the maximal inscribed equilateral triangle, and for $N = 4$ they are the vertices of an inscribed tetrahedron. For $2 \le N \le 20$, the optimal trap arrangements for the energy $\mathcal{H}(\boldsymbol{x}_1,\dots,\boldsymbol{x}_N)$ and the Coulomb energy

$$\mathcal{H}_{\mathrm{C}} = \sum_{i=1}^{N}\sum_{j=i+1}^{N} \frac{1}{|\boldsymbol{x}_i - \boldsymbol{x}_j|}. \tag{1.107}$$

are the same. This result was derived numerically (Cheviakov et al. 2010). For example, for $N = 10, 12$, the minimal energy arrangement has two strips of traps with common latitude, with two traps located at the poles. For large N and charges distributed homogeneously on the sphere, and that there is no charge in the azimuthal neighborhood $0 \le \theta < \theta_0$ of the north pole, where $\theta_0 \ll 1$, the number density of charges is given approximately by

$$P(\theta,\phi) = \begin{cases} \dfrac{N}{4\pi} & \text{for } \theta_0 < \theta < \pi \\[2ex] 0 & \text{for } 0 < \theta < \theta_0, \end{cases} \tag{1.108}$$

where θ_0 is determined from the condition that $\int\limits_0^{2\pi}\int\limits_{\theta_0}^{\pi} P(\theta,\phi)\sin\theta\, d\theta\, d\phi = N - 1$, which yields $\cos\theta_0 = 1 - 2/N$. For $N \gg 1$, we use $\cos\theta_0 \approx 1 - \theta_0^2/2$, to obtain $\theta_0 \approx \sqrt{4/N}$. Assuming the form

$$\begin{aligned} \mathcal{H} \approx \mathcal{F}(N) = \frac{N^2}{2}(1 - \log 2) + b_1 N^{3/2} + b_2 N \log N + b_3 N \\ + b_4 N^{1/2} + b_5 \log N + b_6, \end{aligned} \tag{1.109}$$

a least squares fit of (1.109) to the data yields

$$\begin{aligned} &b_1 \approx -0.5668,\ b_2 \approx 0.0628,\ b_3 \approx -0.8420 \\ &b_4 \approx 3.8894,\ b_5 \approx -1.3512,\ b_6 \approx -2.4523. \end{aligned}$$

Using the approximation $\mathcal{H} \approx N^2 (1 - \log 2)/2 + b_1 N^{3/2}$ for large N, we obtain the following rough estimate of the minimum value of the average (with respect to the initial position) MFPT $\bar{v}$ for the case of $N \gg 1$ identical circular traps of radius ε,

$$\bar{v} \sim \frac{|\Omega|}{4\varepsilon D N}\left[1 - \frac{\varepsilon}{\pi}\log\varepsilon + \frac{\varepsilon N}{\pi}\left(\frac{1}{5} + \frac{4b_1}{\sqrt{N}}\right)\right]. \tag{1.110}$$

Equation (1.110) can be written in terms of the trap surface area fraction $f = N\varepsilon^2/4$ as

$$\bar{v} \sim \frac{|\Omega|}{8D\sqrt{fN}}\left[1 - \frac{\sqrt{f/N}}{\pi}\log\left(\frac{4f}{N}\right) + \frac{2\sqrt{fN}}{\pi}\left(\frac{1}{5} + \frac{4b_1}{\sqrt{N}}\right)\right]. \tag{1.111}$$

In order that the expansions (1.110) and (1.111) remain ordered, we require that the third term in the bracket in (1.110) is asymptotically smaller than the second term. This enforces the requirement that $\varepsilon = o\left(e^{-N/5}\right)$. The breakdown of such general expansions for large N is yet to be fully explored.

1.8 NET from a General Domain with Two Absorbing Windows

The NET through two small absorbing windows was resolved in Holcman and Schuss (2008a,b).

Theorem 1.8.1 (NET from Two Windows). *The leading order expansion of the NET through two circular absorbing windows A and B of dimensionless radii a and b, respectively, whose centers are $\Delta = a + \Delta' + b$ apart on the smooth boundary $\partial\Omega$ of a bounded domain $\Omega \subset \mathbb{R}^3$, is given in the limit $a, b, \Delta' \to 0$ by*

$$\bar{\tau}_{A\cup B} = \frac{|\Omega|}{4(a+b)D\tilde{r}}\,\frac{1 - 16ab\tilde{r}^2\left(\dfrac{1}{2\pi\,|a+\Delta'+b|} + O(1)\right)^2}{1 - \dfrac{8ab\tilde{r}}{a+b}\left(\dfrac{1}{2\pi\,|a+\Delta'+b|} + O(1)\right)}. \tag{1.112}$$

Here $\tilde{r} = \tilde{r}(\Delta', a, b)$ is a function of Δ', a, b that varies monotonically between $\tilde{r}(0,0,0) \approx 0.6$ and $\tilde{r}(\Delta', 0, 0) \to 1$ as $\Delta' \to \infty$.

Proof. The analysis of the three-dimensional case differs from that in Sect. 1.4.4 in the explicit computation of the solution of the Helmholtz integral equation (1.60),

$$\int_A N(\boldsymbol{x},\boldsymbol{\xi})g_A(\boldsymbol{x})\,dS_{\boldsymbol{x}} \approx \begin{cases} \dfrac{1}{2\pi}\tilde{\alpha}a\tilde{g}_A & \text{for} \quad \boldsymbol{\xi} \in A \\[2ex] a^2\tilde{g}_A\alpha[N(\mathbf{0}_A, \mathbf{0}_B) + O(1)], \text{for } \boldsymbol{\xi} \in B, \end{cases} \tag{1.113}$$

$$\int_B N(\boldsymbol{x},\boldsymbol{x}')g_B(\boldsymbol{x})\,dS_{\boldsymbol{x}} \approx \begin{cases} \dfrac{\tilde{\beta}b\tilde{g}_B(1+o(1))}{2D\pi} & \text{for} \quad \boldsymbol{x}' \in B, \quad b < 1 \\[2ex] b^2\tilde{g}_B\beta\,[N(\mathbf{0}_A, \mathbf{0}_B) + O(1)] & \text{for} \quad \boldsymbol{x}' \in A, \quad b < 1, \end{cases} \tag{1.114}$$

where b is the radius of B and

$$\tilde{\alpha} = \tilde{\beta} = \tilde{\beta} = \int_0^{2\pi} d\theta \int_0^1 \frac{f(r,\theta) r\, dr}{\sqrt{1-r^2}}, \tag{1.115}$$

where $f(r,\theta)$ is a positive smooth function in the windows and equals 1 in their centers, as described in Sect. 1.4.6.

Now we approximate Eq. (1.45) by

$$\begin{aligned} -C =& \frac{1}{2\pi}\tilde{\alpha} a \tilde{g}_A(1+o(1)) + b^2 \tilde{g}_B \beta (N(\mathbf{0}_A, \mathbf{0}_B) + O(1)) \\ -C =& \frac{1}{2\pi}\tilde{\beta} b \tilde{g}_B(1+o(1)) + a^2 \tilde{g}_A \alpha (N(\mathbf{0}_A, \mathbf{0}_B) + O(1)) \end{aligned}$$

and find that the flux integral in a window is

$$\int_A g_A(\boldsymbol{x})\, dS_x = a^2 \alpha \tilde{g}_A(1+o(1)). \tag{1.116}$$

The condition (1.44) for two windows of radii a and b, respectively, is

$$a^2\alpha\tilde{g}_A + b^2\beta\tilde{g}_B = -|\Omega|(1+o(1)).$$

It follows that the NET is

$$\bar{\tau}_{A\cup B} = \frac{|\Omega|[1+o(1)]}{4(a+b)r} \frac{1 - 16r^2 ab\left[\dfrac{1}{2\pi\, |a+\Delta'+b|}[1+O(\rho)]\right]^2}{1 - \dfrac{8abr}{a+b}\left[\dfrac{1}{2\pi\, |a+\Delta'+b|}[1+O(\rho)]\right]}, \tag{1.117}$$

where

$$\rho = \min\left(1, \left|a+\Delta'+b\right| \log\frac{1}{|a+\Delta'+b|}\right).$$

Here $r = \pi\alpha/2\tilde{\alpha}$ and α is defined by (1.49). The expression (1.59) was used for the Neumann function. For a fixed D, the parameter r depends on Δ', a, and b so we write $r = r(\Delta', a, b)$. If Δ' is large, then $f(x,\theta) = \text{const}$, so $\lim_{\Delta'\to\infty} r(\Delta', a, b) = 1$. For $a, b, \Delta' \to 0$, we determine the value of $r(0, a, b)$ by fitting to numerical simulations of Brownian motion in a sphere with two tangent circular holes (see below). Equation (1.117) is (1.112). □

Brownian simulations and comparison of (1.117) to the MFPT (Fig. 1.8) give a good agreement with the approximation

$$r(\Delta', a, a) = \frac{0.6+\Delta'}{1+\Delta'}.$$

A striking consequence of (1.117) is that moving the two windows apart from $\Delta' = 0$ to $\Delta' = \infty$ changes r from 0.6 to 1 and changes the MFPT by the factor 0.6. This means that clustering decreases the first eigenvalue (the flux) by about 40 %.

1.8.1 Multiple Absorbing Windows

We consider Brownian motion with diffusion coefficient D in a bounded domain $\Omega \subset \mathbb{R}^3$, whose smooth boundary $\partial\Omega$ reflects Brownian trajectories, except for M circular absorbing windows $A_i \subset \partial\Omega$, $(i = 1, 2, \ldots, M)$ of small dimensionless radii ε_i, clustered in the sense that every window A_i has within a distance comparable to ε_i a neighboring window A_j.

Theorem 1.8.2 (NET Through Multiple Windows (Holcman and Schuss 2008a,b)). *The leading order asymptotic approximation of the NET through* $\bigcup_1^M A_i$ *for* $\sum_1^M \varepsilon_i \ll 1$ *is given by*

$$C = \bar{\tau}_{\bigcup A_i} \approx \frac{|\Omega|}{4D} \frac{1}{\displaystyle\sum_{i=1}^{M} \varepsilon_i \left(1 - 2\sum_{i\neq j} \varepsilon_j N(i,j)\right)}, \tag{1.118}$$

where $N(i,j)$ *is the Neumann function for* Ω *at the centers of* A_i *and* A_j*, respectively.*

Proof. The NET $u(\boldsymbol{x})$ has the representation (1.14)

$$u(\boldsymbol{\xi}) = \int\limits_{\Omega} N(\boldsymbol{x}, \boldsymbol{\xi})\, d\boldsymbol{x} + D \int\limits_{\partial\Omega_a} N(\boldsymbol{x}, \boldsymbol{\xi}) \frac{\partial u(\boldsymbol{x})}{\partial n}\, dS_{\boldsymbol{x}} + C, \tag{1.119}$$

where C is a constant to be determined from the absorbing boundary condition. The condition that $u(\boldsymbol{x})$ vanishes on $\bigcup_1^M A_i$ is

$$F(\boldsymbol{\xi}) = \sum_{i=1}^{M} \int\limits_{A_i} N(\boldsymbol{x}, \boldsymbol{\xi}) g_i(\boldsymbol{x})\, dS_{\boldsymbol{x}} \quad \text{for } \boldsymbol{\xi} \in \bigcup_{i=1}^{M} A_i, \tag{1.120}$$

where

$$F(\boldsymbol{\xi}) = -\left(\int\limits_{\Omega} N(\boldsymbol{x}, \boldsymbol{\xi})\, d\boldsymbol{x} + C \right). \tag{1.121}$$

The probability flux density in window A_i is denoted $g_i(\boldsymbol{x})$. Integration of the Poisson equation (1.4) over Ω gives the total flux in $\bigcup_{i=1}^{M} A_i$ as

$$\sum_{i=1}^{M} \int\limits_{A_i} g_i(\boldsymbol{x})\, dS_{\boldsymbol{x}} = -\frac{|\Omega|}{D}. \tag{1.122}$$

We denote by $\mathbf{0}_i$ the center of A_i. Proceeding as in the derivation of (1.113) and (1.114) in the proof of Theorem 1.8.1, we obtain for $\boldsymbol{\xi} = \boldsymbol{\xi}_j \in A_j$ a system of $M + 1$ linear equations for the unknown constants $\tilde{g}_i$ and C,

$$\frac{\pi}{2}\varepsilon_j \tilde{g}_j + \sum_{i \neq j}^{M} 2\pi \varepsilon_i^2 \tilde{g}_i N(i,j) = F(\boldsymbol{\xi}_j) \approx -C, \quad j = 1, \ldots, M, \tag{1.123}$$

$$2\pi \sum_{i=1}^{M} \varepsilon_i^2 \tilde{g}_i = -\frac{|\Omega|}{D}, \tag{1.124}$$

where $N(i,j) = N(\mathbf{0}_i, \mathbf{0}_j)$. Equation (1.124) is the solvability condition (1.122). If all radii ε_i can be scaled by $\varepsilon_i = \varepsilon \tilde{\varepsilon}_i$, where $\varepsilon = \min_{1 \leq i \leq M} \varepsilon_i \ll 1$ and $\tilde{\varepsilon}_i = O(1)$ as $\varepsilon \to 0$, then for windows separated by distances $\Delta_{i,j}$,

$$\max_{i,j}\,[2\varepsilon N(i,j)] = \max_{i,j} \frac{1}{\pi\left(\tilde{\varepsilon}_i + \tilde{\varepsilon}_j + \dfrac{\Delta_{i,j}}{\varepsilon}\right)}\,[1 + o(1)] < 1. \tag{1.125}$$

Scaling $G_j = \pi \varepsilon_j \tilde{g}_j / C$, we write the symmetric matrix of the system (1.123) (with $1/2$ on the diagonal) as

$$\boldsymbol{M} = \begin{pmatrix} 1/2 & 2\tilde{\varepsilon}_2 N(1,2) \ldots & 2\tilde{\varepsilon}_M N(1,M) \\ 2\tilde{\varepsilon}_2 N(1,2) & . \quad\quad . & . \\ . & . \quad\quad . & . \\ 2\tilde{\varepsilon}_M N(1,M) & \ldots \quad\quad . & 1/2 \end{pmatrix}. \tag{1.126}$$

We decompose $\boldsymbol{M}$ as

$$\boldsymbol{M} = \frac{1}{2}\boldsymbol{I}_M + \varepsilon \boldsymbol{A},$$

where $\boldsymbol{I}_M$ is the identity matrix and $\boldsymbol{A}$ contains off-diagonal terms. Writing $\mathbf{1}_M$ (resp. $\tilde{\boldsymbol{G}}_M$) for a vector of 1 (respectively, of G_j), (1.123) becomes

$$\left(\frac{1}{2}\boldsymbol{I}_M + \varepsilon \boldsymbol{A}\right) \tilde{\boldsymbol{G}}_M = -\mathbf{1}_M \tag{1.127}$$

and can be inverted as the convergent series

$$\tilde{\boldsymbol{G}}_M = -2\sum_{k=0}^{\infty}(-2\varepsilon \boldsymbol{A})^k \mathbf{1}_M. \tag{1.128}$$

All terms can contribute to the sum, because $\varepsilon N(i,j)$ can be of order 1. The interaction of the cluster with window j is given by

$$G_j = -2 - 2\sum_{k=0}^{\infty}(-2\varepsilon)^k \sum_{i_1,..,i_k} N(j,i_1)N(i_1,i_2)\ldots N(i_{k-1},i_k), \tag{1.129}$$

where the sum is over all non-diagonal pairs (not all i_k are different). The nonlinearity depends on the number of windows. In the first approximation,

$$\tilde{\boldsymbol{G}}_M \approx -2(\boldsymbol{I}_M - 2\varepsilon \boldsymbol{A})\mathbf{1}_M \tag{1.130}$$

and

$$\pi\frac{\varepsilon_j \tilde{g}_j}{C} = G_j = -2\left(1 - 2\varepsilon\sum_{i\neq j}\tilde{\varepsilon}_i N(i,j)\right). \tag{1.131}$$

Using the condition (1.124), we obtain for the constant C the equation

$$-4C\sum_{i=1}^{M}\varepsilon_i\left(1 - 2\sum_{i\neq j}\varepsilon_i N(i,j)\right) = -\frac{|\Omega|}{D},$$

thus the NET through $\bigcup A_i$ is (1.118). □

If the number of absorbing windows on a surface increases while their combined surface area remains constant, the NET decreases through the holes increases (Holcman and Schuss 2008a; Reingruber et al. 2009; Cheviakov et al. 2010). However, the asymptotics for a large number of windows, N with surface fraction $N\varepsilon^2 = o(1)$ has not yet been elucidated. Such analysis requires the computation of three terms in the expansion (1.118). The NET does not necessarily tend to zero as N goes to infinity, depending on the windows organization and the initial distribution of the Brownian trajectories. This is the case, for example, in an annular domain with holes only on the inner circle (sphere), while Brownian trajectories start on the outer circle (sphere). Some analysis was initiated in Berg and Purcell (1977), however this problem calls for further analysis to treat the double asymptotics of large N and small ε.

1.9 Diffusion Leak in a Conductor

A conductor of diffusion flux from a source to an absorbing target is a bounded domain Ω containing a source on the boundary or in the interior and a part $\partial\Omega_a$ of the boundary is absorbing (the target). The remaining boundary $\partial\Omega_r$ is impermeable to the diffusing trajectories. Some of the diffusion flux may leak out of Ω if a part $S(\varepsilon)$ of the absorbing boundary $\partial\Omega_a$ is isolated from $\partial\Omega_a - S(\varepsilon)$ by a finite distance and $|S(\varepsilon)| \ll |\partial\Omega_a|$ [see Fig. 3.9(right)]. The calculation of the leakage flux is not the same as that in the narrow escape problem, because the total flux on the boundary remains bounded as the small hole shrinks. Our purpose is to find the portion that leaks through the small hole out of the total flux.

The (dimensionless) stationary density $u(\boldsymbol{x})$ of the diffusive trajectories satisfies the mixed boundary value problem

$$\begin{aligned} D\Delta u(\boldsymbol{x}) &= 0 \quad \text{for } \boldsymbol{x} \in \Omega \\ \frac{\partial u(\boldsymbol{x})}{\partial \nu} &= 0 \quad \text{for } \boldsymbol{x} \in \partial\Omega_r \\ -D\frac{\partial u(\boldsymbol{x})}{\partial \nu} &= \phi(\boldsymbol{x}) \quad \text{for } \boldsymbol{x} \in \partial\Omega_s \\ u(\boldsymbol{x}) &= 0 \quad \text{for } \boldsymbol{x} \in \partial\Omega_a \cup S(\varepsilon). \end{aligned} \tag{1.132}$$

Our aim is to derive an asymptotic expression for the flux through $S(\varepsilon)$,

$$J_\varepsilon = D \int\limits_{S(\varepsilon)} \frac{\partial u(\boldsymbol{x})}{\partial \nu}\, dS_{\boldsymbol{x}}, \tag{1.133}$$

in terms of the solution $u_0(\boldsymbol{x})$ of the reduced problem [without $S(\varepsilon)$]. First, we find the flux of each eigenfunction and then, using eigenfunction expansion, we calculate J_ε. Every eigenfunction $u_\varepsilon(\boldsymbol{x})$ of the homogeneous problem (1.132) satisfies

$$-D\Delta u_\varepsilon(\boldsymbol{x}) = \lambda(\varepsilon) u_\varepsilon(\boldsymbol{x}) \quad \text{for } \boldsymbol{x} \in \Omega \tag{1.134}$$

$$\frac{\partial u_\varepsilon(\boldsymbol{x})}{\partial \nu} = 0 \quad \text{for } \boldsymbol{x} \in \partial\Omega_s \cup \partial\Omega_r \tag{1.135}$$

$$u_\varepsilon(\boldsymbol{x}) = 0 \quad \text{for } \boldsymbol{x} \in S(\varepsilon) \cup \partial\Omega_a. \tag{1.136}$$

The eigenvalues have a regular expansion

$$\lambda(\varepsilon) = \lambda(0) + \lambda_1 \varepsilon + o(\varepsilon) = \frac{D \displaystyle\int_{\partial\Omega_a} \frac{\partial u_0(\boldsymbol{y})}{\partial \nu}\, dS_{\boldsymbol{y}}}{\displaystyle\int_\Omega u_0(\boldsymbol{x})\, d\boldsymbol{x}} + O(\varepsilon), \tag{1.137}$$

where $\lambda(0)$ is the eigenvalue of the reduced problem (for Ω without the small hole $S(\varepsilon)$) and $u_0(\boldsymbol{x})$ is the principal eigenfunction of the reduced problem (see for details Ward and Keller 1993; Ward et al. 1993; Ward and Van De Velde 1992; Kolokolnikov et al. 2005; Singer et al. 2008a).

According to Popov's Theorem 1.5.1, the reduced Green function (without the small hole) has the form

$$G(\boldsymbol{x},\boldsymbol{y}) = \frac{1}{2\pi|\boldsymbol{x}-\boldsymbol{y}|} + H(\boldsymbol{x},\boldsymbol{y})\log|\boldsymbol{x}-\boldsymbol{y}| + v_S(\boldsymbol{x},\boldsymbol{y}), \tag{1.138}$$

for $\boldsymbol{x} \in \partial\Omega$, $\boldsymbol{y} \in \Omega \cup \partial\Omega$, where $H(\boldsymbol{x},\boldsymbol{y})$ depends locally on the curvatures of the boundary and $v_S(\boldsymbol{x},\boldsymbol{y})$ is a continuous function of $\boldsymbol{x},\boldsymbol{y} \in \Omega$ and on $\partial\Omega$ and we assume it is bounded (see Sect. 1.6).

We can express the eigenfunction in terms of $G(\boldsymbol{x},\boldsymbol{y})$ as

$$u_\varepsilon(\boldsymbol{x}) = -\lambda(\varepsilon)\int\limits_{\Omega} G(\boldsymbol{x},\boldsymbol{y})u_\varepsilon(\boldsymbol{y})\,d\boldsymbol{y} + \int\limits_{S(\varepsilon)} G(\boldsymbol{x},\boldsymbol{y})\frac{\partial u_\varepsilon(\boldsymbol{y})}{\partial\nu}\,dS_{\boldsymbol{y}} \tag{1.139}$$

and expand the integrals about the center of $S(\varepsilon)$ in the form

$$\int\limits_{\Omega} \lambda(\varepsilon)G(\boldsymbol{x},\boldsymbol{y})u_\varepsilon(\boldsymbol{y})\,d\boldsymbol{y} = G_0(\varepsilon) + O(|\boldsymbol{x}|) \;\text{ for } \boldsymbol{x} \in S(\varepsilon), \tag{1.140}$$

where the origin is assumed to be in the center of $S(\varepsilon)$ and the (x_1,x_2) plane is that of $S(\varepsilon)$. Using (1.138) and expanding all the integrals for small ε, we get at $\boldsymbol{x} = \boldsymbol{0}$ the equation

$$G_0(\varepsilon) = \left[\frac{\pi\varepsilon}{2} + O(\varepsilon^2\log\varepsilon)\right]C_0(\varepsilon) + O(\varepsilon^2\log\varepsilon),$$

where $C_0(\varepsilon)$ is an unknown constant [see detailed computations in Singer et al. (2008a) and Schuss (2013)]. Integrating (1.134) and expanding for small ε, as above, we get the two equations

$$\lambda(\varepsilon)\int\limits_{\Omega} u_\varepsilon(\boldsymbol{x})\,d\boldsymbol{x} = 4\varepsilon D\frac{G_0(\varepsilon) + O(\varepsilon^2\log\varepsilon)}{1 + O(\varepsilon\log\varepsilon)} + O(\varepsilon^2\log\varepsilon) + D\int\limits_{\partial\Omega_a}\frac{\partial u_\varepsilon(\boldsymbol{y})}{\partial\nu}\,dS_{\boldsymbol{y}}$$

$$G_0(\varepsilon) = \lambda(\varepsilon)\int\limits_{\Omega} G(\boldsymbol{0},\boldsymbol{y})u_\varepsilon(\boldsymbol{y})\,d\boldsymbol{y}. \tag{1.141}$$

Solving for $\lambda(\varepsilon)$ and taking the limit $\varepsilon \to 0$ in (1.137), we find that the flux of $u_\varepsilon(\boldsymbol{x})$ through the small hole is

$$
\begin{aligned}
J(\varepsilon) &= D\int\limits_{S(\varepsilon)} \frac{\partial u_\varepsilon(\boldsymbol{y})}{\partial \nu}\, dS_{\boldsymbol{y}} = 4\varepsilon\lambda(0)D\int\limits_{\Omega} G(\boldsymbol{0},\boldsymbol{y})u_0(\boldsymbol{y})\, d\boldsymbol{y} + O(\varepsilon^2\log\varepsilon)\\
&= 4\varepsilon D u_0(\boldsymbol{0}) + O(\varepsilon^2\log\varepsilon). \qquad (1.142)
\end{aligned}
$$

The function $DG(\boldsymbol{x},\boldsymbol{y})$ is Green's function for the mixed boundary value problem with diffusion coefficient D, rather than 1. Finally, expanding the solution $u(\boldsymbol{x})$ of (1.132) in eigenfunctions, we obtain from (1.142)

$$
J_\varepsilon = 4\varepsilon D u_0(\boldsymbol{0})\left(1 + O(\varepsilon\log\varepsilon)\right), \qquad (1.143)
$$

where $u_0(\boldsymbol{x})$ is the solution of the reduced problem (1.132). In dimensional variables, we obtain

$$
J_\varepsilon = 4aDp_0(\boldsymbol{0}) + O\left(\frac{a^2}{|\Omega|^{2/3}}\log\frac{a}{|\Omega|^{1/3}}\right), \qquad (1.144)
$$

where $p_0(\boldsymbol{0})$ is the value of the reduced stationary density (without the perforation) at the hole.

1.9.1 Activation Through a Narrow Opening

The escape of a Brownian motion through a narrow absorbing window in an otherwise reflecting boundary of a domain is a rare event. In the presence of a deep potential well, there are two long time scales, the mean escape time from the well and the mean time to reach the absorbing window. The two time scales are expressed in an Arrhenius-like formula for the activation rate through narrow openings. The activation rates for the different geometries are summarized in Eqs. (1.167)–(1.171).

As in classical theories, our point of departure is the Smoluchowski equation (Schuss 2010b)

$$
\dot{\boldsymbol{x}} + \frac{1}{\gamma}\nabla\phi(\boldsymbol{x}) = \sqrt{\frac{2k_{\mathrm{B}}T}{m\gamma}}\,\dot{\boldsymbol{w}}, \qquad (1.145)
$$

where m is the mass, $\gamma = \eta/m$ is the dynamics viscosity, while η is the friction coefficient, $\phi = \Phi/m$ is the potential per unit mass and $\Phi(\boldsymbol{x})$ is the potential, T is temperature, k_{B} is Boltzmann's constant, and $\dot{\boldsymbol{w}}$ is a vector of n independent δ-correlated Gaussian white noises.

The motion of the Brownian particle is confined to a bounded domain Ω, whose boundary $\partial\Omega$ is reflecting, but for a small absorbing window $\partial\Omega_a$ ($\partial\Omega = \partial\Omega_a \cup \Omega_r$). The assumption that the window is small means that

$$
\delta = \left(\frac{|\partial\Omega_a|}{|\partial\Omega|}\right)^{1/(d-1)} \ll 1 \qquad (1.146)
$$

(δ is a small parameter).

The probability density function (pdf) $p_\delta(\boldsymbol{x},t)$ of finding the Brownian particle at location $\boldsymbol{x}$ at time t satisfies the Fokker–Planck equation

$$\gamma\frac{\partial p_\delta}{\partial t} = \varepsilon\Delta p_\delta + \nabla\cdot(p_\delta\nabla\phi) \equiv \mathcal{L}_\delta p_\delta, \tag{1.147}$$

with the initial condition

$$p_\delta(\boldsymbol{x},0) = p_0(\boldsymbol{x}), \tag{1.148}$$

and the mixed Dirichlet–Neumann boundary conditions for $t>0$

$$p_\delta = 0, \quad \text{for } \boldsymbol{x}\in\partial\Omega_a \tag{1.149}$$

$$\varepsilon\frac{\partial p_\delta}{\partial n} + p_\delta\frac{\partial\phi}{\partial n} = 0, \quad \text{for } \boldsymbol{x}\in\partial\Omega_r, \tag{1.150}$$

where $\varepsilon = k_\mathrm{B}T/m$ and $p_0(\boldsymbol{x})$ is the initial probability density function (e.g., $p_0(\boldsymbol{x}) = \mathbf{1}_\Omega(\boldsymbol{x})/|\Omega|$ for a uniform distribution). The function

$$u_\delta(\boldsymbol{x}) = \int_0^\infty p_\delta(\boldsymbol{x},t)\,dt, \tag{1.151}$$

which is the mean time the particle spends at $\boldsymbol{x}$ before it escapes through the narrow window, is the solution of the boundary value problem

$$\mathcal{L}_\delta u_\delta = -\gamma p_0, \quad \text{for } \boldsymbol{x}\in\Omega \tag{1.152}$$

$$u_\delta = 0, \quad \text{for } \boldsymbol{x}\in\partial\Omega_a \tag{1.153}$$

$$\varepsilon\frac{\partial u_\delta}{\partial n} + u_\delta\frac{\partial\phi}{\partial n} = 0, \quad \text{for } \boldsymbol{x}\in\partial\Omega_r. \tag{1.154}$$

The function $g_\delta = u_\delta e^{\phi/\varepsilon}$ is the solution of the adjoint problem

$$\mathcal{L}_\delta^* g_\delta = -\gamma p_0 e^{\phi/\varepsilon} \quad \text{for } \boldsymbol{x}\in\Omega \tag{1.155}$$

$$\frac{\partial g_\delta(\boldsymbol{x})}{\partial n} = 0 \quad \text{for } \boldsymbol{x}\in\partial\Omega_r, \qquad g_\delta(\boldsymbol{x}) = 0 \quad \text{for } \boldsymbol{x}\in\partial\Omega_a. \tag{1.156}$$

Equation (1.155) can be written in the divergence form

$$\nabla\left(e^{-\phi/\varepsilon}\nabla g_\delta\right) = -\frac{\gamma p_0}{\varepsilon}. \tag{1.157}$$

The adjoint operators $\mathcal{L}_\delta$ and $\mathcal{L}_\delta^*$, defined by (1.147), (1.152), (1.153), (1.154) and (1.155), (1.156), respectively, have bi-orthogonal systems of normalized eigenfunctions, $\{\psi_i(\boldsymbol{x},\delta)\}$ and $\{\varphi_i(\boldsymbol{x},\delta)\}$ $(i=0,1,\dots)$ and we can expand

$$p_\delta(\boldsymbol{x},t) = \sum_{i=0}^\infty a_i(\delta)\psi_i(\boldsymbol{x},\delta)e^{-\lambda_i(\delta)t/\gamma}, \tag{1.158}$$

where $\lambda_i(\delta)$ are the eigenvalues of $\mathcal{L}_\delta$. The $a_i(\delta)$ are the Fourier coefficients of the initial function $p_0(\boldsymbol{x})$. In the limit $\delta \to 0$ the Dirichlet part of the boundary conditions, (1.149), is dropped, so that $\lambda_0(\delta) \to 0$ (the first eigenvalue of the problem (1.147), (1.150) with $\partial\Omega_r = \partial\Omega$), with the normalized eigenfunction

$$\psi_0(\boldsymbol{x}, 0) = \frac{\exp\{-\phi(\boldsymbol{x})/\varepsilon\}}{\displaystyle\int_\Omega \exp\{-\phi(\boldsymbol{x})/\varepsilon\}\, d\boldsymbol{x}}, \tag{1.159}$$

and $a_0(\delta) \to 1$. It follows from (1.151) and (1.158) that for all $\boldsymbol{x} \in \Omega$

$$u_\delta(\boldsymbol{x}) = \gamma \sum_{i=0}^{\infty} \frac{a_i(\delta)\psi_i(\boldsymbol{x}, \delta)}{\lambda_i(\delta)} \to \infty, \quad \text{as} \quad \delta \to 0. \tag{1.160}$$

In particular, the first passage time $\tau_\delta = \inf\{t > 0 \,|\, \boldsymbol{x}(t) \in \partial\Omega_a\}$ diverges. That is, $\lim\limits_{\delta\to 0} \tau_\delta = \infty$ on almost every trajectory $\boldsymbol{x}(t)$. Obviously, the mean first passage time,

$$\mathbb{E}\tau_\delta = \int\limits_\Omega u_\delta(\boldsymbol{x})\, d\boldsymbol{x} = \gamma \sum_{i=0}^{\infty} \frac{a_i(\delta)}{\lambda_i(\delta)}, \tag{1.161}$$

also diverges as $\delta \to 0$. It is the purpose of this chapter to find the orders of magnitude of $u_\delta(\boldsymbol{x})$ and $\mathbb{E}\tau_\delta$ for small δ.

1.9.2 The NET

The Helmholtz integral equation for the potential case is to leading order

$$\frac{1}{2\pi} \int\limits_{\partial\Omega_a} \frac{\partial u_0(\boldsymbol{y})}{\partial n_{\boldsymbol{y}}} \frac{dS_{\boldsymbol{y}}}{|\boldsymbol{x} - \boldsymbol{y}|} = -C_\delta e^{-\phi_0/\varepsilon}, \tag{1.162}$$

where ϕ_0 is the potential at the window. For an elliptical absorbing window $\partial\Omega_a$ the value of the constant C_δ, as calculated in Sect. 1.5.2, is found from the compatibility condition

$$\int\limits_{\partial\Omega_a} \frac{\partial u_\delta}{\partial n}\, dS = -\frac{\gamma}{\varepsilon} \tag{1.163}$$

to be

$$C_\delta = \frac{\gamma K(e)}{2\pi\varepsilon a} e^{\phi_0/\varepsilon}. \tag{1.164}$$

In a three-dimensional domain, the density of the mean time spent at point $\boldsymbol{x}$ before escape through an elliptical absorbing window is given by

$$u_\delta(\boldsymbol{x}) \approx \frac{\gamma K(e)}{2\pi\varepsilon a} \exp\left\{\frac{\phi_0 - \phi(\boldsymbol{x})}{\varepsilon}\right\}. \tag{1.165}$$

Equations (1.161) and (1.165) give now the mean escape time as

$$\mathbb{E}\tau_\delta = \frac{\gamma K(e) e^{\phi_0/\varepsilon}}{2\pi\varepsilon a} \int_\Omega \exp\left\{-\frac{\phi(\boldsymbol{x})}{\varepsilon}\right\} d\boldsymbol{x}. \tag{1.166}$$

If the barrier is sufficiently high, we evaluate the integral in (1.166) by the Laplace method, assuming that ϕ has a single global minimum ϕ_m at $\boldsymbol{x}_m$,

$$\int_\Omega \exp\left\{-\frac{\phi(\boldsymbol{x})}{\varepsilon}\right\} d\boldsymbol{x} \approx \frac{(2\pi\varepsilon)^{n/2}}{\prod_{i=1}^n \omega_i} \exp\left\{-\frac{\phi_m}{\varepsilon}\right\},$$

where ω_i are the frequencies at the minimum $\boldsymbol{x}_m$. For reactions that consist in passing through a small elliptical window (assuming no returns are possible) the reaction rate is the modified Kramers formula

$$\kappa_\delta = \frac{1}{\mathbb{E}\tau_\delta} \sim \frac{a\omega_1\omega_2\omega_3}{\sqrt{2\pi\varepsilon}\,\gamma K(e)}\, e^{-\Delta E/\varepsilon}, \tag{1.167}$$

where $\Delta E = \phi_0 - \phi_m$. In the special case of a circular window, we obtain

$$\kappa_\delta \sim \frac{4a\omega_1\omega_2\omega_3}{(2\pi)^{3/2}\gamma\sqrt{\varepsilon}}\, e^{-\Delta E/\varepsilon}, \tag{1.168}$$

where a is the radius of the window. Note that ΔE is not the barrier height. We conclude that the activation rate is of Arrhenius form and has two contributions. The first is due to the potential, while the second is due to geometry of the absorbing window alone. Unlike the free diffusion case considered in the previous sections, geometrical properties of the domain, such as its volume, are not included in the leading order asymptotics of the reaction rate.

In two dimensions the singularity of the Neumann function is logarithmic, so the leading order approximation to the activation rate through the absorbing window is

$$\begin{aligned} k &\sim \frac{\pi\varepsilon}{\gamma|\Omega|}\frac{e^{-\langle\Delta E\rangle/\varepsilon}}{[\ln\delta^{-1} + O(1)]} \quad \text{for } \varepsilon \gg \Delta E \\ k &\sim \frac{\varepsilon\sqrt{\omega_1\omega_2}}{2\gamma}\frac{e^{-\Delta E/\varepsilon}}{[\ln\delta^{-1} + O(1)]}, \quad \text{for } \varepsilon \ll \Delta E. \end{aligned} \tag{1.169}$$

The remainder $O(1)$ is important, because in real life applications even if δ is small, $\ln\delta^{-1}$ is not necessarily large.

If the boundary of the absorbing window contains a singular point of $\partial\Omega$, such as a corner or a cusp, the order of magnitude of the activation rate may change. As in Sect. 1.4, if the window is at a corner of angle α, then the rate is

$$\begin{aligned} k &\sim \frac{\alpha\varepsilon}{\gamma|\Omega|}\frac{e^{-\langle\Delta E\rangle/\varepsilon}}{[\ln\delta^{-1}+O(1)]}, \quad \text{for } \varepsilon \gg \Delta E \\ k &\sim \frac{\alpha\varepsilon\sqrt{\omega_1\omega_2}}{2\pi\gamma}\frac{e^{-\Delta E/\varepsilon}}{[\ln\delta^{-1}+O(1)]}, \quad \text{for } \varepsilon \ll \Delta E. \end{aligned} \tag{1.170}$$

If the absorbing window is near a cusp, then $\mathbb{E}\tau_\delta$ grows algebraically, rather than logarithmically. For example, in the domain bounded between two tangent circles, the activation rate is

$$\begin{aligned} k &\sim \frac{(d^{-1}-1)\varepsilon}{\gamma|\Omega|}\left[\delta+O(\delta^2)\right]e^{-\langle\Delta E\rangle/\varepsilon}, \quad \text{for } \varepsilon \gg \Delta E \\ k &\sim \frac{(d^{-1}-1)\varepsilon\sqrt{\omega_1\omega_2}}{2\pi\gamma}\left[\delta+O(\delta^2)\right]e^{-\Delta E/\varepsilon}, \quad \text{for } \varepsilon \ll \Delta E, \end{aligned} \tag{1.171}$$

where $d<1$ is the ratio of the radii.

1.9.3 Deep Well: A Markov Chain Model

The modified Kramers formulas (1.167) or (1.169) can be explained by coarse-graining the diffusive motion into a simplified 3-state Markov model (see Schuss 2010b, Chap. 10), when the domain contains a deep well $\Omega_W \subset \Omega$. The three states of the Markov process are (1) state W—the trajectory is trapped in the deep well; (2) state $\mathcal{D}$—the trajectory diffuses in the domain $\Omega_{\mathcal{D}} = \Omega - \Omega_W$, outside the well; (3) state A—the trajectory is absorbed in the small hole. Once the trajectory is absorbed in the small hole, its motion is terminated, so A is a terminal state of the Markov chain. For simplicity, we assume $\Omega \subset \mathbb{R}^2$.

In the deep well case the mean time that the particle spends at state W is exponentially larger than the mean time spent at state $\mathcal{D}$. Therefore, the mean time to absorbtion is approximately the average number of visits at state $\mathcal{D}$ times the average time of a single visit in the deep well. The average number of visits in state $\mathcal{D}$ prior to absorbtion is $1/\Pr\{\tau_{\mathcal{D}\to A} < \tau_{\mathcal{D}\to W}\}$, as in a geometric distribution, hence

$$\mathbb{E}\tau_{W\to A} \sim \frac{\mathbb{E}\tau_{W\to\mathcal{D}}}{\Pr\{\tau_{\mathcal{D}\to A} < \tau_{\mathcal{D}\to W}\}}. \tag{1.172}$$

We conclude that

$$\mathbb{E}\tau_{\mathcal{D}\to A} \sim \mathbb{E}\tau_{W\to A}, \tag{1.173}$$

that is, the initial state (or location) of the particle has no (leading order) significance for the mean absorbtion time $\mathbb{E}\tau_{\delta}$, which by (1.172) and

$$\Pr\{\tau_{\mathcal{D}\to A} < \tau_{\mathcal{D}\to W}\} \sim \frac{\mathbb{E}[\tau_{\mathcal{D}\to W} \mid \tau_{\mathcal{D}\to W} < \tau_{\mathcal{D}\to A}]}{\mathbb{E}[\tau_{\mathcal{D}\to A} \mid \tau_{\mathcal{D}\to A} < \tau_{\mathcal{D}\to W}]}. \tag{1.174}$$

is

$$\mathbb{E}\tau_{\delta} \sim \mathbb{E}\tau_{W\to A} \sim \frac{\mathbb{E}\tau_{W\to\mathcal{D}}}{\Pr\{\tau_{\mathcal{D}\to W} < \tau_{\mathcal{D}\to A}\}}. \tag{1.175}$$

It follows from the second equation in (1.169) that

$$\mathbb{E}\tau_{\delta} = \frac{2\gamma \ln \delta^{-1}}{\varepsilon\sqrt{H(x_W)}} \exp\left\{\frac{\phi_0 - \phi(x_W)}{\varepsilon}\right\}. \tag{1.176}$$

Chapter 2
Special Asymptotics for Stochastic Narrow Escape

The method of Chap. 1 obviously fails for Brownian motion in two-dimensional domains whose boundaries are smooth and reflecting, except for a small absorbing window at the end of a cusp-shaped funnel, as shown in Figs. 1.2(left) and 2.1. The cusp can be formed by a partial block of a planar domain, as shown in the schematic Fig. 2.2(left). The MFPT from $\boldsymbol{x} \in \Omega$ to the absorbing boundary $\partial\Omega_a$, denoted $\bar{\tau}_{\boldsymbol{x}\to\partial\Omega_a}$, is the NET from the domain Ω to the small window $\partial\Omega_a$ (of length a), such that

$$\varepsilon = \frac{\pi|\partial\Omega_a|}{|\partial\Omega|} = \frac{\pi a}{|\partial\Omega|} \ll 1. \tag{2.1}$$

We consider the NET problem in an asymmetric planar domain, as in Fig. 2.2(left) or in an asymmetric version of the (dimensional) domain Ω' in Fig. 2.1(left). We use the (dimensional) representation of the boundary curves for the upper and lower parts, respectively,

$$y' = r_\pm(x'),\ \Lambda' < x' < 0, \tag{2.2}$$

where the x'-axis is horizontal with $x' = \Lambda'$ at AB. We assume that the parts of the curve that generate the funnel have the form

$$\begin{aligned} r_\pm(x') &= O(\sqrt{|x'|})\ \text{ near } x' = 0 \\ r_\pm(x') &= \pm a' \pm \frac{(x'-\Lambda')^{1+\nu_\pm}}{\nu_\pm(1+\nu_\pm)\ell_\pm^{\nu_\pm}}(1+o(1))\ \text{ for } \nu_\pm > 0 \text{ near } x' = \Lambda', \end{aligned} \tag{2.3}$$

where $a' = \frac{1}{2}\overline{AB} = \varepsilon'/2$ is the radius of the gap, and the constants $\ell_\pm$ have dimension of length. For $\nu_\pm = 1$ the parameters $\ell_\pm$ are the radii of curvature

D. Holcman, Z. Schuss, *Stochastic Narrow Escape in Molecular and Cellular Biology*, DOI 10.1007/978-1-4939-3103-3_2

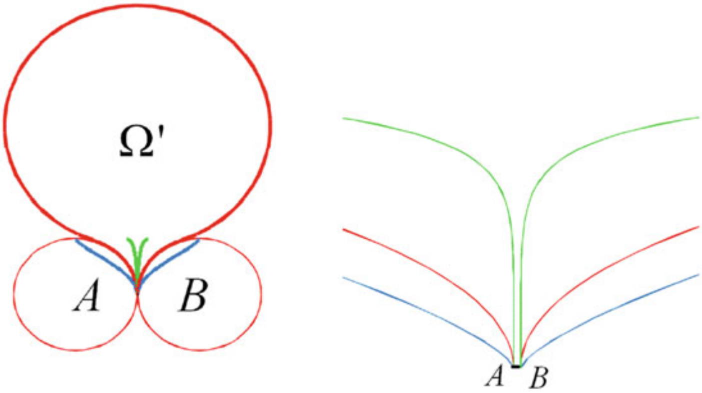

Fig. 2.1 *Left*: the planar domain Ω' is bounded by a large circular arc connected smoothly to a funnel formed by moving ε apart two tangent circular arcs of radius R_c (i.e., $\overline{\boldsymbol{AB}} = \varepsilon$). *Right*: blowup of the cusp region. The *red*, *green*, and *blue* necks correspond to $\nu = 1,\ 0.4$, and 5 in (2.3), respectively

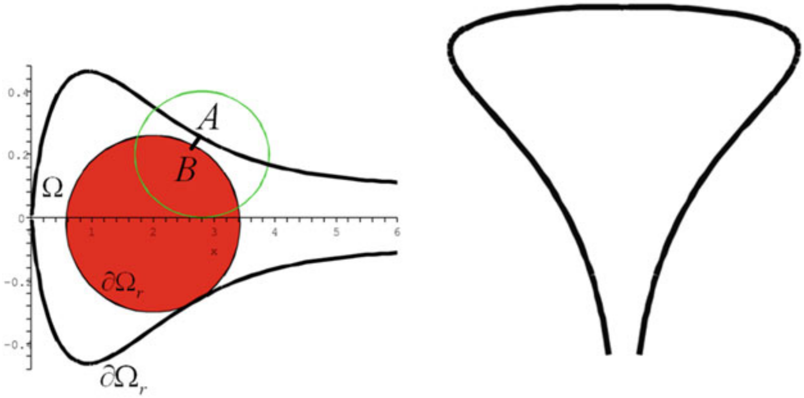

Fig. 2.2 *Left*: the domain Ω is enclosed between the *black curve*, the *red obstacle*, and the segment $\boldsymbol{AB}$. The reflecting boundary $\partial\Omega_r$ consists of the curve and the boundary of the obstacle. The absorbing boundary $\partial\Omega_a$ is the segment $\boldsymbol{AB}$. *Right*: a surface of revolution with a funnel. The z-axis points down

$R_c^{\pm}$ at $x' = \Lambda'$. To simplify the conformal mapping, we first rotate the domain by $\pi/2$ clockwise to assume the shape in Fig. 2.2(right). The rotated axes are renamed (x', y') as well.

2.1 Brownian Motion in Dire Straits

Theorem 2.1.1 (The MFPT to a Bottleneck). *The NET of Brownian motion to the end of the bottleneck in the domain* Ω' *bounded by the curves* (2.2)*, formula* (2.3) *is given by*

$$\bar{\tau} \sim \frac{\pi|\Omega'|}{2D\sqrt{\tilde{\varepsilon}}}, \tag{2.4}$$

where $\tilde{\varepsilon} = 2r_c\varepsilon/(R_c + r_c)$*. In dimensional units (2.4) is*

$$\bar{\tau} = \sqrt{\frac{R_c(R_c + r_c)}{2r_c\varepsilon'}}\frac{\pi|\,\Omega'|}{2D}\,(1 + o(1)) \quad \textit{for } \varepsilon' \ll |\partial\Omega'|, R_c, r_c. \tag{2.5}$$

In the symmetric case $R_c = r_c$ *(2.5) reduces to*

$$\bar{\tau} = \frac{\pi|\,\Omega'|}{2D\sqrt{\varepsilon'/R_c}}\,(1 + o(1)) \quad \textit{for } \varepsilon' \ll |\partial\Omega'|, R_c. \tag{2.6}$$

Proof. We consider Brownian motion in a domain Ω', with diffusion coefficient D and with reflection at the boundary $\partial\Omega'$, except for an absorbing boundary $\partial\Omega'_a$ at the bottom of the neck. The MFPT from a point $\boldsymbol{x}' = (x', y')$ inside the domain Ω' to $\partial\Omega'_a$ is the solution of the Pontryagin–Andronov–Vitt boundary value problem (1.4)–(1.6), which we rewrite in dimensional variables as

$$D\Delta\bar{u}(\boldsymbol{x}') = -1 \quad \text{for } \boldsymbol{x}' \in \Omega' \tag{2.7}$$
$$\frac{\partial\bar{u}(\boldsymbol{x}')}{\partial n} = 0 \quad \text{for } \boldsymbol{x}' \in \partial\Omega' - \partial\Omega'_a, \quad \bar{u}(\boldsymbol{x}') = 0 \quad \text{for } \boldsymbol{x}' \in \partial\Omega'_a.$$

Converting to dimensionless variables by setting $\boldsymbol{x}' = \ell_+\boldsymbol{x},\ \Lambda' = \ell_+\Lambda$, the domain Ω' is mapped into Ω and we have [see (2.8) below]

$$|\Omega'| = \ell_+^2|\Omega|,\ |\partial\Omega'| = \ell_+|\partial\Omega|,\ |\partial\Omega'_a| = \varepsilon' = \ell_+|\partial\Omega_a| = \ell_+\varepsilon. \tag{2.8}$$

Setting $\bar{u}(\boldsymbol{x}') = u(\boldsymbol{x})$, we write (2.7) as

$$\frac{D}{\ell_+^2}\Delta u(\boldsymbol{x}) = -1 \quad \text{for } \boldsymbol{x} \in \Omega$$
$$\frac{\partial u(\boldsymbol{x})}{\partial n} = 0 \quad \text{for } \boldsymbol{x} \in \partial\Omega - \partial\Omega_a, \quad u(\boldsymbol{x}) = 0 \quad \text{for } \boldsymbol{x} \in \partial\Omega_a. \tag{2.9}$$

First, we consider the case $\nu_\pm = 1$, $\ell_+ = R_c$, and $l_- = r_c$, radius 1, and A has dimensionless radius r_c/R_c. This case can represent a partial block described in Fig. 2.2(left). Under the scaling (2.8) the bounding circle B has dimensionless radius 1. We construct an asymptotic solution for small gap ε by first mapping the domain Ω in Fig. 2.1(left) conformally into its image under the Möbius transformation of the two osculating circles A and B into concentric circles. To this end we move the origin of the complex plane to the center of the osculating circle B and set

$$w = w(z) = \frac{z-\alpha}{1-\alpha z}, \tag{2.10}$$

where

$$\begin{aligned}\alpha =& -\frac{2\varepsilon R_c + 2R_c + \varepsilon^2 R_c + 2r_c\varepsilon + 2r_c}{2(\varepsilon R_c + r_c + R_c)}\\ &\pm \frac{\sqrt{\varepsilon(8R_c r_c + 4\varepsilon R_c^2 + 12\varepsilon R_c r_c + 4\varepsilon^2 R_c^2 + 8r_c^2 + 4\varepsilon^2 R_c r_c + \varepsilon^3 R_c^2 + 4\varepsilon r_c^2)}}{2(\varepsilon R_c + r_c + R_c)}\\ =& -1 \pm \sqrt{\frac{2r_c\varepsilon}{R_c + r_c}} + O(\varepsilon).\end{aligned} \tag{2.11}$$

The Möbius transformation (2.10) maps circle B into itself and Ω is mapped onto the domain $\Omega_w = w(\Omega)$ in Fig. 2.3. The straits in Fig. 2.1(left) are mapped onto the ring enclosed between the like-style arcs and the large disk is mapped onto the small black disk. The radius of the small black disk and the elevation of its center

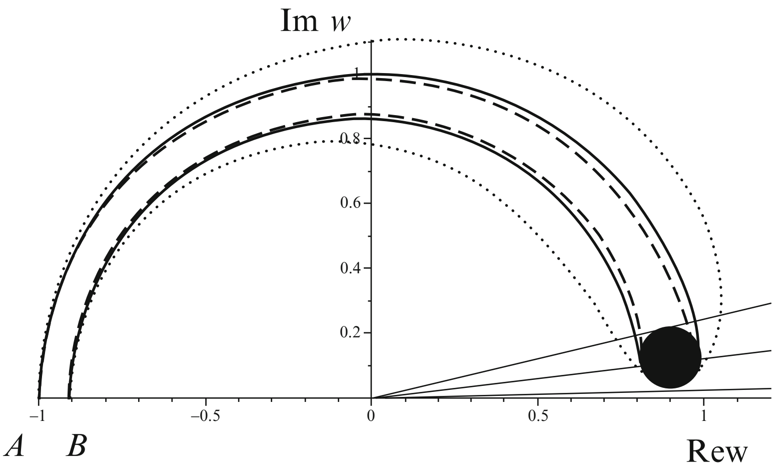

Fig. 2.3 The image $\Omega_w = w(\Omega)$ of the (dimensionless) domain Ω in Fig. 2.1(left) under the conformal mapping (2.10). The different necks in Fig. 2.1(right) are mapped onto the semi-annuli enclosed between the like-style arcs and the large disk in Ω is mapped onto the small black disk. The short black segment AB in Fig. 2.1(right) (of length ε) is mapped onto the *thick black segment* AB (of length $2\sqrt{\varepsilon} + O(\varepsilon)$). The rays from the origin are explained in the text below

above the real axis are $O(\sqrt{\varepsilon})$. The short black segment of length ε in Fig. 2.1(right) is mapped onto a segment of length $2\sqrt{\varepsilon}+O(\varepsilon)$.

Setting $u(z)=v(w)$ and $\tilde{\varepsilon}=2r_c\varepsilon/(R_c+r_c)$, the system (2.9) is converted to

$$\Delta_w v(w) = -\frac{\ell_+^2}{D|w'(z)|^2} = -\frac{(4\tilde{\varepsilon}+O(\tilde{\varepsilon}^{3/2}))\ell_+^2}{D|w(1-\sqrt{\tilde{\varepsilon}})-1+O(\tilde{\varepsilon})|^4} \quad \text{for } w\in\Omega_w \tag{2.12}$$
$$\frac{\partial v(w)}{\partial n} = 0 \ \text{ for } w\in\partial\Omega_w-\partial\Omega_{w,a}, \quad v(w)=0 \ \text{ for } w\in\partial\Omega_{w,a}.$$

The MFPT is bounded above and below by that from the inverse image of a circular ring cut by lines through the origin, tangent to the black disk at polar angles $\theta = c_1\sqrt{\tilde{\varepsilon}}$ (top) and $\theta = c_2\sqrt{\tilde{\varepsilon}}$ (bottom) for some positive constants c_1, c_2, independent of $\tilde{\varepsilon}$. Therefore the MFPT from Ω equals that from the inverse image of a ring cut by an intermediate angle $\theta = c\sqrt{\tilde{\varepsilon}}$ (middle).

The asymptotic analysis of (2.12) begins with the observation that the solution of the boundary value problem (2.12) is to leading order independent of the radial variable in polar coordinates $w = re^{i\theta}$. Fixing $r = 1$, we impose the reflecting boundary condition at $\theta = c\sqrt{\tilde{\varepsilon}}$, where $c = O(1)$ is a constant independent of $\tilde{\varepsilon}$ to leading order, and the absorbing condition at $\theta = \pi$. The outer solution, obtained by a regular expansion of $v(e^{i\theta})$, is given by

$$v_0(e^{i\theta}) = A(\theta-\pi), \tag{2.13}$$

where A is yet an undetermined constant. It follows that

$$\left.\frac{\partial v_0(e^{i\theta})}{\partial\theta}\right|_{\theta=\pi} = -A. \tag{2.14}$$

To determine A, we integrate (2.12) over the domain to obtain at the leading order

$$2\sqrt{\tilde{\varepsilon}}\left.\frac{\partial v_0(e^{i\theta})}{\partial\theta}\right|_{\theta=\pi} = -2\sqrt{\tilde{\varepsilon}}A \sim -\frac{|\Omega'|}{D}, \tag{2.15}$$

hence

$$A \sim \frac{|\Omega'|}{2D\sqrt{\tilde{\varepsilon}}}. \tag{2.16}$$

Now (2.13) gives for $\theta = c\sqrt{\tilde{\varepsilon}}$ the leading order approximation (2.4). Returning to dimensional units (2.4) becomes (2.5) and in the symmetric case $R_c = r_c$ (2.5) reduces to (2.6). □

Remarks. The symmetric case with $\nu_+ = \nu_- > 1$ for which the curvature vanishes, that is, $R_c = r_c = \infty$ is still open. After scaling the boundary value problem (1.4)–(1.6) with (2.8), we can choose the bounding circles at A and B to have radius 1 and repeat the above analysis in the domain Ω_w enclosed by the dashed curves, shown in Fig. 2.3. The result (2.6) becomes

$$\bar{\tau} = \frac{\pi|\,\Omega'|}{2D\sqrt{\varepsilon'/\ell_+}}[1+o(1)] \;\text{ for } \varepsilon' \ll |\partial\Omega'|, \ell_+. \tag{2.17}$$

A more direct resolution of the boundary layer, based on the observation that the boundary layer equation (2.12) is an ordinary differential equation, is given in Holcman et al. (2011), Holcman and Schuss (2011), and Schuss (2013).

2.1.1 Exit from Several Bottlenecks

In the case of exit through any one of N well-separated necks with dimensionless curvature parameters l_j and widths $\tilde{\varepsilon}_j$, we construct the outer solution (2.13) at any one of the N absorbing windows so that (2.14) holds at each window. The integration of (2.12) over Ω gives the following analog of (2.15),

$$\sum_{j=1}^{N} 2\sqrt{\tilde{\varepsilon}_j}\frac{\partial v_0(e^{i\theta})}{\partial\theta}\bigg|_{\theta=\pi} = -\sum_{j=1}^{N} 2\sqrt{\tilde{\varepsilon}_j}A \sim -\frac{|\Omega'|}{D}, \tag{2.18}$$

hence

$$A \sim \frac{|\Omega'|}{2D\sum_{j=1}^{N}\sqrt{\tilde{\varepsilon}_j}}. \tag{2.19}$$

Equation (2.17) is then generalized to

$$\bar{\tau} = \frac{\pi|\Omega'|}{2D\sum_{j=1}^{N}\sqrt{\varepsilon'_j/\ell_j}}[1+o(1)] \;\text{ for } \varepsilon'_j/\ell_j \ll |\partial\Omega|. \tag{2.20}$$

Equation (2.6) is generalized in a similar manner.

To calculate the exit probability through any one of the N necks, we apply the transformation (2.10) separately for each bottleneck at the absorbing images $\partial\Omega_{w,a_1},\ldots,\partial\Omega_{w,a_N}$ to obtain images Ω_{w_j} for $j=1,2,\ldots,N$. Then the probability of exiting through $\partial\Omega_{w,a_i}$ is the solution of the mixed boundary value problem

$$\Delta_w v(w) = 0 \;\text{ for } w\in\Omega_{w_i}, \quad \frac{\partial v(w)}{\partial n} = 0 \;\text{ for } w\in\partial\Omega_{w_i} - \bigcup_{i=1}^{N}\partial\Omega_{w,a_i} \tag{2.21}$$

$$v(w) = 1 \;\text{ for } w\in\partial\Omega_{w,a_i}, \quad v(w) = 0 \;\text{ for } w\in\partial\Omega_{w,a_j},\ j\neq i.$$

The outer solution, which is the exit probability through window $\partial\Omega_{w,i}$, is an unknown constant p_i. We construct boundary layers at each absorbing boundary $\partial\Omega_{w,a_j}$ for $j\neq i$ by solving the boundary value problem in Ω_{w_j}, which is of the type shown in Fig. 2.3 with a neck of width ε_j. In each case the boundary layer is a linear function

$$v_j(\theta) = \delta_{i,j} - A_j(\theta-\pi) \;\text{ for all } j, \tag{2.22}$$

such that

$$v_j(0) \sim \delta_{i,j} + A_j\pi = p_i \text{ for all } j. \tag{2.23}$$

To determine the value of the constant p_i, we note that

$$\left.\frac{\partial v\left(e^{i\theta}\right)}{\partial n}\right|_{\partial\Omega_{w,a}} = \left.\frac{\partial v_j(\theta)}{\partial\theta}\right|_{\theta=\pi} = -A_j, \tag{2.24}$$

so the integration of (2.21) over Ω_{w_i} gives to leading order

$$\sum_{j=1}^{N} A_j|\partial\Omega_{w,a_j}| = \sum_{j=1}^{N} 2A_j\sqrt{\tilde{\varepsilon}_j} = 0. \tag{2.25}$$

The $N+1$ equations (2.23) and (2.25) for the unknowns $p_i, A_1, \ldots, A_N$ give the exit probability from an interior point in the planar case as

$$p_i = \frac{\sqrt{\varepsilon'/\ell_i}}{\sum_{j=1}^{N}\sqrt{\varepsilon_j'/\ell_j}}. \tag{2.26}$$

2.1.2 Two-Dimensional Bottlenecks

A planar composite domain with a bottleneck Ω consists of a head Ω_1 connected through a small interface $\partial\Omega_i$ to a narrow cylindrical neck Ω_2. The boundary of Ω is assumed reflecting to Brownian particles, except the far end of Ω_2, denoted $\partial\Omega_a$, which is absorbing. For example, in Fig. 1.2(left) the interface $\partial\Omega_i$ is the black segment AB and the absorbing boundary $\partial\Omega_a$ is the segment CD at the bottom of the strip. The surface of revolution obtained by rotating the domain in the figure about its axis of symmetry has a similar structure. The interface $\partial\Omega_i$ in this case is a circle. Thus the length of the interface $|\partial\Omega_i|$ is given by

$$|\partial\Omega_i| = \begin{cases} a & \text{for a line segment} \\ 2\pi a & \text{for a circle.} \end{cases} \tag{2.27}$$

Theorem 2.1.2 (The NET from a Domain with a Long Neck). *The MFPT of Brownian motion from a composite domain Ω with reflecting boundary to an absorbing boundary at the end of a narrow cylindrical neck of length L is given by*

$$\bar{\tau}_{x\to\partial\Omega_a} = \bar{\tau}_{x\to\partial\Omega_i} + \frac{L^2}{2D} + \frac{|\Omega_1|L}{|\partial\Omega_a|D}. \tag{2.28}$$

.

First, we prove the following lemma.

Lemma 2.1.1. *The MFPT from a point* $\boldsymbol{x} \in \Omega_1$ *to* $\partial\Omega_a$ *satisfies the renewal equation*

$$\bar{\tau}_{\boldsymbol{x}\to\partial\Omega_a} = \bar{\tau}_{\boldsymbol{x}\to\partial\Omega_i} + \int\limits_{\partial\Omega_i} G(\boldsymbol{x}\,|\,\boldsymbol{\xi})\bar{\tau}_{\boldsymbol{\xi}\to\partial\Omega_a}\,ds_{\boldsymbol{\xi}}, \tag{2.29}$$

where $G(\boldsymbol{x}\,|\,\boldsymbol{\xi})$ *is Green's function for the mixed boundary value problem*

$$\begin{aligned} \Delta u(\boldsymbol{x}) &= 0 \ \textit{for}\, \boldsymbol{x} \in \Omega_1 \\ \frac{\partial u(\boldsymbol{x})}{\partial n} &= 0 \ \textit{for}\, \boldsymbol{x} \in \partial\Omega_1 - \partial\Omega_i \\ u(\boldsymbol{x}) &= \varphi(\boldsymbol{x}) \ \textit{for}\, \boldsymbol{x} \in \partial\Omega_i. \end{aligned} \tag{2.30}$$

The identity (2.30) follows from the fact that both sides of (2.29) satisfy (2.30) for $\boldsymbol{x} \in \Omega_1$ and coincide on $\partial\Omega_i$. The identity (2.29) can be interpreted as

$$\bar{\tau}_{\boldsymbol{x}\to\partial\Omega_a} = \bar{\tau}_{\boldsymbol{x}\to\partial\Omega_i} + \bar{\tau}_{\partial\Omega_i\to\partial\Omega_a}, \tag{2.31}$$

where the MFPT $\bar{\tau}_{\partial\Omega_i\to\partial\Omega_a}$ is $\bar{\tau}_{\boldsymbol{x}\to\partial\Omega_a}$, averaged over $\partial\Omega_i$ with respect to the flux density of Brownian trajectories in Ω_1 into an absorbing boundary at $\partial\Omega_i$ [see Schuss (2010b) for further details].

Proof. We use Lemma 2.1.1 to sum the MFPTs. First, we calculate $\bar{\tau}_{\partial\Omega_i\to\partial\Omega_a}$ and the absorption flux at the interface. In the narrow neck Ω_2 the boundary value problem (1.4)–(1.6) can be approximated by the one-dimensional boundary value problem

$$Du_{zz} = -1 \ \text{ for } 0 < z < L, \quad u(0) = 0, \quad u(L) = u_H,$$

where the value at the interface $u(L) = u_H$ is yet unknown. The solution is given by

$$u(z) = -\frac{z^2}{2D} + Bz, \tag{2.32}$$

so that

$$u(L) = u_H = -\frac{L^2}{2D} + BL, \tag{2.33}$$

which relates the unknown constants B and u_H. The constant B is found by multiplying equation (1.4) by the Neumann function $N(\boldsymbol{x},\boldsymbol{y})$, integrating over Ω_1, applying Green's formula, and using the boundary conditions (1.5) and (1.6). Specifically, we obtain for all $\boldsymbol{y} \in \partial\Omega_i$

$$v(\boldsymbol{y}) = -\frac{1}{D}\int\limits_{\Omega_1} N(\boldsymbol{x},\boldsymbol{y})\,d\boldsymbol{x} - \int\limits_{\partial\Omega_i} N(\boldsymbol{x},\boldsymbol{y})\frac{\partial v(\boldsymbol{x})}{\partial n}\,dS_{\boldsymbol{x}} + \frac{1}{|\Omega_1|}\int\limits_{\Omega_1} v(\boldsymbol{x})\,d\boldsymbol{x}. \tag{2.34}$$

Approximating, as we may, $v(\boldsymbol{y}) \approx u(L)$ and using (2.33), we obtain

$$-\frac{L^2}{2D} + BL = -\frac{1}{D}\int\limits_{\Omega_1} N(\boldsymbol{x},\boldsymbol{y})\,d\boldsymbol{x} - \int\limits_{\partial\Omega_i} N(\boldsymbol{x},\boldsymbol{y})\frac{\partial v(\boldsymbol{x})}{\partial n}\,dS_{\boldsymbol{x}} \tag{2.35}$$
$$+\frac{1}{|\Omega_1|}\int\limits_{\Omega_1} v(\boldsymbol{x})\,d\boldsymbol{x}.$$

Because $v(\boldsymbol{x})$ is the solution of the boundary value problem (1.4)–(1.6) in the entire domain $\Omega = \Omega_1 \bigcup \Omega_2$, the meaning of (2.35) is the connecting rule (2.31), where

$$\bar{\tau}_{\boldsymbol{x}\to\partial\Omega_a} = \frac{1}{|\Omega_1|}\int\limits_{\Omega_1} v(\boldsymbol{x})\,d\boldsymbol{x} \tag{2.36}$$

$$\bar{\tau}_{\partial\Omega_i\to\partial\Omega_a} = u(L) \tag{2.37}$$

$$\bar{\tau}_{\boldsymbol{x}\to\partial\Omega_i} = -\frac{1}{D}\int\limits_{\Omega} N(\boldsymbol{x},\boldsymbol{y})\,d\boldsymbol{x} - \int\limits_{\partial\Omega_i} N(\boldsymbol{x},\boldsymbol{y})\frac{\partial v(\boldsymbol{x})}{\partial n}\,dS_{\boldsymbol{x}}. \tag{2.38}$$

Equation (2.36) gives the MFPT, averaged over Ω_1. The averaging is a valid approximation, because the MFPT to $\partial\Omega_i$ is constant to begin with (except in a negligible boundary layer). Equation (2.37) is the MFPT from the interface to the absorbing end $\partial\Omega_a$ of the strip, and (2.38) follows from (1.15).

Matching the solutions in Ω_1 and Ω_2 continuously across $\partial\Omega_i$, we obtain the total flux on $\partial\Omega_i$ as

$$J = D\int\limits_{\partial\Omega_i} \frac{\partial v(\boldsymbol{x})}{\partial \nu}\,dS_{\boldsymbol{x}} = -\left(|\Omega_1| + |\Omega_2|\right), \tag{2.39}$$

Noting that $\partial v(\boldsymbol{x})/\partial n = -u'(0) = -B$, we get from (2.27) and (2.39) that

$$B = -\begin{cases} \dfrac{|\Omega_1|}{aD} + \dfrac{L}{D} & \text{for a line segment} \\[2ex] \dfrac{|\Omega_1|}{2\pi aD} + \dfrac{L}{D} & \text{for a circle} \\[2ex] \dfrac{|\Omega_1|}{\pi a^2 D} + \dfrac{L}{D} & \text{for a circular disk.} \end{cases} \tag{2.40}$$

Finally, we put (2.31)–(2.40) together to obtain (2.28). The MFPT $\bar{\tau}_{\boldsymbol{x}\to\partial\Omega_i}$ for the various domains is given in this chapter above. □

The expression (2.28) for the NET from a domain with a bottleneck in the form of a one-dimensional neck, such as a dendritic spine, can be summarized as follows. Consider a domain Ω with head Ω_1 and a narrow cylindrical neck Ω_2 of length L and radius a, connected smoothly to the head. The radius of curvature at the connection is R_c. In the two-dimensional case

$$\bar{\tau}_{x\to\partial\Omega_a} = \begin{cases} \dfrac{|\Omega_1|}{\pi D}\ln\dfrac{|\partial\Omega_1|}{a} + \dfrac{O(1)}{D} + \dfrac{L^2}{2D} + \dfrac{|\Omega_1|L}{aD} \\ \text{planar spine connected to the neck at a right angle} \\[2ex] \dfrac{\pi|\Omega_1|}{D}\sqrt{\dfrac{R_c}{a}}\,(1+o(1)) + \dfrac{L^2}{2D} + \dfrac{|\Omega_1|L}{2\pi aD} \\ \text{planar spine with a smooth connecting funnel} \\[2ex] \dfrac{|\Omega_1|}{2\pi D}\log\dfrac{\sin\frac{\theta}{2}}{\sin\frac{\delta}{2}} + \dfrac{L^2}{2D} + \dfrac{|\Omega_1|L}{2\pi aD} \\ \text{spherical spine surface connected to the neck at a right angle,} \\ \dfrac{|\Omega_1|}{2D}\dfrac{\left(\dfrac{\ell}{(1+\nu)a}\right)^{\nu/1+\nu}\nu^{1/1+\nu}}{\sin\dfrac{\nu\pi}{1+\nu}} + \dfrac{L^2}{2D} + \dfrac{|\Omega_1|L}{2\pi aD} \\ \text{spherical spine surface with a smooth connecting funnel (2.3),} \end{cases} \tag{2.41}$$

where R is the radius of the sphere, $a = R\sin\delta/2$, and θ is the initial elevation angle on the sphere. If $|\Omega_1| \gg aL$ and $L \gg a$, the last term in (2.41) is dominant, which is the manifestation of the many returns of Brownian motion from the neck to the head prior to absorption at $\partial\Omega_a$. Further cases are considered in Schuss (2013). Note that modulation of neck length changes the residence time significantly.

2.1.3 Annotations to Sect. 2.1

Section 2.1 develops a boundary layer theory for the solution of the mixed Neumann–Dirichlet problem for the Poisson equation in geometries in which the methodologies of Ward and Keller (1993), Ward et al. (1993), Ward and Van De Velde (1992), Kolokolnikov et al. (2005), Cheviakov et al. (2010), Coombs et al. (2009), Grigoriev et al. (2002), Holcman and Schuss (2004), Singer et al. (2006a,b,c), Singer and Schuss (2006), Bénichou and Voituriez (2008), and Schuss et al. (2007) fail. In the case of sufficiently smooth boundaries near the absorbing window considered in Ward and Keller (1993), Ward et al. (1993), Ward and Van De Velde (1992), Kolokolnikov et al. (2005), Cheviakov et al. (2010), Coombs et al. (2009), and Bénichou and Voituriez (2008) the leading order boundary layer problem is that of the exactly solvable electrified disk problem (Jackson 1975), which gives no indication that the second order asymptotics ansatz should be logarithmic. The Neumann function approach of Holcman and Schuss (2004), Singer et al. (2006a,b,c), Singer and Schuss (2006), and Schuss et al. (2007), which is based on the standard leading order singularity of Neumann's function (Garabedian 1964), also fails to indicate the ansatz for second order boundary layer expansion. It is the insight that Popov's Theorem 1.5.1 gives about the asymptotics of Neumann's function that points at the correct ansatz for both the boundary layer method and the Neumann function method in the smooth case.

In the geometries considered in Sect. 2.1 the small Dirichlet part is located at the end of narrow straits with an absorbing end, connected smoothly to the Neumann boundary of the domain. The boundary layer near the absorbing boundary is not mapped in an obvious way to an exactly solvable problem as in the smooth case. Conformal mapping replaces the standard local stretching in resolving the boundary layer in narrow necks. Additional problems related to Brownian motion in composite domains that contain a cylindrical narrow neck connected smoothly or sharply to the head are considered in Holcman and Schuss (2011). These include the asymptotic evaluation of the NET, of the leading eigenvalue in dumbbell-shaped domains and domains with many heads interconnected by narrow necks, the escape probability through any one of several narrow necks, and more.

The effect of obstacles on the diffusion constant has been studied in the biological context for the last two decades (Edidin et al. 1991; Sheetz 1993; Suzuki and Sheetz 2001; Kusumi et al. 2005, 1993; Saxton 1995; Saxton and Jacobson 1997; Eisinger et al. 1986) and more recently it was demonstrated, using single-particle imaging (Borgdorff and Choquet 2002; Tardin et al. 2003; Triller and Choquet 2003; Choquet 2010), that the effective diffusion constant can span a large spectrum of values, from 0.001 to 0.2 μm^2/s (Choquet 2010).

The calculation of the NET in composite domains with long necks was attempted in Korkotian et al. (2004), Schuss et al. (2007), Grigoriev et al. (2002), Berezhkovskii et al. (2009), and ultimately accomplished in Holcman and Schuss (2011). The NET problem in a planar domain with an absorbing window at the end of a funnel was considered in Holcman et al. (2011). The case of planar domains that consist of large compartments interconnected by funnel-shaped bottlenecks was also considered in Holcman et al. (2011). The result (2.6) was found in Holcman et al. (2011). The coarse-graining of diffusion into a Markov chain is discussed in Hänggi et al. (1990) (see also Holcman and Schuss 2005c; Holcman et al. 2011). Results of this section are based on Holcman et al. (2011).

2.2 Brownian Needle in Dire Straits

As an application of the methodology described above, we study the planar diffusion of a stiff thin rod (needle) of length l in an infinite horizontal strip of width $l_0 > l$. We assume that the rod is a long thin right circular cylinder with radius

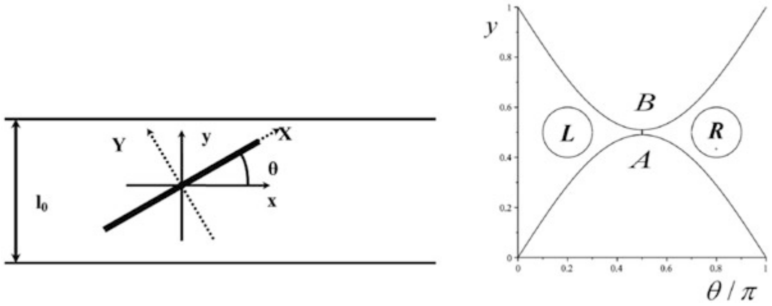

Fig. 2.4 Rod in strip. *Left*: the strip width is l_0 and the rod length is $l < l_0$. The position of the rod is characterized by the angle θ and the fixed coordinates x and y and the rotating system of coordinates (X, Y, θ). *Right*: the motion of the rod is confined to the domain Ω in the (θ, y) plane

$a \ll l_0$ [Fig. 2.4(left)]. The planar motion of the rod is described by two coordinates of the centroid and the rotational angle θ between the axes of the strip and the rod. The y-coordinate of the center of the rod is measured from the axis of the strip. The motion of the rod is confined to the dumbbell-shaped domain Ω shown in Fig. 2.4(right). The rod turns around if the point (θ, y) crosses from the left domain L into the right domain R or in the reverse direction (see Schuss 2010a, 2013). If

$$\varepsilon = \frac{l_0 - l}{l_0} \ll 1, \tag{2.42}$$

the window AB becomes narrow and the mean first passage times $\tau_{L\to AB}$ and $\tau_{R\to AB}$, from the left or right domains to the segment AB, which is the stochastic separatrix SS (Schuss 2013), become much longer than those from AB to L or R. They also become independent of the starting position outside a boundary layer near the segment AB. Thus the definition of the time to turn around is independent of the choice of the domains L and R in Fig. 2.4(right) as long as they are well separated from the segment AB. The neck near the segment is the boundary layer region near $\theta = \pi/2$. We neglect henceforward the short times relative to the long ones.

To turn across the vertical position the rod has to reach the segment AB from the left domain L for the first time and then to reach the right domain R for the first time, having returned to L any number of times prior to reaching R. The mean time to turn, $\tau_{L\to R}$, is asymptotically given by

$$\tau_{L\to R} \sim 2\tau_{L\to AB} \quad \text{for } \varepsilon \ll 1, \tag{2.43}$$

because on the average the rod trajectory hits the stochastic separatrix twice before it crosses over from one side of the SS to the other (see Schuss 2010a, 2013 for further details). The time to turn around is invariant to translations along the strip (the x-axis), therefore it suffices to describe the rod movement by its angle θ and the y-coordinate of its center. The position of the rod is defined for $\theta (\text{mod}\ \pi)$. Therefore the motion of the rod in the invariant strip can be mapped into that in the (θ, y) planar domain Ω [see Fig. 2.4(right)]:

$$\Omega = \left\{ (\theta, y) \;:\; |y| < \frac{l_0 - l\sin\theta}{2}, \quad 0 < \theta < \pi \right\}. \tag{2.44}$$

Our purpose is to calculate the mean turnaround time $\tau_{\boldsymbol{L}\to\boldsymbol{R}}$.

2.2.1 *The Diffusion Law of a Brownian Needle in a Planar Strip*

In a rotating system of coordinates (X, Y, θ), where the instantaneous X-axis is parallel to the long axis of the rod and the Y-axis is perpendicular to it, the diffusive motion of the rod is an anisotropic Brownian motion, and can be described by the stochastic equations (Holcman and Schuss 2012b)

$$\dot{X} = \sqrt{2D_X}\dot{w}_1, \quad \dot{Y} = \sqrt{2D_Y}\dot{w}_2, \quad \dot{\theta} = \sqrt{2D_r}\dot{w}_3,$$

where D_X is the longitudinal diffusion coefficient along the axis, D_Y the transversal diffusion constant, and D_r the rotational diffusion coefficient. Due to the anisotropy, the rod makes in general larger excursions in the X-direction than in the Y-direction and this is usually characterized by the ratio D_Y/D_X. Transforming into a fixed system of Cartesian coordinates (x, y), the motion of the centroid $(x(t), y(t))$ and the angle of rotation $\theta(t)$ of the rod is governed by the Itô equation (2.45).

In a fixed system of Cartesian coordinates (x, y), the translational and rotational motion of the centroid $(x(t), y(t))$ and the angle of rotation $\theta(t)$ of the rod is governed by the Itô equations

$$\begin{aligned}
\dot{x} &= \cos(\theta)\sqrt{2D_X}\,\dot{w}_1 - \sin(\theta)\sqrt{2D_Y}\,\dot{w}_2\\
\dot{y} &= \sin(\theta)\sqrt{2D_X}\,\dot{w}_1 + \cos(\theta)\sqrt{2D_Y}\,\dot{w}_2\\
\dot{\theta} &= \sqrt{2D_r}\dot{w}_3
\end{aligned} \tag{2.45}$$

with co-normal reflection at the boundary of the domain in Fig. 2.4(bottom panel). Putting (2.45) in the matrix form

$$\dot{\boldsymbol{x}}(t) = \boldsymbol{B}(\theta)\,\dot{\boldsymbol{w}}, \tag{2.46}$$

where

$$\boldsymbol{x} = \begin{pmatrix} x \\ y \\ \theta \end{pmatrix}, \quad \boldsymbol{w} = \begin{pmatrix} w_1 \\ w_2 \\ w_3 \end{pmatrix}$$

and

$$\boldsymbol{B}(\theta)=\sqrt{2}\begin{pmatrix}\cos\theta & -\sin\theta & 0\\ \sin\theta & \cos\theta & 0\\ 0 & 0 & 1\end{pmatrix}\begin{pmatrix}\sqrt{D_X} & 0 & 0\\ 0 & \sqrt{D_Y} & 0\\ 0 & 0 & \sqrt{D_r}\end{pmatrix},$$

we define the probability density function (pdf) $p(t,x,y,\theta)$ of the rod in the (x,y,θ) space by

$$p(t,x,y,\theta)\,d\boldsymbol{x}=\Pr\{(x(t),y(t),\theta(t))\in\boldsymbol{x}+d\boldsymbol{x}\},\tag{2.47}$$

which satisfies the Fokker–Planck equation (Schuss 2010b)

$$\frac{\partial p(t,\boldsymbol{x})}{\partial t}=-\nabla\cdot\boldsymbol{J}(t,\boldsymbol{x}),$$

where the flux is given by

$$\boldsymbol{J}(t,\boldsymbol{x})=-\begin{pmatrix}\left[D_X\cos^2\theta+D_Y\sin^2\theta\right]\dfrac{\partial p}{\partial x}+\dfrac{1}{2}\left[(D_X-D_Y)\sin 2\theta\right]\dfrac{\partial p}{\partial y}\\ \left[D_X\sin^2\theta+D_Y\cos^2\theta\right]\dfrac{\partial p}{\partial y}+\dfrac{1}{2}\left[(D_X-D_Y)\sin 2\theta\right]\dfrac{\partial p}{\partial x}\\ D_r\dfrac{\partial p}{\partial\theta}\end{pmatrix}.\tag{2.48}$$

Because $\boldsymbol{J}(t,\boldsymbol{x})$ is π-periodic in θ and the position of the rod is defined modulo π, the boundary conditions are π-periodic in θ and the normal flux $-D_r\partial p(t,x,y,\theta)/\partial\theta$ is π-antiperiodic in θ.

The MFPT $\tau_{\boldsymbol{L}\to\boldsymbol{AB}}$ is the solution $u(\theta,y)$ of the Pontryagin–Andronov–Vitt (Schuss 2010b) boundary value problem

$$D_r\frac{\partial^2 u(\theta,y)}{\partial\theta^2}+D_y(\theta)\frac{\partial^2 u(\theta,y)}{\partial y^2}=-1\quad\text{for }(\theta,y)\in\Omega_1,\tag{2.49}$$

where $D_y(\theta)=D_X\sin^2\theta+D_Y\cos^2\theta$ and $\Omega_1=\Omega\cap\{\theta<\pi/2\}$, with the mixed boundary conditions

$$\frac{\partial u}{\partial\tilde{n}}=0\quad\text{for }(\theta,y)\text{ on the curved boundary and at }\theta=0\tag{2.50}$$

$$u\left(\frac{\pi}{2},y\right)=0\quad\text{for }|y|<l_0-l,\tag{2.51}$$

where the co-normal derivative of $u(\theta, y)$ is given by

$$\frac{\partial u}{\partial \tilde{n}} = \nabla u(\theta, y) \cdot \tilde{\boldsymbol{n}}(\theta) \text{ for } (\theta, y) \text{ on the curved boundary} \tag{2.52}$$

and the co-normal vector $\tilde{\boldsymbol{n}}(\theta)$ is given by

$$\tilde{\boldsymbol{n}}(\theta) = \begin{pmatrix} D_r & 0 \\ 0 & D_y(\theta) \end{pmatrix} \boldsymbol{n}(\theta) \tag{2.53}$$

with $\boldsymbol{n}(\theta)$—the unit outer normal vector at the curved boundary.

The MFPT is the solution of the Pontryagin–Andronov–Vitt boundary value problem for (2.49)–(2.51), which corresponds to the stochastic system (2.46). Because the equation is translation-invariant with respect to x it reduces to (2.49). The boundary conditions at a curved boundary for anisotropic diffusion with state-dependent diffusion tensor follow from Singer et al. (2008b) and Schuss (2013, Sect. 2.6.2).

2.2.2 *The Turnaround Time*

Equation (2.43) shows that it suffices to calculate the MFPT $\tau_{\boldsymbol{L}\to\boldsymbol{AB}}$ in order to calculate the turnaround time $\tau_{\boldsymbol{L}\to\boldsymbol{R}}$.

Theorem 2.2.1 (The Turnaround Time). *The mean turnaround time of a Brownian needle of length l in a narrow strip of width l_0, such that $\varepsilon = (l_0 - l)/l_0 \ll 1$, is given by*

$$\tau_{\boldsymbol{L}\to\boldsymbol{R}} = \frac{\pi(\pi-2)}{D_r\sqrt{l_0(l_0-l)}}\sqrt{\frac{D_X}{D_r}}\left(1 + O\left(\sqrt{\frac{l_0-l}{l_0}}\right)\right). \tag{2.54}$$

Proof. Introducing the dimensionless variables

$$X' = \frac{X}{l_0}, \quad Y' = \frac{Y}{l_0}, \quad \xi(t) = \frac{x(t)}{l_0}, \quad \eta(t) = \frac{y(t)}{l_0}$$

and the normalized diffusion coefficients

$$D_X' = \frac{D_X}{l_0^2}, \quad D_Y' = \frac{D_Y}{l_0^2}, \quad D_\eta(\theta) = \frac{D_y(\theta)}{l_0^2},$$

we find that the domain Ω in (2.44) is mapped into

$$\Omega' = \left\{(\theta, \eta) \,:\, |\eta| < \frac{1-(1-\varepsilon)\sin\theta}{2}, \quad 0 < \theta < \pi\right\}. \tag{2.55}$$

To convert (2.49) to canonical form, we introduce the variable

$$\varphi(\theta)=\int\limits_0^\theta \sqrt{\frac{D_\eta(\theta')}{D_r}}\,d\theta', \tag{2.56}$$

which defines the inverse function $\theta=\theta(\varphi)$, and set $u(\theta,y)=U(\varphi,\eta)$ to obtain

$$U_{\varphi\varphi}(\varphi,\eta)+U_{\eta\eta}(\varphi,\eta)=U_\varphi(\varphi,\eta)\sqrt{D_r}\,\frac{dD_\eta^{-1/2}(\theta)}{d\theta}-\frac{1}{D_\eta(\theta)}. \tag{2.57}$$

The domain Ω', defined in (2.55), is mapped into the similar domain

$$\Omega''=\left\{(\varphi,\eta)\,:\,|\eta|<\frac{1-(1-\varepsilon)\sin\theta(\varphi)}{2},\quad 0<\varphi<\varphi(\pi)\right\} \tag{2.58}$$

in the (φ,η) plane. Because the co-normal direction at the boundary becomes normal, so does the co-normal derivative. The curved boundary in the scaled Fig. 2.4(right) is denoted $\partial\Omega''$. It follows that the no-flux boundary condition (2.50) and the absorbing condition (2.51) become

$$\begin{aligned}&\frac{\partial U(\varphi,\eta)}{\partial n}=0\ \text{ for } (\theta(\varphi),\eta) \text{ on } \partial\Omega'' \\ &\frac{\partial U(0,\eta)}{\partial\varphi}=0\ \text{ for } |\eta|<\frac{1}{2},\quad U\left(\varphi\left(\frac{\pi}{2}\right),\eta\right)=0\ \text{ for } |\eta|<\frac{\varepsilon}{2},\end{aligned} \tag{2.59}$$

respectively. The gap at $\theta=\pi/2$ is preserved and the (dimensionless) radius of curvature of the boundary at the gap is

$$R'=\frac{2D_\eta\left(\frac{\pi}{2}\right)}{(1-\varepsilon)D_r}=\frac{2D_X}{(1-\varepsilon)l_0^2D_r}. \tag{2.60}$$

First, we simplify (2.57) by setting

$$g(\varphi)=\sqrt{D_r}\,\frac{dD_\eta^{-1/2}(\theta)}{d\theta},\quad U(\varphi,\eta)=f(\varphi)V(\varphi,\eta) \tag{2.61}$$

and choosing $f(\varphi)$ such that $f'(\varphi)=\frac{1}{2}f(\varphi)g(\varphi)$. Note that

$$\left.\frac{dD_\eta^{-1/2}(\theta)}{d\theta}\right|_{\theta=0,\pi/2,\pi}=0. \tag{2.62}$$

Equation (2.57) becomes

$$V_{\varphi\varphi}+V_{\eta\eta}=\frac{1}{f(\varphi)}\left\{\left[g(\varphi)f'(\varphi)-f''(\varphi)\right]V-\frac{1}{D_\eta(\theta(\varphi))}\right\}. \tag{2.63}$$

Next, we move the origin to the center of curvature of the lower boundary by setting

$$\zeta=-\left(\eta-R'-\frac{\varepsilon}{2}\right)+i\left[\varphi-\varphi\left(\frac{\pi}{2}\right)\right]$$

and use the conformal mapping (2.10),

$$\omega=\frac{\zeta-R'\alpha}{R'-\alpha\zeta}, \tag{2.64}$$

with $\omega=\rho e^{i\psi}$. We also have

$$w'(\zeta)=\frac{1}{R'}\,\frac{(1+\alpha w)^2}{1-\alpha^2} \tag{2.65}$$

$$|w'(\zeta)|^2=\frac{1}{R'^2}\left|\frac{(1+w\alpha)^2}{1-\alpha^2}\right|^2=\frac{|1-w+\sqrt{\varepsilon}\,w|^4}{4\varepsilon R'^2}(1+O(\sqrt{\varepsilon})), \tag{2.66}$$

The image Ω_ω of the domain Ω is given in Fig. 2.5 and is similar to Ω_w in Fig. 2.3, except for a small distortion near $\psi=c\sqrt{\varepsilon}$, which we neglect, as we may. Setting $V(\varphi,\eta)=W(\rho,\psi)$, fixing $\rho=1$ in Ω_ω, as in Chap. 2, and abbreviating $W=W(\psi,1)$, Eq. (2.63) becomes to leading order

$$W_{\psi\psi}+\frac{h(\psi)}{|\omega'(\zeta|^2}W=-\frac{1}{|\omega'(\zeta)|^2k(\psi)}, \tag{2.67}$$

where

$$h(\psi)=\left.\frac{f''(\varphi)-g(\varphi)f'(\varphi)}{f(\varphi)}\right|_{\rho=1},\quad k(\psi)=f(\varphi)D_\eta(\theta(\varphi))|_{\rho=1}. \tag{2.68}$$

Using (2.12) and neglecting terms of order $O(\varepsilon)$, we rewrite (2.67) as

$$W_{\psi\psi}+\frac{4\varepsilon R'^2h(\psi)}{|e^{i\psi}(1-\sqrt{\varepsilon})-1|^4}W=-\frac{4\varepsilon R'^2}{|e^{i\psi}(1-\sqrt{\varepsilon})-1|^4k(\psi)}. \tag{2.69}$$

In view of (2.62), the boundary conditions (2.59) become

$$W_\psi(c\sqrt{\varepsilon})=0,\quad W(\pi)=0. \tag{2.70}$$

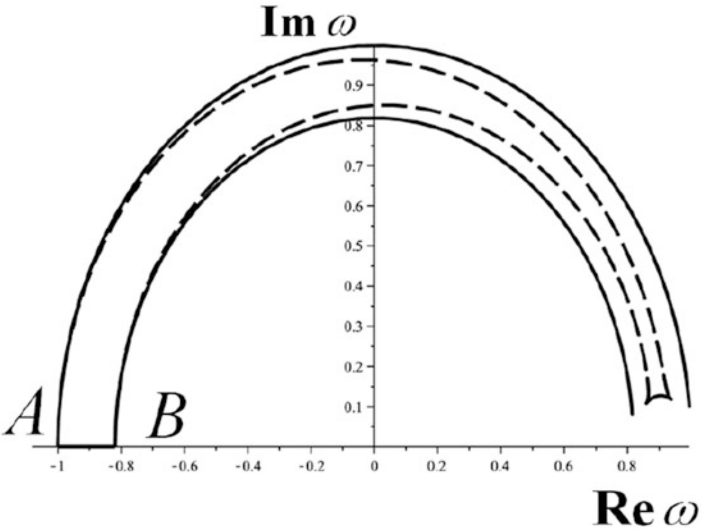

Fig. 2.5 The image Ω_ω of the domain Ω under the mapping (2.64). The values of the parameters are $\varepsilon = 0.01$ with the approximation $D_Y \ll D_X$. The domain is enclosed by the real segment *AB*, the *dashed arcs*, and the *small closing cap*. The *solid circular arcs* are the conformal images of arcs of the osculating *circles* at the narrow neck, as in Fig. 2.3

The outer solution of (2.69) is a linear function $W_{\text{outer}}(\psi) = a\psi + b$, where a and b are yet undetermined constants. The uniform approximation is constructed as $W_{\text{uniform}}(\psi) = W_{\text{outer}}(\psi) + W_{\text{bl}}(\psi)$, where the boundary layer $W_{\text{bl}}(\psi)$ is a function $Y(\xi)$ of the boundary layer variable $\xi = \psi/\sqrt{\varepsilon}$. The boundary layer equation is

$$Y''(\xi) + \frac{4R'^2 h(0)}{(1+\xi^2)^2} Y(\xi) = -\frac{4R'^2}{(1+\xi^2)^2 k(0)}, \tag{2.71}$$

which is simplified by the substitution $Y(\xi) = \tilde{Y}(\xi) + 1/h(0)k(0)$ to

$$\tilde{Y}''(\xi) + \frac{4R'^2 h(0)}{(1+\xi^2)^2} \tilde{Y}(\xi) = 0. \tag{2.72}$$

The boundary conditions (2.70) become $\tilde{Y}'(c) = 0$ and $\tilde{Y}(\infty) = 1/h(0)k(0)$.

The boundary layer equation (2.72) has two linearly independent solutions, $\tilde{Y}_1(\xi)$ and $\tilde{Y}_2(\xi)$, which are linear for sufficiently large ξ. Initial conditions for $\tilde{Y}_1(\xi)$ and $\tilde{Y}_2(\xi)$ can be chosen so that $\tilde{Y}_2(\xi) \to$ *const* as $\xi \to \infty$ (e.g., $\tilde{Y}_2(0) = -4.7$, $\tilde{Y}_2'(0) = -1$, see Fig. 2.6). Thus the boundary layer function is given by

$$W_{\text{bl}}(\psi) = A\tilde{Y}_1\left(\frac{\psi}{\sqrt{\varepsilon}}\right) + B\tilde{Y}_2\left(\frac{\psi}{\sqrt{\varepsilon}}\right) + C, \tag{2.73}$$

where A and B are constants to be determined and C is related to the constant $1/h(0)k(0)$ and is also determined below from the boundary and matching conditions.

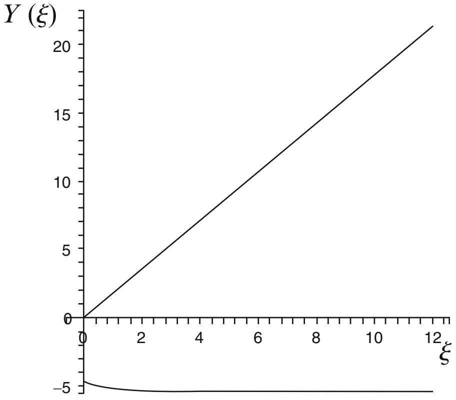

Fig. 2.6 Two linearly independent solutions of (2.72). The linearly growing solution $Y_1(\xi)$ satisfies the initial conditions $Y_1(0) = 0,\ Y_1'(0) = 2$. The asymptotically constant solution $Y_2(\xi)$ satisfies the initial conditions $Y_2(0) = -4.7,\ Y_2'(0) = -1$. The asymptotic value is $Y_2(\infty) \approx -5$

The matching condition is that $W_{\rm bl}(\psi) = A\tilde{Y}_1\left(\psi/\sqrt{\varepsilon}\right) + B\tilde{Y}_2\left(\psi/\sqrt{\varepsilon}\right) + C$ remains bounded as $\xi \to \infty$, which implies $A = 0$. It follows that at the absorbing boundary $\psi = \pi$ we have

$$W_{\rm unif}(\pi) = a\pi + b' = 0, \quad W'_{\rm unif}(\pi) = a, \tag{2.74}$$

where the constant b' incorporates all remaining constants. At the reflecting boundary we have to leading order

$$W'_{\rm unif}(c\sqrt{\varepsilon}) = W'_{\rm outer}(c\sqrt{\varepsilon}) + W'_{\rm bl}(c\sqrt{\varepsilon}) = a + B\frac{\tilde{Y}_2'(c)}{\sqrt{\varepsilon}} = 0, \tag{2.75}$$

which gives

$$B = -\frac{a\sqrt{\varepsilon}}{\tilde{Y}_2'(c)}, \quad b' = -a\pi. \tag{2.76}$$

The uniform approximation to $W(\omega)$ is given by

$$W_{\rm unif}(\rho e^{i\psi}) = a\left(\psi - \pi - \frac{\sqrt{\varepsilon}}{\tilde{Y}_2'(c)}\right), \tag{2.77}$$

so that using (2.61), (2.62), and (2.65), we obtain from (2.77)

$$\begin{aligned}\left.\frac{\partial u}{\partial n}\right|_{\zeta\in\partial\Omega_a} &= f\left(\varphi\left(\frac{\pi}{2}\right)\right)\left.\frac{\partial W(\rho e^{i\psi})}{\partial\psi}\right|_{\psi=\pi}\left.\omega'(\zeta)\right|_{\zeta=-1}\left.\frac{\partial\varphi}{\partial\theta}\right|_{\theta=\pi/2}\\ &= a\sqrt{\frac{2}{\varepsilon R'}}(1 + O(\sqrt{\varepsilon})).\end{aligned} \tag{2.78}$$

Because $W(\omega)$ scales with $1/f(\varphi)$ relative to $V(\varphi,\eta)$, we may choose at the outset $f(\varphi(\pi/2)) = 1$.

Finally, to determine the value of a, we integrate (2.49) over Ω, use (2.78), and the fact that

$$\int_{\partial\Omega_a} dy = l_0\varepsilon,$$

to obtain $a = -|\Omega|\sqrt{R'}/l_0 D_r\sqrt{2\varepsilon}$. Now (2.77) gives the MFPT at any point $\boldsymbol{x}$ in the head as

$$\tau_{\boldsymbol{L}\to\boldsymbol{AB}} = u(\boldsymbol{x}) \sim W\left(\rho e^{ic\sqrt{\varepsilon}}\right) \sim -a\pi = \frac{\pi|\Omega|\sqrt{R'}}{l_0 D_r\sqrt{2\varepsilon}}(1+O(\sqrt{\varepsilon}) \text{ for } \varepsilon \ll 1. \tag{2.79}$$

Reverting to the original dimensional variables, we get

$$\tau_{\boldsymbol{L}\to\boldsymbol{AB}} = \frac{\pi\left(\frac{\pi}{2}-1\right)}{D_r\sqrt{l_0(l_0-l)}}\sqrt{\frac{D_X}{D_r}}\left(1+O\left(\sqrt{\frac{l_0-l}{l_0}}\right)\right), \tag{2.80}$$

which together with (2.43) is (2.54). □

2.2.3 The NET in a Solid Funnel-Shaped Domain

We consider now the NET problem in the solid of revolution in Fig. 2.2(right), obtained by rotating the symmetric planar domain Ω' in Fig. 2.1(left) about its axis of symmetry. The absorbing end of the neck becomes a circular disk of radius $a' = \varepsilon'/2$.

Theorem 2.2.2. *The MFPT to the absorbing boundary at the end of the funnel of a solid of revolution obtained by rotating the symmetric planar domain of Fig. 2.2(right) is given by*

$$\bar{\tau} = \frac{1}{\sqrt{2}}\left(\frac{\ell_+}{a'}\right)^{3/2}\frac{V}{\ell_+ D}(1+o(1)) \textit{ for } a' \ll \ell_+, \tag{2.81}$$

where $V = |\Omega'|$ is the volume of the domain.

Proof. Due to cylindrical symmetry of the mixed boundary value problem (2.9) the MFPT in cylindrical coordinates centered on the axis of symmetry is independent of the angle. It follows that with the scaling (2.8) the boundary value problem (2.9) in the scaled spatial domain Ω can be written in cylindrical coordinates as

$$\Delta u = \frac{\partial^2 u}{\partial r^2} + \frac{1}{r}\frac{\partial u}{\partial r} + \frac{\partial^2 u}{\partial z^2} = -\frac{\ell_+^2}{D}. \tag{2.82}$$

Equation (2.82) can be considered as a two-dimensional problem in the planar cross section by a plane through the axis of symmetry of Ω in the (r, z) plane. Here r is the distance to the axis of symmetry of Ω, the z axis is perpendicular to that axis and the origin is inside the cross section of Ω, at the intersection of the axis with the tangent to the osculating circle to the cross section at the gap. Setting $u_1 = ur^{1/2}$, the MFPT equation (2.82) takes the form

$$\frac{\partial^2 u_1(r,z)}{\partial r^2} + \frac{\partial^2 u_1(r,z)}{\partial z^2} = -\frac{\ell_+^2}{D}\left(r^{1/2} + \frac{u_1(r,z)}{4r^2}\right) \tag{2.83}$$

in the cross section, with mixed Neumann–Dirichlet boundary conditions, as in the planar case. We assume that in dimensionless variables $\overline{AB} = \varepsilon \ll 1 < |\Omega|^{1/3}$, so the funnel is a narrow passage. The transformation to the rotated and translated coordinates is given by $\tilde{r} = r - 1 - \varepsilon/2$, $\tilde{z} = -z + 1$. Setting $u_1(r,z) = \tilde{u}(\tilde{r}, \tilde{z})$, Eq. (2.83) becomes

$$\frac{\partial^2 \tilde{u}(\tilde{r},\tilde{z})}{\partial \tilde{r}^2} + \frac{\partial^2 \tilde{u}(\tilde{r},\tilde{z})}{\partial \tilde{z}^2} = -\frac{\ell_+^2}{D}\left(\left(\tilde{r} + 1 + \frac{\varepsilon}{2}\right)^{1/2} - \frac{\tilde{u}(\tilde{r},\tilde{z})}{4\left(\tilde{r} + 1 + \frac{\varepsilon}{2}\right)^2}\right). \tag{2.84}$$

The construction of the asymptotic expansion of the solution of the boundary layer equation (2.69) is similar to that in Sect. 2.2.2. We construct an asymptotic solution for small gap ε by first mapping the cross section in the (r, z)-plane conformally into its image under the Möbius transformation (2.10),

$$w(\zeta) = \rho e^{i\eta} = \frac{\zeta - \alpha}{1 - \alpha\zeta}, \tag{2.85}$$

where α is given in (2.11) for the symmetric case $R_c = r_c = 1$. Setting $\tilde{u}(\zeta) = v(w)$, Eq. (2.84) becomes

$$\Delta_w v(w) = \frac{\ell_+^2}{D|w'(\zeta)|^2}\left(-\left|\left|\mathcal{R}\mathrm{e}\frac{w+\alpha}{1+\alpha w}\right| + 1 + \frac{\varepsilon}{2}\right|^{1/2} - \frac{v}{4\left|\left|\mathcal{R}\mathrm{e}\frac{w+\alpha}{1+\alpha w}\right| + 1 + \frac{\varepsilon}{2}\right|^2}\right). \tag{2.86}$$

Because the normalized head of Fig. 2.1(left) is mapped into the narrow hot dog-shaped region in Fig. 2.3 of width $\sqrt{\varepsilon}$ at $\rho = 1$, we approximate

$$w = e^{i\eta} + O(\sqrt{\varepsilon}), \qquad \left|\frac{w+\alpha}{1+\alpha w}\right| = 1 + O(\sqrt{\varepsilon}). \tag{2.87}$$

We also have

$$w'(\zeta)=\frac{(1+\alpha w)^2}{\alpha^2-1},\quad |w'(\zeta)|^2=\frac{|1-w+\sqrt{\varepsilon}\,w|^4}{4\varepsilon}(1+O(\sqrt{\varepsilon})),\tag{2.88}$$

so that (2.83) reduces to

$$\Delta_w v=-\frac{\ell_+^2}{D}\frac{4\varepsilon(1+O(\sqrt{\varepsilon}))}{|1-w+\sqrt{\varepsilon}\,w|^4}\left(\sqrt{2}+\frac{1}{16}v\right),\tag{2.89}$$

or equivalently,

$$v''+\frac{\varepsilon}{4|e^{i\eta}-1-e^{i\eta}\sqrt{\varepsilon}|^4}v=\frac{\ell_+^2}{D}\frac{4\sqrt{2}\varepsilon}{|e^{i\eta}-1-e^{i\eta}\sqrt{\varepsilon}|^4}\left(1+O(\sqrt{\varepsilon})\right).\tag{2.90}$$

Setting $v=\ell_+^2(y-16\sqrt{2})/D$, we obtain the leading order equation

$$y''(\eta)+\frac{\varepsilon}{4|e^{i\eta}-1-e^{i\eta}\sqrt{\varepsilon}|^4}y(\eta)=0.\tag{2.91}$$

The boundary conditions are

$$y'(c\sqrt{\varepsilon})=0,\quad y(\pi)=16\sqrt{2}.\tag{2.92}$$

The outer solution is the linear function

$$y_{\text{outer}}(\eta)=M\eta+N,\tag{2.93}$$

where M and N are yet undetermined constants. The absorbing boundary condition in (2.92) gives

$$y_{\text{outer}}(\pi)=M\pi+N=16\sqrt{2}.\tag{2.94}$$

A boundary layer correction is needed to satisfy the boundary conditions at the reflecting boundary at $\eta=c\sqrt{\varepsilon}$. To resolve the boundary layer at $\eta=c\sqrt{\varepsilon}$, we set $\eta=\sqrt{\varepsilon}\xi$ and expand

$$\frac{\varepsilon^2}{|e^{i\eta}-1-e^{i\eta}\sqrt{\varepsilon}|^4}=\frac{1}{(1+\xi^2)^2}+O(\sqrt{\varepsilon}).$$

Writing $y_{\text{bl}}(\eta)=Y(\xi)$, we obtain to leading order the boundary layer equation

$$Y''(\xi)+\frac{1}{4(1+\xi^2)^2}Y(\xi)=0,\tag{2.95}$$

which has two linearly independent solutions, $Y_1(\xi)$ and $Y_2(\xi)$ that are linear functions for sufficiently large ξ. Initial conditions for $Y_1(\xi)$ and $Y_2(\xi)$ can be chosen so that $Y_2(\xi) \to$ *const* as $\xi \to \infty$ (e.g., $Y_2(0) = -4.7,\ Y_2'(0) = -1$, see Fig. 2.6). Setting

$$y_{\mathrm{bl}}(\eta) = AY_1\left(\frac{\eta}{\sqrt{\varepsilon}}\right) + BY_2\left(\frac{\eta}{\sqrt{\varepsilon}}\right), \tag{2.96}$$

where A and B are constants to be determined, we seek a uniform approximation to $y(\eta)$ in the form $y_{\mathrm{unif}}(\eta) = y_{\mathrm{outer}}(\eta) + y_{\mathrm{bl}}(\eta)$. The matching condition is that $AY_1\left(\eta/\sqrt{\varepsilon}\right) + +BY_1\left(\eta/\sqrt{\varepsilon}\right)$ remains bounded as $\xi \to \infty$, which implies $A = 0$. It follows that at the absorbing boundary $\eta = \pi$ we have

$$y_{\mathrm{unif}}(\pi) = M\pi + \beta - 5B = 16\sqrt{2}, \quad y_{\mathrm{unif}}'(\pi) = M. \tag{2.97}$$

At the reflecting boundary we have to leading order

$$y_{\mathrm{unif}}'(c\sqrt{\varepsilon}) = y_{\mathrm{outer}}'(c\sqrt{\varepsilon}) + y_{\mathrm{bl}}'(c\sqrt{\varepsilon}) = M + B\frac{Y_2'(c)}{\sqrt{\varepsilon}} = 0, \tag{2.98}$$

which gives

$$B = -\frac{M\sqrt{\varepsilon}}{Y_2'(c)}, \quad N = 16\sqrt{2} - \frac{5M\sqrt{\varepsilon}}{Y_2'(c)} - M\pi. \tag{2.99}$$

The uniform approximation to $v(w)$ is given by

$$v_{\mathrm{unif}}(\rho e^{i\eta}) = M\left(\eta - \pi - \frac{5\sqrt{\varepsilon}}{Y_2'(c)}\right), \tag{2.100}$$

so that using (2.88), we obtain from (2.100)

$$\left.\frac{\partial u}{\partial n}\right|_{\zeta\in\partial\Omega_a} = \left.\frac{\partial v(\rho e^{i\eta})}{\partial\eta}\right|_{\eta=\pi} \left.w'(\zeta)\right|_{\zeta=-1} = \frac{2M}{\sqrt{\varepsilon}}(1 + O(\sqrt{\varepsilon})). \tag{2.101}$$

To determine the value of M, we integrate (2.9) over Ω, use (2.101), and the fact that

$$\int_{\partial\Omega_a} dS = \frac{\pi\varepsilon^2}{4}, \tag{2.102}$$

to obtain $M = -2\ell_+^2|\Omega|/D\pi\varepsilon^{3/2}$. Now (2.100) gives the MFPT at any point $\boldsymbol{x}$ in the head as

$$\bar{\tau} = u(\boldsymbol{x}) \sim v\left(\rho e^{c\sqrt{\varepsilon}}\right) \sim 2\varepsilon^{-3/2}\frac{\ell_+^2|\Omega|}{D} = 2\varepsilon^{-3/2}\frac{|\Omega'|}{\ell_+ D} \quad \text{for } \varepsilon \ll 1. \tag{2.103}$$

The dimensional radius of the absorbing end of the funnel is $a' = \ell_+\varepsilon/2$ [see (2.8)], so (2.103) can be written in physical units as (2.81). □

The generalization of (2.81) to exit through N well-separated necks is found by noting that (2.102) becomes

$$\int\limits_{\partial\Omega_a} dS = \sum_{j=1}^{N} \frac{\pi\varepsilon_j^2}{4}, \tag{2.104}$$

and the integration of (2.7) over Ω' gives the compatibility condition (dimensional)

$$\int\limits_{\partial\Omega'} \frac{\partial u(\boldsymbol{x}')}{\partial n'}\, dS' = M\sum_{j=1}^{N} \frac{\ell_j\pi\varepsilon_j^2}{4\sqrt{\varepsilon_j}} = -\frac{|\Omega'|}{D} \tag{2.105}$$

which determines

$$M = -\frac{4|\Omega'|}{D\sum_{j=1}^{N}\ell_j\pi\varepsilon_j^{3/2}}. \tag{2.106}$$

Hence, using the dimensional $a_j' = \ell_j\varepsilon_j/2$, we obtain

$$\bar{\tau} = -M\pi = \frac{1}{\sqrt{2}}\,\frac{|\Omega'|}{D\sum_{j=1}^{N}\ell_j\left(\dfrac{a_j'}{\ell_j}\right)^{3/2}}. \tag{2.107}$$

To calculate the exit probability from one of N necks, we note that the boundary layer function is to leading order linear, as in Sect. 2.1.1. Therefore in the three-dimensional case the exit probability is given by

$$p_i = \frac{\varepsilon_i^{3/2}\ell_i}{\sum_{j=1}^{N}\varepsilon_j^{3/2}\ell_j} = \frac{a_i'^{3/2}\ell_i^{-1/2}}{\sum_{j=1}^{N}a_j'^{3/2}\ell_j^{-1/2}}. \tag{2.108}$$

Finally, the analogous expression for the NET (2.41) in three dimensions is as follows.

Theorem 2.2.3 (The NET from a Composite Domain in $\mathbb{R}^3$). *The NET of a Brownian motion from a three-dimensional composite domain Ω with a bottleneck in the form of a narrow circular cylinder of cross section area πa^2 is given by*

$$\bar{\tau}_{\boldsymbol{x}\to\partial\Omega_a} = \begin{cases} \dfrac{|\Omega_1|}{4aD}\left[1+\dfrac{a}{\pi R}\log\dfrac{R}{a}\right]+\dfrac{O(1)}{D}+\dfrac{L^2}{2D}+\dfrac{|\Omega_1|L}{\pi a^2 D} \\ \textit{solid spherical head of radius R connected to the neck at a right angle} \\ \\ \dfrac{|\Omega_1|}{4aD}\left(1+\dfrac{L(\partial\Omega_a)+N(\partial\Omega_a)}{2\pi}\left|\dfrac{\partial\Omega_a}{\pi}\right|^{1/2}\log\sqrt{\dfrac{|\partial\Omega_1|}{|\partial\Omega_a|}}\right) \\ +\dfrac{L^2}{2D}+\dfrac{|\Omega_1|L}{\pi a^2 D}+\dfrac{O(1)}{D} \\ \textit{a general head connected to the neck at a right angle} \\ \\ \dfrac{1}{\sqrt{2}}\left(\dfrac{R_c}{a}\right)^{3/2}\dfrac{|\Omega_1|}{R_c D}(1+o(1))+\dfrac{L^2}{2D}+\dfrac{|\Omega_1|L}{\pi a^2 D} \\ \textit{a general head connected smoothly to the neck by a funnel.} \end{cases} \tag{2.109}$$

Here $L(\partial\Omega_a)$ and $N(\partial\Omega_a)$ are the principal curvatures of the boundary at the neck and R_c is the boundary curvature at the cusp.

The $O(1)$ term in (2.109) can be computed for the sphere using the explicit expression of the Neumann–Green function (Cheviakov et al. 2010). Modulation of neck length changes the residence time significantly. Comparing (2.41) with (2.109), we note that the geometry of the connection affects the residence time stronger in two than in three dimensions.

2.2.4 The MFPT in a Dumbbell-Shaped Domain

A dumbbell-shaped domain consists of two compartments Ω_1 and Ω_3 and a connecting neck Ω_2 that is effectively one-dimensional, such as shown in Fig. 2.7, or in a similar domain with a long neck. A Brownian trajectory that hits the segment $\boldsymbol{AB}$ in the center of the neck Ω_2 is equally likely to reach either compartment before the other; thus, $\boldsymbol{AB}$ is the stochastic separatrix (SS). Therefore the mean time to traverse the neck from compartment Ω_1 to compartment Ω_3 is asymptotically twice the MFPT $\bar{\tau}_{\Omega_1\to SS}$. Neglecting, as we may, the mean residence time of a Brownian trajectory in Ω_2 relative to that in Ω_1 or in Ω_3 we can write the transition rates from Ω_1 to the Ω_3 and vv as

$$\lambda_{\Omega_1\to\Omega_3} = \frac{1}{2\bar{\tau}_{\Omega_1\to SS}}, \quad \lambda_{\Omega_3\to\Omega_1} = \frac{1}{2\bar{\tau}_{\Omega_3\to SS}}. \tag{2.110}$$

These rates can be found from the explicit expression (3.1) for the flux into an absorbing window

$$\lambda_1 \sim \frac{1}{\bar{\bar{\tau}}}, \tag{2.111}$$

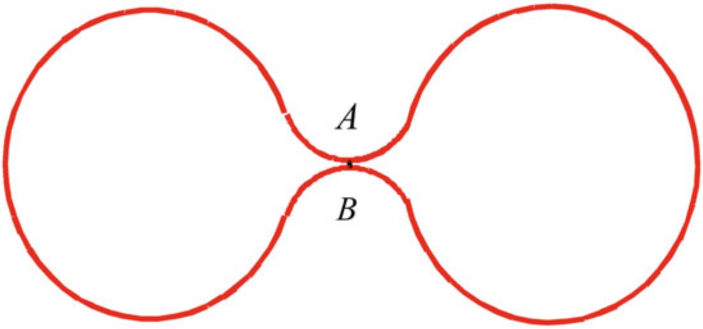

Fig. 2.7 A dumbbell-shaped domain is a composite domain that consists of two large compartments Ω_1 and Ω_3 connected by a narrow neck Ω_2. The bottleneck is the interval ***AB***

where $\bar{\tau}$ is given in (2.28). Here $\bar{\tau}_{\boldsymbol{x}\to\partial\Omega_i}$ is any one of the MFPTs given above, depending on the geometry of Ω_1 with L half the length of the neck and with $SS = \partial\Omega_a$. The radii of curvature $R_{c,1}$ and $R_{c,3}$ at the two funnels may be different in Ω_1 and Ω_3. The smallest positive eigenvalue λ of the Neumann problem for the Laplace equation in the dumbbell is to leading order $\lambda = -(\lambda_{\Omega_1\to\Omega_3}+\lambda_{\Omega_3\to\Omega_1})$. For example, if the solid dumbbell consists of two general heads connected smoothly to the neck by funnels [see (3.27)], the two rates are given by

$$\frac{1}{\lambda_{\Omega_1\to\Omega_3}} = \sqrt{2}\left[\left(\frac{R_{c,1}}{a}\right)^{3/2}\frac{|\Omega_1|}{R_{c,1}D}\right](1+o(1)) + \frac{L^2}{4D} + \frac{|\Omega_1|L}{\pi a^2 D}$$

$$\frac{1}{\lambda_{\Omega_3\to\Omega_1}} = \sqrt{2}\left[\left(\frac{R_{c,3}}{a}\right)^{3/2}\frac{|\Omega_3|}{R_{c,3}D}\right](1+o(1)) + \frac{L^2}{4D} + \frac{|\Omega_3|L}{\pi a^2 D} \qquad (2.112)$$

(see Holcman and Schuss 2012a). Formulas (2.112) indicate that the unidirectional fluxes between the two compartments of a dumbbell-shaped domain can be controlled by the area (or surface area) of the two and by the type of obstacles to the access to the connecting neck. The equilibration rate in the dumbbell, λ, is thus controlled by the geometry.

2.3 The MFPT to a Ribbon

A Brownian search for a small target hidden between a membrane and a vesicle (see Fig. 2.9) can be modelled locally by diffusion between two tangent spheres of different radii R_1 and R_2 ($R_1 < R_2$).

There are two natural scales of magnitude here, the size of the vesicle relative to that of the pre-synaptic terminal and the size of the calcium ion that squeezes between them, relative to that of the vesicle. The smaller scale is that of the ion, so on this scale the radii R_1 and R_2 are $O(1)$ relative to the ion size. Under these conditions a secondary expansion, with $R_1 \ll R_2$, can be applied to the final result (see below). If the two scales are commensurate, a different expansion has to be constructed. The search target is a narrow ribbon of (dimensional) width ε (dimensionless width $\varepsilon' << 1$) with $\varepsilon = \varepsilon' R$, where R is a typical length. The radius of the ribbon is

$$r_a = \sqrt{\alpha\varepsilon}\,(1 + O(\varepsilon)) = \sqrt{\varepsilon'}\sqrt{\frac{2RR_2R_1}{\sqrt{R_1^2 + R_2^2}}}\,(1 + O(\varepsilon')), \tag{2.113}$$

where

$$\alpha = \frac{2R_2R_1}{\sqrt{R_1^2 + R_2^2}}. \tag{2.114}$$

A ribbon is a two-dimensional manifold with a nontrivial topology and thus the absorbing part of the boundary is not a small window in the sense of the narrow escape theory developed above. Therefore the method has to be adjusted to this geometry. Scaling the cylindrical coordinates $(r, z) = R_2(r', z')$ by setting

$$R_1' = \frac{R_1}{R_2}, \quad R' = \frac{R}{R_2}, \quad r_a' = \frac{r_a}{R_2} = \sqrt{\varepsilon'}\sqrt{\frac{2R'R_1'}{\sqrt{1 + R_1'^2}}}\,(1 + O(\varepsilon')). \tag{2.115}$$

maps domain Ω into the dimensionless domain Ω', enclosed between spheres of dimensionless radii R_1' and 1. Projecting the cylindrically symmetric domain Ω' enclosed between the two spheres into a plane of symmetry (through the common axis of the two spheres), maps Ω' into a planar domain enclosed between the circles $r'^2 + z'^2 - 2z'R_1' = 0$ and $r'^2 + z'^2 - 2z' = 0$ in the (r', z') plane, shown as the cusp in the middle frame of Fig. 2.8 (denoted $\bar{\Omega}'$). The absorbing band in Ω' is mapped into the short circular arc $\partial\bar{\Omega}_a'$ joining the two circles (marked red). The radius r_a' of the ribbon and the radius of the arc are to leading order the same for $\varepsilon' \ll 1$ [see (2.115)].

Due to the cylindrical symmetry of the three-dimensional boundary value problem (1.4)–(1.6) for the MFPT in cylindrical coordinates (r', z', θ) to the ribbon, $V(r', z', \theta)$ is independent of θ. Thus we are left with the two-dimensional boundary value problem in $\bar{\Omega}'$

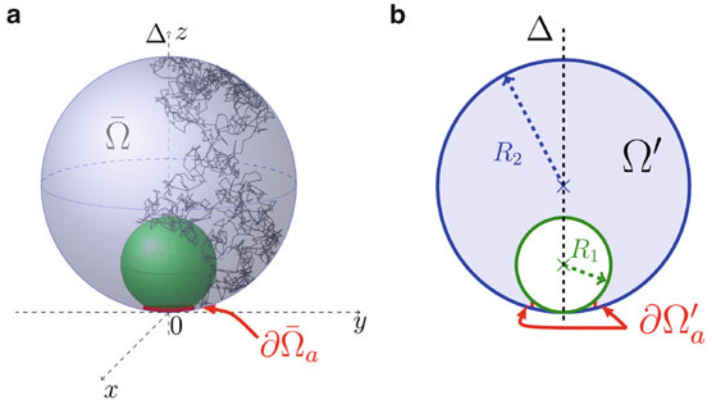

Fig. 2.8 (**a**) Brownian search for a narrow ribbon (*red*) in the domain $\bar{\Omega}$ enclosed between tangent reflecting spheres (*blue* and *green*). (**b**) The projection of $\bar{\Omega}$ on its the plane of symmetry is the planar domain Ω' enclosed by *two circles*. The projection of the ribbon target consists of two short arcs (*red*)

$$\begin{aligned}\frac{\partial^2 V(r',z')}{\partial r'^2}+\frac{1}{r'}\frac{\partial V(r',z')}{\partial r'}+\frac{\partial^2 V(r',z')}{\partial z'^2} &= -\frac{1}{D'} \text{ for } (r',z')\in\bar{\Omega}'\\ \frac{\partial V(r',z')}{\partial n'} &= 0 \text{ for } (r',z')\in\bar{\Omega}'\setminus\partial\bar{\Omega}'_a\\ V(r',z') &= 0 \text{ for } (r',z')\in\bar{\Omega}',\end{aligned} \tag{2.116}$$

where $D' = D/R_2^2$. Note that the dimension of (2.116) is time.

To construct a uniform asymptotic expansion of the solution of (2.116) for $\varepsilon' \ll 1$, we introduce the complex variable $\xi = r' + iz'$ and apply the inversion $\omega = x + iy = f(\xi) = 1/\xi$, which maps the right half of $\bar{\Omega}'$ into the rectangle

$$\tilde{\Omega} = \left\{0 < t < \frac{1}{r'_a}, -\frac{1}{2R'_1} < z < -\frac{1}{2}\right\}, \tag{2.117}$$

shown in Fig. 2.9b (Guerrier and Holcman 2015). Setting $V(\xi) = u(\omega)$, Eq. (2.116) becomes

$$(t^2+z^2)^2\Delta u + \frac{t^2+z^2}{t}\left(\frac{\partial t}{\partial r'}\frac{\partial u}{\partial t}+\frac{\partial z}{\partial r'}\frac{\partial u}{\partial z}\right) = -\frac{1}{D'} \text{ for } (t,z)\in\tilde{\Omega} \tag{2.118}$$

$$u_t(0,z) = 0, \quad u\left(\frac{1}{r'_a},z\right) = 0 \text{ for } -\frac{1}{2R'_1} < z < -\frac{1}{2} \tag{2.119}$$

$$u_z\left(t,-\frac{1}{2}\right) = 0, \quad u_z\left(t,-\frac{1}{2R'_1}\right) = 0 \text{ for } 0 < t < \frac{1}{r'_a}. \tag{2.120}$$

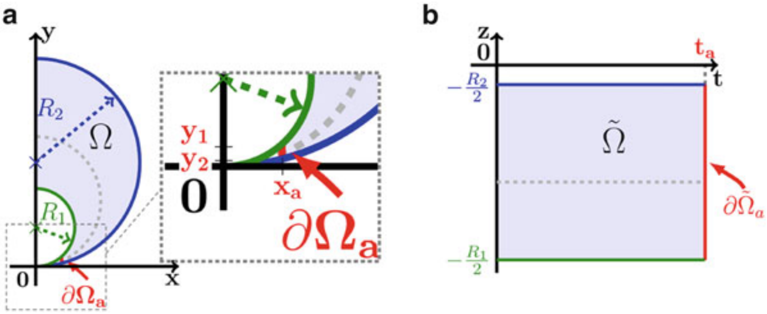

Fig. 2.9 Conformal mapping. The domain $\tilde{\Omega}$ in frame (**b**) is the conformal image of the domain $\bar{\Omega}'$ in frame (**a**) under the inversion $\omega = f(\xi) = 1/\xi$. Circles of radius r' centered at $(0, r')$ are mapped into the *lines* $\Re(\xi) = 1/2r'$: the *gray dashed circle* in frame (**a**) is mapped into the *dashed horizontal line* in frame (**b**)

Note that

$$\frac{\partial t}{\partial r'} = -t^2 + z^2, \quad \frac{\partial z}{\partial r'} = -2tz.$$

Scaling

$$t = \frac{X}{r'_a}, \quad u(x, z) = U(X, z),$$

Equation (2.118) becomes

$$r'^{-4}_a X^4 U_{zz} + r'^{-2}_a (X^2 z^2 U_{zz} - 2X^2 z U_z + X^4 U_{XX} - X^3 U_X)$$
$$+ 2X^2 z^2 U_{XX} + z^4 U_{zz} - 2z^3 U_z + \frac{1}{D'} = O(r'_a)$$

for $0 < X < 1$ and $-1/2 < y < -1/2R'_1$. The boundary conditions (2.119), (2.120) become

$$U_X(0, z) = 0 = U(1, z) = 0 \text{ for } -\frac{1}{2R'_1} < z < -\frac{1}{2} \tag{2.121}$$

$$U_z\left(X, -\frac{1}{2}\right) = U_z\left(X, -\frac{1}{2R'_1}\right) = 0 \quad \text{for } 0 < X < 1. \tag{2.122}$$

A regular expansion in powers of r'_a,

$$U(X, z) = U^0(X, z) + r'_a U^1(X, z) + r'^2_a U^2(X, z) + \cdots, \tag{2.123}$$

gives at the leading-order $O({r'_a}^{-2})$ the equation $X^4 U^0_{zz}(X,z) = 0$, hence $U^0(X,z) = U^0(X)$ (independent of z). At order $O({r'_a}^{-1})$, we obtain the equation

$$X^4 U^1_{zz} + X^4 U^0_{XX} - X^3 U^0_X = 0. \tag{2.124}$$

The solvability condition for (2.124) is

$$\int\limits_{-1/2}^{-1/2R'_1} [X^4 U^0_{XX} - X^3 U^0_X]\, dz = 0,$$

so that

$$X^4 U^0_{XX} - X^3 U^0_X = 0. \tag{2.125}$$

It follows that $U^0(X) = A(1-X^2)$, where A is an unknown constant. To compute the unknown constant A, we use the leading term $U^0(X) = A(1-X^2) = A[1-(r'_a x)^2]$ to evaluate

$$\left.\frac{\partial u}{\partial n}\right|_{\partial\bar{\Omega}_a} \approx \left.\frac{dA[1-(r'_a x)^2]}{dx}\right|_{x=1/r'_a} = -2Ar'_a. \tag{2.126}$$

The compatibility condition (1.7), obtained by integrating (2.116) over the planar domain $\bar{\Omega}'$, is

$$-\frac{|\bar{\Omega}'|}{D'} = \int_{\partial\Omega'_a} \frac{\partial V(r',z')}{\partial n'}\, ds, \tag{2.127}$$

which under the change of variables given by the inversion $t + iz = 1/(r' + iz')$ becomes

$$\frac{|\bar{\Omega}'|}{D'} = \int_{-1/2}^{-1/2R'_1} \frac{\partial u(x,y)}{\partial x} \frac{y^2 - {r'_a}^{-2}}{(y^2 + {r'_a}^{-2})^{3/2}}\, dy \approx \frac{1}{2}\left(\frac{1}{R'_1} - 1\right) A{r'_a}^2. \tag{2.128}$$

Hence

$$A = \frac{2|\bar{\Omega}'|}{D'\left(\dfrac{1}{R'_1} - 1\right){r'_a}^2} = \frac{2|\bar{\Omega}|}{D\,(R_2 - R_1)\left(\varepsilon' \dfrac{2RR_1}{\sqrt{R_1^2 + R_2^2}}\right)},$$

so the MFPT to the ribbon is to leading order in ε'

$$\mathbb{E}[\tau \mid r, z, \theta] = \frac{2|\bar{\Omega}|}{D\varepsilon' \left(\dfrac{2R(R_2 - R_1)}{R_2\sqrt{R_1^2 + R_2^2}} \right)} \times \left[1 - \varepsilon' \frac{2RR_1R_2}{\sqrt{R_1^2 + R_2^2}} \left(\frac{r}{r^2 + z^2} \right)^2 \right] (1 + o(\varepsilon')). \tag{2.129}$$

Note that $|\bar{\Omega}| = \pi(R_2^2 - R_1^2)$ in (2.129) is the area of the cross section, not the volume of the domain Ω. In the limit $R_1 \ll R_2$ and with $R = R_2$, Eq. (2.129) reduces in dimensional variables to

$$\mathbb{E}[\tau \mid r, z, \theta] = \frac{\mathrm{vol}(\Omega)}{4D\varepsilon} \left[1 - 2\varepsilon R_1 \left(\frac{r}{r^2 + z^2} \right)^2 \right] \left(1 + o\left(\frac{\varepsilon}{R_2} \right) \right). \tag{2.130}$$

Diffusion to a ribbon can describe, for example, calcium ions near a vesicle in the pre-synaptic terminal. The rare event of hitting the ribbon determines the rate of vesicular release, which likely depends on the distance of the hitting spot to the calcium channels on the membrane. It is yet unclear how the rate of vesicular release can vary over 6 orders of magnitude for the same synapse (Kochubey et al. 2011). The cusp geometry and rare events may hold the key to the resolution of this drastic modulation of the vesicular release rate (Guerrier and Holcman 2015).

2.4 Conditioning and Splitting Probability

Conditioning a stochastic process on a given event reduces the Brownian probability space to a subset of the trajectories and assigns to them a new probability measure. For example, if in a simulation of Brownian motion in a field of force in a domain Ω with reflecting boundary that contains two absorbing patches we want to calculate the pdf of the NET through one of the patches for $0 \le t \le T$, we reduce the Brownian probability space to that of trajectories that are absorbed in that patch in the given time interval. The probability measure is re-normalized to 1 at time $t = 0$ on this set of trajectories (see Sect. 2.4.1 below). The process can also be conditioned on the future, for example, on reaching a certain subset of Ω at a given future time, such as in the case of the Brownian bridge (Schuss 2010b).

2.4.1 Conditioning

Consider the Itô system

$$d\boldsymbol{x} = \boldsymbol{a}(\boldsymbol{x})\,dt + \sqrt{2}\boldsymbol{B}(\boldsymbol{x})\,d\boldsymbol{w} \tag{2.131}$$

in a domain D, whose boundary consists of two parts, A and B. If the trajectories $\boldsymbol{x}(t)$ that reach B before A are eliminated, the remaining trajectories form a process conditioned on reaching A before B. We denote this process by $\boldsymbol{x}^*(t)$ and the first passage times to A and to B by τ_A and τ_B, respectively. Thus $\boldsymbol{x}^*(t)$ is obtained from $\boldsymbol{x}(t)$ by conditioning on the event $\{\tau_A < \tau_B\}$. We set, as usual, $\boldsymbol{\sigma}(\boldsymbol{x}) = \boldsymbol{B}(\boldsymbol{x})\boldsymbol{B}^T(\boldsymbol{x})$ and denote by L and L^* the corresponding Fokker–Planck and backward Kolmogorov operators, respectively.

Theorem 2.4.4 (Conditioned Diffusion). *Conditioning the solution of (2.131) on reaching a set A before reaching a set B results in a diffusion process $\boldsymbol{x}^*(t)$, whose drift vector and diffusion matrix are given by*

$$\boldsymbol{a}^*(\boldsymbol{x}) = \boldsymbol{a}(\boldsymbol{x}) + \boldsymbol{\sigma}(\boldsymbol{x})\frac{\nabla P(\boldsymbol{x})}{P(\boldsymbol{x})}, \quad \boldsymbol{\sigma}^*(\boldsymbol{x}) = \boldsymbol{\sigma}(\boldsymbol{x}), \tag{2.132}$$

respectively, where the splitting probability $P(\boldsymbol{x})$ is determined from the boundary value problem

$$\begin{aligned} L^*P(\boldsymbol{x}) &= 0 \ \textit{for}\, \boldsymbol{x} \in D \\ P(\boldsymbol{x}) &= 1 \ \textit{for}\, \boldsymbol{x} \in A, \quad P(\boldsymbol{x}) = 0 \ \textit{for}\, \boldsymbol{x} \in B, \end{aligned} \tag{2.133}$$

provided boundary conditions can be posed at A and B.[1]

Proof. Obviously, the trajectories of $\boldsymbol{x}^*(t)$ are continuous. The pdf of $\boldsymbol{x}^*(t)$, denoted $p^*(\boldsymbol{y}, t\,|\,\boldsymbol{x})$, is given by

$$p^*(\boldsymbol{y}, t\,|\,\boldsymbol{x})\,d\boldsymbol{y} = \Pr\{\boldsymbol{x}(t) \in \boldsymbol{y} + d\boldsymbol{y}, t\,|\,\boldsymbol{x}(0) = \boldsymbol{x},\ \tau_A < \tau_B\}.$$

Bayes' rule gives

$$\begin{aligned} &\Pr\{\boldsymbol{x}(t) \in \boldsymbol{x} + \Delta\boldsymbol{y}, t\,|\,\boldsymbol{x}(0) = \boldsymbol{x},\ \tau_A < \tau_B\} \\ &\quad = \Pr\{\boldsymbol{x}(t) \in \boldsymbol{y} + \Delta\boldsymbol{y}, t\,|\,\boldsymbol{x}(0) = \boldsymbol{x}\}\,\frac{\Pr\{\tau_A < \tau_B\,|\,\boldsymbol{x}(0) = \boldsymbol{x},\ \boldsymbol{x}(t) = \boldsymbol{y}\}}{\Pr\{\tau_A < \tau_B\,|\,\boldsymbol{x}(0) = \boldsymbol{x}\}}, \end{aligned}$$

---

[1] It is known in partial differential equations theory in higher dimensions that at boundary points where $\sum_{i,j}\sigma^{ij}(\boldsymbol{x})\nu^i(\boldsymbol{x})\nu^j(\boldsymbol{x}) = 0$, boundary conditions can be imposed only at points where $\boldsymbol{a}(\boldsymbol{x}) \cdot \boldsymbol{\nu}(\boldsymbol{x}) < 0$.

hence, using the Markov property and time homogeneity, we obtain

$$\Pr\{\tau_A < \tau_B \,|\, \boldsymbol{x}(0) = \boldsymbol{x},\, \boldsymbol{x}(t) = \boldsymbol{y}\} = \Pr\{\tau_A < \tau_B \,|\, \boldsymbol{x}(0) = \boldsymbol{y}\}$$

so that

$$p^*(\boldsymbol{y}, t \,|\, \boldsymbol{x}) = p\,(\boldsymbol{y}, t \,|\, \boldsymbol{x}) \frac{\Pr\{\tau_A < \tau_B | \, \boldsymbol{x}(0) = \boldsymbol{y}\}}{\Pr\{\, \tau_A < \tau_B \,|\, \boldsymbol{x}(0) = \boldsymbol{x}\}}. \tag{2.134}$$

It is evident from Eq. (2.134) that $p^*(\boldsymbol{y}, t \,|\, \boldsymbol{x})$ is a probability density function and that it satisfies the properties of a pdf of a diffusion process. It remains to calculate its infinitesimal drift vector and diffusion matrix. Note that the function $P(\boldsymbol{x}) = \Pr\{\tau_A < \tau_B \,|\, \boldsymbol{x}(0) = \boldsymbol{x}\}$ can be determined from the boundary value problem (2.133).

Next, we calculate the infinitesimal drift vector of $\boldsymbol{x}^*(t)$. By definition,

$$\begin{aligned}
\boldsymbol{a}^*(\boldsymbol{x}) &= \lim_{h \downarrow 0} \frac{1}{h} \int p^*(\boldsymbol{y}, h \,|\, \boldsymbol{x})(\boldsymbol{y} - \boldsymbol{x})\, d\boldsymbol{y} \\
&= \lim_{h \downarrow 0} \frac{1}{h} \int p\,(\boldsymbol{y}, h \,|\, \boldsymbol{x}) \frac{P(\boldsymbol{y})}{P(\boldsymbol{x})} (\boldsymbol{y} - \boldsymbol{x})\, d\boldsymbol{x}.
\end{aligned} \tag{2.135}$$

We expand $P(\boldsymbol{y})$ about $\boldsymbol{y} = \boldsymbol{x}$ in Taylor's series,

$$P(\boldsymbol{y}) = P(\boldsymbol{x}) + (\boldsymbol{y} - \boldsymbol{x}) \cdot \nabla P(\boldsymbol{x}) + \frac{1}{2} (\boldsymbol{y} - \boldsymbol{x})^T \mathcal{H}\,(P(\boldsymbol{x}))\,(\boldsymbol{y} - \boldsymbol{x}) + o\left(|\boldsymbol{y} - \boldsymbol{x}|^2\right),$$

where $\mathcal{H}\,(P(\boldsymbol{x}))$ is the Hessian matrix of $P(\boldsymbol{x})$. Substituting the expansion in Eq. (2.135), we obtain

$$\begin{aligned}
\boldsymbol{a}^*(\boldsymbol{x}) = &\lim_{h \downarrow 0} \frac{1}{h} \int p\,(\boldsymbol{y}, h \,|\, \boldsymbol{x}) \Bigg[(\boldsymbol{y} - \boldsymbol{x}) + (\boldsymbol{y} - \boldsymbol{x}) \cdot \frac{\nabla P(\boldsymbol{x})}{P(\boldsymbol{x})} (\boldsymbol{y} - \boldsymbol{x}) \\
&+ o\left(|\boldsymbol{y} - \boldsymbol{x}|^2\right) \Bigg] d\boldsymbol{y} = \boldsymbol{a}(\boldsymbol{x}) + \boldsymbol{\sigma}(\boldsymbol{x}) \frac{\nabla P(\boldsymbol{x})}{P(\boldsymbol{x})},
\end{aligned}$$

which is (2.132). Similarly,

$$\begin{aligned}
\boldsymbol{\sigma}^*(\boldsymbol{x}) = &\lim_{h \downarrow 0} \frac{1}{h} \int p^*(\boldsymbol{y}, h \,|\, \boldsymbol{x})(\boldsymbol{y} - \boldsymbol{x})(\boldsymbol{y} - \boldsymbol{x})^T\, d\boldsymbol{y} \\
= &\lim_{h \downarrow 0} \frac{1}{h} \int p\,(\boldsymbol{y}, h \,|\, \boldsymbol{x})(\boldsymbol{y} - \boldsymbol{x})(\boldsymbol{y} - \boldsymbol{x})^T \\
&\times \left[1 + \frac{\nabla P(\boldsymbol{x})}{P(\boldsymbol{x})} \cdot (\boldsymbol{y} - \boldsymbol{x}) + O\left(|\boldsymbol{y} - \boldsymbol{x}|^2\right) \right] d\boldsymbol{y} = \boldsymbol{\sigma}(\boldsymbol{x}).
\end{aligned}$$

□

Note that Eq. (2.133) implies that the second term in Eq. (2.132) becomes infinite as $\boldsymbol{x}$ approaches the part B of the boundary. The direction of $\boldsymbol{a}^*(\boldsymbol{x})$ is into the domain, away from the boundary. Indeed, assume that B is an open subset of the boundary ∂D. We have $\nabla P(\boldsymbol{x})/|\nabla P(\boldsymbol{x})| = -\boldsymbol{\nu}(\boldsymbol{x})$, where $\boldsymbol{\nu}(\boldsymbol{x})$ is the unit outer normal at the boundary point $\boldsymbol{x}$, because $P(\boldsymbol{x}) = 0$ at all points $\boldsymbol{x} \in B$ and $P(\boldsymbol{x}) > 0$ for $\boldsymbol{x} \in D$. It follows that for points $\boldsymbol{x} \in D$ near B,

$$\begin{aligned}\boldsymbol{a}^*(\boldsymbol{x}) \cdot \boldsymbol{\nu}(\boldsymbol{x}) &= \boldsymbol{a}(\boldsymbol{x}) \cdot \boldsymbol{\nu}(\boldsymbol{x}) + \boldsymbol{\sigma}(\boldsymbol{x}) \frac{\nabla P(\boldsymbol{x})}{P(\boldsymbol{x})} \cdot \boldsymbol{\nu}(\boldsymbol{x}) + o(1)\\ &= \boldsymbol{a}(\boldsymbol{x}) \cdot \boldsymbol{\nu}(\boldsymbol{x}) - \frac{|\nabla P(\boldsymbol{x})|}{P(\boldsymbol{x})} \boldsymbol{\nu}^T(\boldsymbol{x}) \boldsymbol{\sigma}(\boldsymbol{x}) \boldsymbol{\nu}(\boldsymbol{x}) + o(1).\end{aligned} \tag{2.136}$$

If $\boldsymbol{\sigma}(\boldsymbol{x})$ is a positive definite matrix, then

$$\boldsymbol{a}^*(\boldsymbol{x}) \cdot \boldsymbol{\nu}(\boldsymbol{x}) \to -\infty \quad \text{as}\, \boldsymbol{x} \to B, \tag{2.137}$$

because $P(\boldsymbol{x}) \to 0$ as $\boldsymbol{x} \to B$. If $\boldsymbol{\nu}^T(\boldsymbol{x})\boldsymbol{\sigma}(\boldsymbol{x})\boldsymbol{\nu}(\boldsymbol{x}) = 0$ on B, then necessarily $\boldsymbol{a}(\boldsymbol{x}) \cdot \boldsymbol{\nu}(\boldsymbol{x}) < 0$, whenever boundary conditions can be imposed at B (see preceding footnote). Equation (2.137) also means that $\boldsymbol{a}^*(\boldsymbol{x}) \cdot \boldsymbol{\nu}(\boldsymbol{x}) < 0$ near B. This means that the angle between $\boldsymbol{a}^*(\boldsymbol{x})$ and $\boldsymbol{\nu}(\boldsymbol{x})$ is obtuse; that is, $\boldsymbol{a}^*(\boldsymbol{x})$ points into D. It follows that the trajectories $\boldsymbol{x}^*(t)$ cannot exit D at B. When the diffusion in the normal direction vanishes at the boundary, and the drift vector pushes the trajectories $\boldsymbol{x}(t)$ away from B, a trajectory $\boldsymbol{x}^*(t)$ cannot leave D through B, either.

The effect of conditioning on reaching A before reaching B is that the drift vector $\boldsymbol{a}(\boldsymbol{x})$ is replaced by the drift vector $\boldsymbol{a}^*(\boldsymbol{x})$, and the diffusion matrix remains unchanged. The dynamics (2.131) changes so that the dynamics of the conditioned process becomes

$$d\boldsymbol{x}^* = \boldsymbol{a}^*(\boldsymbol{x}^*)\, dt + \sqrt{2}\boldsymbol{B}(\boldsymbol{x}^*)\, d\boldsymbol{w}. \tag{2.138}$$

To simulate only those trajectories that satisfy the condition, the function $P(\boldsymbol{x})$ has to be known. Finding this function from the simulation may be as costly as running the unconditioned simulation.

The conditional MFPT to A is the MFPT of the conditional process $\boldsymbol{x}^*(t)$. Thus $u^*(\boldsymbol{x}) = \mathbb{E}[\tau \mid \tau_A < \tau_B]$ is the solution of the PAV boundary value problem

$$\begin{aligned}\mathcal{L}^* u^*(\boldsymbol{x}) &= -1 \quad \text{for}\, \boldsymbol{x} \in \Omega\\ u^*(\boldsymbol{x}) &= 0 \quad \text{for}\, \boldsymbol{x} \in A,\end{aligned} \tag{2.139}$$

where $\mathcal{L}^*$ is the backward operator of the conditional diffusion (2.138). Note that no boundary conditions can be imposed at B.

Remark 2.4.1. In the NET condition, the boundary for the splitting probability is partitioned into pieces where on the larger part, the boundary condition is reflecting, while if on A $p = 1$, the condition on B can be absorbing or partially absorbing (Robin boundary conditions) (Delgado et al. 2015).

2.5 The Splitting Probability for Small Targets

Consider the case that A is a small absorbing part of the boundary and B is either a small or large part of the absorbing boundary, whereas the remaining part of the boundary is impermeable to Brownian trajectories. This case can be viewed as a refinement of the model discussed in Sect. 1.9.1. Specifically, consider Brownian motion in a circular annulus Ω of outer radius R and inner radius δ. Assume that the outer disk $D(R)$ has reflecting boundary, except for a small absorbing arc $\partial\Omega_a$. The boundary of the inner disk $D(\delta)$ is assumed absorbing. A Brownian trajectory that reaches $\partial\Omega_a$ is terminated (absorbed), never to return to Ω, while a trajectory that reaches the boundary of the inner disk stays there for an exponentially distributed random waiting time with rate k_1 and is then restarted with a uniform distribution in Ω. The reflecting part of the boundary is $\partial\Omega_r = \partial D(R) - \partial\Omega_a$. The first passage time of a Brownian trajectory from Ω to $\partial\Omega_a$ is denoted T_A and that to the boundary S of $D(\delta)$ is denoted T_S. For $\boldsymbol{x} \in \Omega$, the conditional probability $p(\boldsymbol{x})$ that a trajectory $\boldsymbol{x}(t)$ is absorbed in $\partial\Omega_a$ without spending any time in $D(\delta)$, given $\boldsymbol{x}(0) = \boldsymbol{x}$, is

$$p(\boldsymbol{x}) = \Pr\{T_A < T_S \,|\, \boldsymbol{x}(0) = \boldsymbol{x}\}.$$

The splitting probability $p(\boldsymbol{x})$ is the solution of the boundary value problem derived in Sect. 2.4.1 for the conditional diffusion $\boldsymbol{x}^*(t)$, conditioned on the event $\{T_A < T_S\}$. The complementary splitting probability $q(\boldsymbol{x}) = 1 - p(\boldsymbol{x}) = \Pr\{T_S < T_A \,|\boldsymbol{x}(0) = \boldsymbol{x}\}$ is the solution of the boundary value problem

$$\begin{aligned} \Delta q(\boldsymbol{x}) &= 0 \;\text{ for } \boldsymbol{x} \in \Omega, \quad & \frac{\partial q(\boldsymbol{x})}{\partial n} &= 0 \;\text{ for } \boldsymbol{x} \in \partial\Omega_r \\ q(\boldsymbol{x}) &= 0 \;\text{ for } \boldsymbol{x} \in \partial\Omega_a, \quad & q(\boldsymbol{x}) &= 1 \;\text{ for } \boldsymbol{x} \in S, \end{aligned} \tag{2.140}$$

where $\partial\Omega_a$ is the small opening, $\partial\Omega_r$ is the remaining reflecting part of the external boundary.

2.5.1 *The Splitting Probability in an Annulus*

We consider the case of the annular domain shown in Fig. 2.10. In polar coordinates (r, θ), the portion of the boundary $\partial\Omega_a$ is parameterized by θ when $|\theta - \pi| \leq \varepsilon$. An explicit solution of (2.140) for the annulus Ω is constructed in Sneddon (1966) and Fabrikant (1989, 1991) by the double series method. Specifically,

$$q(r,\theta) = \frac{a_0}{2} + \sum_{n=1}^{\infty} \left[a_n \left(\frac{r}{R}\right)^n + b_n \left(\frac{\delta}{r}\right)^n \right] \cos(n\theta) + \gamma \log \frac{r}{\delta},$$

where $\beta = \delta/R$. The boundary conditions on at $r = \delta$ and $r = R$ give

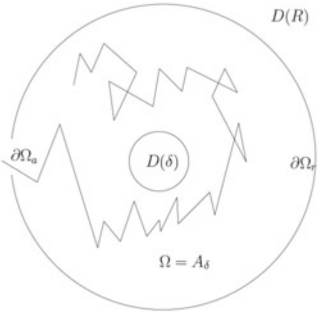

Fig. 2.10 Model of a cellular microdomain in two dimensions. The domain is a disk $D(R)$ of radius R, made of two compartments: an inner disk $D(\delta)$ of radius δ and the annulus $\Omega = D(R) - D(\delta)$. A Brownian particle evolves inside Ω until it hits $D(\delta)$ or the absorbing boundary $\partial\Omega_a \in \partial D(R)$. When it enters into $D(\delta)$, which represents the domain of chemical reactions, it stays there with a mean time (reciprocal of the backward binding rate), while its motion in $D(\delta)$ is frozen. The molecule is released uniformly inside the annulus. This scenario repeats until the molecule hits the absorbing boundary $\partial\Omega_a$, where the molecule is finally removed

$$\frac{a_0}{2} + \sum_{n=1}^{\infty} \left[a_n \left(\frac{\delta}{R} \right)^n + b_n \right] \cos n\theta = 1 \text{ for all } \theta \tag{2.141}$$

$$\sum_{n=1}^{\infty} n \left[\frac{a_n}{R} - \frac{b_n}{R} \beta^n \right] \cos(n\theta) + \frac{\gamma}{R} = 0 \text{ for } \theta - \pi| > \varepsilon \tag{2.142}$$

$$1 + \sum_{n=1}^{\infty} \left[a_n + b_n \beta^n \right] \cos(n\theta) + \gamma \log \frac{1}{\beta} = 0 \text{ for } |\theta - \pi| \le \varepsilon, \tag{2.143}$$

where γ is a constant to be determined. Equation (2.141) gives the identities

$$a_0 = 2, \quad b_n = -a_n \beta^n \text{ for } n \ge 1.$$

Together with (2.142) and (2.143), these give the double series equations

$$\sum_{n=1}^{\infty} n \left[\frac{a_n}{R} + \frac{a_n}{R} \beta^{2n} \right] \cos(n\theta) + \frac{\gamma}{R} = 0 \text{ for } |\theta - \pi| > \varepsilon \tag{2.144}$$

$$1 + \sum_{n=1}^{\infty} \left[a_n - a_n \beta^{2n} \right] \cos(n\theta) - \gamma \log(\beta) = 0 \text{ for } |\theta - \pi| \le \varepsilon. \tag{2.145}$$

Substituting $c_n = a_n(1 + \beta^{2n})$ and $H_n = 2\beta^{2n}/1 - \beta^{2n}$ Eqs. (2.144) and(2.145) take the form

$$\frac{c_0}{2} + \sum_{n=1}^{\infty} \frac{c_n}{1 + H_n} \cos(n\theta) = 0 \text{ for } \theta \in [\pi, \pi - \varepsilon] \tag{2.146}$$

$$\gamma + \sum_{n=1}^{\infty} nc_n \cos(n\theta) = 0 \ \text{ for } \theta \in [0, \pi - \varepsilon], \tag{2.147}$$

where

$$\frac{c_0}{2} = 1 - \gamma \log \beta. \tag{2.148}$$

The asymptotic solution of Eqs. (2.146)–(2.147) uses the double series expansion, developed in Sneddon (1966). The leading coefficient c_0 for the solution of Eqs. (2.146)–(2.147) is

$$c_0 \sim 2\alpha \left(2\log\frac{1}{\varepsilon} + 2\log 2 + \mathrm{O}(\beta^2, \varepsilon) \right) \tag{2.149}$$

where α is as yet an undetermined constant (Singer et al. 2006b; Taflia and Holcman 2007). Using Eqs. (2.148) and (2.149), we get

$$\alpha = \frac{1}{\log\frac{1}{\beta} + 2\log\frac{1}{\varepsilon} + 2\log 2 + 4\beta^2 + O(\beta^2, \varepsilon)}, \tag{2.150}$$

and

$$\gamma = -\frac{1}{\log\frac{1}{\beta} + 2\log\frac{1}{\varepsilon} + 2\log 2 + 4\beta^2 + O(\beta^2, \varepsilon)}. \tag{2.151}$$

The constant α depends on β and ε ($\alpha = \alpha(\beta, \varepsilon)$). For sufficiently small ε and δ, the remaining coefficients a_n and b_n are negligible,

$$a_n \sim O(\alpha(\beta, \varepsilon)), \quad b_n \sim O(\alpha(\beta, \varepsilon)\beta^n).$$

Thus for sufficiently small δ, the leading order expansion of $q(r, \theta)$ is given by

$$q(r,\theta) = \begin{cases} 1 - \alpha(\beta,\varepsilon)\log\left(\frac{r}{\delta}\right) + O(\beta) \text{ for } r \sim \delta \\ \\ 1 - \alpha(\beta,\varepsilon)\log\left(\frac{r}{\delta}\right) + O(\alpha) \text{ for } r \sim R. \end{cases} \tag{2.152}$$

If $|\partial D(\delta)|/|\partial D(R)| \ll 1$, then the splitting probability $p(\boldsymbol{x})$ is, to leading order in this parameter, independent of $\boldsymbol{x}$, that is,

$$m = \Pr\{T_A < T_S\} \sim \frac{1}{|\Omega|} \int_{\Omega} p(r,\theta) r \, dr \, d\theta$$

$$=\gamma\left[\ln\left(\frac{R}{\delta}\right)-\frac{1}{2}\left(1-\left(\frac{\delta^2}{R^2}\right)\right)\right]$$

$$=\frac{\log\dfrac{1}{\beta}-\dfrac{1}{2}+O(\beta^2,\varepsilon)}{\log\dfrac{1}{\beta}+2\log\dfrac{1}{\varepsilon}+2\log 2+4\beta^2+O(\beta^2,\varepsilon)}. \tag{2.153}$$

The probability of exactly n visits in $D(\delta)$ prior to escape is $(1-m)^n m$, therefore the expected number of visits M in $D(\delta)$ prior to escape at $\partial\Omega_a$ and the variance V are given by

$$M=\sum_{n=0}^{\infty}n(1-m)^n m=\frac{1-m}{m}\sim\frac{2\log\dfrac{1}{\varepsilon}+2\ln 2+\dfrac{1}{2}}{\log\dfrac{1}{\beta}-\dfrac{1}{2}}$$

$$V=\sum_{n=0}^{\infty}n^2(1-m)^n m-M^2$$

$$\sim\frac{\left(2\log\dfrac{1}{\varepsilon}+2\ln 2+\dfrac{1}{2}\right)\left(\log\dfrac{1}{\beta}+2\log\dfrac{1}{\varepsilon}+2\log 2\right)}{\left(\log\dfrac{1}{\beta}-\dfrac{1}{2}\right)^2}. \tag{2.154}$$

These approximations are valid for $\varepsilon,\beta\ll 1$. The case $\beta\sim 1$ remains to be examined.

2.6 Asymptotic Computation of the Dwell Time

The dwell time is the MFPT $\mathbb{E}[\tau]$ of a trajectory from $D(R)$ to $\partial\Omega_a$. We assume that after exiting the trap $D(\delta)$ a trajectory is thermalized, that is, it is restarted in $D(R)-D(\delta)$ outside the boundary layers near $S=\partial D(\delta)$ and near $\partial\Omega_a$. Therefore, if $|\partial D(\delta)|/|\partial D(R)|\ll 1$ and $\varepsilon\ll 1$, the dwell time is to leading order independent of the restarting point of a trajectory.

The dwell time, conditioned on n visits in $D(\delta)$ prior to exit at $\partial\Omega_a$, is

$$\mathbb{E}[\tau\mid n\text{ visits in }D(\delta)]=n\left(\mathbb{E}[T_S\mid T_S<T_A]+\frac{1}{k_1}\right)+\mathbb{E}[T_A\mid T_A<T_S],$$

where $1/k_1$ is the mean trapping time in $D(\delta)$. Therefore, as in Sect. 2.5.1,

$$\begin{aligned}\mathbb{E}[\tau] &= \sum_{n=0}^{\infty} \mathbb{E}[\tau \,|\, n \text{ visits in } D(\delta)] \Pr\{n \text{ visits in } D(\delta) \text{ prior to escape}\}\\ &= \sum_{n=0}^{\infty} \left\{ n\left(\mathbb{E}[T_S \,|\, T_S < T_A] + \frac{1}{k_1}\right) + \mathbb{E}[T_A \,|\, T_A < T_S]\right\} (1-m)^n m\\ &= M\left(\mathbb{E}[T_S \,|\, T_S < T_A] + \frac{1}{k_1}\right) + \mathbb{E}[T_A \,|\, T_A < T_S], \end{aligned} \tag{2.155}$$

To conditional MFPT $\mathbb{E}[T_A \,|\, T_A < T_S]$ is the MFPT of the conditional diffusion process $\boldsymbol{x}^*(t)$, which is the solution of the stochastic differential equation (see Sect. 2.4),

$$d\boldsymbol{x}^*(t) = 2D\frac{\nabla p(\boldsymbol{x}^*(t))}{p(\boldsymbol{x}^*(t))}dt + \sqrt{2D}\,d\boldsymbol{w}(t),$$

where $p(\boldsymbol{x}) = \Pr\{T_A < T_S \,|\, \boldsymbol{x}(0) = \boldsymbol{x}\}$ is the splitting probability and $\boldsymbol{w}(t)$ is standard two-dimensional Brownian motion. The portion $\partial D(R) - \partial\Omega_a$ of the outer boundary is reflecting for the process $\boldsymbol{x}^*(t)$ and $\partial\Omega_a$ is absorbing. The boundary $\partial D(\delta)$ is unattainable for $\boldsymbol{x}^*(t)$, because the drift $2D\nabla p(\boldsymbol{x})/p(\boldsymbol{x})$ is infinite and points away from $D(\delta)$. Thus the conditional mean time

$$\bar{\tau}_A(\boldsymbol{x}) = \mathbb{E}[T_A \,|\, T_A < T_S, \boldsymbol{x}(0) = \boldsymbol{x}] \tag{2.156}$$

is the solution of the PAV boundary value problem

$$\begin{aligned} Dp(\boldsymbol{x})\Delta\bar{\tau}_A(\boldsymbol{x}) + 2D\nabla\bar{\tau}_A(\boldsymbol{x})\cdot\nabla p(\boldsymbol{x}) &= -p(\boldsymbol{x}) \quad \text{for } \boldsymbol{x} \in \Omega\\ \frac{\partial\bar{\tau}_A(\boldsymbol{x})}{\partial n} &= 0 \quad \text{for } \boldsymbol{x} \in \partial\Omega_r\\ \bar{\tau}_A(\boldsymbol{x}) &= 0 \quad \text{for } \boldsymbol{x} \in \partial\Omega_a. \end{aligned} \tag{2.157}$$

Setting $v(\boldsymbol{x}) = \bar{\tau}_A(\boldsymbol{x})p(\boldsymbol{x})$ the boundary value problem (2.157) reduces to

$$\begin{aligned} D\Delta v(\boldsymbol{x}) &= -p(\boldsymbol{x}) \quad \text{for } \boldsymbol{x} \in \Omega\\ \frac{\partial v(\boldsymbol{x})}{\partial n} &= 0 \quad \text{for } \boldsymbol{x} \in \partial\Omega_r\\ v(\boldsymbol{x}) &= 0 \quad \text{for } \boldsymbol{x} \in \partial\Omega_a\\ v(\boldsymbol{x}) &= 0 \quad \text{for } \boldsymbol{x} \in \partial D(\delta). \end{aligned} \tag{2.158}$$

An explicit representation of the solution uses the Green function $G(\boldsymbol{x},\boldsymbol{y})$ solution of the mixed boundary value problem

$$-\Delta_{\boldsymbol{x}} G(\boldsymbol{x},\boldsymbol{y}) = \delta(\boldsymbol{x}-\boldsymbol{y}) \text{ in } \Omega, \tag{2.159}$$

with $v(\boldsymbol{x}) = -\int\limits_{\Omega} G(\boldsymbol{x},\boldsymbol{y})p(\boldsymbol{y})d\boldsymbol{y}$. Because outside the boundary layer near $\partial\Omega_a$ the problem is to leading order radial, an explicit expression for $G(\boldsymbol{x},\boldsymbol{y}) = G(r,\theta,r_0,\theta_0)$ is for $\theta_0 = 0$

$$G(r,\theta,r_0,0) = g_0(r,r_0) + \sum_{n=1}^{\infty} g_n(r,r_0)\cos(n\theta).$$

where (Taflia and Holcman 2007)

$$g_0 \approx \begin{cases} \left(\alpha \log \dfrac{r_0}{\delta} - 1\right) \log \dfrac{r}{\delta} \text{ for } r < r_0 \\ \\ \left(\alpha \log \dfrac{r}{\delta} - 1\right) \log \dfrac{r_0}{\delta} \text{ for } r > r_0. \end{cases} \tag{2.160}$$

The contribution of $g_n(r,r_0)$ can be neglected in the first approximation. We conclude that the mean escape time is to leading order given by

$$\begin{aligned} \mathbb{E}[T_A \mid T_A < T_S, \boldsymbol{x}(0) = \boldsymbol{x}] &= \frac{1}{|\Omega|} \int\limits_{\Omega} p(r,\theta)\bar{\tau}_A(r,\theta])\, r\,dr\,d\theta \\ &= \frac{(2\pi)^2}{D} \int\limits_{\delta}^{R}\int\limits_{\delta}^{R} g_0(r,r_0)\left(-\alpha \log \frac{r_0}{\delta}\right) r_0 dr_0 r dr. \end{aligned}$$

Using (2.160), we get for $\varepsilon \ll 1$ and $|\partial D(\delta)|/\partial D(R)| \ll 1$ the asymptotic approximation

$$\begin{aligned} &\mathbb{E}[T_A \mid T_A < T_S] \\ &\sim \frac{R^2}{2D}\left(-\alpha^2 \log^3 \frac{1}{\beta} + \alpha \log^2 \frac{1}{\beta} + \frac{3}{2}\alpha^2 \log^2 \frac{1}{\beta} - \frac{5}{4}\alpha \log \frac{1}{\beta}\right). \end{aligned} \tag{2.161}$$

With α given in (2.150), the leading order term is

$$\mathbb{E}[T_A \mid T_A < T_S] \sim \frac{R^2}{2D} \frac{\log \dfrac{1}{\beta}\left(2\log \dfrac{1}{\varepsilon} + \dfrac{1}{4} + 2\log 2 - \dfrac{5\log \dfrac{1}{\varepsilon}}{2\log \dfrac{1}{\beta}}\right)}{\left(\log \dfrac{1}{\beta} + 2\log \dfrac{1}{\varepsilon} + 2\log 2 + O(\beta^2,\varepsilon)\right)}. \tag{2.162}$$

Other explicit examples where an asymptotic expression for the splitting probability is needed appear in models of the synaptic cleft, where the probability of a molecule to bind a receptor before absorption in a glia cell has to be estimated (Reingruber and Holcman 2011b; Taflia and Holcman 2011; Holcman and Schuss 2014). The derivations of this section form the basis for a molecular description of the postsynaptic density (PSD) as a domain with many traps. Obviously, the diffusion in the PSD needs to be coarse-grained. The inner disk $D(\delta)$ can represent a coarse-grained effective model of small scattered traps (e.g., scaffolding molecules), which are pooled together to form a single bigger trap, while preserving the absorption flux and the distribution of the trapping time. Such a coarse-grained model is presumably derivable by homogenization of a more microscopic model of diffusion in a potential landscape with many small and deep wells (relative to the thermal energy), which represent the potential of the chemical bond in the traps (Fig. 2.10) (Taflia and Holcman 2007).

2.7 NET with Killing

If the trajectories of a diffusion process $\boldsymbol{x}(t)$ in a domain Ω can be terminated at any time t and at each point $\boldsymbol{x} \in \Omega$ with probability $k(\boldsymbol{x},t)\,\Delta t + o(\Delta t)$, the function $k(\boldsymbol{x},t)$ is called a *killing measure* (Schuss 2010b). If the boundary $\partial\Omega$ reflects the trajectories $\boldsymbol{x}(t)$, except for a small absorbing window $\partial\Omega_a$, the NET problem is to find the absorption flux of trajectories that reach $\partial\Omega_a$. Thus there are two random termination times defined on the trajectories $\boldsymbol{x}(t)$, the time T to termination by killing and the time τ to termination by absorption in $\partial\Omega_a$.

2.7.1 The Probability of Absorbed Trajectories

We consider a diffusion process $\boldsymbol{x}(t)$ in a domain Ω, defined by the stochastic dynamics

$$d\boldsymbol{x} = \boldsymbol{b}(\boldsymbol{x})\,dt + \sqrt{2}\boldsymbol{B}(\boldsymbol{x})\,d\boldsymbol{w}(t) \quad \text{for } \boldsymbol{x} \in \Omega, \tag{2.163}$$

where $\boldsymbol{b}(\boldsymbol{x})$ is a smooth drift vector, $\boldsymbol{B}(\boldsymbol{x})$ is a diffusion tensor, and $\boldsymbol{w}(t)$ is a vector of independent standard Brownian motions. We assume that a killing measure $k(\boldsymbol{x},t)$ is defined in Ω and that $\partial\Omega = \partial\Omega_a \cup \partial\Omega_r$, where $\partial\Omega_a$ is a small absorbing part and $\partial\Omega_r$ is reflecting.

The transition probability density function of the process $\boldsymbol{x}(t)$ with killing and absorption is the probability density function of trajectories that have neither been killed nor absorbed in $\partial\Omega_a$ by time t,

$$p(\boldsymbol{x},t\,|\,\boldsymbol{y})\,d\boldsymbol{x} = \Pr\{\boldsymbol{x}(t) \in \boldsymbol{x} + d\boldsymbol{x},\ T > t,\ \tau > t\,|\,\boldsymbol{y}\}. \tag{2.164}$$

It is the solution of the Fokker–Planck equation (Holcman et al. 2005a; Schuss 2010b, Sect. 6.6)

$$\frac{\partial p(\boldsymbol{x},t\,|\,\boldsymbol{y})}{\partial t} = \mathcal{L}_{\boldsymbol{x}} p(\boldsymbol{x},t\,|\,\boldsymbol{y}) - k(\boldsymbol{x})p(\boldsymbol{x},t\,|\,\boldsymbol{y}) \quad \text{for } \boldsymbol{x},\boldsymbol{y} \in \Omega, \tag{2.165}$$

where $\mathcal{L}_{\boldsymbol{x}}$ is the forward operator

$$\mathcal{L}_{\boldsymbol{x}} p(\boldsymbol{x},t\,|\,\boldsymbol{y}) = \sum_{i,j=1}^{d} \frac{\partial^2 \sigma^{i,j}(\boldsymbol{x})p(\boldsymbol{x},t\,|\,\boldsymbol{y})}{\partial x^i \partial x^j} - \sum_{i=1}^{d} \frac{\partial b^i(\boldsymbol{x})p(\boldsymbol{x},t\,|\,\boldsymbol{y})}{\partial x^i}, \tag{2.166}$$

and $\boldsymbol{\sigma}(\boldsymbol{x}) = \frac{1}{2}\boldsymbol{B}(\boldsymbol{x})\boldsymbol{B}^T(\boldsymbol{x})$. The operator $\mathcal{L}_{\boldsymbol{x}}$ can be written in the divergence form $\mathcal{L}_{\boldsymbol{x}} p(\boldsymbol{x},t\,|\,\boldsymbol{y}) = -\nabla\cdot\boldsymbol{J}(\boldsymbol{x},t\,|\,\boldsymbol{y})$, where the components of the flux density vector $\boldsymbol{J}(\boldsymbol{x},t\,|\,\boldsymbol{y})$ are

$$J^i(\boldsymbol{x},t\,|\,\boldsymbol{y}) = -\sum_{j=1}^{d} \frac{\partial \sigma^{i,j}(\boldsymbol{x})p(\boldsymbol{x},t\,|\,\boldsymbol{y})}{\partial x^i} + b^i(\boldsymbol{x})p(\boldsymbol{x},t\,|\,\boldsymbol{y}), \quad (i = 1,2,\ldots,d).$$

The initial and boundary conditions for the Fokker–Planck equation (2.165) are

$$p(\boldsymbol{x},0\,|\,\boldsymbol{y}) = \delta(\boldsymbol{x}-\boldsymbol{y}) \quad \text{for } \boldsymbol{x},\boldsymbol{y} \in \Omega \tag{2.167}$$

$$p(\boldsymbol{x},t\,|\,\boldsymbol{y}) = 0 \quad \text{for } t > 0,\ \boldsymbol{x} \in \partial\Omega_a,\ \boldsymbol{y} \in \Omega \tag{2.168}$$

$$\boldsymbol{J}(\boldsymbol{x},t\,|\,\boldsymbol{y})\cdot\boldsymbol{n}(\boldsymbol{x}) = 0 \quad \text{for } t > 0,\ \boldsymbol{x} \in \partial\Omega - \partial\Omega_a,\ \boldsymbol{y} \in \Omega. \tag{2.169}$$

The probability of trajectories that are killed before reaching $\partial\Omega_a$ is given by

$$\Pr\{T < \tau\,|\,\boldsymbol{y}\} = \int_0^\infty \int_\Omega k(\boldsymbol{x})p(\boldsymbol{x},t\,|\,\boldsymbol{y})\,d\boldsymbol{x}\,dt. \tag{2.170}$$

The absorption probability flux on $\partial\Omega_a$ is

$$J(t\,|\,\boldsymbol{y}) = \oint_{\partial\Omega} \boldsymbol{J}(\boldsymbol{x},t\,|\,\boldsymbol{y})\cdot\boldsymbol{n}(\boldsymbol{x})\,dS_{\boldsymbol{x}}$$

and $\int_0^\infty J(t\,|\,\boldsymbol{y})\,dt$ is the probability of trajectories that have ever been absorbed at $\partial\Omega_a$.

The probability distribution function of the killing time T is the conditional probability of killing before time t of trajectories that have not been absorbed in $\partial\Omega_a$ by that time,

$$\Pr\{T < t\,|\,\tau > T,\boldsymbol{y}\} = \frac{\Pr\{T < t, \tau > T\,|\,\boldsymbol{y}\}}{\Pr\{\tau > T\,|\,\boldsymbol{y}\}} = \frac{\displaystyle\int_0^t \int_\Omega k(\boldsymbol{x})p(\boldsymbol{x},s\,|\,\boldsymbol{y})\,d\boldsymbol{x}\,ds}{\displaystyle\int_0^\infty \int_\Omega k(\boldsymbol{x})p(\boldsymbol{x},s\,|\,\boldsymbol{y})\,d\boldsymbol{x}\,ds}.$$

The probability distribution of the time to absorption at $\partial\Omega_a$ is the conditional probability of absorption before time t of trajectories that have not been killed by that time,

$$\Pr\{\tau < t \,|\, T > \tau, \boldsymbol{y}\} = \frac{\displaystyle\int_0^t J(s \,|\, \boldsymbol{y})\, ds}{1 - \displaystyle\int_0^\infty \int_\Omega k(\boldsymbol{x}) p(\boldsymbol{x}, s \,|\, \boldsymbol{y})\, d\boldsymbol{x}\, ds}. \tag{2.171}$$

Thus the NET is the conditional expectation of the absorption time of trajectories that are not killed in Ω, that is,

$$\begin{aligned}\mathbb{E}[\tau \,|\, T > \tau, \boldsymbol{y}] &= \int\limits_0^\infty \Pr\{\tau > t \,|\, T > \tau, \boldsymbol{y}\}\, dt \\ &= \frac{\displaystyle\int_0^\infty sJ(s \,|\, \boldsymbol{y})\, ds}{1 - \displaystyle\int_0^\infty \int_\Omega k(\boldsymbol{x}) p(\boldsymbol{x}, s \,|\, \boldsymbol{y})\, d\boldsymbol{x}\, ds}. \end{aligned} \tag{2.172}$$

The survival probability of trajectories that have not been terminated by time t is given by

$$S(t \,|\, \boldsymbol{y}) = \int\limits_\Omega p(\boldsymbol{x}, t \,|\, \boldsymbol{y})\, d\boldsymbol{x}. \tag{2.173}$$

The mean time spent at $\boldsymbol{x}$ prior to termination,

$$\tilde{p}(\boldsymbol{x}|\boldsymbol{y}) = \int\limits_0^\infty p(\boldsymbol{x}, t \,|\, \boldsymbol{y})\, dt,$$

is the solution of the boundary value problem

$$\begin{aligned}\mathcal{L}_x \tilde{p}(\boldsymbol{x} \,|\, \boldsymbol{y}) - k(\boldsymbol{x})\tilde{p}(\boldsymbol{x} \,|\, \boldsymbol{y}) &= -\,\delta(\boldsymbol{x} - \boldsymbol{y}) \quad \text{for}\, \boldsymbol{x}, \boldsymbol{y} \in \Omega \\ \tilde{p}(\boldsymbol{x} \,|\, \boldsymbol{y}) &= 0 \quad \text{for}\, \boldsymbol{x} \in \partial\Omega_a,\ \boldsymbol{y} \in \Omega \\ \boldsymbol{J}(\boldsymbol{x} \,|\, \boldsymbol{y}) \cdot \boldsymbol{n}(\boldsymbol{x}) &= 0 \quad \text{for}\, t > 0,\ \boldsymbol{x} \in \partial\Omega - \partial\Omega_a,\ \boldsymbol{y} \in \Omega. \end{aligned} \tag{2.174}$$

If the initial pdf $p_I(\boldsymbol{x})$ is a sufficiently smooth function, the density of the time spent at $\boldsymbol{x}$ prior to termination,

$$\tilde{p}(\boldsymbol{x}) = \int\limits_\Omega \tilde{p}(\boldsymbol{x} \,|\, \boldsymbol{y}) p_I(\boldsymbol{y})\, d\boldsymbol{y}, \tag{2.175}$$

is the solution of the inhomogeneous boundary value problem

$$\begin{aligned}\mathcal{L}_{\boldsymbol{x}}\tilde{p}(\boldsymbol{x})-k(\boldsymbol{x})\tilde{p}(\boldsymbol{x}) &= -p_I(\boldsymbol{x}) \ \text{ for } \boldsymbol{x}\in\Omega \\ \tilde{p}(\boldsymbol{x}) &= 0 \ \text{ for } \boldsymbol{x}\in\partial\Omega_a \\ \tilde{\boldsymbol{J}}(\boldsymbol{x})\cdot\boldsymbol{n}(\boldsymbol{x}) &= 0 \ \text{ for } t>0,\ \boldsymbol{x}\in\partial\Omega-\partial\Omega_a.\end{aligned} \tag{2.176}$$

The probability P_N of trajectories that are terminated at $\partial\Omega_a$ is

$$P_N=\int\limits_{\Omega}\Pr\{\tau<T\,|\,\boldsymbol{y}\}p_I(\boldsymbol{y})\,d\boldsymbol{y}=1-\int\limits_{\Omega}k(\boldsymbol{x})\tilde{p}(\boldsymbol{x})\,d\boldsymbol{x}. \tag{2.177}$$

Averaging $\mathbb{E}[\tau\,|\,T>\tau,\,\boldsymbol{y}]$ with respect to the initial density $p_I(\boldsymbol{x})$ gives in (2.172)

$$\mathbb{E}[\tau\,|\,T>\tau]=\frac{\displaystyle\int_0^\infty sJ(s)\,ds}{1-\int_\Omega k(\boldsymbol{x})\tilde{p}(\boldsymbol{x})\,d\boldsymbol{x}}, \tag{2.178}$$

where $J(s)=\int_\Omega J(s\,|\,\boldsymbol{y})p_I(\boldsymbol{y})\,d\boldsymbol{y}$.

2.7.2 Decay of the Survival Probability in One Dimension

To compare the survival probability of Brownian motion with and without a Dirac killing (a trap or hot spot) at a point x_1 in the interval $[0,\pi]$, with absorbing boundaries, we write the boundary value problem (2.165) as

$$\begin{aligned}\frac{\partial u(x,t\,|\,x_1,y)}{\partial t} &= D\frac{\partial^2 u(x,t\,|\,x_1,y)}{\partial x^2}-V\delta(x-x_1)u(x,t\,|\,x_1,y) \quad \text{for} \quad 0<x<\pi \\ u(x,0\,|\,x_1,y) &= \delta(x-y) \\ u(0,t\,|\,x_1,y) &= u(\pi,t\,|\,x_1,y)=0,\end{aligned} \tag{2.179}$$

and expand Green's function for the initial-boundary-value-problem (2.179) for free diffusion ($V=0$) as

$$G(x,t\,|\,y)=\frac{2}{\pi}\sum_{n=1}^{\infty}\sin nx\sin nye^{-n^2t}.$$

The survival probability for this problem in the interval is given by

$$S_0(t\,|\,y)=\int\limits_0^\pi G(x,t\,|\,y)\,dx=\frac{4}{\pi}\sum_{n=1}^{\infty}\frac{\sin(2n-1)y}{2n-1}e^{-(2n-1)^2t}. \tag{2.180}$$

Next, we solve (2.179) with $V > 0$ for the Laplace transform $\hat{u}_V(x, q \,|\, x_1, y)$ of $u(x, t \,|\, x_1, y)$,

$$\hat{u}_V(x, q \,|\, x_1, y) = \hat{G}(x, q \,|\, y) - \frac{V\hat{G}(x, q \,|\, x_1)}{1 + V\hat{G}(x_1, q \,|\, x_1)}\hat{G}(x_1, q \,|\, y), \tag{2.181}$$

where

$$\hat{G}(x, q \,|\, y) = \frac{2}{\pi}\sum_{n=1}^{\infty}\frac{\sin nx \sin ny}{q + n^2}. \tag{2.182}$$

Note that

$$\hat{S}_0(q \,|\, y) = \int_0^{\pi} \hat{G}(x, q \,|\, y)\, dx = \frac{4}{\pi}\sum_{n=1}^{\infty}\frac{\sin(2n-1)y}{(2n-1)\left(q + (2n-1)^2\right)}.$$

According to Eq. (2.173), the survival probability $S_V(t \,|\, y)$ is given by

$$S_V(t \,|\, x_1, y) = \int_0^{\pi} u_V(x, t \,|\, x_1, y)\, dx \tag{2.183}$$

and the Laplace transform is

$$\hat{S}_V(q \,|\, y) = \int_0^{\pi} \hat{u}_V(x, q \,|\, x_1, y)\, dx. \tag{2.184}$$

Using (2.181), we find that the survival probabilities, without and with the Dirac killing, differ by

$$\hat{S}_0(q \,|\, y) - \hat{S}_V(q \,|\, x_1, y) = \frac{V\hat{G}(x_1, q \,|\, y)}{1 + V\hat{G}(x_1, q \,|\, x_1)}\frac{4}{\pi}\sum_{n=1}^{\infty}\frac{\sin(2n-1)x_1}{(2n-1)\left(q + (2n-1)^2\right)}.$$

The difference $\hat{S}_0(q \,|\, y) - \hat{S}_V(q \,|\, x_1, y)$ has no poles other than the zeros of $1 + V\hat{G}(x_1, q \,|\, x_1)$, which are written as $q = -\xi^2$, where ξ is the smallest positive root of the equation

$$\sin\xi(\pi - x_1)\sin\xi x_1 = -\frac{\xi \sin\xi\pi}{V}$$

Holcman et al. (2005a) (see Appendix I below). For small V, we have

$$q = -1 - V\frac{2}{\pi}\sin(\pi - x_1)\sin x_1 + O\left(V^2\right). \tag{2.185}$$

The result (2.185) means that killing is most effective when the killing site is in the middle of the interval.

For large V and $x_1 > \pi/2$, we have

$$q = -\left(\frac{\pi}{x_1}\right)^2 + \frac{2\pi^2}{x_1^3}\frac{1}{V} + O\left(\frac{1}{V^2}\right), \tag{2.186}$$

which means that for large killing V the decay rate is the same as that in the interval enclosed between the killing site x_1 and the more distant endpoint of the interval $[0, \pi]$, with absorbing boundaries. Note that the decay rate in this case is independent of the initial point y.

The conditional MFPT $E[T \,|\, T < \tau, y]$ is (see Appendix II below)

$$\begin{aligned} E[T \,|\, T < \tau, y] &= -\left.\frac{\partial}{\partial q}\ln\{\hat{p}(x_1, q \,|\, y)\}\right|_{q=0} \\ &= \frac{x_1 y(x_1^2 + y^2 + 2\pi^2) - \pi(x_1^3 + y^3)}{6(\pi - x_1)y}\,\frac{\pi}{\pi + V(\pi - x_1)y}. \end{aligned} \tag{2.187}$$

Appendix I: Details of Computations Used in Sect. 2.7.2

The Laplace transform $\hat{G}(x_1, q \,|\, x_1)$ is given by

$$\hat{G}(x_1, q \,|\, x_1) = \frac{2}{\pi}\sum_{n=1}^{\infty}\frac{\sin nx_1 \sin nx_1}{q + n^2}. \tag{2.188}$$

Replacing x by $x - \pi$ in the identity

$$\frac{\pi\cos(ax)}{2\sin(ax)} = \frac{1}{2a} + \sum_{n=1}^{\infty}\frac{(-1)^n a\cos(ax)}{a^2 - n^2} \quad \text{for } -\pi < x < \pi, \tag{2.189}$$

gives for the function

$$F(z) = \sum_{n=1}^{\infty}\frac{\cos(nx)}{q + n^2}, \tag{2.190}$$

the explicit expression

$$F(z) = -\frac{1}{2q} - \frac{\pi\cos[\sqrt{-q}(z - \pi)]}{2\sqrt{-q}\sin(\sqrt{-q}\pi)}.$$

Consequently,

$$\hat{G}(x_1, q \,|\, x_1) = \frac{F(0) - F(2x_1)}{\pi} = \frac{\cos[\sqrt{-q}(2x_1 - \pi)] - \cos(\sqrt{-q}\,\pi)}{2\sqrt{-q}\sin(\sqrt{-q}\pi)}.$$

Remark. The expansions for small and large V of the zeros in Sect. 2.7.2 are obtained by a regular perturbation scheme in terms of the potential and the inverse of the potential.

2.7.3 The Ratio of Absorption to Killing

According to the Fokker–Planck equation (2.165), the time-dependent ratio $R(t)$ of the absorption flux up to time t to the probability of killed trajectories by time t is defined as

$$R(t) = \frac{\displaystyle\int_\Omega d\boldsymbol{y} \int_{\partial\Omega_a} \boldsymbol{J}(\boldsymbol{x}, t \,|\, \boldsymbol{y}) \cdot \boldsymbol{\nu}(\boldsymbol{x}) p_I(\boldsymbol{y})\, dS_{\boldsymbol{x}}}{\displaystyle\int_\Omega d\boldsymbol{y} \int_\Omega k(\boldsymbol{x}) p(\boldsymbol{x}, t \,|\, \boldsymbol{y})\, d\boldsymbol{x}\, p_I(\boldsymbol{y})}. \tag{2.191}$$

The steady state ratio R_∞ is given by

$$R_\infty = \lim_{t\to\infty} R(t) = \frac{\displaystyle\int_\Omega d\boldsymbol{y} \int_{\partial\Omega_a} \boldsymbol{J}(\boldsymbol{x} \,|\, \boldsymbol{y}) \cdot \boldsymbol{\nu}(\boldsymbol{x})\, dS_{\boldsymbol{x}} p_I(\boldsymbol{y})}{\displaystyle\int_\Omega d\boldsymbol{y} \int_\Omega k(\boldsymbol{x}) G(\boldsymbol{x} \,|\, \boldsymbol{y})\, d\boldsymbol{x} p_I(\boldsymbol{y})}, \tag{2.192}$$

where $G(\boldsymbol{x} \,|\, \boldsymbol{y})$ is defined by the boundary value problem for the equation

$$-p_I(\boldsymbol{y}) = \mathcal{L}_{\boldsymbol{x}} G(\boldsymbol{x}, |\, \boldsymbol{y}) - k(\boldsymbol{x}) G(\boldsymbol{x} \,|\, \boldsymbol{y}) \quad \text{for}\, \boldsymbol{x}, \boldsymbol{y} \in \Omega \tag{2.193}$$

with the forward operator $\mathcal{L}_{\boldsymbol{x}}$ defined in (2.166), and $\boldsymbol{J}(\boldsymbol{x} \,|\, \boldsymbol{y})$—the flux density vector at point $\boldsymbol{x}$, computed with respect to the function $G(\boldsymbol{x} \,|\, \boldsymbol{y})$. When $p_I(\boldsymbol{y}) = \delta(\boldsymbol{y} - \boldsymbol{x})$, the function $G(\boldsymbol{x} \,|\, \boldsymbol{y})$ is the standard Green function for the specified boundary value problem.

2.7.4 Splitting Influx into Absorption and Killing Effluxes

A related problem is that of splitting a steady-state influx through a part $\partial\Omega_i$ of the boundary into efflux through $\partial\Omega_a$ and efflux by killing. Thus, we define the ratio R_s of the two parts of the efflux. The boundary value problem for the steady state Fokker–Planck equation is

$$\begin{aligned}
\mathcal{L}_{\boldsymbol{x}} p(\boldsymbol{x}) - k(\boldsymbol{x}) p(\boldsymbol{x}) &= 0 \quad \text{for}\, \boldsymbol{x} \in \Omega \\
p(\boldsymbol{x}) &= 0 \quad \text{for}\, \boldsymbol{x} \in \partial\Omega_a \\
\boldsymbol{J}(\boldsymbol{x}) \cdot \boldsymbol{\nu}(\boldsymbol{x}) &= 0 \quad \text{for}\, \boldsymbol{x} \in \partial\Omega - \partial\Omega_a - \partial\Omega_i,\ t > 0 \\
\boldsymbol{J}(\boldsymbol{x}) \cdot \boldsymbol{\nu}(\boldsymbol{x}) &= -\,\Phi(\boldsymbol{x}) \quad \text{for}\, \boldsymbol{x} \in \partial\Omega_i,
\end{aligned} \tag{2.194}$$

where the forward operator $\mathcal{L}_{\boldsymbol{x}}$ is defined in (2.166), $\Phi(\boldsymbol{x}) \geq 0$ is the steady influx density, and

$$J_a = \int\limits_{\partial\Omega_a} \boldsymbol{J}(\boldsymbol{x}) \cdot \boldsymbol{\nu}(\boldsymbol{x}) dS_{\boldsymbol{x}} \tag{2.195}$$

is the steady absorption efflux. Thus the total influx is

$$J_i = \int\limits_{\partial\Omega_i} \Phi(\boldsymbol{x})\, dS_{\boldsymbol{x}}. \tag{2.196}$$

The efflux ratio R_s is defined as

$$R_s = \frac{\displaystyle\int_{\partial\Omega_a} \boldsymbol{J}(\boldsymbol{x}) \cdot \boldsymbol{\nu}(\boldsymbol{x})\, dS_{\boldsymbol{x}}}{\displaystyle\int_{\Omega} k(\boldsymbol{x}) p(\boldsymbol{x})\, d\boldsymbol{x}} = \frac{\displaystyle\int_{\partial\Omega_i} \Phi(\boldsymbol{x})\, dS_{\boldsymbol{x}} - \int_{\Omega} k(\boldsymbol{x}) p(\boldsymbol{x})\, d\boldsymbol{x}}{\displaystyle\int_{\Omega} k(\boldsymbol{x}) p(\boldsymbol{x})\, d\boldsymbol{x}}. \tag{2.197}$$

The second part of the identity expresses conservation of probability. The ratios R_∞ and R_s can be evaluated explicitly in a one-dimensional finite interval. We distinguish between two cases: in the first one the killing measure is uniformly distributed and in the second it is the Dirac measure $k(x) = k\delta(x - x_1)$ at x_1 with some positive constant k. The boundary value problem (2.194) becomes

$$D\frac{\partial^2 p(x)}{\partial x^2} - k\delta(x - x_1) p(x) = 0 \quad \text{for } 0 < x < L$$

$$\frac{\partial p(L)}{\partial x} = \Phi, \quad p(0) = 0$$

where $\Phi < 0$ and the efflux ratio is

$$R_s = \frac{-D\dfrac{\partial p(0)}{\partial x}}{kp(x_1)}. \tag{2.198}$$

An explicit computation of $p(x)$ gives

$$Dp'(L) = -\frac{D\Phi}{1 + \dfrac{k}{D}(L - x_1)}, \quad kp(x_1) = \frac{k\Phi(x_1 - L)}{1 + \dfrac{k}{D}(L - x_1)},$$

and

$$R_s = \frac{D}{k(L - x_1)}. \tag{2.199}$$

Similarly, from relation 2.192, the ratio R_∞ computed for a uniform distribution in the interval $[0, L]$ is given by

$$R_\infty \sim \frac{1}{\cosh(bL)} \quad \text{for } L \to \infty, \quad \text{where} \tag{2.200}$$

$$b = \sqrt{\frac{k}{D}}.$$

Appendix II: Derivation of (2.187)

The Laplace transform of Eq. (2.179) with absorbing boundary conditions is given by

$$\hat{u}(x, q \,|\, y) = -\frac{2V}{\pi} \sum_{1}^{+\infty} \frac{\sin nx \sin ny}{q + n^2} \hat{u}(x_1, q \,|\, y) + \hat{G}(x, q \,|\, y),$$

which gives for $x = x_1$

$$\hat{u}(x_1, q \,|\, y) = \frac{\hat{G}(x_1, q \,|\, y)}{1 + \dfrac{2V}{\pi} \displaystyle\sum_{1}^{\infty} \frac{\sin nx_1 \sin ny}{q + n^2}},$$

and

$$\begin{aligned}\frac{\partial}{\partial q} \ln \hat{p}(x_1, q \,|\, y) &= \frac{\partial}{\partial q} \ln \hat{G}(x_1, q \,|\, y) - \frac{\partial}{\partial q} \ln\left(1 + \frac{2V}{\pi} \sum_{1}^{\infty} \frac{\sin nx_1 \sin ny}{q + n^2}\right)\\ &= \alpha(x_1 \,|\, y) + \beta(x_1 \,|\, y)\end{aligned}$$

with

$$\alpha(x_1 \,|\, y) = \frac{\partial}{\partial q} \ln \hat{G}(x_1, q \,|\, y)\bigg|_{q=0} = -\frac{\displaystyle\sum_{n=1}^{\infty} \frac{\sin nx_1 \sin ny}{n^4}}{\displaystyle\sum_{n=1}^{\infty} \frac{\sin nx_1 \sin ny}{n^2}}$$

and

$$\beta(x_1 \,|\, y) = -\frac{\partial}{\partial q} \ln\left(1 + \frac{2V}{\pi} \sum_{1}^{+\infty} \frac{\sin nx_1 \sin ny}{q + n^2}\right)\bigg|_{q=0}$$

$$
= \frac{\dfrac{2V}{\pi} \displaystyle\sum_{n=1}^{\infty} \frac{\sin nx_1 \sin ny}{n^4}}{1 + \dfrac{2V}{\pi} \displaystyle\sum_{1}^{+\infty} \frac{\sin nx_1 \sin ny}{n^2}}.
$$

It is well known that for $x_1, y \in (0, \pi)$,

$$
\begin{aligned}
\frac{2}{\pi} \sum_{n=1}^{\infty} \frac{\sin nx_1 \sin ny}{n^2} &= \frac{(\pi - x_1)y}{\pi} \\
\frac{2}{\pi} \sum_{n=1}^{\infty} \frac{\sin nx_1 \sin ny}{n^4} &= \frac{x_1 y}{6\pi}(x_1^2 + y^2 + 2\pi^2) - \frac{(x_1^3 + y^3)}{6},
\end{aligned}
$$

hence

$$
\begin{aligned}
E[T \mid T < \tau, y] &= -\alpha(x_1 \mid y) + \beta(x_1 \mid y) \\
&= \frac{x_1 y (x_1^2 + y^2 + 2\pi^2) - \pi(x_1^3 + y^3)}{6(\pi - x_1)y} \, \frac{\pi}{\pi + V(\pi - x_1)y},
\end{aligned}
$$

which is (2.187).

Chapter 3
NET in Molecular and Cellular Biology

3.1 Introduction

Critical biological processes, such as synaptic plasticity and transmission, activation of genes by transcription factors, or double stranded DNA break repair, are controlled by diffusion in structures that have both large and small spatial scales. These may be small binding sites inside or on the surface of a cell, or narrow passages between subcellular compartments. The great disparity in spatial scales is the key to controlling cell function by structure. This disparity poses analytical and numerical difficulties in extracting properties from experimental data, from biophysical models, and from Brownian dynamics simulations of diffusion in multi-scale structures. Some of these difficulties are resolved by the methods described in Chaps. 1 and 2, which are applied here to the analysis and simulations of subcellular processes and to the quantification of their biological functions.

The great disparity between spatial scales in a biological cell structure leads to time scale separation between molecular events in the cell and in its physiological response. Specifically, the time scale of diffusion at large is much shorter than that of diffusing into small and hidden targets in cells. This separation indicates that the conversion of molecular events into cellular response, which is a rare event (on the time scale of diffusion) is controlled by structure. It is well known in the theory of ionic channels that structure is the main determinant of channel selectivity and gating (Hille 2001) (see also R. MacKinnon Nobel lecture MacKinnon 2003). Traditionally, when the crystallographic structure of a channel is unknown, recordings of channel current–voltage characteristics are used to reconstruct the spatial organization of protein and ions that define the channel pore (Chen et al. 1997; Burger et al. 2007). But even when the crystallographic structure of a channel is known, the determination of the function of different channel components, such as gating, ionic selectivity, and channel conductances from the molecular structure, is only partially known (Chen et al. 1999; Boda et al. 2007). A possible approach for an answer relies on either solving the Poisson–Nernst–Planck equations (Eisenberg

D. Holcman, Z. Schuss, *Stochastic Narrow Escape in Molecular and Cellular Biology*, DOI 10.1007/978-1-4939-3103-3_3

and Chen 1993) or Brownian or molecular dynamics simulations of the joint diffusive motion of protein and ions as well as the computation of the time-dependent electric field (see, for example, Aboud et al. 2003).

The resolution of the structure-function relationship in channels is more accurate than in cells due to the nano-scale resolution of channel structure. The coarser scale of structural resolution of cellular and subcellular compartments necessitates perforce much coarser mathematical and biophysical models than channel models. The former can be expected to give much coarser functional information on cellular function than the latter for channel function. In order to produce manageable cell models many physical features have to be given up, for example, interactions between mobile particles, which are the determinants of channel conductance and selectivity. Also the structural model of the cell, which is by and large unknown, has to be simplified. The functional information that can be extracted from the simplified models of cell structure calls for different analytical and simulation tools than in channels. To address the structure-function question in cell models, we focus on several examples of simplified structures of cellular microdomains, such as the structure of enzymatic active sites, confined chromatin structure, the transient structure during cell division, and the flow of genetic materials exchanged by diffusion; in particular, on the regulation of diffusion flux in synapses and dendritic spines of neurons, whose spatial structure has been extensively studied (Harris and Stevens 1988; Bourne and Harris 2008).

There are about 10^{11} neurons in the human brain, each containing about 10^3 synapses, which consist of pre- and post-synaptic terminals. In excitatory connections the latter can be a dendritic spine-like structure (Fig. 3.1). There are also stand-alone spines that all in all can number about 10^5 in a hippocampal neuron. The function of synapses and dendritic spines is still unclear, though their morphological changes in cognitive pathology, such as in epilepsy and autism spectrum disorders, indicate that they may be involved in regulating the synaptic function. The structure-function approach in modeling and analyzing these structures can possibly be the key to bridging the gap between the molecular and the cellular scales (Figs. 3.2 and 3.3).

Recognized more than 100 years ago by Ramón y Cajal (1909), dendritic spines are small terminal protrusions on neuronal dendrites and are considered to be the main locus of excitatory synaptic connections. The general spine geometry, as observed in Fig. 3.1(right), consists of a relatively narrow cylindrical neck connected to a bulky head (the round part in the schematic Fig. 3.4). Indeed, spine shapes can fall into one of these categories. In addition, spine geometrical shapes correlate with their physiological functions. Change of spine morphology can be induced by synaptic potentiation protocols and indeed, intracellular signaling, such as calcium release from stores, alters the morphology of dendritic spines in cultured hippocampal neurons. These changes in geometry can affect the spine-dendrite communication. One of the first quantitative assessments of geometry was obtained by a direct measurement of diffusion through the spine neck. Concentration gradients between spines and shafts in rat CA1 pyramidal neurons were established by photo-bleaching and photo-release of fluorescein dextran in order to track the

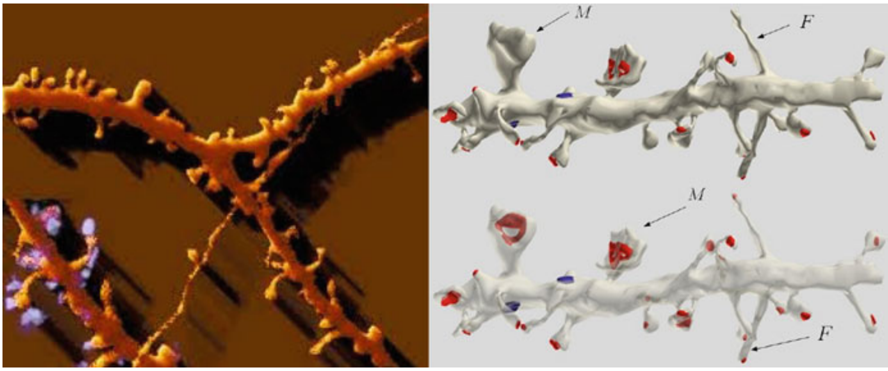

Fig. 3.1 *Left*: spines on a dendrite. *Right*: three-dimensional EM reconstruction of two dendrites from the hippocampus. The PSDs of excitatory synapses are marked *red* and of inhibitory synapses—*blue*. Filopodia (marked *F*) and mushroom spines (marked *M*) are clearly seen (Bourne and Harris 2008)

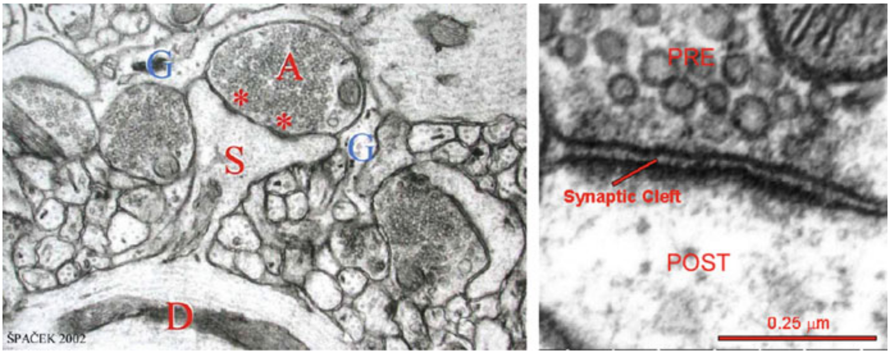

Fig. 3.2 *Left*: electron-microscopy of an excitatory synapse. Vesicles containing NT can be seen inside the pre-synaptic terminal (marked *A*). The spine (marked *S*) is connected to the dendritic shaft (marked *D*) by a neck. The synaptic cleft separating pre- and post-synaptic membranes is 20–25 nm wide. Glia cells surrounding the synaptic cleft are marked *G*. The *arrow* points at organelles inside the spine. *Right*: blowup of the synaptic cleft vicinity. The synaptic cleft is 20–25 nm wide. Vesicles with NT molecules are clearly seen in this enlargement

time course of re-equilibration. It was well approximated by a single exponential decay, with a time constant in the range of 20–100 ms. The role of the spine neck was further investigated experimentally with flash photolysis of caged calcium and theoretically, with the main conclusion that geometrical changes in the spine neck, such as the length or the radius, are key modulators of calcium dynamics in the process of spine-dendrite communication

The connection between the head and the neck is not only relevant to three-dimensional diffusion in the bulk, but also for two-dimensional surface diffusion. Indeed, synaptic transmission and plasticity involve the trafficking of receptors on cell membranes such as AMPA or NMDA glutamatergic receptors, which mediate

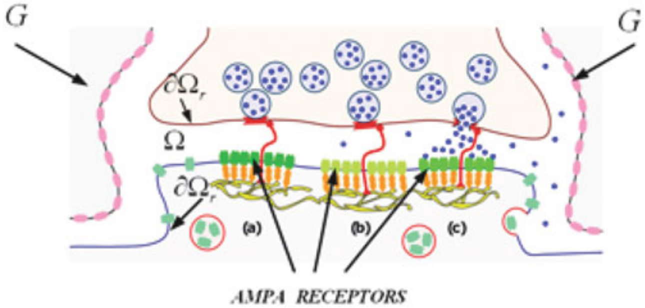

Fig. 3.3 Schematic diagram of the synaptic cleft. The cleft domain is marked Ω. The pre- and post-synaptic membranes are reflecting boundaries ($\partial\Omega_r$) for the Brownian trajectories of the NT molecules (*blue dots*). The glia cells G and the AMPA receptors form the absorbing boundary $\partial\Omega_a$. Clusters of AMPARs (a,b,c) are co-localized with release sites of vesicle fusion, mediated by adhesion molecules (*red*)

Fig. 3.4 Schematic diagram of a dendritic spine with a smoothly connected neck (*left*) and with a neck connected at a finite angle (*right*)

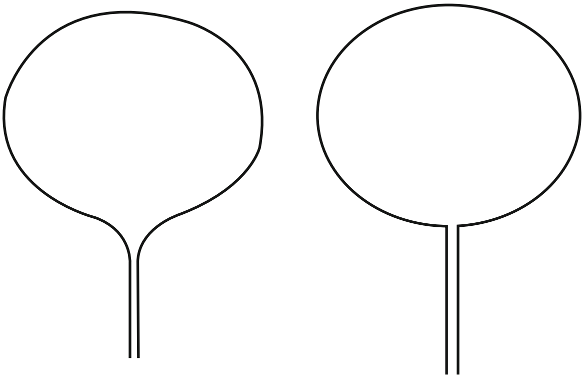

the post-synaptic current. The number and type of receptors that shape the synaptic current could be regulated by spine geometry. Regulation of synaptic current by spine geometry was explored theoretically by using asymptotic expressions for the residence time and experimentally by monitoring the motion of AMPA receptors on the surface of mature neurons.

3.2 From Molecular to Cellular Description

In this section, we describe how to bridge between physical models at the molecular scale and the micrometer scale, at which cells filter and convert molecular signals into cellular response. The latter defines cellular or subcellular function. We report here recent progress in quantifying analytically the control of diffusion flux into small absorbing targets or through narrow passages in cells. This case is especially important in molecular searches that are not directed at long distances by a field of force and the only flux control mechanism is the geometrical structure. We discuss specific applications of the flux formulas in dendritic spines, in the case of synaptic transmission, for enzyme structure and hidden target sites, for diffusion in the confined chromatin structure in the context of DNA-repair, and the unilateral flow of genetic materials exchanged by diffusion during cell division.

The behavior of molecules is complex not only because of their individual structure, but also because they form clusters, interact, reflect, and so on. At this stage we only have access to certain sampled molecular trajectories, thus it is unclear how to reconstruct their dynamics from the statistics of the samples. In order to interpret molecular data, we adopt the widely accepted model of molecular motion as diffusion in a field of force. The force field may represent electric interactions with fixed or mobile charges, dielectric interactions with obstacles, such as lipid bilayers and other fixed cell components, hydrodynamical interactions with an ambient flow field, and so on. The task of molecular level model is to extract cellular level properties and infer from it cell function.

3.2.1 Flux Through Narrow Passages Identifies Cellular Compartments

The random movement of ions, proteins, and other particles in cells is traditionally described as Brownian motion, as mentioned above. The Brownian trajectories are reflected at the cell membrane and at other obstacles, but can be absorbed (terminated) at receptors and other binding sites or when they exit the cell (or a subcellular compartment) and enter another structure. Different compartments for Brownian trajectories are defined here by the probability density of the trajectories or the statistics of the time a trajectory spends at a point. As in segmentation of images (or other data, see Wikipedia), a histogram is computed from all points visited by a trajectory (or trajectories) and the peaks and valleys in the histogram are used to identify the compartments as clusters. What makes the clusters, be it membranes, obstacles, or forces, is an active field of experimental live cell imaging by super-resolution microscopy (Manley et al. 2008; Huang et al. 2010). By its very definition, the passage of a trajectory from one compartment to the other is a rare event. The rare events may be thermal activation over a potential barrier and/or traversing a narrow passage, such as a channel, a nano-pore, or a narrow neck.

The mean first passage time (MFPT) $\bar{\tau}$ of a Brownian trajectory from a compartment to an absorbing target or through a narrow passage is a fundamental concept in the description of rare events. Specifically, the probability density function of the time spent in a compartment prior to termination or escape from the compartment in the limit of small target is exponential for sufficiently long times,

$$p_{\bar{\tau}}(t) \sim \bar{\tau}^{-1} \exp\{-t/\bar{\tau}\}. \tag{3.1}$$

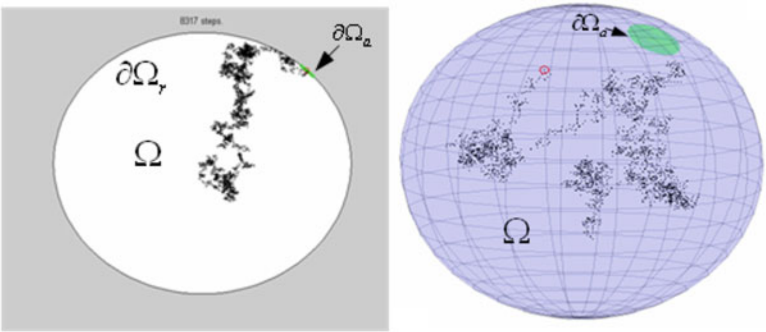

Fig. 3.5 *Left*: Brownian motion in a circular disk whose boundary is reflecting, except for a short absorbing arc $\partial\Omega_a$ (marked *green*). *Right*: Brownian motion on the surface of a decapitated sphere. The circumference of the spherical cap (marked *green*) is the absorbing boundary $\partial\Omega_a$

The exponential rate $\bar{\tau}^{-1}$ is therefore the flux into the absorbing target. In the case of crossing from one compartment to another through a narrow neck the crossing rate is $1/2\bar{\tau}$, where $\bar{\tau}$ is the MFPT to the stochastic separatrix between the compartments. The latter is the locus of initial points of a Brownian trajectory from which it ends up in one compartment or the other with equal probabilities (Schuss 2010a).

3.2.2 *The MFPT and the Survival Probability*

We consider again a compartment Ω whose boundary $\partial\Omega$ consists of a part $\partial\Omega_r$ that is impermeable to Brownian trajectories, such as a cell membrane, and a small part $\partial\Omega_a$ that absorbs them (see Figs. 3.5, 3.6, 3.7, 3.8). The MFPT $\bar{\tau}(\boldsymbol{x})$ from $\boldsymbol{x} \in \Omega$ to $\partial\Omega_r$ is the solution of the mixed boundary value problem (1.4)–(1.6), which we rewrite for convenience as

$$D\Delta\bar{\tau}(\boldsymbol{x}) = -1 \quad \text{for } \boldsymbol{x} \in \Omega \tag{3.2}$$

$$\frac{\partial\bar{\tau}(\boldsymbol{x})}{\partial n} = 0 \quad \text{for } \boldsymbol{x} \in \partial\Omega_r \tag{3.3}$$

$$\bar{\tau}(\boldsymbol{x}) = 0 \quad \text{for } \boldsymbol{x} \in \partial\Omega_a, \tag{3.4}$$

where D is the diffusion coefficient and $\boldsymbol{n}$ is the unit outer normal to the boundary (Schuss 2010b). The system (3.2)–(3.4) follows from the backward Kolmogorov equation (Schuss 2010b) (the adjoint of the Fokker–Planck equation) for the transition probability density function $p(\boldsymbol{y}, t \,|\, \boldsymbol{x})$ of the Brownian trajectories,

$$\frac{\partial p(\boldsymbol{y}, t \,|\, \boldsymbol{x})}{\partial t} = D\Delta_{\boldsymbol{x}} p(\boldsymbol{y}, t \,|\, \boldsymbol{x}) \quad \text{for } \boldsymbol{x}, \boldsymbol{y} \in \Omega \tag{3.5}$$

$$\frac{\partial p(\boldsymbol{y}, t \,|\, \boldsymbol{x})}{\partial n_{\boldsymbol{x}}} = 0 \quad \text{for } \boldsymbol{y} \in \Omega, \boldsymbol{x} \in \Omega_r \tag{3.6}$$

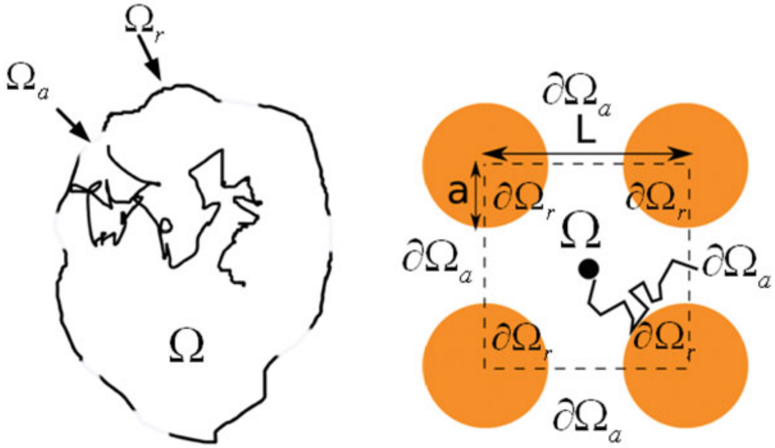

Fig. 3.6 Brownian trajectory inside a compartment containing well-separated absorbing windows. *Left*: the reflecting boundary $\partial\Omega_r$ consists of arcs and the absorbing boundary $\partial\Omega_a$ consists of well-separated small absorbing windows. *Right*: the domain Ω is the *white area inside the dashed square*. The absorbing boundary $\partial\Omega_a$ consists of the four segments of length L. The reflecting boundary $\partial\Omega_r$ consists of the four arcs of the *orange disks*

Fig. 3.7 A composite domain consists of a bulky head Ω_1 connected by a funnel to a narrow neck Ω_2 at an interface $\partial\Omega_i = \boldsymbol{AB}$. The entire boundary is reflecting for Brownian motion, except for a small absorbing window $\partial\Omega_a$ at the end $\boldsymbol{CD}$ of the neck Ω_2

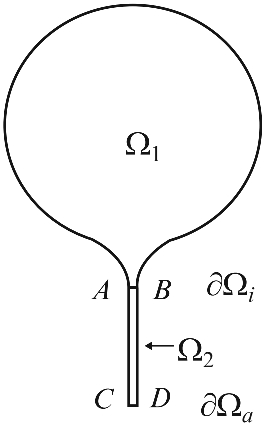

$$p(\boldsymbol{y}, t \,|\, \boldsymbol{x}) = 0 \quad \text{for } \boldsymbol{y} \in \Omega, \boldsymbol{x} \in \Omega_a \tag{3.7}$$

$$p(\boldsymbol{y}, 0 \,|\, \boldsymbol{x}) = \delta(\boldsymbol{y} - \boldsymbol{x}) \quad \text{for } \boldsymbol{x}, \boldsymbol{y} \in \Omega. \tag{3.8}$$

The survival probability of Brownian trajectories that start at $\boldsymbol{x} \in \Omega$ is

$$\Pr\{\tau > t \,|\, \boldsymbol{x}\} = \int\limits_{\Omega} p(\boldsymbol{y}, t \,|\, \boldsymbol{x})\, d\boldsymbol{y} \tag{3.9}$$

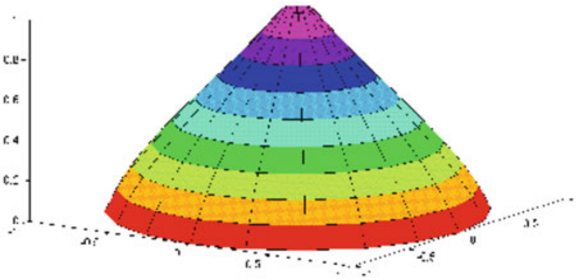

Fig. 3.8 $\partial\Omega_a$ is an opening at the end of a funnel of finite angle [see Fig. 2.1(right)]

and its mean value is

$$\mathbb{E}[\tau \,|\, \boldsymbol{x}(0) = \boldsymbol{x}] = \bar{\tau}(\boldsymbol{x}) = \int\limits_0^\infty \Pr\{\tau > t \,|\, \boldsymbol{x}\}\, dt. \tag{3.10}$$

It follows from (3.5) and (3.8) that

$$D\Delta\bar{\tau}(\boldsymbol{x}) = \int\limits_0^\infty D\Delta_{\boldsymbol{x}} \Pr\{\tau > t \,|\, \boldsymbol{x}\}\, dt = \int\limits_0^\infty \int\limits_\Omega \frac{\partial p(\boldsymbol{y}, t \,|\, \boldsymbol{x})}{\partial t}\, d\boldsymbol{y}\, dt = -1. \tag{3.11}$$

The Neumann and Dirichlet boundary conditions (3.3) and (3.4) are inherited from (3.6) and (3.7), respectively. Asymptotic expansions of the solution to (3.2)–(3.4) are constructed in Chap. 1 above.

3.3 Geometrical Classification of Cellular Domains

The determination of cell function from its known structure relies on the geometrical properties of the structure. Specifically, the geometry of small targets and narrow passages is the determinant of the diffusion influx and efflux of ions and molecules between cellular compartments or on cellular membranes. These can be determined analytically by calculating the MFPT of two- and three-dimensional Brownian trajectories from compartments to small targets.

The MFPT of two-dimensional Brownian motion on a membrane surface is described by the two-dimensional version (1.18)–(1.20) of the boundary value problem (3.2)–(3.4). The boundary of a surface compartment consists of a curve that reflects Brownian trajectories on the surface and a small absorbing curve at which trajectories are terminated. The physical domain Ω can be represented in parameter space as a planar domain, which we again denote Ω, whose boundary $\partial\Omega$ consists of an impermeable curve $\partial\Omega_r$ and a small opening for the passage of trajectory, which is a short curve $\partial\Omega_a$, at which trajectories are terminated in the sense that once a Brownian trajectory exits Ω through $\partial\Omega_a$ it does not return to Ω within the observation time (Fig. 3.5).

The small absorbing window $\partial\Omega_a$ studied here can be classified as follows:

1. $\partial\Omega_a$ is a short part of the smooth boundary curve $\partial\Omega$ [Figs. 1.1 and 3.5(left)].
2. $\partial\Omega_a$ can be placed at a corner (Fig. 1.4) or at a cusp (Fig. 1.5).
3. $\partial\Omega_a$ can be placed at the end of a cusp-shaped funnel of the boundary (Figs. 2.1(left), 3.6(right), or 3.7, or the surface of revolution in Fig. 2.2(right), obtained by rotating it about its axis of symmetry).
4. The compartment Ω can consist of a bulky head connected to an essentially one-dimensional cylinder of small radius a and length L, as is the case of a neuronal spine membrane [see Fig. 3.7(left)].
5. More complicated structures are formed by joining two or more bulky heads by short or long narrow strips or cylinders [dumbbell-shaped domains, see Fig. 3.7(right)]. The former can be formed on a spine membrane that contains closely bunched obstacles, such as pickets, fences, non-interacting molecules, actin filaments, and so on, between which a diffusing receptor has to squeeze on its way to the PSD (Fig. 3.6). In this case the effective motion of the diffusing receptor is dominated by the mean time $\bar{\tau}$ to squeeze through the narrow straits formed by the obstacles (see Sect. 4.3).
6. A collection of well-separated windows (Fig. 3.6).

In the context of the above classification, we define the following categories of narrow escape problems for solid structures with a small absorbing window $\partial\Omega_a$:

1. $\partial\Omega_a$ is a circular disk on a regular boundary $\partial\Omega$ [Fig. 3.5(right) of a decapitated ball (Fig. 1.6) with an absorbing disk (marked green) in Fig. 3.5(right)].
2. $\partial\Omega_a$ is a disk at the end of a funnel, as in Fig. 2.2(right) (e.g., obtained by rotating Fig. 2.1(left) about its axis of
3. $\partial\Omega_a$ is a disk at the end of a narrow cylindrical neck (e.g., obtained by rotating Fig. 3.7(left) about its axis of symmetry).
4. In dumbbell-shaped structures, obtained by rotating Fig. 3.7(right) about its axis of symmetry, the middle surface is a small target. A key quantification is given by the principal eigenvalue of the Laplace equation.
5. Leakage through a small window in a structure that conducts Brownian particles from a source to a relatively large absorbing part of the boundary and the particles can leak out through small absorbing windows in the reflecting part of the boundary. This is the case, for example, of the synaptic cleft that conducts neurotransmitter molecules, released from a vesicle at the presynaptic terminal, either to receptors in the post-synaptic distribution on the spine membrane or to the surrounding glia cells [Fig. 3.9(left)]. The structure of the cleft is approximately a short cylinder with a source of Brownian particles in one of the impermeable bases, small absorbing windows in the other impermeable base, and absorbing lateral envelop. Another example is that of calcium leakage through channels in the spine neck that conducts calcium to the absorbing end at the dendrite [Fig. 3.9(right)].

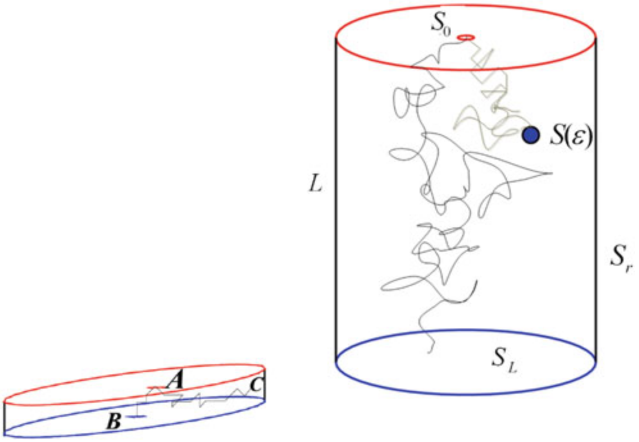

Fig. 3.9 *Left*: a schematic model of the synaptic cleft Figs. 3.2(right) and 3.3. *Right*: a schematic model of the spine neck as a conductor of diffusion flux [Fig. 3.3(left) and $\partial\Omega_2$ in Fig. 3.7(left)]. A Brownian trajectory enters a cylindrical neck (e.g., of a neuronal spine) at a source S_0 and can leak through a small window $S(\varepsilon)$ (e.g., a pump) or reach the absorbing bottom $\partial\Omega_a = S_L$ (e.g., the dendritic shaft)

6. $\partial\Omega_a$ consists of a number of well-separated absorbing windows [Fig. 3.6(left)]. The absorbing windows can be at regular a boundary [Fig. 3.5(right)] or at the ends of funnels [Fig. 3.7(left) with several necks].

As shown in Chap. 1, the MFPT to the small absorbing target or through the narrow neck depends strongly on the detailed geometrical features of the listed types of compartments and their connections to necks. Differences of orders of magnitude in the MFPTs through a neck can arise between necks connected to the head at an angle or smoothly by a funnel. The local curvature of the connection can change $\bar{\tau}$ by orders of magnitude.

3.3.1 The Formula for the NET $\bar{\tau}$

The analytical expression for the MFPT $\bar{\tau}$ strongly depends on the geometrical features of the compartment. It thereby defines time scales of diffusion influx (respectively efflux) to (respectively from) the compartment, which can be interpreted as regulation of the flux. Thus the analytical asymptotic approximation to $\bar{\tau}$ expresses the influence of geometrical structure on cellular functions that consist in controlling diffusion fluxes.

The asymptotic formulas for $\bar{\tau}$ can be classified according to the local geometry of the compartment near the absorbing sites or narrow passages, which are the main controllers of the diffusion flux. Obviously, the formulas in two-dimensional compartments are different than in three-dimensional ones.

3.3.2 Formulas for Two-Dimensional Domains

The MFPT from a domain Ω in the plane to a small sub arc $\partial\Omega_a$ (of length a) of the boundary $\partial\Omega$, according to the classification in Sect. 3.3, is given by

1. For type (I) $\partial\Omega_a$ is a sub-arc of a smooth boundary [see the schematic Figs. 1.1 and 3.5(left)]. The MFPT from any point $\boldsymbol{x}$ in Ω to $\partial\Omega_a$ is denoted $\bar{\tau}_{\boldsymbol{x}\to\partial\Omega_a}$. This is due to the fact that for

$$\varepsilon = \frac{\pi|\partial\Omega_a|}{|\partial\Omega|} = \frac{\pi a}{|\partial\Omega|} \ll 1 \tag{3.12}$$

   the MFPT is independent of $\boldsymbol{x}$ outside a small vicinity of $\partial\Omega_a$ (called a boundary layer). According to Theorem 1.4.1, for $\boldsymbol{x} \in \Omega$, outside a boundary layer near $\partial\Omega_a$,

$$\bar{\tau}_{\boldsymbol{x}\to\partial\Omega_a} = \frac{|\Omega|}{\pi D}\ln\frac{1}{\varepsilon} + O(1), \tag{3.13}$$

   where $O(1)$ depends on the initial distribution of $\boldsymbol{x}$ (Ward and Keller 1993; Singer et al. 2006b). In particular, if Ω is a disc of radius R, then for $\boldsymbol{x}$ at the center of the disk,

$$\bar{\tau}_{\boldsymbol{x}\to\partial\Omega_a} = \frac{R^2}{D}\left[\log\frac{R}{a} + 2\log 2 + \frac{1}{4} + O(\varepsilon)\right],$$

   and averaging with respect to a uniform distribution of $\boldsymbol{x}$ in the disk

$$\bar{\tau} = \frac{R^2}{D}\left[\log\frac{R}{a} + 2\log 2 + \frac{1}{8} + O(\varepsilon)\right].$$

   Formula (3.13) indicates that the flux through a hole in a smooth wall on a flat membrane surface (e.g., a corral) is regulated by the following parameters, the area $|\Omega|$ inside the wall, the diffusion coefficient D, and the aspect ratio ε (3.12).

   In the case of Brownian motion on a sphere of radius R the MFPT to an absorbing circle centered on the north-south axis near the south pole with small radius $a = R\sin\delta/2$ [see the schematic Figs. 1.6 and 3.5(right)], is given in Sect. 1.4.2 by (1.38) as

$$\bar{\tau} = \frac{2R^2}{D}\log\frac{\sin\frac{\theta}{2}}{\sin\frac{\delta}{2}},$$

   where θ is the angle between $\boldsymbol{x}$ and the south-north axis of the sphere
2. For type (II), if the absorbing window is located at a corner of angle α (Fig. 1.4), then, according to Sect. 1.4.1,

$$\bar{\tau} = \frac{|\Omega|_g}{D\alpha}\left[\log\frac{1}{\varepsilon} + O(1)\right], \tag{3.14}$$

where $|\Omega|_g$ is the surface area of the domain on the curved surface, calculated according to the Riemannian metric on the surface [see (1.21), (1.22), and Singer et al. 2006c]. Formula (3.14) indicates that control of flux is regulated also by the access to the absorbing window afforded by the angle of the corner leading to the window (see Fig. 1.4).

3. For type (III), if the absorbing window is located at a cusp (see Fig. 1.5), then the NET $\bar{\tau}$ grows algebraically, rather than logarithmically. Thus, in the domain bounded between two tangent circles, the expected lifetime is given in (1.32) (see Sect. 1.4.1) as

$$\bar{\tau} = \frac{|\Omega|}{(d^{-1}-1)D}\left(\frac{1}{\varepsilon} + O(1)\right), \tag{3.15}$$

where $d < 1$ is the ratio of the radii. Formula (3.15) indicates that a drastic reduction of flux can be achieved by putting an obstacle that limits the access to the absorbing window by forming a cusp-like passage [see Fig. 2.2(left)].

4. For type (IV), when $\partial\Omega_a$ (of length a) is at the end of a narrow neck with radius of curvature R_c [see the schematics Fig. 1.2(left) and Fig. 2.1], the MFPT is given in Theorem 2.1.1 as

$$\bar{\tau} = \frac{|\Omega|}{4D\sqrt{2a/R_c}}(1 + O(1)) \quad \text{for } a \ll |\partial\Omega|. \tag{3.16}$$

The MFPT to the narrow straits formed by a partial block of a planar domain [see Fig. 2.2(left)] is given in Theorem 2.1.1 as

$$\bar{\tau} = \sqrt{\frac{R_c(R_c + r_c)}{2r_c\varepsilon}}\,\frac{\pi|\,\Omega|}{2D}(1 + o(1)) \quad \text{for } \varepsilon \ll |\partial\Omega_a|, R_c, r_c, \tag{3.17}$$

where R_c and r_c are the curvatures at the neck and ε is the width of the straits.

For the surface of revolution in Fig. 2.2(right), generated by rotating the curve in Fig. 2.1(left) about its axis of symmetry, we use the representation of the generating curve

$$y = r(x),\ \Lambda < x < 0,$$

where the x-axis is horizontal with $x = \Lambda$ at the absorbing end $\boldsymbol{AB}$. We assume that the parts of the curve that generate the funnel have the form

$$\begin{aligned} r(x) &= O(\sqrt{|x|}) \ \text{ near } x = 0 \\ r(x) &= a + \frac{(x-\Lambda)^{1+\nu}}{\nu(1+\nu)\ell^{\nu}}(1 + o(1)) \ \text{ for } \nu > 0 \text{ near } x = \Lambda, \end{aligned} \tag{3.18}$$

where $a = \frac{1}{2}\overline{\boldsymbol{AB}} = \varepsilon/2$ is the radius of the gap, and the constant ℓ has dimension of length. For $\nu = 1$ the parameter ℓ is the radius of curvature R_c at $x = \Lambda$. The MFPT from the head to the absorbing end $\boldsymbol{AB}$ is given by

$$\bar{\tau} \sim \frac{\mathcal{S}(\Lambda)}{2D} \frac{\left(\dfrac{\ell}{(1+\nu)a}\right)^{\nu/1+\nu} \nu^{1/1+\nu}}{\sin \dfrac{\nu\pi}{1+\nu}}, \tag{3.19}$$

where $\mathcal{S}$ is the entire unscaled area of the surface. In particular, for $\nu = 1$ the MFPT (3.19) reduces to

$$\bar{\tau} \sim \frac{\mathcal{S}}{4D\sqrt{a/2\ell}} \tag{3.20}$$

[compare to (1.38)]. The case $\nu = 0$ corresponds to a conical funnel with an absorbing circle of small radius a (see Fig. 3.8). Equation (3.20) for a sphere reduces to (1.38) [see Figs. 1.6 and 3.5(right)]. Formulas (3.16)–(3.20) indicate that efficient control of the flux can be achieved by putting the absorbing window at the end of a narrow symmetric or asymmetric funnel [see Figs. 2.1 and 2.2(right)]. This type of funnel can be formed by crowding obstacles on the membrane surface (Fig. 4.4a below), which results in an effective coarse-grained diffusion coefficient on the surface, different from the microscopic diffusion coefficient (see Sect. 4.3 below).

5. In domains of type (V) a bulky head is connected to an essentially one-dimensional strip (or cylinder) of small radius a and length L, as is the case of a neuronal spine membrane. The connection of the head to the neck can be at an angle or by a smooth funnel [Figs. 3.4 and 3.7(left)], the narrow cylindrical neck is Ω_2. The boundary of the domain is impermeable to Brownian trajectories and only the end of the cylinder $\partial\Omega_a$ absorbs them. In the three-dimensional case the Dirichlet boundary $\partial\Omega_a$ is a small absorbing disk at the end of the cylinder. The domain Ω_1 is the one shown in Fig. 2.1 and it is connected to the cylinder at an interface $\partial\Omega_i$, which in this case is the interval AB in Fig. 2.1. Theorem 2.1.2 gives the MFPT from $\boldsymbol{x} \in \Omega_1$ to $\partial\Omega_a$ as (2.28), that is,

$$\bar{\tau}_{\boldsymbol{x}\to\partial\Omega_a} = \bar{\tau}_{\boldsymbol{x}\to\partial\Omega_i} + \frac{L^2}{2D} + \frac{|\Omega_1|L}{|\partial\Omega_a|D}.$$

   Figure 3.10 shows that the smoothness of the neck connection makes a big difference in the MFPT. Formula (2.28) explains the role of a narrow neck in flux regulation. The flux dependence on the neck length is quite strong.

6. A dumbbell-shaped domain [of type (VI)] consists of two compartments Ω_1 and Ω_3 and a connecting neck Ω_2 that is effectively one-dimensional, such as shown in Fig. 3.7(right), or in a similar domain with a long neck. A Brownian

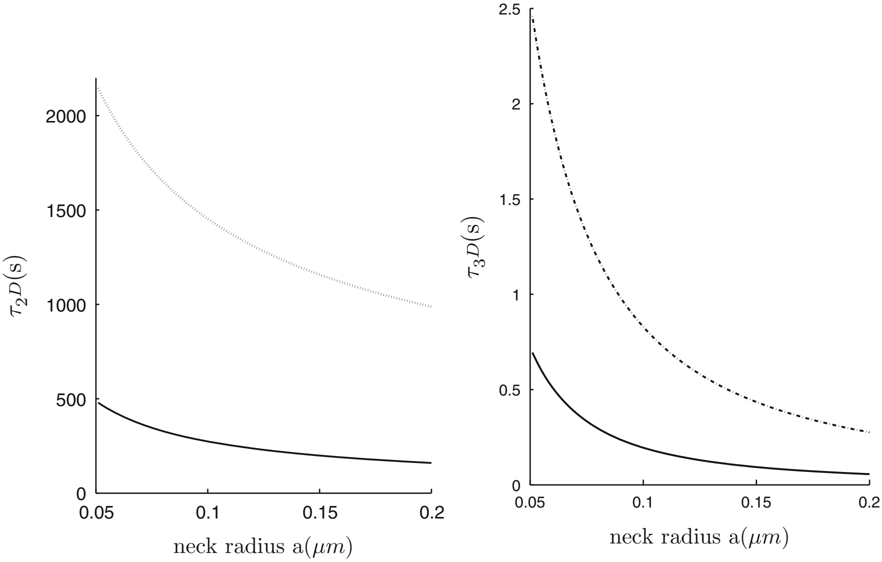

Fig. 3.10 *Left*: the NET of Brownian motion on the surface of revolution in Fig. 2.2(right), obtained by revolving one of the curves in Fig. 3.4 about its axis of symmetry. *Right*: the NET in the corresponding solids of revolution. The smoothness of the connection makes a big difference

trajectory that hits the segment $\boldsymbol{AB}$ in the center of the neck Ω_2 is equally likely to reach either compartment before the other; thus, $\boldsymbol{AB}$ is the stochastic separatrix (SS). Therefore the mean time to traverse the neck from compartment Ω_1 to compartment Ω_3 is asymptotically twice the MFPT $\bar{\tau}_{\Omega_1\to SS}$. Neglecting, as we may, the mean residence time of a Brownian trajectory in Ω_2 relative to that in Ω_1 or in Ω_3 we can write the transition rates from Ω_1 to the Ω_3 and vv as

$$\lambda_{\Omega_1\to\Omega_3} = \frac{1}{2\bar{\tau}_{\Omega_1\to SS}}, \quad \lambda_{\Omega_3\to\Omega_1} = \frac{1}{2\bar{\tau}_{\Omega_3\to SS}}. \tag{3.21}$$

These rates can be found from the explicit expression (3.1) for the flux into an absorbing window

$$\lambda_1 \sim \frac{1}{\bar{\tau}}, \tag{3.22}$$

where $\bar{\tau}$ is given in (2.28). Here $\bar{\tau}_{\boldsymbol{x}\to\partial\Omega_i}$ is any one of the MFPTs given above, depending on the geometry of Ω_1 with L half the length of the neck and with $SS = \partial\Omega_a$. The radii of curvature $R_{c,1}$ and $R_{c,3}$ at the two funnels may be different in Ω_1 and Ω_3. The smallest positive eigenvalue λ of the Neumann problem for the Laplace equation in the dumbbell is to leading order $\lambda = -(\lambda_{\Omega_1\to\Omega_3} + \lambda_{\Omega_3\to\Omega_1})$. For example, if the solid dumbbell consists of two general heads connected smoothly to the neck by funnels [see (3.27)], then Theorem 2.2.2 implies that the two rates are given by

$$\frac{1}{\lambda_{\Omega_1\to\Omega_3}} = \sqrt{2}\left[\left(\frac{R_{c,1}}{a}\right)^{3/2}\frac{|\Omega_1|}{R_{c,1}D}\right](1+o(1)) + \frac{L^2}{4D} + \frac{|\Omega_1|L}{\pi a^2 D}$$

$$\frac{1}{\lambda_{\Omega_3\to\Omega_1}} = \sqrt{2}\left[\left(\frac{R_{c,3}}{a}\right)^{3/2}\frac{|\Omega_3|}{R_{c,3}D}\right](1+o(1)) + \frac{L^2}{4D} + \frac{|\Omega_3|L}{\pi a^2 D}. \tag{3.23}$$

Formulas (3.23) indicate that the unidirectional fluxes between the two compartments of a dumbbell-shaped domain can be controlled by the area (or surface area) of the two and by the type of obstacles to the access to the connecting neck. The equilibration rate in the dumbbell, λ, is thus controlled by the geometry.

7. The mean time to escape through N well-separated absorbing windows of lengths a_j at the ends of funnels with radii of curvature ℓ_j, respectively, in the boundary $\partial\Omega$ of a planar domain Ω is given by (2.107) as

$$\bar{\tau} = \frac{\pi|\Omega|}{2D\sum_{j=1}^{N}\sqrt{a_j/\ell_j}}(1+o(1)) \quad \text{for } a_j/\ell_j \ll |\partial\Omega|. \tag{3.24}$$

The probability to escape through window i is given by (2.108) as

$$p_i = \frac{\sqrt{a_i/\ell_i}}{\sum_{j=1}^{N}\sqrt{a_j/\ell_j}}. \tag{3.25}$$

Formulas (3.24) and (3.25) are significant for diffusion in a network of compartments connected by narrow passages (e.g., on a membrane strewn with obstacles). The dependence of the MFPT $\bar{\tau}$ and of the transition probabilities p_i on the local geometrical properties of the compartments renders the effective diffusion tensor in the network position-dependent and can give rise to anisotropic diffusion.

8. If the domain contains a deep potential trap the Brownian trajectory can be in any one of the following three states: trapped in the well, diffusing in the domain outside the well, and be absorbed in the small absorbing window. The MFPT to the window was calculated in Sect. 1.9.3.

3.3.3 Formulas for $\bar{\tau}$ in Three-Dimensional Domains

The interpretation of the formulas for the cases (1)–(6) is much the same as for the two-dimensional case.

1. The MFPT to a circular absorbing window $\partial\Omega_a$ of small radius a centered at $\mathbf{0}$ on the boundary $\partial\Omega$ is given in Theorem 1.6.1 as

$$\bar{\tau}_{\boldsymbol{x}\to\partial\Omega_a} = \frac{|\Omega|}{4aD\left[1+\dfrac{L(\mathbf{0})+N(\mathbf{0})}{2\pi}a\log a + o(a\log a)\right]}, \tag{3.26}$$

   where $L(\mathbf{0})$ and $N(\mathbf{0})$ are the principal curvatures of the boundary at the center of $\partial\Omega_a$.
2. The MFPT from the head of the solid of revolution in Fig. 2.2(right), obtained by rotating the symmetric domain in Fig. 2.1(left) about its axis of symmetry, to a small absorbing window $\partial\Omega_a$ at the end of a funnel is given in Theorem 2.2.2 by

$$\bar{\tau} = \frac{1}{\sqrt{2}}\left(\frac{R_c}{a}\right)^{3/2}\frac{|\Omega|}{R_cD}(1+o(1)) \text{ for } a \ll R_c, \tag{3.27}$$

   where R_c is the radius of curvature of the rotated curve at the end of the funnel.
3. The MFPT from a point $\boldsymbol{x}$ in a bulky head Ω to an absorbing disk $\partial\Omega_a$ of a small radius a at the end of a narrow neck of length L, connected to the head at an interface $\partial\Omega_i$ is given by the connection formula (2.28). When the cylindrical neck is attached to the head at a right angle the interface $\partial\Omega_i$ is a circular disk and $\bar{\tau}_{\boldsymbol{x}\to\partial\Omega_i}$ is given by (3.26). When the neck is attached smoothly through a funnel, $\bar{\tau}_{\boldsymbol{x}\to\partial\Omega_i}$ is given by (3.27).
4. The mean time to escape through N well-separated absorbing circular windows or radii a_j at the ends of funnels with curvatures ℓ_j, respectively, is given in Sect. 2.1.1 as

$$\bar{\tau} = \frac{1}{\sqrt{2}}\frac{|\Omega|}{D\sum_{j=1}^{N}\ell_j\left(\dfrac{a_j}{\ell_j}\right)^{3/2}} \tag{3.28}$$

   and the exit probability through window i is given by

$$p_i = \frac{{a_i}^{3/2}\ell_i^{-1/2}}{\sum_{j=1}^{N}{a_j}^{3/2}\ell_j^{-1/2}}. \tag{3.29}$$

5. The principal eigenvalue of the Laplace equation in a dumbbell-shaped structure is given in Eqs. (2.110)–(2.112) above.
6. The leakage flux through a circular hole of small radius a centered at $\mathbf{0}$ in the reflecting boundary is given in Sect. 1.9 as

$$J_a = 4aDu_0(\mathbf{0}) + O\left(\frac{a^2}{|\Omega|^{2/3}}\log\frac{a}{|\Omega|^{1/3}}\right), \tag{3.30}$$

where $u_0(\mathbf{0})$ is the concentration of diffusers at the window in the same model without the absorbing window.

7. The MFPT to a two-dimensional ribbon of width ε separating spherical membranes of radii $R_1 \ll R_2$ (see Fig. 2.8 and in the notation of Sect. 2.3) is given by (2.130) as

$$\mathbb{E}[\tau \mid r, z, \theta] = \frac{\text{vol}(\Omega)}{4D\varepsilon}\left(1 + O\left(\frac{\varepsilon}{R_2}\right)\right). \tag{3.31}$$

3.4 Annotations

It was shown in Harris and Stevens (1988), Bourne and Harris (2008), Korkotian et al. (2004), Hotulainen and Hoogenraad (2010), and Newpher and Ehlers (2009) that spine geometrical shapes correlate with their physiological functions. It was also shown by serial electron microscopy and three-dimensional reconstruction of dendritic spines from Purkinje spiny branchlets of normal adult rats that spine geometry relates to synaptic efficacy (Harris and Stevens 1988). In Papa and Segal (1996), Collin et al. (1997), and Korkotian and Segal (1999) it was shown that change of spine morphology can be induced by synaptic potentiation protocols and indeed, intracellular signaling, such as calcium release from stores, alters the morphology of dendritic spines in cultured hippocampal neurons. These changes in geometry can affect the spine-dendrite communication. One of the first quantitative assessments of geometry was obtained by a direct measurement (Svoboda et al. 1996) of diffusion through the spine neck. Concentration gradients between spines and shafts in rat CA1 pyramidal neurons were established by photo-bleaching and photo-release of fluorescein dextran in order to track the time course of re-equilibration. It was well approximated by a single exponential decay, with a time constant in the range of 20–100 ms. The role of the spine neck was further investigated experimentally with flash photolysis of caged calcium in Korkotian et al. (2004) and Bloodgood and Sabatini (2005) and theoretically in Holcman et al. (2005a), with the main conclusion that geometrical changes in the spine neck, such as the length or the radius, are key modulators of calcium dynamics in the process of spine-dendrite communication (Holcman et al. 2005b; Biess et al. 2007; Holcman and Kupka 2010).

The connection between the head and the neck is relevant both to three-dimensional diffusion in the bulk and to two-dimensional surface diffusion. Indeed, synaptic transmission and plasticity involve the trafficking of receptors on cell membranes (Chen et al. 2000; Bredt and Nicoll 2003; Adesnik et al. 2005; Shi et al. 1999; Malinow and Malenka 2002; Malinow 2003), such as AMPA or NMDA glutamatergic receptors, which mediate the post-synaptic current. The number and type of receptors that shape the synaptic current (Bredt and Nicoll 2003) could be regulated by spine geometry. Regulation of synaptic current by spine geometry was explored theoretically by using asymptotic expressions for the residence time (Earnshaw and Bressloff 2006; Holcman and Triller 2006), and experimentally by monitoring the motion of AMPA receptors on the surface of mature neurons (Ashby et al. 2006). A recent review of early results on the NET problem with many biological applications is given in Bressloff and Newby (2013).

Chapter 4
Applications to Cellular Biology and Simulations

Some applications of the analytical approximations to the MFPT are listed below. The formulas quantify the structures and predict their functions. They are also used to verify the validity of large Brownian simulations, such as the ones used for predicting the synaptic current.

4.1 Applications to Brownian Dynamics Simulations

Brownian dynamics simulations of rare events are difficult and inefficient. Thus predicting the diffusion current through narrow passages from a simulation is often impossible, because the sample of simulated Brownian trajectories passing through the opening is too small for any significant statistic. However, analytical approximations may give reliable information where simulations fail. For example, the bottleneck in simulations of ionic permeation in protein channels is the arrival of ions from the salt solution to the channel. The arrival rate at a given small neighborhood of the channel can be calculated analytically and used in the simulation of the permeation process.

A similar situation arises in the simulation of the entire synaptic transmission process, which contains the simulation of the arrival of neurotransmitter molecules at receptors on the post-synaptic membrane. A significant reduction of the simulation complexity is achieved by using the analytically computed neurotransmitter flux rather than simulating it. Analytical formulas are also used for quantifying diffusion in dendritic spines. Further progress is achieved by modeling and simulating chemical reactions as Markov processes rather than as complex Brownian dynamics. Indeed, using the fact that the stationary arrival process of Brownian particles from the continuum to an absorbing boundary is Poissonian, it is possible to coarse-grain the binding and unbinding process of Brownian particles in microdomains into a Markov jump process, thus opening the way for a complete analysis of

D. Holcman, Z. Schuss, *Stochastic Narrow Escape in Molecular and Cellular Biology*, DOI 10.1007/978-1-4939-3103-3_4

stochastic chemical reactions, which is impossible by simulating complex reaction-diffusion equations that in general cannot be solved analytically and are hard to solve numerically. A recent application of this Markovian approximation gives new range for the rate of molecular dynamics underlying the spindle assembly checkpoint during cell division (see Sect. 6.2.1).

Another application of asymptotic analytical results is the verification of molecular dynamics simulations in domains that contain small passages or targets. The convergence of the simulation can be measured by the convergence of the statistics of rare events to the statistics predicted by the analytical asymptotic approximation for dendritic spines (see Sect. 3.3).

4.2 Diffusion in the Synaptic Cleft

The neuronal cleft conducts neurotransmitters by diffusion from a vesicle released at the excitatory presynaptic membrane to receptors such as NMDA and AMPA on the postsynaptic membrane [Figs. 3.2(right) and 3.3]. Synaptic transmission depends on various parameters such as the location of a released vesicle, the number and type of receptors, trafficking between the post-synaptic density (PSD), and extra-synaptic compartments, as well as the synapse organization. It is now possible to quantify separately each of them by Brownian simulations and by mixed analytical approaches. These can lead to better understanding of pathological synapses, implicated in many cognitive disorders such as spectral autism disorders, epilepsy, and many others. For example, using a combination of simulations and electrophysiological recordings, it was possible to reduce the number of released neurotransmitters, when ketone bodies were used in the physiological preparation, which mimics starvation or the effect of ketogenic diet.

In the mathematical description of neurotransmitter diffusion in the synaptic cleft, the cleft geometry is simplified to a circular cylinder of length L and radius R, whose bases S_0 and S_L are centered at the z-axis, at $z = 0$ and $z = L$, respectively, and are parallel to the (x, y) plane. Neurotransmitters that are injected at S_0 with a constant flux density ϕ are absorbed at the lateral surface S_r, which is surrounded by glia cells [Figs. 3.3g and 3.9(left)]. A receptor is represented as a small absorbing circular hole $S(a)$ of radius a on S_L. Both S_0 and $S_L - S(a)$ are impermeable to the Brownian neurotransmitters. Changing the distance of the small hole $S(a)$ (receptor) to the center can control the flux through the hole. For a point source at $(z, r, \theta) = (0, 0, 0)$ (in cylindrical coordinates), the density at the other end $z = L$ is found in a straightforward manner to be

$$u_0(r, L, 0) = \sum_{m=1}^{\infty} \frac{LJ_0\left(\frac{\gamma_{0,m} r}{R}\right)}{D\pi R\gamma_{0,m} J_0'^2(\gamma_{0,m}) \sinh \frac{\gamma_{0,m} L}{R}}, \tag{4.1}$$

where $\gamma_{n,m}$ are the roots of the Bessel function $J_n(\cdot)$. The probability that a Brownian particle, injected at the source, will ever reach a receptor centered at $(r, L, 0)$ is the splitting probability that the time τ_{hole} to reach the absorbing window is shorter than the time τ_{S_r} to reach the lateral absorbing boundary (glia cells), given by

$$\Pr\{\tau_{\text{hole}} < \tau_{S_r}\} = \frac{4a}{\pi R} \sum_{m=1}^{\infty} \frac{J_0\left(\frac{\gamma_{0,m} r}{R}\right)}{\gamma_{0,m} J_0'^{\,2}(\gamma_{0,m}) \sinh \frac{\gamma_{0,m} L}{R}} + O\left(\frac{a^2}{L^2} \log \frac{a}{L}\right). \tag{4.2}$$

For $r = 0$ this reduces to

$$\Pr\{\tau_{\text{hole}} < \tau_{S_r}\} = \frac{4a}{\pi R} \sum_{m=1}^{\infty} \frac{1}{\gamma_{0,m} J_0'^{\,2}(\gamma_{0,m}) \sinh \frac{\gamma_{0,m} L}{R}} + O\left(\frac{a^2}{L^2} \log \frac{a}{L}\right). \tag{4.3}$$

The graph of (4.2) in Fig. 4.1 shows that a slight misalignment of the synaptic release or terminals may lead to a significant change in the number of neurotransmitters bound to receptors in the process of synaptic transmission. This suggests that a misalignment of the vesicular release with the receptor clustering can drastically reduce the number of open channels. This, in turn, can explain the key role of adhesion molecules such as the Ephrin B, which regulate the localization of AMPA receptors (see Dalva et al. 2007). Moreover, overexpression or knockdown of scaffolding molecules, such as PSD-95 in the postsynaptic cell, modulates presynaptic release probability, thus confirming the tight control of the release site compared to the accumulation of post-synaptic receptors (Futai et al. 2007).

This analysis of the physical model of the synaptic cleft reveals that changing the relative position of pre- and post-synaptic elements can drastically affect the open probability of receptors. The mathematical analysis of the physical model sheds

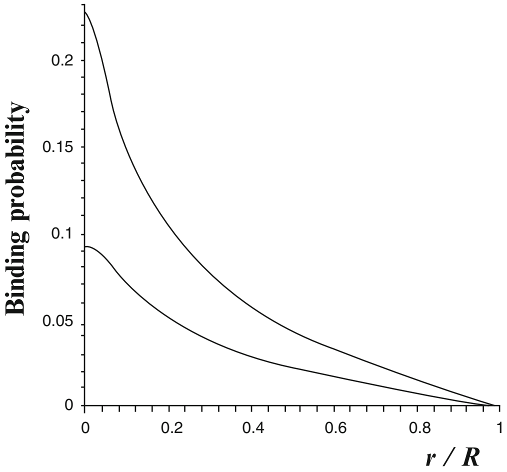

Fig. 4.1 The probability that a neurotransmitter molecule injected to the cleft at $(0, 0, 0)$ will reach an AMPA receptor at $(r, L, 0)$ is the probability that the time τ_{hole} to reach the absorbing window is shorter than the time τ_{S_r} to reach the lateral absorbing boundary (glia cells), according to (4.2) (see Fig. 3.3). $\varepsilon = 1$ nm, a single AMPAR in the PSD

some light on the complex electrophysiological data. Including additional synaptic components in the model may further clarify the specific role of adhesion molecules in controlling synaptic transmission. This includes glial transmitters or ATP.

Another application of the MFPT formula is to the homogenization of boundary conditions for problems with many binding sites on the boundary. The homogenized boundary conditions simplify complex molecular or Brownian dynamics simulations that include neurotransmitter release, binding to receptors, and flux through open channels.

4.2.1 *Leak of Ions from a Dendritic Spine Neck*

Although the function of dendritic spines is still unclear, one of their identified roles is to dynamically filter calcium ions. One mechanism to filter ions would be to extrude them from exchangers on the spine apparatus in the neck.

In the mathematical description of diffusion of calcium ions from the spine head to the dendrite, the spine neck is modelled as a circular cylinder of length L and radius R, whose bases S_0 and S_L are centered at the z-axis, at $z = 0$ and $z = L$, respectively, and are parallel to the (x, y) plane. The lateral surface S_r, which in general represents the internal membrane of the endoplasmic reticulum, is reflecting. A constant net flux ϕ is injected at S_0. A rapid exchanger is modeled as a small absorbing circular hole $S(a)$ of radius a on S_r, which may represent an ion pump [Fig. 3.9(right)]. The leakage formula (3.30) and the explicit expression $u(\mathbf{0}) = \phi(L - z)/\pi D R^2$, which replaces (4.1) in this case, give the flux through $S(a)$ as $J_a = 4a\phi(L - z)/\pi R^2$. It is thus possible to estimate the leak of any ion in the spine neck. Note that the asymptotic formula (1.143) holds if $\varepsilon \ll L/R$, so the source is outside the boundary layer near the hole.

4.3 Diffusion on a Membrane Crowded with Obstacles

The organization of a cellular membrane is to a large extent the determinant of the efficiency of molecular trafficking of receptors to their destination. The arrival rates of these molecules at their specific destinations control their role and performance, and thus steer the cell toward its function. After two decades of intense research on membrane organization, it is still unclear how the heterogeneity of the membrane controls diffusion (see Fig. 4.2). Recently, using single molecule tracking (Fig. 4.3), the diffusion coefficient of a molecule freely diffusing on intact and treated neuronal membranes, cleared of almost all obstacles was found. In this case the diffusion of a protein on the membrane is described by the Saffman–Delbrück theory. If, however, the membrane is crowded with obstacles, such as fixed proteins, fences and pickets, and so on, the effective diffusion coefficient differs significantly from that predicted in and depends strongly on the degree of crowding. The latter can be estimated from

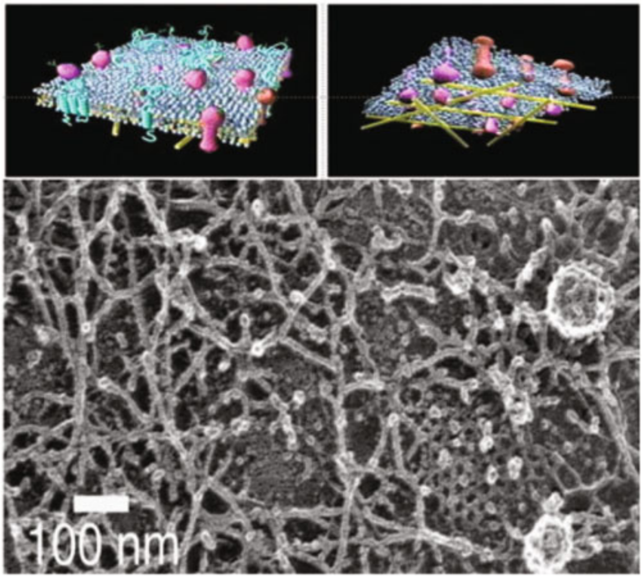

Fig. 4.2 Organization of a neuronal membrane (Kusumi et al. 2005) containing microdomains made of overlapping filaments (see schematic Fig. 4.4a)

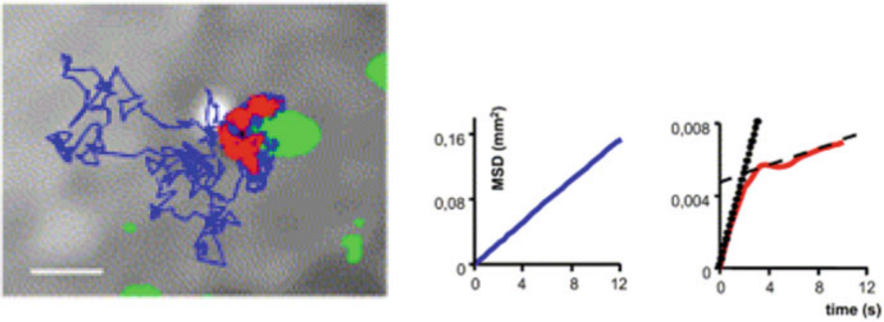

Fig. 4.3 *Left*: trajectories of receptors moving on a neuronal membrane (Triller and Choquet 2003). The trajectory switches between confined (*red*) and free (*blue*) periods. The synaptic domain is marked *green*. *Right*: mean square displacement (MSD) vs time without confinement and with confinement

diffusion data and from an appropriate model and its analysis, as explained below. The key to assessing the crowding is to estimate the local diffusion coefficient from the measured molecular trajectories and the analytic formula for the MFPT through a narrow passage between obstacles (Fig. 4.4).

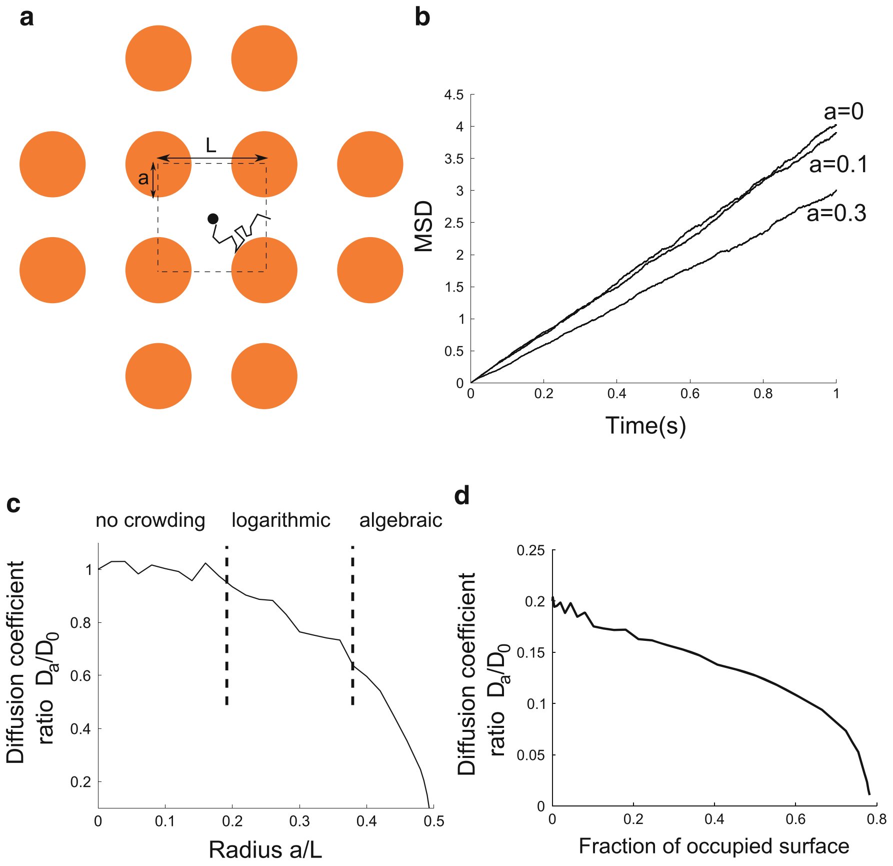

Fig. 4.4 (**a**) Schematic representation of a Brownian particle diffusing in a crowded microdomain. (**b**) Effective diffusion coefficient $\bar{D} = L^2/2\bar{\tau}$ as a function of time. (**c**) $\bar{D}$ for different radii of the obstacles. The three regions of $\bar{\tau}$ are separated by *dashed lines*. The *solid curve* represents Brownian simulations. While there is no crowding for $a < 0.2$, the decreasing of the effective diffusion coefficient for $0.2 < a < 0.4$ is logarithmic, and like square root for $a > 0.4$. (**d**) Effective diffusion coefficient vs fraction of occupied surface

4.3.1 A Coarse-Grained Model of Membrane Crowding Organization

A simplified model of a crowded membrane can be a square lattice of circular obstacles of radius a centered at the corners of lattice squares of side L (Fig. 4.4a). The mean exit time from a lattice box, formula (3.28), is to leading order independent of the starting position (x, y) and can be approximated by (2.20) as

$$\bar{\tau}_4 = \frac{\bar{\tau}}{4}, \tag{4.4}$$

where $\bar{\tau}$ is the MFPT to a single absorbing window in a narrow strait with the other windows closed (reflecting instead of absorbing). It follows that the waiting time in the cell enclosed by the obstacles is exponentially distributed (3.1) with rate

$$\lambda = \frac{2}{\bar{\tau}_4}, \tag{4.5}$$

where $\bar{\tau}$ is given by (3.14) and (3.17) as

$$\bar{\tau} \approx \begin{cases} c_1 \text{ for } 0.8 < \varepsilon < 1, \\ c_2|\Omega| \log \dfrac{1}{\varepsilon} + d_1 \text{ for } 0.55 < \varepsilon < 0.8, \\ c_3 \dfrac{|\Omega|}{\sqrt{\varepsilon}} + d_2 \text{ for } \varepsilon < 0.55, \end{cases} \tag{4.6}$$

with $\varepsilon = (L-2a)/a$ and $d_1, d_2 = O(1)$ for $\varepsilon \ll 1$ (see Fig. 4.5). The MFPT c_1 from the center to the boundary of an unrestricted square is computed from

$$u(x,y) = \frac{4L^2}{\pi^3 D}\sum_0^\infty \frac{\left[\cosh(k+\frac{1}{2})\pi - \cosh(k+\frac{1}{2})\pi(2y/L-1)\right]\sin(2k+1)\pi x/L}{(2k+1)^3\cosh(2k+1)\pi}, \tag{4.7}$$

so $c_1 = u(L/2, L/2) \approx [4L^2/\pi^3 D][\cosh(\pi/2 - 1)/\cosh\pi]$. For $L = 1, D = 1$, we find $c_1 \approx 0.076$, in agreement with Brownian dynamics simulations (Fig. 4.5b). The coefficient c_2 is obtained from (3.13) as $c_2 = 1/2\pi D \approx 0.16$. Similarly, the

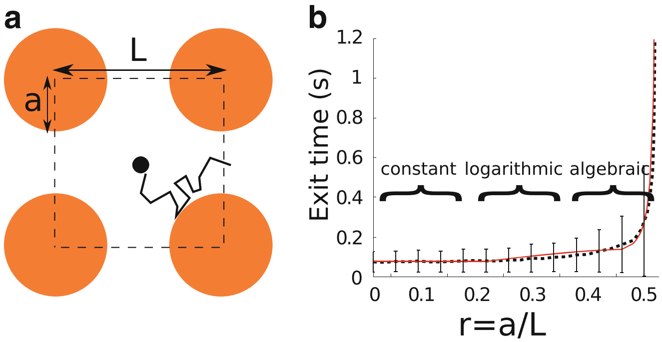

Fig. 4.5 MFPT vs scaled radius of obstacle in Fig. 3.6. NET from the domain **(a)** with $D = 1$, $L = 1$. Statistics were obtained from 1000 exit times/point of simulated Brownian trajectories (*dashed line*). **(b)** NET vs obstacle scaled radius $r = a/L = \frac{1}{2}(1-\varepsilon)$. The simulated (*dotted curve*) and analytical approximation (4.6) (*continuous curve*) for $0 < r = r_1 = 0.2$, $r_1 < r < r_2 = 0.45$, and $0.45 < r < 0.5$

coefficient c_3 is obtained from (3.16) as $c_3 \approx \pi/4\sqrt{2}D \approx 0.56$. The coefficients d_i are chosen by patching $\bar{\tau}$ continuously between the different regimes. We get

$$d_1 = c_1 + c_2|\Omega(r_1)|\log(1-2r_1), \tag{4.8}$$

and

$$\begin{aligned} d_2 = c_1 - c_2\left[|\Omega(r_1)|\log(1-2r_1) + |\Omega(r_2)|\log(1-2r_2)\right] \\ -c_3|\Omega(r_2)|(1-2r_2)^{-1/2}, \end{aligned}$$

where $|\Omega(r)| = L^2 - \pi r^2$. Simulations with $D = 1$ in a square of radius $L = 1$ with four reflecting circles of radius r, centered at the corners, show that the uniform approximation by the patched formula (4.6) is in good agreement with Brownian results (Fig. 4.5b), where the statistics were collected from 1000 escape times of Brownian trajectories per graph point. The trajectories start at the square center. Equation (4.6) holds in the full range of values of $a \in [0, L/2]$ and all L.

The Brownian motion around the obstacles (Fig. 4.5a) can be coarse-grained into a Markovian jump process whose state are the connected domains enclosed by the obstacles and the jump rates are determined from the reciprocals of the mean first passage times and exit probabilities. This random walk can in turn be approximated by an effective coarse-grained anisotropic diffusion, as done for atomic migration in crystals (Schuss 1980, Chap. 8, Sect. 2) and for effective diffusion on a surface with obstacles (Holcman et al. 2011). The diffusion approximation to the transition probability density function of an isotropic random walk that jumps at exponentially distributed waiting times with rate λ on a square lattice with step size L is given by Schuss (1980)

$$\frac{\partial p}{\partial t} = \bar{D}\left(\frac{\partial^2 p}{\partial x^2} + \frac{\partial^2 p}{\partial y^2}\right), \quad \bar{D} = \frac{\lambda L^2}{4}. \tag{4.9}$$

To illustrate this theory, we assume a reduction of the effective diffusion coefficient from 0.01 on a clear membrane to 0.2 μm^2/s on an obstructed membrane (Triller and Choquet 2003), which leads to the estimate of 70 % of the membrane surface being covered with obstacles (Holcman et al. 2011), as can be seen from Fig. 4.4b–d.

4.3.2 Diffusion of Receptors on the Neuronal Membrane

The results of the previous section can be used to estimate the density of obstacles on the membrane of cell such as a neuronal dendrite. The effective diffusion coefficient of a receptor on the neuronal membrane can be estimated from the experimentally measured single receptor trajectory by a single particle tracking method. The receptor effective diffusion coefficient of a receptor is found in Triller and Choquet (2003) to vary between 0.01 and 0.2 μm^2/s. In the simplified model of crowding, the circular obstacles are as in Fig. 4.4a. Simulated Brownian trajectories give the MFPT from one square to the next one as shown in Fig. 4.4a, where L is fixed and a is variable. According to (4.6), (4.5), and (4.9), as a increases the effective diffusion coefficient $\bar{D}$ decreases. It is computed as the mean square displacement (MSD) $\langle \frac{\text{MSD}(t)}{4t} \rangle$. Brownian simulations show that $\bar{D}$ is linear, thus confirming that in the given geometry crowding does not affect the nature of the Brownian motion for sufficiently long times. Specifically, for Brownian diffusion coefficient $D = 0.2\,\mu\text{m}^2/\text{s}$ the time considered is longer than 10 s. In addition, Fig. 4.4c shows the diffusion coefficient ratio D_a/D_0, where D_a is the effective diffusion coefficient of Brownian motion on the square lattice described above with obstacles of radius a. For $a = 0.3$ the value $D_a/D_0 \approx 0.7$ is found whereas a direct computation from the mean exit time formula (4.6) gives

$$\frac{\tau_0}{\tau_a} = \frac{c_1}{c_2|\Omega| \log \dfrac{1}{\varepsilon} + d_1} \approx 0.69, \tag{4.10}$$

where $\varepsilon = (L - 2a)/L = 0.4$.

It can be concluded from the Brownian simulations that the coarse-grained motion is plain diffusion with effective diffusion coefficient $D_a/D_0 = \tau_0/\tau_a$, which decreases nonlinearly as a function of the radius a, as given by the uniform formula (4.6). Figure 4.4c recovers the three regimes of (4.6): the uncrowded regime for $a < 0.2L$, where the effective diffusion coefficient does not show any significant decrease, a region $0.2L < a < 0.4L$, where the leading order term of the effective diffusion coefficient is logarithmic, and for $a > 0.4L$ the effective diffusion coefficient decays as $\sqrt{(L-2a)/L}$, in agreement with (4.6).

Finally, to estimate the density of obstacles in a neuron from (4.6), (4.5), and (4.9), a reference density has to be chosen. The reference diffusion coefficient is chosen to be that of receptors moving on a free membrane (with removed cholesterol), estimated to be $0.17 \leq D \leq 0.2\,\mu\text{m}^2/\text{s}$ (Renner et al. 2009), while with removing actin, the diffusion coefficient is 0.19 μm^2/s. The reference value $D = 0.2\,\mu\text{m}^2/\text{s}$ gives an estimate of the crowding effect based on the measured diffusion coefficient (Fig. 4.6d). The reduction of the diffusion coefficient from $D = 0.2\,\mu\text{m}^2/\text{s}$ to $D = 0.04\,\mu\text{m}^2/\text{s}$ is achieved when 70 % of the membrane surface is occupied by obstacles. Thus obstacles impair the diffusion of receptors and are therefore responsible for the large decrease of the measured diffusion coefficient (up to five times).

4.4 Synaptic Transmission and the Synaptic Current

Synapses are local active micro-contacts underlying direct neuronal communication and they can vary in size and molecular composition, depending on their location in the brain and on their specificity. The molecular processes underlying synaptic

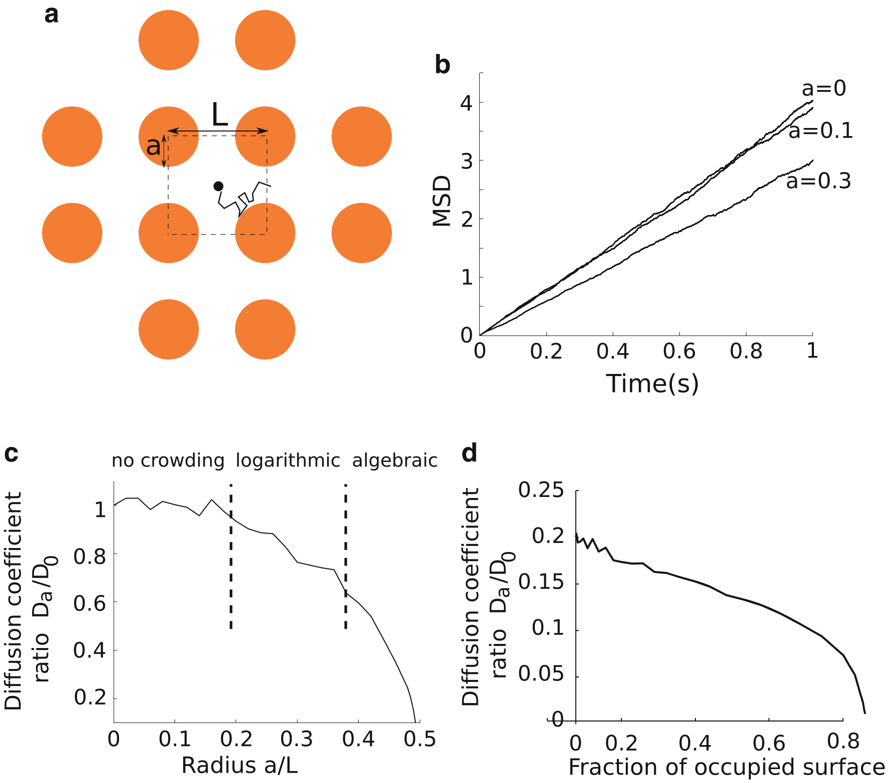

Fig. 4.6 Organization of the neuronal membrane. (**a**) Schematic representation of a Brownian particle diffusing in a crowded microdomain. (**b**) Mean square displacement (MSD) of the particle in a domain paved with microdomains. The MSD is linear, showing that crowding does not affect the nature of diffusion. The effective diffusion coefficient is computed as $\bar{D} = \lim_{t\to\infty}\langle \text{MSD}(t)/4t\rangle$ for $D = 1$. (**c**) The effective diffusion coefficient computed from the MSD for different radiuses of the obstacles. Brownian simulations (*continuous curve*): there are three regions (separated by the *dashed lines*). While there is no crowding for $a < 0.2$, the decreasing of the effective diffusion coefficient for $0.2 < a < 0.4$ is logarithmic, and like square root for $a > 0.4$. (**d**) Effective diffusion coefficient of a particle diffusing in a domain as a function of the fraction of the occupied surface. An AMPAR has a diffusion coefficient of 0.2 $\mu m^2/s$ in a free membrane (Renner et al. 2009)

transmission are well known (Kandel et al. 2000). After neurotransmitters, such as glutamate, are released into the synaptic cleft from a vesicle on the surface of a pre-synaptic neuron (see Fig. 4.7), they can either find a specific receptor protein on the membrane of the postsynaptic terminal, such as NMDA, AMPA, and so on,[1] or are absorbed by the surrounding glia cells and recycled (see Sect. 4.2).

---

[1] See, e.g., http://en.wikipedia.org/wiki/Biochemical_receptor.

Fig. 4.7 A neuronal synapse. Schematic representation of a synapse between neurons. Neurotransmitters (*blue*) are released to the synaptic cleft at the presynaptic terminal and can find a receptor (*Green*) on the postsynaptic terminal or be absorbed by the surrounding glial cells (*red*). The postsynaptic density (PSD) is the dense region above the yellow sheet holding the scaffolding molecules (*orange*)

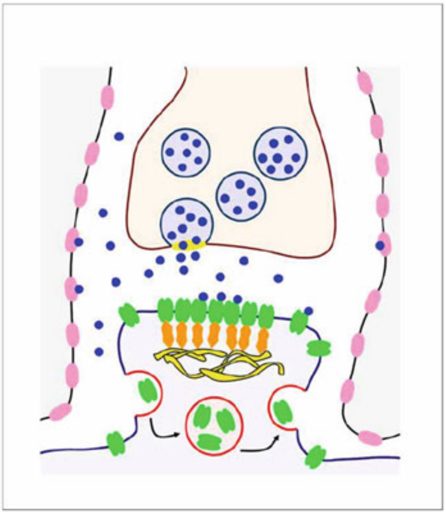

The ionotropic glutamate receptors, such as AMPA and NMDA, may open upon binding neurotransmitters. We refer to Wikipedia for the terminology, illustration, and movies for the biological material. The synaptic current originates when these ligand-gated channels on the post-synaptic membrane open and admit positive ions, such as calcium and sodium from the cleft into the post-synaptic terminal (the neuronal spine), thereby changing the depolarization of the post-synaptic membrane potential. The ions in the spine ultimately leave the spine by both diffusion in the potential field and hydrodynamical flow induced by the twitching of the spine. This occurs when calcium binds to actin-myosin filaments which contract and push the ionic solution through the spine neck into the neuronal shaft.

The synaptic current in the cell plays a fundamental role in neuronal communication. It is the direct and fast signal of synaptic transmission. This current depends not only on receptors such as AMPA, but also on the complex molecular machinery edifice that controls them. Possible changes in the current dynamics are the readout of synaptic plasticity, a process that underlies learning and memory (Kerchner and Nicoll 2008). Many properties of synaptic transmission result in from diffusion in microdomains, as described above.

4.4.1 The Synaptic Cleft

Glutamate receptors are activated by neurotransmitters diffusing in the cleft geometry, which is approximated by a flat cylinder. This activation is described below in terms of AMPA-receptors conductances rather than by the standard Markov description, obtained from optimal fitting of measurements outside a synapse. The model proposed here for the synaptic current accounts for the four glutamate binding sites per receptor. While glutamate molecules are Brownian inside the cylindrical synaptic cleft Ω, AMPARs are positioned on the PSD [see Figs. 4.7(right) and 3.9(right)]. The model of glutamate binding to an AMPAR is a radiative boundary condition on the PSD (Ω_{PSD}), as described below.

When a glutamate molecule hits the lateral boundary ($\partial\Omega_{\text{Lat}}$) of the cleft (modeled as a cylinder Ω), it is absorbed by glia cells and no longer can contribute to the activation of AMPARs. The pdf $p(\boldsymbol{x}, t|\boldsymbol{x}_0)$ of a Brownian trajectory $\boldsymbol{x}(t)$ of a glutamate molecule, given $\boldsymbol{x}(0) = \boldsymbol{x}_0 \in \Omega$, is the solution of the initial-boundary value problem for the diffusion equation

$$
\begin{aligned}
\frac{\partial p(\boldsymbol{x}, t\,|\,\boldsymbol{x}_0)}{\partial t} &= D\Delta p(\boldsymbol{x}, t\,|\,\boldsymbol{x}_0) \ \text{ for } \boldsymbol{x} \in \Omega,\ t > 0 \\
p(\boldsymbol{x}, 0\,|\,\boldsymbol{x}_0) &= \delta(\boldsymbol{x} - \boldsymbol{x}_0) \ \text{ for } \boldsymbol{x} \in \Omega \\
\frac{\partial p(\boldsymbol{x}, t\,|\,\boldsymbol{x}_0)}{\partial \nu} &= 0 \ \text{ for } \boldsymbol{x} \in \partial\Omega_r \\
p(\boldsymbol{x}, t\,|\,\boldsymbol{x}_0) &= 0 \ \text{ for } \boldsymbol{x} \in \partial\Omega_{\text{Lat}} \\
-D\frac{\partial p(\boldsymbol{x}, t\,|\,\boldsymbol{x}_0)}{\partial \nu} &= -\kappa p(\boldsymbol{x}, t\,|\,\boldsymbol{x}_0) \ \text{ for } \boldsymbol{x} \in \partial\Omega_{\text{PSD}},
\end{aligned}
\tag{4.11}
$$

where D is the diffusion coefficient of a free glutamate molecule. The partial absorption rate constant κ accounts not only for the fraction of AMPARs inside the PSD, but also for the activation barrier of a single glutamate to a glutamate receptor binding site. The rate constant

$$
\kappa = \frac{D}{2\pi R_{\text{PSD}}^2} \frac{1}{\dfrac{1}{N_a a} + \dfrac{D}{\kappa_e 2\pi a^2 N_a}}. \tag{4.12}
$$

The absorption rate constant κ_e in (4.12) is obtained by calibration with the experimental value $\kappa_e \approx 1.6$ (see Sect. 4.7 below and Taflia and Holcman 2011). Here a and R_{PSD} are the radii of a single receptor and the PSD, respectively, and N_a is the number of AMPARs. The derivation starts by considering that the N_a receptors are placed on the PSD, whose surface area is πR_{PSD}^2. The criterion for choosing κ is that the absorption flux be equal to the flux on the last line of (4.11) (see Schuss 2013, Sect. 2.5). Here D is the diffusion constant of glutamate molecules in the cleft and κ_e is the partial reflection rate constant of a single AMPAR on a glutamate molecule. This constant is calibrated from (patch-clamp) experimental data.

The probability $p(\boldsymbol{x}_0)$ that a glutamate molecule binds a receptor released at $\boldsymbol{x}_0$, is the total probability flux into the receptors, that is, into the absorbing boundary $\partial\Omega_{\text{PSD}}$,

$$
p(\boldsymbol{x}_0) = D\int_0^\infty \int_{\partial\Omega_{\text{PSD}}} \frac{\partial p(\boldsymbol{y}, t\,|\,\boldsymbol{x}_0)}{\partial n}\, dS_{\boldsymbol{y}}\, dt = D\int_{\partial\Omega_{\text{PSD}}} \frac{\partial u(\boldsymbol{y}\,|\,\boldsymbol{x}_0)}{\partial n}\, dS_{\boldsymbol{y}}, \tag{4.13}
$$

where the function $u(\boldsymbol{x}\,|\,\boldsymbol{x}_0) = \int_0^\infty p(\boldsymbol{x},t\,|\,\boldsymbol{x}_0)\,dt$ is the solution of the boundary value problem

$$\begin{aligned} D\Delta u(\boldsymbol{x}\,|\,\boldsymbol{x}_0) &= -\,\delta(\boldsymbol{x}-\boldsymbol{x}_0) \;\; \text{for } \boldsymbol{x}\in\Omega \\ \frac{\partial u(\boldsymbol{x}\,|\,\boldsymbol{x}_0)}{\partial \nu} &= 0 \;\; \text{for } \boldsymbol{x}\in\partial\Omega_r \\ u(\boldsymbol{x}\,|\,\boldsymbol{x}_0) &= 0 \;\; \text{for } \boldsymbol{x}\in\partial\Omega_{\text{Lat}} \\ D\frac{\partial u(\boldsymbol{x}\,|\,\boldsymbol{x}_0)}{\partial \nu} &= \kappa u(\boldsymbol{x}\,|\,\boldsymbol{x}_0) \;\; \text{for } \boldsymbol{x}\in\partial\Omega_{\text{PSD}}. \end{aligned} \tag{4.14}$$

Absorption of a Brownian trajectory in a small receptor is a rare event that can hardly be expected to provide sufficient statistical data for a reliable estimate of the number of saturated receptors. It is necessary, therefore, to coarse-grain Brownian simulations of such events by deriving analytical approximations to $u(\boldsymbol{x}\,|\,\boldsymbol{x}_0)$ and $p(\boldsymbol{x}_0)$ [see (4.13)], to be used in numerical simulations.

4.5 The Mean and Variance of the Synaptic Current $\boldsymbol{I_s}$

To compute the mean and the variance of the synaptic current the number of bound glutamate molecules and the probability of a given configuration of bound AMPARs has to be calculated. To estimate it, we construct a combinatorial model of the synaptic current. First, we recall that the probability distribution of k independent bound glutamate molecules, after a vesicle is released at $\boldsymbol{x}_0$ is binomial,

$$\Pr_k(\boldsymbol{x}_0) = C_{4N_a}^k p(\boldsymbol{x}_0)^k (1-p(\boldsymbol{x}_0))^{4N_a-k}, \tag{4.15}$$

where N_a is the expected number of bound glutamates and $p(\boldsymbol{x}_0)$ is the probability that a glutamate binds one of the receptors before it escapes the cleft. The latter is given by (4.13) as

$$p(\boldsymbol{x}_0) = \kappa \int\limits_{\partial\Omega_{\text{PSD}}} u(\boldsymbol{x}\,|\,\boldsymbol{x}_0)\,dS_{\boldsymbol{x}}. \tag{4.16}$$

The mean and the variance of the number of bound receptors are given by

$$M(\boldsymbol{x}_0) = N_g p(\boldsymbol{x}_0), \quad \sigma^2(\boldsymbol{x}_0) = N_g p(\boldsymbol{x}_0)(1-p(\boldsymbol{x}_0)),$$

respectively. When a vesicle is released at the center of the synapse, for PSD and synaptic radii of, respectively, 300 nm and 500 nm (the effective surface area of a single AMPAR is 10 nm^2 and $\kappa = 0.25$, see Fig. 4.8).

An additional source of fluctuations in the number of bound AMPARs is as follows. AMPARs can bind up to four glutamate molecules. Therefore the probability $\Pr\{\vec{n}\,|\,k\}$ of a given configuration $\vec{n} = (n_4, n_3, n_2, n_1)$ of n_1 AMPARs that bind one glutamate molecule, n_2 AMPARs that bind 2, and so on, when there are N_a AMPA receptors and $k < 4N_a$ bound glutamate molecules, is given by

$$\Pr\{\vec{n}\,|\,k\} = \frac{N_a!}{n_4!n_3!n_2!n_1!(N_a - (n_4 + n_3 + n_2 + n_1))!}\frac{1}{F(k, N_a)}. \tag{4.17}$$

This is the probability of choosing at random n_4 AMPARs out of N_a, n_3 out of $N_a - n_4$, and so on. $F(k, N_a)$ is the total number of possibilities to partition the number k to a sum of N_a integers from the set $\{4, 3, 2, 1, 0\}$ as

$$k = 4n_4 + 3n_3 + 2n_2 + n_1, \tag{4.18}$$

with the constraint that $n_4 + n_3 + n_2 + n_1 \leq N_a$. The number $F(k, N_a)$ can be computed numerically as the $(k + 1)$th coefficient in the expansion of $(1 + x + x^2 + x^3 + x^4)^{N_a}$ in powers of x. With the notation V for the potential and $\vec{\gamma} = (\gamma_1, \gamma_2, \gamma_3, \gamma_4)$ for the vector of conductances, all moments of the current can be found, given these probabilities, and in particular, the mean and variance are given by

$$\begin{aligned}
\mathbb{E}[I_s(\boldsymbol{x}_0)] &= \sum_{k=1}^{N_g}\sum_{n\in S_k} \vec{n}\cdot\vec{\gamma}\,\Pr\{\vec{n}\,|\,k\}V\Pr_k(\boldsymbol{x}_0)\\
&= \sum_{k=1}^{4N_a}\sum_{n\in S_k} \vec{n}\cdot\vec{\gamma}\,\Pr\{\vec{n}\,|\,k\}\Pr_k(\boldsymbol{x}_0)V + N_a\gamma_4 V\left(1 - \sum_{k=0}^{4N_a}\Pr_k(\boldsymbol{x}_0)\right)\\
\mathbb{E}[I_s^2(\boldsymbol{x}_0)] &= \sum_{k=1}^{N_g}\sum_{n\in S_k} (\vec{n}\cdot\vec{\gamma})^2\,\Pr\{\vec{n}\,|\,k\}\Pr_k(\boldsymbol{x}_0)V^2\\
&\quad - (\mathbb{E}[I_s(\boldsymbol{x}_0)])^2 \sum_{k=1}^{4N_a}\sum_{n\in S_k} (\vec{n}\cdot\vec{\gamma}V)^2\,\Pr\{\vec{n}\,|\,k\}\Pr_k(\boldsymbol{x}_0)\\
&\quad + (N_a\gamma_4 V)^2\left(1 - \sum_{k=0}^{4N_a}\Pr_k(\boldsymbol{x}_0)\right) - (\mathbb{E}[I_s(\boldsymbol{x}_0)])^2.
\end{aligned} \tag{4.19}$$

Here S_k is the set of all the possible configurations of $\vec{n} = (n_1, n_2, n_3, n_4)$ such that $4n_4 + 3n_3 + 2n_2 + n_1 = k$. The formulas for the mean and variance consist of two terms: in the first one, the summation extends over sites that are partially bound by glutamate molecules. The probability for such an event is the product of the probability $\Pr_k$, that k glutamates are bound $(k < 4N_a)$ and the probability $\Pr\{\vec{n}\,|\,k\}$ for a given binding configuration $k = 4n_4 + 3n_3 + 2n_2 + n_1$. The second term in

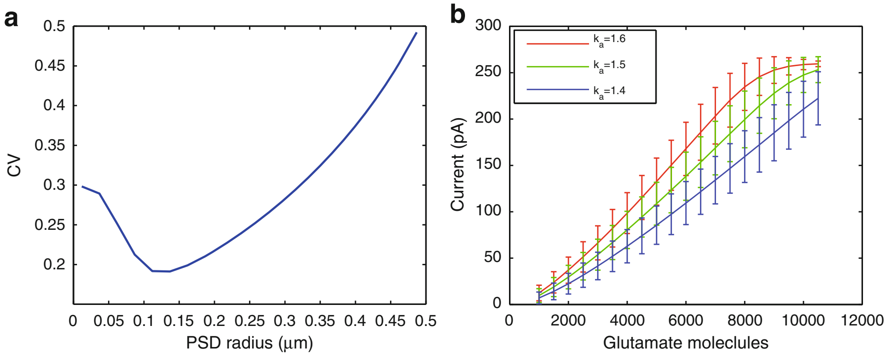

Fig. 4.8 (**a**) For a PSD radius of 0.3 μm, the coefficient of variation (CV) reaches a maximum. This shows that for a given size of the active zone (AZ), where vesicles are released, the CV is minimum when receptors are spread over an optimal PSD area. (**b**) Calibration of the partial absorption rate constant κ. The synaptic current is simulated according to Eq. (4.19) for different values of the activation coefficient κ [see (4.12)]. The optimal synaptic response in the range of 3000–12,000 glutamate molecules is achieved at $\kappa = 1.6$

the mean current experssion (4.19) accounts for the event that all AMPAR binding sites are occupied ($4N_a$) and its probability equals to the one complementary to the that of partial binding described by in the first terms. Figure 4.8a shows that the coefficient of variation (CV $=$ SD/Mean, where SD stands for standard deviation) has a minimum as a function of the size of the PSD. This unexpected result is further discussed in Taflia and Holcman (2011). The optimal PSD size, as shown in Figs. 4.8 and 4.9, is due to a nonlinear phenomenon involving the receptor multi-binding cooperativity described below.

4.5.1 Properties of the Synaptic Current I_s

The mean and variance of I_s, as functions of the PSD radius, when one vesicle is released at the center for different active zone (AZ) sizes (Fig. 4.9a), show that for a given number of receptors, the moments of the current are decreasing functions of the PSD and AZ radii. The number of AMPARs bound to two and four glutamate molecules is a function of the PSD radius when the AZ radius is fixed at 50 nm (blue) and 150 nm (red) (Fig. 4.9b, c). For a small AZ radius, most of the AMPARs are bound to four glutamate molecules and thus the synaptic-current amplitude is much higher than that for a large AZ radius. In the latter case, the current is primarily generated by receptors bound to two glutamate molecules. The large current difference observed in Fig. 4.9a with the radii 50 and 150 nm is due to the nonlinear properties of conductivities, generated by the number of bound glutamate molecules. But in all cases, the moments of the synaptic current are decreasing functions of the AZ radius (Fig. 4.9d).

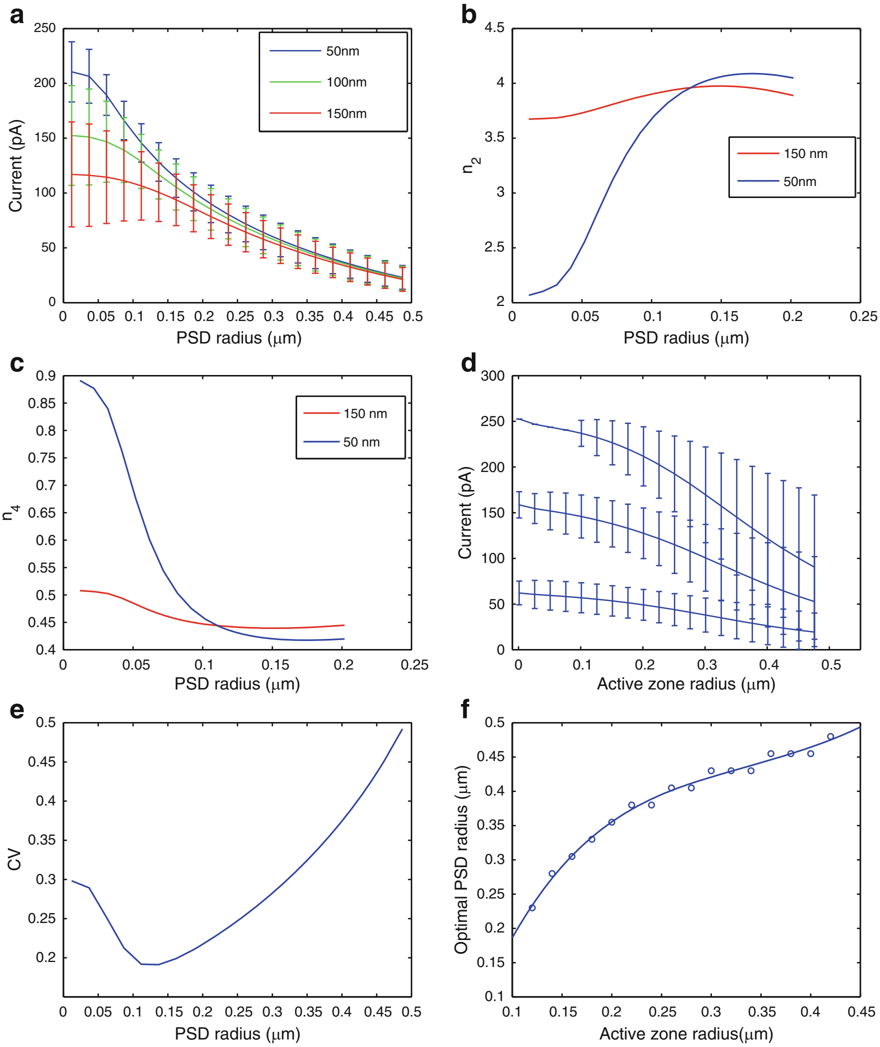

Fig. 4.9 Optimal PSD radius. (**a**) The mean current and SD are plotted as a function of the PSD size for three different active zones (50, 100, and 150 nm) (the synaptic radius is 500 nm and the height is 20 nm). (**b**, **c**) The mean number of AMPA receptors bound by 2 (resp. 4) glutamate molecules as a function of the PSD radius. (**d**) Current vs active zone (AZ) radius. The PSD size is fixed at 300 nm and each curve represents 1, 2, and 3 released vesicles. (**e**) CV vs PSD size. The CV achieves a minimum when the PSD and the active zone are approximately equal. In that case the AZ is 100 nm and the CV minimum is achieved for a PSD of radius of 120 nm. (**f**) Optimal PSD radius: It is plotted as a function of the AZ radius obtained by minimizing the CV for a fixed AZ

The reliability of the synaptic response is measured in terms of the coefficient of variation (CV) of the synaptic current I_s. For a fixed AZ radius, the CV has a minimum as a function of the PSD radius. Indeed, simulation results show, for example, that with an AZ of radius 100 nm, the CV reaches its minimum for a PSD radius of 120 nm (Fig. 4.9e). The radii of the PSD and the AZ shown in Fig. 4.9f show the optimal PSD radius as a function of the AZ radius. The figure indicates that the optimal PSD size increases with the radius of the AZ.

Another aspect of the combinatorial model has to do with the description of AMPARs. The synaptic current is computed from conductances that originate in patch-clamp experiments of isolated AMPARs (Gebhardt and Cull-Candy 2006; Smith and Howe 2000), where the relation between the number of bound glutamates and the associated conductances is found for different fixed glutamate concentrations. Although more than four conductance levels have been reported, it is still unclear how to relate them to the number of bound glutamate molecules. In addition, having four glutamates bound to a single receptor lead to a current amplitude of 13 pA, which has to be compared with that for two bound AMPARs to two glutamates, which should lead to $2 \cdot 4 = 8$ pA. This difference suggests that binding four glutamates to a single AMPAR has a nonlinear effect and is different from having two receptors bound by two glutamates, as shown in Fig. 4.9a–c.

4.5.2 Nonlinearity of the Synaptic Current I_s

The minimum of the CV is due to the nonlinear dependence on the PSD radius of the number of glutamates bound to receptors. Consider, for simplicity, a reduced model of one among N receptors. The receptor can be in one of the following three states, depending on the number of bound glutamates, for which the current I can switch between the three values $[I_1, I_2, I_3]$. Each receptor binds a glutamate with probability $q \in [0, 1]$ and the probability of I is given by

$$\Pr\{I = I_k\} = \begin{cases} \binom{N}{k} q^k (1-q)^{N-k} & \text{for } k = 1, 2 \\ \\ 1 - \Pr\{I = I_1\} - \Pr\{I = I_2\} - (1-q)^N & \text{for } k = 3, \end{cases} \tag{4.20}$$

where the probability for $k = 1, 2$ is binomial while the probability for the current I_3 is the complementary probability to having no binding, one binding, and two bindings. The CV of the current I can be computed analytically as a function of the probability q. Figure 4.10 shows that only for a certain range of the parameters, such as $I_1, I_2 \ll I_3$, the CV exhibits a local minimum. Changing the parameter q in this model is equivalent to varying the AZ or PSD size, or both.

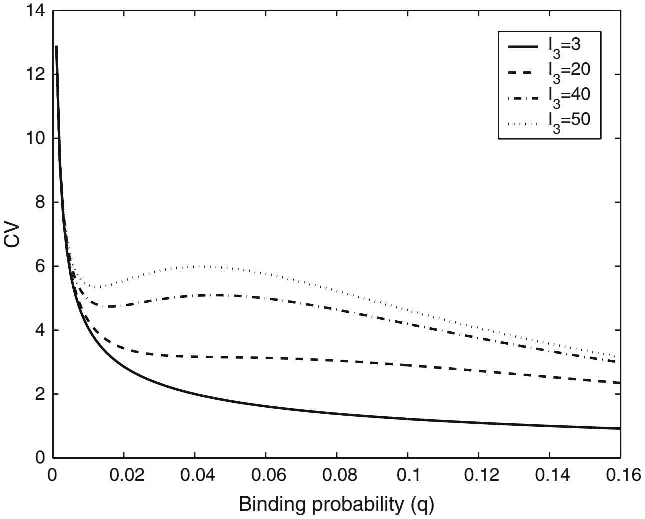

Fig. 4.10 Analysis of a simplified model showing discrete current levels: the random variable I can have any one of the values I_1, I_2, I_3. The probabilities of these events are given by Eq. (4.20). The model describes a single receptor with three conductivity levels, which depend on the number of bound glutamate molecules, each of which can bind to a receptor with a probability q. The figure shows a plot CV vs q for different values of I_3, where $I_1 = 1, I_2 = 2$ are fixed. When $I_3 \gg I_1, I_2$, the CV has a local maximum point. This is a manifestation of the nonlinear cooperative effect of multiple bindings

4.6 Coarse-Grained Glutamate Partial Absorption Rate of the PSD

The goal of this section is to coarse-grain the single glutamate absorption rate in a receptor to an effective partial absorption rate constant κ of glutamate in the PSD,

$$-D\frac{\partial p(\boldsymbol{x},t)}{\partial n} = \kappa p(\boldsymbol{x},t) \quad \text{for } \boldsymbol{x} \in \text{PSD}. \tag{4.21}$$

The coarse-grained rate constant κ can be computed from a model of a population of N_a partially reflecting AMPA receptors of size a in the PSD. When a glutamate molecule hits a single receptor, the receptor can either be activated or not. The homogenization is based on the partially absorbing condition for a single glutamate in a receptor,

$$-D\frac{\partial p(\boldsymbol{x},t)}{\partial n} = \kappa_a p(\boldsymbol{x},t) \quad \text{for } \boldsymbol{x} \text{ in a receptor}. \tag{4.22}$$

Here κ_a is the single glutamate partial absorption rate at an AMPAR's partially reflecting activation barrier ($\kappa_a = \infty$ if there is no activation barrier and the receptor is activated when hit by glutamate), while for $\kappa_a = 0$, the barrier is so large that all glutamate molecules are reflected. The value of κ_a depends on the intrinsic properties of the AMPA binding site and should be recovered from the experimental literature (Gebhardt and Cull-Candy 2006).

To compute κ in the PSD, we assume that all the binding sites are confined in the PSD to a disk of radius R_{PSD}. The homogenized partial absorbing boundary condition is given in (4.21). The homogenization consists in choosing the partial absorption rate κ so that the influx to the N_a individual binding sites and the influx through the partially absorbing PSD are equal.

The influx through the partially absorbing PSD is determined from the solution of the PAV equation

$$D\Delta u(\boldsymbol{x}) = -1 \quad \text{for } \boldsymbol{x} \text{ in the synaptic cleft } \Omega \tag{4.23}$$

with the boundary condition (4.21) instead of an absorbing boundary condition and

$$\begin{aligned} \frac{\partial u(\boldsymbol{x})}{\partial n} &= 0 \quad \text{for } \boldsymbol{x} \in \partial\Omega_r \\ -D\frac{\partial u(\boldsymbol{x})}{\partial n} &= \kappa\, u(\boldsymbol{x}) \quad \text{for } \boldsymbol{x} \in \text{PSD}. \end{aligned} \tag{4.24}$$

The solution of the PAV boundary value problem (4.23), (4.24) is constructed by the NET method described in Chaps. 1 and 2. In three dimensions, the MFPT $\bar{\tau} = u(\boldsymbol{x})$ from a point $\boldsymbol{x}$ in the synaptic cleft to the PSD is independent of the starting point $\boldsymbol{x} \in \Omega$ and is given by (see Reingruber et al. 2009; Taflia and Holcman 2011)

$$\bar{\tau} \approx \frac{|\Omega|}{D}\left(\frac{1}{4R_{\text{PSD}}} + \frac{D}{2\pi\kappa R_{\text{PSD}}^2}\right), \tag{4.25}$$

so the probability flux is

$$J = \frac{1}{\bar{\tau}} \approx \frac{D}{|\Omega|}\frac{1}{\dfrac{1}{4R_{\text{PSD}}} + \dfrac{D}{2\pi\kappa R_{\text{PSD}}^2}}. \tag{4.26}$$

The flux into N_a fully absorbing AMPA binding sites of size a in a PSD disk of radius R_{PSD} is calculated as follows. The MFPT to the PSD is given by

$$\bar{\tau} = \frac{|\Omega|}{4R_{\text{PSD}}D}\frac{N_a a + f(\sigma)R}{N_a a}, \tag{4.27}$$

where $f(\sigma) = 1 - \sigma$ and the fraction of absorbing surface is $\sigma = N_a a^2/R_{\text{PSD}}^2$ (see Sect. 4.8 for references). Equating (4.27) with (4.25),

$$\frac{|\Omega|}{D}\left(\frac{1}{4R_{\text{PSD}}} + \frac{D}{2\pi\kappa_P R_{\text{PSD}}^2}\right) = \frac{|\Omega|}{4R_{\text{PSD}}D}\frac{N_a a + f(\sigma)R_{\text{PSD}}}{N_a a}, \tag{4.28}$$

leads to the expression for the homogenized partial absorption rate constant

$$\kappa = \frac{D}{2\pi R_{\mathrm{PSD}}^2}\frac{N_a a}{f(\sigma)}.$$

Using the relation (see Dudko et al. 2004)

$$\bar{\tau} = \frac{|\Omega|}{D}\left(\frac{1}{4R_{\mathrm{PSD}}} + \frac{f}{N_a a} + \frac{D}{\kappa_a 2\pi a^2 N_a}\right) \tag{4.29}$$

for a partially reflecting hole, we obtain the homogenized partial reflection rate constant

$$\kappa = \frac{D}{2\pi R_{\mathrm{PSD}}^2}\frac{1}{\dfrac{f(\sigma)}{N_a a} + \dfrac{D}{\kappa_a 2\pi a^2 N_a}}. \tag{4.30}$$

4.7 Estimate of the Molecular Rate κ_a from Experimental Data

A Markovian kinetic model of the initial binding step of glutamate to AMPAR can be used for estimating the partial absorption rate constant κ_a. The homogenized partial absorption rate coefficient κ and (4.30) are used as follows: the process of binding and unbinding of a glutamate molecule to an AMPAR can be described as a two-state Markov chain

$$C \underset{k_{-1}}{\overset{k_1}{\rightleftarrows}} O, \tag{4.31}$$

in which the forward binding rate k_1 is given in units of Mole/s (k_{-1} is the unbinding rate). On the one hand, the binding rate can be calculated by the flux formula (4.13) as

$$J_{\mathrm{Markov}} = k_1 A^{-1} N_g V^{-1} \int\limits_{\partial\Omega_a} p(x)\,dx \approx k_1 A^{-1} N_g V^{-1} \pi a^2 p(x), \tag{4.32}$$

where A is the Avogadro number, $p(x)$ is the density of glutamate near the receptor, and $V = \pi R h^2$ is the volume of the synaptic cleft. Using the diffusion model (4.22), the flux term is given by

$$J_{\mathrm{diff}} = N_g \kappa_a \int\limits_{\partial\Omega_a} p(x)\,dx \approx N_g \kappa_a \pi a^2 p(x), \tag{4.33}$$

where a is the radius of a receptor and $\partial\Omega_a$ represents the receptor surface. Setting $J_{\text{diff}} = J_{\text{Markov}}$, we obtain an expression for the partial reflection constant

$$\kappa_a = k_1 A^{-1} V^{-1}.$$

Using the published value $k_1 = 10^7\,\text{M}^{-1}\,\text{s}^{-1}$ (taken from Milstein et al. 2007), we obtain that $\kappa_a \approx 1.06$. The two-state chain model is an adequate approximation even in the case that there are more states in the Markov chain.

4.8 Annotations

A simulation of the entire synaptic transmission process, which contains the arrival of neurotransmitter molecules at receptors on the post-synaptic membrane, was done in Holcman and Triller (2006). Using the analytically computed neurotransmitter flux rather than simulating it leads to significant improvement in Reingruber and Holcman (2011b). Analytical formulas were also used for quantifying diffusion in dendritic spines in Biess et al. (2007). Modeling and simulation of chemical reactions as coarse-grained Markov processes speeds up the simulation of complex Brownian dynamics (Holcman and Schuss 2005a; Dao Duc and Holcman 2010). Taking into consideration the fact that the stationary arrival process of Brownian particles from the continuum to an absorbing boundary is Poissonian (Nadler et al. 2002; Schuss et al. 2007), it is possible to coarse-grain the binding and unbinding process of Brownian particles in microdomains into a Markov process (Holcman and Schuss 2005a). A recent application of such a coarse-grained Markovian approximation gives new range for the rate of molecular dynamics underlying the spindle assembly checkpoint during cell division (see Sect. 6.2.1 and Dao Duc and Holcman 2012).

Another application of asymptotic analytical results is the verification of molecular dynamics simulations in domains that contain small passages or targets (Biess et al. 2007). The convergence of the simulation can be measured by the convergence of the statistics of rare events to the statistics predicted by the analytical asymptotic approximation for dendritic spines (see Sect. 3.3).

Brownian simulations and by mixed analytical approaches were used in Taflia and Holcman (2011) and Freche et al. (2011) and led to better understanding of pathological synapses, implicated in many cognitive disorders such as spectral autism disorders, epilepsy, and many others (Südhof 2008; Durand et al. 2011). A simulation that mimics starvation or the effect of a ketogenic diet was proposed in Fresche et al. (2012). Brownian dynamics simulations that include neurotransmitter release, binding to receptors, and flux through open channels were communicated in Taflia and Holcman (2011) and Freche et al. (2011).

The possible function of dendritic spines is to dynamically filter calcium ions is discussed in Korkotian and Segal (1999), Svoboda et al. (1996), and Bloodgood and Sabatini (2005).

Membrane organization is discussed in Kusumi et al. (1993, 2005), Edidin et al. (1991), Sheetz (1993), Suzuki and Sheetz (2001), Saxton (1995), and Saxton and Jacobson (1997). The diffusion coefficient of a molecule freely diffusing on intact and treated neuronal membranes, cleared of almost all obstacles, was reported in Renner et al. (2009). The diffusion of a protein on the membrane is described in Saffman and Delbrück (1975). The effective diffusion coefficient on a membrane crowded with obstacles differs significantly from that predicted in Saffman and Delbrück (1975) and depends strongly on the degree of crowding (Saxton 1993). It has been estimated from diffusion data and from a model in Holcman et al. (2011).

A similar analysis to that of Sect. 4.3.1 was used in Hoze et al. (2012) to estimate the density of obstacles in dendritic spine (70 %) versus dendritic shaft (50 %). Coarse-grained modeling for three-dimensional crowding in dendrites was used in Biess et al. (2011) to study calcium spread during bursting.

The narrow escape method is used in models of the synaptic current to estimate the mean and variance of the post-synaptic current in Taflia and Holcman (2011) and Freche et al. (2011). The probability that a glutamate molecule hits a cluster of AMPARs is found in Taflia and Holcman (2011) to be $p(\boldsymbol{x}_0) = 8 \times 10^{-3}$ (see Sect. 4.5). Formula (4.27) was derived in the following references: Berg and Purcell (1977), Zwanzig (1990), Zwanzig and Szabo (1991), Reingruber et al. (2009), Berezhkovskii et al. (2004).

Chapter 5
Determination of Features from Super-Resolution Data

5.1 Receptor Motion on a Cellular Membrane

Stochastic narrow escape arises in the problem of determining physical features of a neuronal membrane from a large number of short receptor trajectories generated by the method of single particle tracking with photo-activated localization microscopy (sptPALM) applied to diffusing molecules (Manley et al. 2008) or AMPARs on hippocampal cultured neurons (Hoze et al. 2012). The features, such as potential wells and narrow passages, can be determined from long dwell times of the trajectories in certain parts of the neuronal membrane. However, the dwell time of a receptor diffusing in a microdomain on a neuronal membrane cannot be obtained directly from the short recorded fragments of trajectories, because they are much shorter than the dwell times in potential wells and than NETs from other traps. Moreover, longer trajectories obtained by other techniques (such as quantum dot) provide only partial sampling of space-time, which cannot be used to compute transition probabilities between different regions.

This section describes a simulation method to estimate the residence time of a receptor in a microdomain, such as a dendritic spine, where the local biophysical properties are determined from large samples of single particle data (Hoze et al. 2012). Simulations of the dynamics reconstructed statistically from a large sample of short trajectories can be run for arbitrarily long times and can therefore generate statistically significant samples of rare events, such as narrow escapes.

We adopt the overdamped limit of the Saffman–Delbrück–Langevin equation (Saffman and Delbrück 1975; Saffman 1976) as a physical model of receptor motion on a homogenous surface. Specifically, the diffusion of a receptor embedded in a membrane surface is generated by a diffusion coefficient D and a field of force $\boldsymbol{f}(\boldsymbol{X})$,

$$\dot{\boldsymbol{X}} = \frac{\boldsymbol{f}(\boldsymbol{X})}{\gamma} + \sqrt{2D}\dot{\boldsymbol{w}}, \tag{5.1}$$

D. Holcman, Z. Schuss, *Stochastic Narrow Escape in Molecular and Cellular Biology*, DOI 10.1007/978-1-4939-3103-3_5

where $\dot{\boldsymbol{w}}$ is a vector of independent standard δ-correlated Gaussian white noises and γ is the dynamical viscosity (Schuss 2010b). Impenetrable obstacles, mostly due to dielectric forces, are coarse-grained into a no-flux boundary condition on the boundaries of the obstacles instead of expressing the repulsion of the obstacle in terms of high potential barriers. To account for the local crowding organization, Eq. (5.1) is coarse-grained on a coarser spatiotemporal scale into an effective stochastic equation as (see Hoze et al. 2012)

$$\dot{\boldsymbol{X}} = \boldsymbol{b}(\boldsymbol{X}) + \sqrt{2}\boldsymbol{B}_e(\boldsymbol{X})\,\dot{\boldsymbol{w}}, \tag{5.2}$$

with the empirical drift field $\boldsymbol{b}(\boldsymbol{X})$ and diffusion matrix $\boldsymbol{B}_e(\boldsymbol{X})$, where the effective diffusion tensor $\boldsymbol{D}_e(\boldsymbol{X}) = \frac{1}{2}\boldsymbol{B}_e(\boldsymbol{X})\boldsymbol{B}_e^T(\boldsymbol{X})$ can be expressed in terms of the more microscopic diffusion coefficient D and in terms of the density and geometry of obstacles (see Sect. 4.3.2). The effective diffusion coefficient can be state-dependent whereas the friction coefficient γ, measuring local interaction remains constant. Obviously, the impenetrable obstacles that slow the effective diffusion down affect neither the microscopic physical properties of the diffusing particle nor those of the membrane.

The coefficients of (5.1) can be estimated statistically at each point of the membrane $\boldsymbol{X} = (X^1, X^2)^T$ from a sufficiently large sample of its trajectories, sampled with microscopic resolution in the neighborhood of the point $\boldsymbol{X}$ at time t. Specifically, setting $\Delta\boldsymbol{X}(t) = \boldsymbol{X}(t+\Delta t) - \boldsymbol{X}(t)$, the coefficients are given by Schuss (2010b, 2012)

$$\frac{\boldsymbol{f}(\boldsymbol{X})}{\gamma} = \lim_{\Delta t\to 0}\frac{1}{\Delta t}\mathbb{E}[\Delta\boldsymbol{X}(t)\,|\,\boldsymbol{X}(t) = \boldsymbol{X}], \tag{5.3}$$

and

$$2D^{ij}(\boldsymbol{X}) = \lim_{\Delta t\to 0}\frac{1}{\Delta t}\mathbb{E}[\Delta X^i(t)\Delta X^j(t)\,|\,\boldsymbol{X}(t) = \boldsymbol{X}]. \tag{5.4}$$

In practice, the expectations are estimated by sample averages and Δt is the time-resolution of the recording of the trajectories. In effect, the coarse-grained coefficients of (5.2) are estimated, as described below.

5.1.1 The Empirical Moments

The data set for estimating the coarse-grained expectations (5.3) and (5.4) consists of a large number of short trajectories of receptors moving on neuronal membranes (5 points sampled on the average every 50 ms), generated the above-mentioned sptPALM method. To estimate the expectations in (5.3) and (5.4), the ensemble of points is used, where the number of trajectories passing through a given

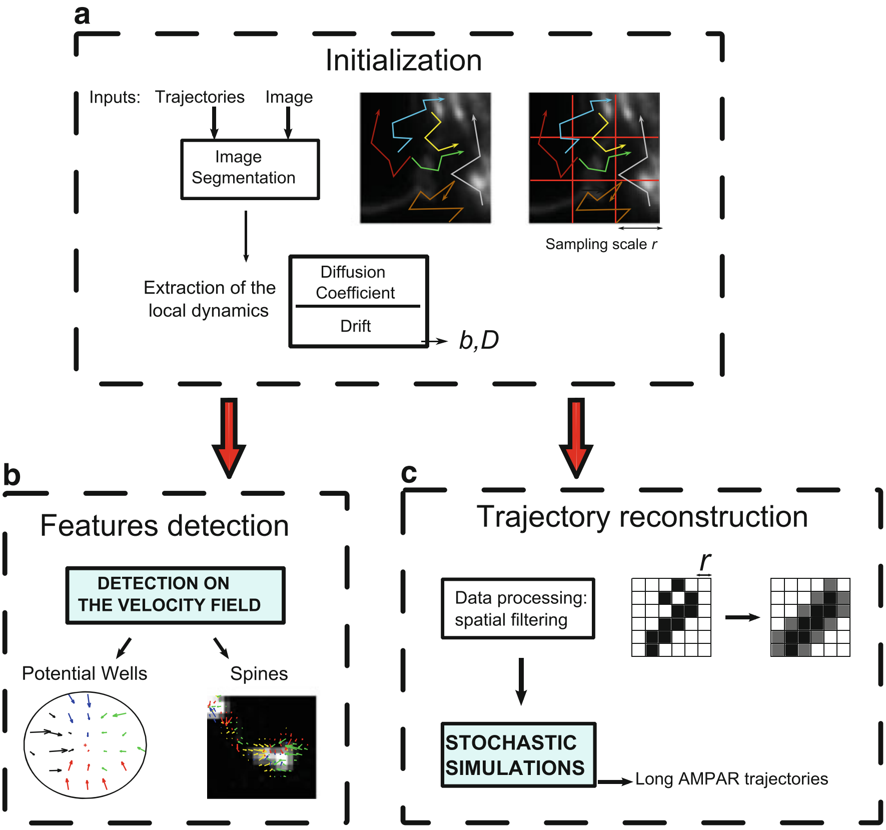

Fig. 5.1 Schematic representation of the estimation algorithm. (**a**) Receptor trajectories recorded in the confocal image of a neuron. The image is decomposed into squares of side r. The estimated components of the drift $\boldsymbol{b}(\boldsymbol{X})$ and diffusion tensor $\boldsymbol{D}_e(\boldsymbol{X})$ are computed according to (5.5) and (5.6), respectively. (**b**) Specific features of the neuron, such as potential wells and properties of dendritic spines, can be detected from the drift field $\boldsymbol{b}(\boldsymbol{X})$. (**c**) Sequential spatial filters require the simulations of trajectories and the re-computation of local values of the drift and diffusion tensor. Trajectories are simulated by Euler's scheme for the stochastic equation (5.2) in the empirical domain for any length of time. Potential wells can be identified by longer dwell times in their domains of attraction

neighborhood of each point is statistically sufficient (around 200). These short trajectories cover only a very small fraction of the space and cannot be used directly to obtain estimates about transition properties between any given regions of interest.

The expectations (5.3) and (5.4) are estimated by the local coarse-grained drift $\boldsymbol{b}(\boldsymbol{X})$ and diffusion tensor $\boldsymbol{D}_e(\boldsymbol{X})$, respectively, at a given resolution, which is the size of the squares $S(\boldsymbol{X}_c, r)$ of side r and center at $\boldsymbol{X}_c$, as described below (Fig. 5.1a). The empirical approximations of (5.3) and (5.4) are discretized in a square $S(\boldsymbol{x}, r)$ of side r centered at $\boldsymbol{X}$. When there are $N(\boldsymbol{X}, r)$ points of sampled trajectories $\boldsymbol{y}_1, \ldots, \boldsymbol{y}_N$ in $S(\boldsymbol{X}, r)$, such that $\boldsymbol{y}_1 = \boldsymbol{X}_{i_1}(t_1), \ldots, \boldsymbol{y}_N = \boldsymbol{X}_{i_N}(t_N)$, the drift $\boldsymbol{b}(\boldsymbol{X}) = \boldsymbol{b}(\boldsymbol{X}, r)$ at position $\boldsymbol{X}$ is approximated by the empirical sum

$$\boldsymbol{b}(\boldsymbol{X}, r) \approx \frac{1}{N(\boldsymbol{X}, r)} \sum_{k=1}^{N(\boldsymbol{X},r)} \frac{\Delta \boldsymbol{X}_{i_k}(t_k)}{\Delta t}. \tag{5.5}$$

As r goes to zero and N is fixed, the quality of the approximation increases.

Similarly, we approximate the tensor $D^{ij}(\boldsymbol{X}) = D^{ij}(\boldsymbol{X}, r)$ at position $\boldsymbol{X}$ and resolution r by

$$2D_e^{ij}(\boldsymbol{x}) \approx \frac{1}{N(\boldsymbol{X}, r)} \sum_{k=1}^{N(\boldsymbol{X},r)} \frac{\Delta \boldsymbol{X}^i(t) \Delta \boldsymbol{X}^j(t)}{\Delta t}. \tag{5.6}$$

The tensor $D_e^{ij}(\boldsymbol{x})$ contains information about the local organization of the neuronal surface. In practice, the diffusion is isotropic and the effective diffusion tensor D_e^{ij} is proportional to the identity matrix.

5.2 Simulations in Empirical Domains

5.2.1 Imaging Analysis, Spatial Filtering, and Discretization

Because the sampled image resolution of the data set is lower than the one of trajectories, there are several artifacts due to the pixelization that are resolved by spatial filtering. Artificial trajectories $\boldsymbol{X}_c(t)$ are generated inside live microscopy empirical images by the empirical equation (5.2). The coefficients $\boldsymbol{b}(\boldsymbol{X})$ and $\boldsymbol{D}_e(\boldsymbol{X})$ are the piecewise constant values of the drift and the diffusion tensor at any point $\boldsymbol{X} \in S(\boldsymbol{X}_c, r)$. This discretization procedure of the space (neuronal dendrite) in small squares $S(\boldsymbol{X}_c, r)$ generates local discontinuities and artificially disconnected regions. These artifacts are overcome by using a sequence of spatial filters. A schematic summary of the algorithm is described in Fig. 5.1.

Construction of the Spatial Filter

The small size of a microdomain is reflected in the small number of pixels dedicated to their representation (around 20–30). This small number poses an additional difficulty in the simulation of stochastic trajectories. Indeed, in a pixelized image, some pixels intersect the region Ω_0 that we shall define here as the set of pixel not covered by experimental trajectories, e.g., at corners, in which case, switching from one pixel to another by a stochastic trajectory corresponds to a very unlikely jump that is a rare event:

$$\Omega_0 = \{S_{i,j} \in \mathcal{E} \text{ such that } \#[X_k \in S_{i,j}] < 15\}. \tag{5.7}$$

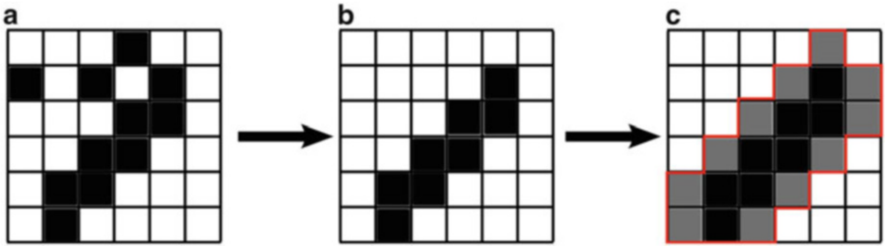

Fig. 5.2 Example of spatial filtering for trajectory simulation. A dendritic spine is pixelized: (**a**) image before reconstruction, (**b**) after suppression of the regions with less than 15 points of trajectories and of isolated regions, and (**c**) after application of the low-pass filter (5.9). The region Ω is in *black* and *gray*, Ω_0 in *white*, and the boundary $\partial\Omega$ is *red*

Consequently, the escape time from such a pixel is a narrow escape time. In that specific case, such trajectory is artificially restricted and the confinement time has no biological relevance. To avoid this confinement, pixels surrounded by the ones in the ensemble Ω_0 or by those touching Ω (the pixel ensemble) at corners are excluded (filtered out, see Fig. 5.2). This exclusion procedure consists in eliminating pixels as follows. A pixel of size r and coordinates (i, j) is suppressed when the four neighbors are in the ensemble Ω_0. In that case, to smooth out the diffusion tensor on the ensemble and to avoid possible jumps due to the discretization procedure at the pixel level, the following local smoothing procedure is applied

$$\begin{cases} D_{i,j}(\boldsymbol{X}) \quad \neq 0 & \text{for } \boldsymbol{X} \in \Omega_0 \\ D_{i+1,j}(\boldsymbol{X}) = D_{i-1,j}(\boldsymbol{X}) = D_{i,j-1}(\boldsymbol{X}) = D_{i,j+1}(\boldsymbol{X}) = 0 & \text{for } \boldsymbol{X} \in \Omega_0, \end{cases} \tag{5.8}$$

where $D_{i,j}(\boldsymbol{X})$ [resp. $\boldsymbol{b}_{i,j}(\boldsymbol{X})$] is the discrete value of the diffusion tensor $\boldsymbol{D}(\boldsymbol{X})$ [resp. drift $\boldsymbol{b}(\boldsymbol{X})$] in the pixel of two-dimensional coordinates (i, j). This procedure corresponds to running a low-pass filter that smoothes out the diffusion and drift coefficient. In fact, the filtered diffusion tensor $\boldsymbol{D}'(\boldsymbol{X})$ is a weighted average on the square centered at (i, j) and on the four adjacent squares, given by

$$D'_{i,j}(\boldsymbol{X}) = \frac{1}{2}D_{i,j}(\boldsymbol{X}) + \frac{1}{8}[D_{i-1,j}(\boldsymbol{X}) + D_{i+1,j}(\boldsymbol{X}) + D_{i,j-1}(\boldsymbol{X}) + D_{i,j+1}(\boldsymbol{X})]. \tag{5.9}$$

To simulate trajectories at each point of the dendrite image, Eq. (5.2) is discretized by Euler's scheme as

$$\boldsymbol{X}(t + \Delta t) = \boldsymbol{X}(t) + \boldsymbol{b}(\boldsymbol{X})\Delta t + \boldsymbol{B}_e(\boldsymbol{X})\sqrt{2\Delta t}\,\boldsymbol{\eta}, \tag{5.10}$$

where $\boldsymbol{\eta}$ is a two-dimensional standard Gaussian random variable and Δt is the simulation time-step. In the region Ω_0, not covered by experimental trajectories, the values $\boldsymbol{B}_e(\boldsymbol{X}) = \boldsymbol{0}$, $\boldsymbol{b}(\boldsymbol{X}) = \boldsymbol{0}$ are chosen. Simulated trajectories are reflected at the boundary $\partial\Omega$ of the pixel ensemble. The squares with insufficient sampling (<15 points) are also added to the uncovered region Ω_0, defined above.

5.2.2 Residence Time of Receptors in Dendritic Spines

The procedure described in Sect. 5.2 is applied in order to estimate the residence time of receptors in a given domain. After estimating the drift and diffusion coefficients, long trajectories are generated from the coarse-grained stochastic equation (5.2) in the chosen dendritic spine geometries. Spines of Type I and Type II (Fig. 5.3a) are chosen with inward and outward drift in the neck. The simulation indicates that the residence time depends on the spine geometry and on the nature of the spine (Fig. 5.3b–d). Residence time of 81 s is found in the Type I spine and of about 279 s for Type II.

To assess the contribution of the drift to the residence time simulations free Brownian trajectories were run. The mean residence time of about 180 s was found for both spine types (see Fig. 5.3e–g). In conclusion, the excess time for Type II is due to the inward drift inside the neck and to an internal potential well in the PSD. Finally, simulations in empirical domains will soon become the gold standard, which allows incorporating geometrical features into molecular dynamics.

5.3 Annotation

In neuronal cells, the regions where the field of force $\boldsymbol{f}(\boldsymbol{X})$ in (5.1) is the gradient of a potential $\boldsymbol{f}(\boldsymbol{X}) = -\nabla U(\boldsymbol{X})$ are mostly synaptic regions, but also other regions have been identified (Hoze et al. 2012; Hoze and Holcman 2014).

▶

Fig. 5.3 are extracted from a data set of single particle trajectories. A trajectory starting at the *red spot* is terminated upon hitting the target area (*red circle*). (**c**) Histograms of the generated residence times showing an asymmetric distribution associated with the different spine types. The values of the rate λ of the exponential decays are indicated. (**d**) Cumulative distribution function of the NET from the spine head. The NET data were generated from 1000 simulated trajectories of (5.2) in each spine. In (**e**–**g**) the drift in (5.2) is set to zero

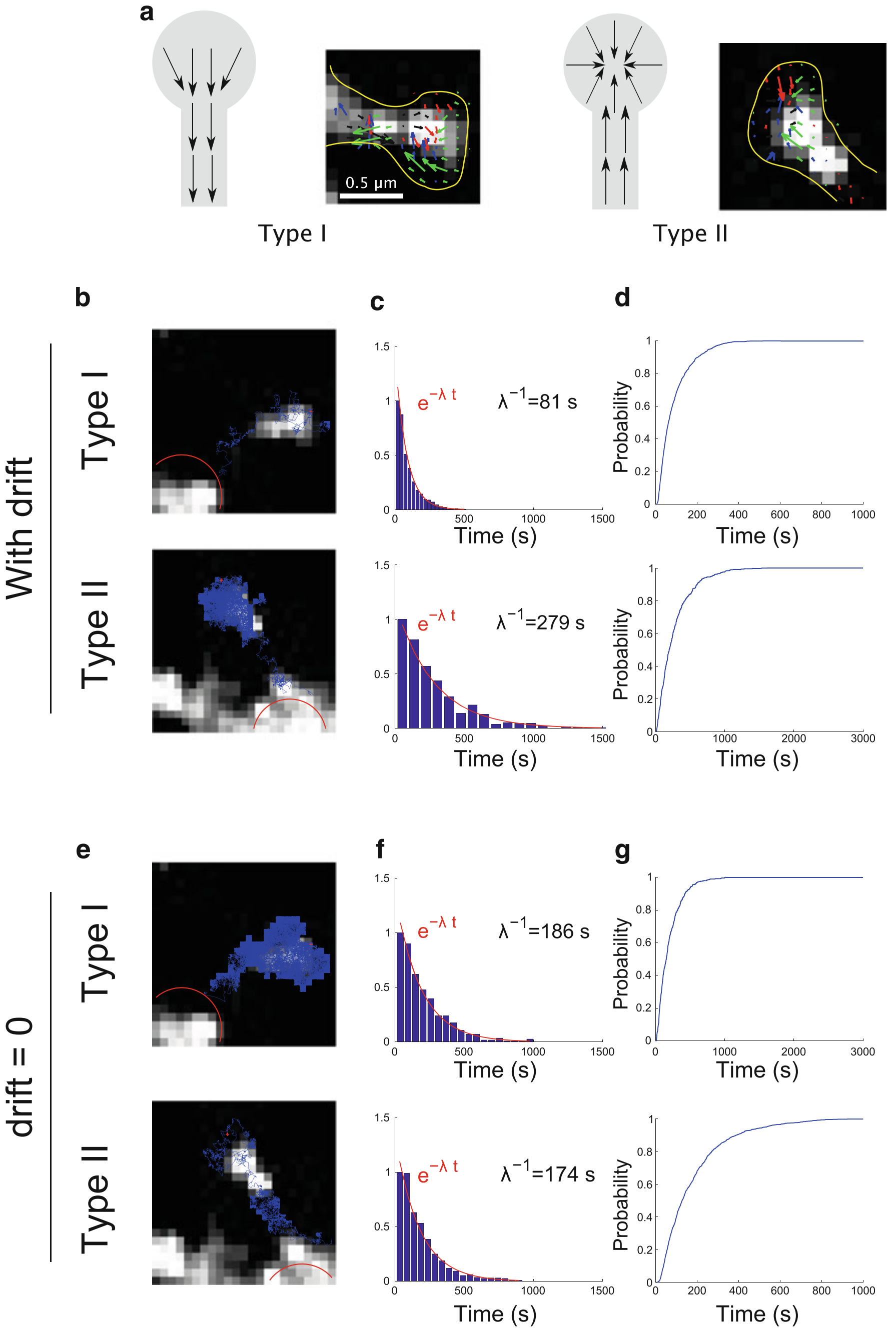

Fig. 5.3 Residence time of a receptor in a dendritic spine obtained by numerical simulations. (**a**) Two types of spines: Type I and Type II spines are characterized by outward and inward drifts, respectively. (**b**) Simulations of trajectories of (5.2) exiting Type I and a Type II spines. Parameters

Chapter 6
Markov Models for Stochastic Chemical Reactions

Traditional chemical kinetics, based on mass action laws or reaction-diffusion equations, provide a deficient description of stochastic chemical reactions in micro-domains, where only a small number of substrate and reactant molecules are involved. The small populations of reactant and substrate give rise to large fluctuations in the number of bound substrate sites that can be manifested as large noise in the efflux and influx of ions through open membrane channels and in other cellular functions. Coarse-graining the binding and unbinding reactions to the time scale of the MFPT of the diffusing reactant into and out of a binding site leads to a Markovian jump process description of the stochastic dynamics of the binding and unbinding of molecules. The goal of this chapter is to present such approach.

6.1 Stochastic Chemical Reactions

6.1.1 Introduction to Stochastic Chemical Reactions

Consider the simplest example of two finite species, the mobile reactant M, which diffuses freely in a bounded domain Ω, and the stationary substrate S (e.g., a protein), which binds M. The boundary $\partial\Omega$ of Ω is partitioned into an absorbing part $\partial\Omega_a$ (e.g., protein channels, pumps, exchangers, another substrate that forms permanent bonds with M, and so on) and a reflecting part $\partial\Omega_r$ (e.g., a cell membrane). In this model the volume of species M is neglected. In terms of traditional chemical kinetics the binding of M to S follows the law

$$M + S_{\text{free}} \underset{k_{-1}}{\overset{k_1}{\rightleftharpoons}} MS, \tag{6.1}$$

D. Holcman, Z. Schuss, *Stochastic Narrow Escape in Molecular and Cellular Biology*, DOI 10.1007/978-1-4939-3103-3_6

where k_1 is the forward binding rate constant, k_{-1} is the backward binding rate constant, and S_{free} is the unbound substrate. We assume in our model of the reaction that the M molecules diffuse in Ω independently of each other and when bound, are released independently of each other at exponential waiting times with rate k_{-1}.

The time to binding of a single M molecule is the first passage time to diffuse to a small portion of the boundary, $\partial\Omega_a$, which is absorbing and represents the active surface of the free substrate (receptor), whereas the remaining part of $\partial\Omega$ is reflecting. Thus it is the NET to $\partial\Omega_a$. Due to the small target and to the deep binding potential well of the binding site, the binding and unbinding of M to S are rare events on the time scale of diffusion (Schuss et al. 2007). This implies that the probability distribution of binding times is approximately exponential (Schuss 2010b) with rate $\lambda_1 = 1/\bar{\tau}_1$, where $\bar{\tau}_1$ is the MFPT to $\partial\Omega_a$. When there are S binding sites, $k(t)$ of which are unbound, there are $N = [M-S+k]^+ = \max\{0, M-S+k\}$ free diffusing molecules in Ω. The arrival time of a molecule to the next unbound site is well approximated by an exponential law with state-dependent instantaneous rate (see discussion in Holcman and Schuss 2005b)

$$\lambda_k = \frac{Nk}{\bar{\tau}_1} = \frac{k(M-S+k)^+}{\bar{\tau}_1}.$$

The number $k = k(t)$ of unbound receptors at time t is a Markovian birth–death process with states $0, 1, 2, \ldots, \max\{M-S, 0\}$ and transition rates $\lambda_{k\to k+1} = \lambda_k$, $\lambda_{k\to k-1} = \mu = k_{-1}$. The boundary conditions are $\lambda_{S\to S+1} = 0$ and $\lambda_{0\to -1} = 0$. Setting $P_k(t) = \Pr\{k(t) = k\}$, the Kolmogorov equations for the transition probabilities take the form

$$\dot{P}_k(t) = -\left[\lambda_k + k_{-1}(S-k)\right] P_k(t) + \lambda_{k+1}P_{k+1}(t) + k_{-1}(S-k+1)P_{k-1}(t) \tag{6.2}$$

for $k = (S-M)^+ + 1, \ldots, S-1$, with the initial and boundary equations

$$\begin{aligned} P_{k,q}(0) &= \delta_{k,S}\delta_{q,0} \\ \dot{P}_{(S-M)^+}(t) &= -k_{-1}SP_{(S-M)^+}(t) + \lambda_1 P_{(S-M)^+ +1}(t) \\ \dot{P}_S(t) &= -\lambda_S P_S(t) + k_{-1}P_{S-1}(t). \end{aligned} \tag{6.3}$$

Our purpose is to calculate the average number of unbound (or bound) sites $\bar{k}(t)$, which for $t \to \infty$ is given by $\bar{k}_\infty = \sum_{j=(S-M)^+}^{S} jP_j$, where $P_j = \lim_{t\to\infty} P_j(t)$. Similarly, the stationary variance of the number of unbound sites is $\sigma^2(M,S) = \bar{k^2_\infty} - (\bar{k}_\infty)^2$, where $\bar{k^2_\infty} = \sum_{j=(S-M)^+}^{S} j^2 P_j$. The results of the Markovian model (6.2)–(6.3), using a direct induction from the steady state equations, are

$$P_S = \frac{1}{1 + \displaystyle\sum_{k=1}^{S-(S-M)^+} \frac{\prod_{i=S-k+1}^{S} i(M-S+i)^+}{k!(\bar{\tau}_1 k_{-1})^k}}$$

$$\langle k_\infty \rangle = P_S \sum_{k=S-1}^{(S-M)^+} (S-k)^+ \frac{\prod_{i=S-k+1}^{S} i(M-S+i)^+}{k!(\bar{\tau}_1 k_{-1})^k}$$

$$\langle k_\infty^2 \rangle = P_S \sum_{k=S-1}^{(S-M)^+} [(S-k)^+]^2 \frac{\prod_{i=S-k+1}^{S} i(M-S+i)^+}{k!(\bar{\tau}_1 k_{-1})^k}$$

$$\sigma_S^2(M) = \langle k_\infty^2 \rangle - \langle k_\infty \rangle^2, \tag{6.4}$$

see Holcman and Schuss (2005b) for further details.

6.1.2 The Mean Time the Number of Bound Molecules Reaches a Threshold

Another application of the Markovian model is the calculation of the mean time the number of bound molecules reaches a threshold (MTT). In a cellular context, the MTT can be used to characterize the stability of chemical processes, especially when they underlie a biological function. The above Markovian description leads to an estimate of the MTT in terms of fundamental parameters, such as the number of molecules, of ligands, and of the forward and backward binding rates. As shown next, the MTT depends nonlinearly on the threshold T.

Consider M Brownian particles (e.g., molecules) that can bind to immobile targets S in a microdomain. The number $[MS](t)$ of MS bound particles at time t is modeled generically by Eq. (6.1). The first time the number $[MS](t)$ reaches the threshold T is defined as

$$\tau_T = \inf\{t > 0 : [MS](t) = T\} \tag{6.5}$$

and its expected value is $\mathbb{E}\,\tau_T = \bar{\tau}_T$. We consider $\bar{\tau}_T$ for an ensemble of initially free targets distributed on the surface of a closed microdomain, assuming first a vanishing backward rate $k_{-1} = 0$ and then assuming $k_{-1} > 0$. The dynamical system for the transition probabilities of the Markov process $MS(t)$ is similar to that in (6.1), but for the absorbing boundary condition at the threshold T, which gives (6.2) (see Dao Duc and Holcman 2010). When the binding is irreversible ($k_{-1} = 0$), $\bar{\tau}_T$ is the sum of the forward rates

$$\tau_T^{\text{irrev}} = \frac{1}{\lambda_0} + \frac{1}{\lambda_1} + \cdots + \frac{1}{\lambda_{T-1}} = \frac{1}{\lambda} \sum_{k=0}^{T-1} \frac{1}{(M_0 - k)(S_0 - k)}. \tag{6.6}$$

In particular, when $M_0 = S_0$ and $M_0 \gg 1$ (6.6) becomes asymptotically $\tau_T^{\text{irrev}} \approx T/\lambda M_0(M_0 - T)$. In addition, when the diffusing molecules largely exceed the number of targets ($M_0 \gg S_0, T$), Eq. (6.6) gives the asymptotic formulas

$$\tau_T^{\text{irrev}} \approx \begin{cases} \dfrac{1}{\lambda M_0} \log \dfrac{S_0}{S_0 - T} & \text{for } M_0 \gg S_0, T \\[2ex] \dfrac{1}{\lambda S_0} \log \dfrac{M_0}{M_0 - T} & \text{for } S_0 \gg M_0, T \\[2ex] \dfrac{T}{\lambda M_0 S_0} & \text{for } M_0, S_0 \gg T. \end{cases} \tag{6.7}$$

Figure 6.1 shows the plot of τ_T^{irrev} for several values of the threshold T, compared to Brownian simulations in a circular disk $\Omega = D(R)$ with reflecting boundary, except at the targets.

When $k_{-1} > 0$, the asymptotic formulas are given by Dao Duc and Holcman (2010)

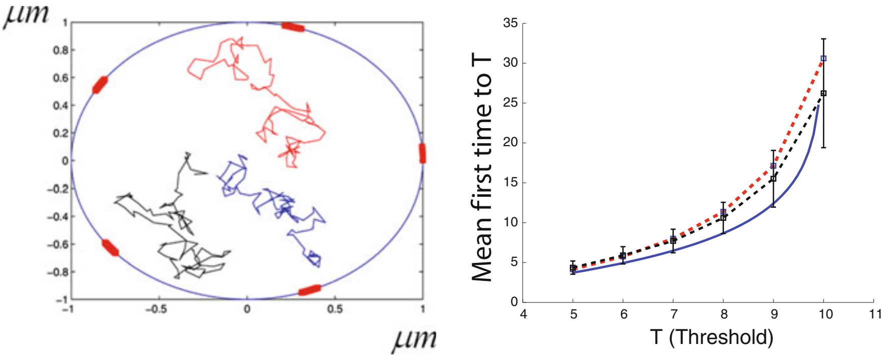

Fig. 6.1 *Left*: trajectories of diffusing molecules in a circular disk containing five binding sites on the boundary. *Right*: MFPT τ_T^{irrev} to threshold T as a function of T in the irreversible case ($k_{-1} = 0$). Brownian simulations (*blue dash*), formula (6.6) (*black dash*), and its approximation (6.7) (*continuous blue line*). The other parameters are $S_0 = 15$, $M_0 = 10$, $\varepsilon = 0.05$, $D = 0.1\,\mu\text{m}^2\,\text{s}^{-1}$ and the radius of the disk is $R = 1\,\mu$m (200 runs)

$$\bar{\tau}_T \approx \begin{cases} \tau_T^{\text{irrev}} + \dfrac{k_{-1}}{(\lambda M_0)^2}\left[\dfrac{T}{S_0 - T} - \log\left(1 + \dfrac{T}{S_0 - T}\right)\right] & \text{for } M_0 \gg S_0, T \\ \tau_T^{\text{irrev}} + \dfrac{k_{-1}}{(\lambda S_0)^2}\left[\dfrac{T}{M_0 - T} - \log\left(1 + \dfrac{T}{M_0 - T}\right)\right] & \text{for } S_0 \gg M_0, T \\ \tau_T^{\text{irrev}} + \dfrac{k_{-1}}{2\lambda^2}\left(\dfrac{T}{M_0^2}\right)^3 & \text{for } S_0 = M_0 \gg T. \end{cases}$$

Thus $\bar{\tau}_T$ varies quadratically with the MFPT $\bar{\tau} = 1/\lambda$, and is a nonlinear increasing function of T. These computations are quite general and can be applied to describe the mean time to reach a threshold for any chemical reaction. Changing the threshold modulates the threshold time in an efficient way.

6.2 Applications of MTT in Cell Biology

Two applications of the above Markovian approximation concern new predictions of the rate of molecular dynamics that underlies the spindle assembly checkpoint (SAC) during cell division and the probability that a messenger RNA (mRNA) escapes degradation through binding a certain number of microRNAs (miRNA) (see Wikipedia) and are discussed below. Recall that during the process of cell division, the spindle checkpoint (see Wikipedia) prevents separation of the duplicated chromosomes until each chromosome is properly attached to an apparatus called the spindle apparatus.

6.2.1 Escaping Degradation by Binding microRNAs

mRNA is responsible for protein production, but its binding by miRNA results in permanent repression. However, when binding sites are blocked, miRNAs cannot bind to their targets. Specific decoy RNAs ("decoys") bind competitively to the same sites as miRNAs, thereby interfering with miRNA–mRNA interactions. If these decoys block the binding sites of mRNAs, they will be up-regulated, because there will be fewer opportunities for miRNAs to bind and repress mRNA translation. A schematic is shown in Fig. 6.2 for the case of phosphatase and tensin homologs (PTENs) mRNAs.

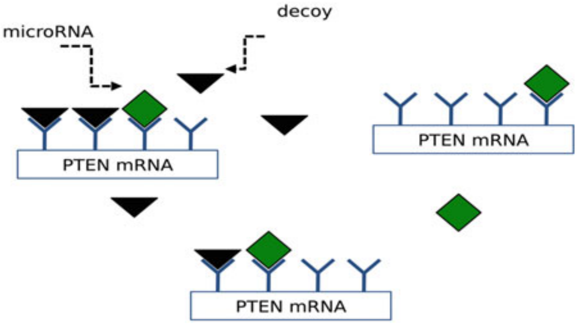

Fig. 6.2 Schematic of the miRNA-PTEN post-transcriptional regulatory process, with miRNAs and decoys competing for binding to PTEN mRNA

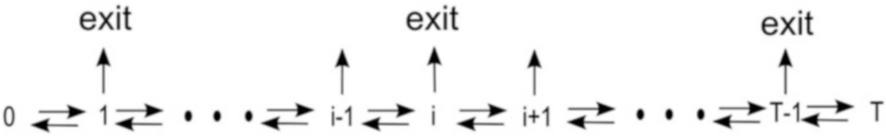

Fig. 6.3 Markov chain diagram for the mRNA state (no decoys)

Escaping Degradation with siRNA Only

Silencing RNA (siRNA) is a class of RNA that interferes with the expression of specific genes (see Wikipedia). We study the escape of mRNA from the nucleus through small nuclear pores before it is degraded by siRNAs. First, we consider the case that there are no decoys in the system, which we study through the process of RNA interference (RNAi) in the nucleus. The model accounts for multiple siRNA binding sites on the mRNA. When the number S of siRNAs bound to an mRNA exceeds a given threshold T the mRNA is considered to be degraded. When an siRNA occupies a site, no other siRNA can bind to this site. We assume that siRNAs diffuse freely in the nucleus and that siRNA-mRNA binding is irreversible. The aim of the model is to compute the escape probability P_a that an mRNA exits the nucleus intact, that is, it escapes through a nuclear pore before binding T siRNAs (see Fig. 6.3). Specifically, we assume in our model of the degradation reaction that M mobile reactant mRNA molecules diffuse independently of each other in a microdomain Ω and bind to S stationary sites. When bound, they are released independently of each other at exponential waiting times with rate k_{-1}. The number $k(t)$ of unbound sites at time t is a Markovian birth–death process with states $0, 1, 2, \ldots, \min\{M, S\}$ and transition rates $\lambda_{k\to k+1} = \lambda_k,\ \lambda_{k\to k-1} = k_{-1}$.

The reduced Markovian model is used for the calculation of the mean time of the number of bound molecules to reach a given threshold T. When there are only degrading miRNAs, the probability P_e that an mRNA exits the nucleus alive is computed from the joint probability density that the mRNA is at $\boldsymbol{x}$ and that there are k bound miRNAs. In terms of the diffusion process $\boldsymbol{X}(t)$ of a siRNA, with killing at the threshold, the joint survival probability and density of $\boldsymbol{X}(t)$ is given by

$$\Pr\{\boldsymbol{X}(t) \in \boldsymbol{x} + d\boldsymbol{x}, k(t) = k\} = p_k(\boldsymbol{x}, t)\, d\boldsymbol{x}. \tag{6.8}$$

When there are less than $T-1$ bounds, the mRNA is still alive, but it is degraded at the threshold T. The survival probability in the nucleus (before reaching the threshold) is the marginal

$$S_k(t) = \int\limits_{\Omega} \Pr\{\boldsymbol{X}(t) \in \boldsymbol{x} + d\boldsymbol{x}, k(t) = k\}\, d\boldsymbol{x}. \tag{6.9}$$

The probability that the mRNA exits the nucleus alive at time t with k bound sites is

$$\Pr\{\text{mRNA exits at time } t, k(t) = k\} = J_k(t), \tag{6.10}$$

where the instantaneous flux is $J_k(t) = \int_{\partial\Omega} \partial p_k(\boldsymbol{x}, t)/\partial n\, dS_{\boldsymbol{x}}$. Finally, the probability that the mRNA exits alive is the sum over all possibilities that $k < T$ sites are bound, $P_a(t) = \sum_0^{T-1} J_k(t)$. The overall probability that an mRNA exits alive is therefore

$$P_a = \int\limits_0^{\infty} P_a(t)\, dt. \tag{6.11}$$

In the narrow escape approximation $\lambda_k = \bar{\tau}^{-1}$ the exit time is exponentially distributed and the survival probability with k bound sites, $p_k(t) = \int_\Omega p_k(\boldsymbol{x}, t)\, d\boldsymbol{x}$, satisfies the Kolmogorov equations for the Markov process $k(t)$

$$\begin{aligned}
\dot{p}_k(t) =& -\left(\frac{1}{\bar{\tau}} + kk_{-1} + (S-k)k_f\right) p_k(t) + k_f(S-k+1)p_{k-1}(t) \\
&+ (k+1)k_{-1}p_{k+1}(t) \\
\dot{p}_0(t) =& -\left(\frac{1}{\bar{\tau}} + Sk_f\right) p_0(t) + k_{-1}p_1(t) \\
\dot{p}_{T-1}(t) =& -\left(\frac{1}{\bar{\tau}} + (T-1)k_{-1} + (S-T+1)k_f\right) p_{T-1}(t) \\
&+ k_f(S-T+2)p_{T-2}(t) \\
\dot{p}_T(t) =& \, k_f(S-T+1)p_{T-1}(t),
\end{aligned} \tag{6.12}$$

where we assume that the transition rate from state T to $T-1$ is zero. The exiting-alive probability is given by

$$P_a = \frac{1}{\bar{\tau}} \sum_0^{T-1} \int\limits_0^{\infty} p_k(t)\, dt. \tag{6.13}$$

In the irreversible case, $k_b^s = 0$, defining the probability of an alive mRNA with s bound siRNAs within the domain at any given time t, as

$$a_s = \int_0^\infty p_s^S(t)dt, \tag{6.14}$$

the system (6.12) gives

$$0 = -\frac{1}{\bar{\tau}} a_s - k_f(N_0 - s)a_s + k_f(N_0 - s + 1)a_{s-1} \text{ for } 0 < s < T - 1, \tag{6.15}$$

with $a_T = 0$, and the conditions (6.3) reduce to

$$-1 = -\frac{1}{\bar{\tau}} a_0 - k_f N_0 a_0 \tag{6.16}$$

$$0 = -\frac{1}{\bar{\tau}} a_{T-1} - k_f(N_0 - T + 1)a_{T-1} + k_f(N_0 - T + 2)a_{T-2} \tag{6.17}$$

$$p_T^S(\infty) = k_f(N_0 - T + 1)a_{T-1}. \tag{6.18}$$

The initial condition is $p_s^V(0) = \delta_s$, because initially the mRNA is not bound by any siRNAs. The escape probability is given by

$$P_a = \frac{1}{\bar{\tau}} \sum_{k=0}^{T-1} a_s, \tag{6.19}$$

while the conservation of probability leads to the relation

$$P_a + p_T^S(\infty) = 1. \tag{6.20}$$

A direct solution of (6.15) and (6.16) gives

$$a_s = \frac{k_f(N_b - s + 1)}{1/\bar{\tau} + k_f(N_b - s)} a_{s-1} \text{ for } s < T, \tag{6.21}$$

where $a_0 = \bar{\tau}/(1 + k_f N_b \bar{\tau})$. Thus,

$$a_s = k_f^k \frac{(N_b)!}{(N_b - s)!} \prod_{j=0}^{s} \frac{1}{1/\bar{\tau} + k_f(N_b - j)}. \tag{6.22}$$

Using (6.19) and (6.22), the probability that the mRNA escapes the domain intact is given by

$$P_a(T, N_b, x) = \sum_{s=0}^{T-1} x^s \frac{N_b!}{(N_b - s)!} \prod_{j=0}^{s} \frac{1}{1 + (N_b - j)x}, \tag{6.23}$$

where $x = \bar{\tau} k_f$.

The reversible case is technically more difficult and Eq. (6.15) becomes

$$0 = -\frac{1}{\bar{\tau}} a_s - k_f(N_b - s)a_s - k_b^s s a_s + k_b^s(s+1)a_{s+1} + k_f(N_b - s + 1)a_{s-1}, \tag{6.24}$$

with boundary conditions

$$\begin{aligned} -1 &= -\frac{1}{\bar{\tau}} a_0 - k_f N_b a_0 + k_b^s a_1 \\ 0 &= -\frac{1}{\bar{\tau}} a_{T-1} - k_f(N_b - T + 1)a_{T-1} - k_b^s(T-1)a_{T-1} \\ &\quad + k_f(N_b - T + 2)a_{T-2} \\ p_T^S(\infty) &= k_f(N_b - T + 1)a_{T-1}. \end{aligned}$$

Note that (6.24) can be written in matrix form as

$$\boldsymbol{M} \begin{pmatrix} a_0 \\ a_1 \\ \vdots \\ a_{T-1} \end{pmatrix} = \begin{pmatrix} -1 \\ 0 \\ \vdots \\ 0 \end{pmatrix} \tag{6.25}$$

with the tridiagonal matrix

$$\boldsymbol{M} = \begin{pmatrix} \alpha_0 & \beta_1 & 0 & & \dots & 0 \\ \gamma_1 & \alpha_1 & \beta_2 & 0 & (0) & \\ 0 & \ddots & \ddots & \ddots & \ddots & \vdots \\ & \ddots & \ddots & \ddots & \ddots & 0 \\ \vdots & (0) & \ddots & \ddots & \ddots & \beta_{T-1} \\ 0 & \dots & & 0 & \gamma_{T-1} & \alpha_{T-1} \end{pmatrix}, \tag{6.26}$$

where

$$\alpha_i = -\left(\frac{1}{\bar{\tau}} + \beta_i + \gamma_{i+1}\right), \quad \beta_i = k_b^s i, \quad \gamma_i = (N_b - i + 1)k_f. \tag{6.27}$$

Thus, the probability to reach the threshold T is given by

$$P_T = k_f(N_b - T + 1)a_{T-1} = -k_f(N_b - T + 1)m_{T1}^{-1}, \tag{6.28}$$

where $m^{-1}_{ij} = (\boldsymbol{M}^{-1})_{ij}$ for $1 \le i, j \le T$. A direct computation gives

$$m^{-1}_{T1} = \frac{(-1)^{T+1} \prod_{k=1}^{T-1} \gamma_k}{\theta_T}, \tag{6.29}$$

where the sequence $(\theta_n)_{n \in \mathbb{N}}$ satisfies the recursion relation with polynomial coefficients, given by

$$\theta_i = \alpha_{i-1}\theta_{i-1} - \beta_{i-1}\gamma_{i-1}\theta_{i-2}, \tag{6.30}$$

with $\theta_0 = 1$ and $\theta_1 = \alpha_0$ (Usmani 1994). Using (6.27), we obtain

$$P_T(\infty) = \frac{k_f^T N_b!}{(N_b - T)! u_T}, \tag{6.31}$$

where the sequence u_n satisfies for $i > 1$

$$u_{i+1} = \left(\frac{1}{\bar{\tau}} + k_b^s i + k_f(N_b - (i+1) + 1) \right) u_i + k_b^s k_f i (N_b - i + 1) u_{i-1},$$

with $u_0 = -1$ and $u_1 = \bar{\tau}^{-1} + k_f N_b$. However, the series u_n cannot be obtained explicitly in a simple closed form. As a particular example, $T = 3$ gives

$$P_T(\infty) = \frac{\bar{k}_f^{\,3} N_b(N_b - 1)(N_b - 2)}{Q(\bar{k}_f, \bar{k}_b^s N_b)}, \tag{6.32}$$

where

$$\begin{aligned} Q(\bar{k}_f, \bar{k}_b^s, N_b) =& 1 + \bar{k}_f \sum_{0 \le i \le 2} (N_b - i) + \bar{k}_f^{\,2} \sum_{0 \le i \ne j \le 2} (N_b - i)(N_b - j) \\ & + \bar{k}_b^s [3 + 2\bar{k}_b^s + \bar{k}_f(2N_b^2 + 2\bar{k}_f N_b(N_b - 1) + 5N_b - 6)] \\ & + \bar{k}_f^{\,3} N(N_b - 1)(N_b - 2). \end{aligned}$$

and

$$\bar{k}_f = k_f \bar{\tau}, \quad \bar{k}_b^s = k_b^s \bar{\tau}. \tag{6.33}$$

The survival probability P_a can be computed in general using Gillespie's stochastic simulation algorithm (SSA) (Gillespie 1976) (see Fig. 6.4). Figure 6.4b shows the good agreement between the analytical expression (6.28) and the results of the SSA. Compared with irreversible binding ($k_b^s = 0$), the survival probability is relatively insensitive to the values of the escape time, τ, when τ is small compared to the chemical times $(k_b^s)^{-1}$ and $(k_f)^{-1}$ (Fig. 6.4a, b for $\bar{\tau} k_f = 0.1$). Indeed, when the

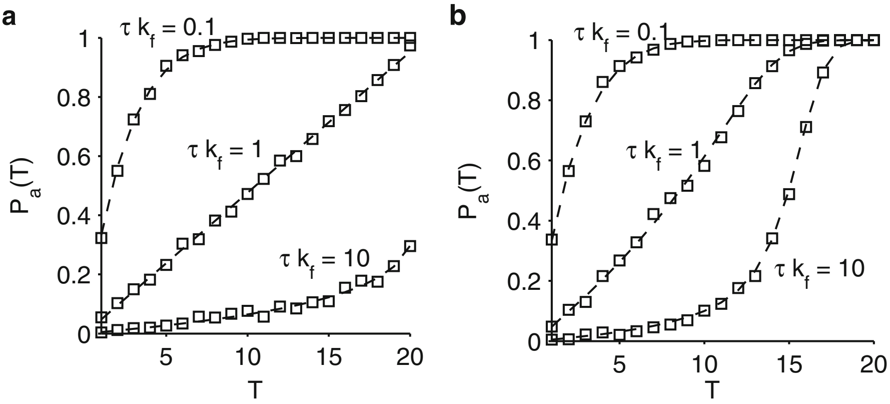

Fig. 6.4 Escape probability as a function of the threshold T (bound miRNAs) for the RNAi problem (no decoys). (**a**) Comparison between stochastic simulations (*square*) and analytical formula (6.23) (*dotted line*) in the irreversible binding case for different values of $x = \tau = 0.1, 1, 10$. (**b**) Same as in (**a**) but with reversible binding case and a comparison with analytical formula (6.28). For each value of T the number of SSA simulations is 1000 with $N_b = 20$ and $k_b^s = k_f = 1$

escape time is short compared to the binding and unbinding times, the miRNAs generally have no time to unbind before the mRNA exits. However, as the mean escape time $\bar{\tau}$ increases, the number of bound miRNAs increases and thus unbinding affects the probability of absorption. These changes become apparent for a high threshold value. Thus unbinding can delay the time to reach the threshold, enabling the mRNA to escape with higher probability than in the irreversible case.

6.2.2 2D-Markov Chain Model of mRNA Escaping Degradation

A more general model of the safe delivery of a PTEN mRNA to the endoplasmic reticulum (ER), by binding to a ribosome (represented by a small, stationary target within the cytoplasm) assumes that mRNAs have binding sites which are complementary to two types of small RNAs: miRNAs, denoted s, which can repress the mRNA, and decoys, denoted d, which can protect the mRNA from repression by blocking the binding sites. We assume that when a decoy is bound to a site, no miRNA can bind to that site, and vice versa. In general, miRNAs and decoys compete for the same binding sites: when the number of miRNAs bound to an mRNA exceeds a certain threshold, T, the mRNA is considered to be irreversibly repressed. Small RNAs diffuse freely with diffusion coefficient D_s, confined to a domain, are present in large proportion relative to the number of mRNAs. The mRNA diffusion process $\boldsymbol{x}(t)$ has diffusion coefficient D_m. The diffusion coefficient of the small RNAs is much bigger than that of mRNAs ($D_s \gg D_m$). Each mRNA has a finite and small number of binding sites, N_b (assumed to be in the range of 10–20). The PTEN model assumes that these interactions between the mRNA, miRNA, and decoys are taking place in the cytoplasm.

The state of each mRNA can be described by the probability density function

$$Pr\{\boldsymbol{x}(t) \in \boldsymbol{x} + d\boldsymbol{x}, s(t) = s, d(t) = d\} = p(\boldsymbol{x}, s, d, t)d\boldsymbol{x}, \tag{6.34}$$

which represents the probability that an mRNA is found at position $\boldsymbol{x}$ at time t with s miRNAs and d decoys bound. When the number of bound miRNAs, s, reaches a threshold, T, the mRNA is repressed. The master equation for the three-dimensional pdf $p(\boldsymbol{x}, s, d, t)$ of the Markov process $(\boldsymbol{x}(t), s(t), d(t))$ (6.34) is derived under the standard assumption (Schuss 2010b) that in the time interval $[t, t+\Delta t]$, the processes $s(t)$ and $d(t)$ of bound miRNAs and decoys, respectively, an miRNA or decoy can bind with rate $k_f(N_b - s - d)\Delta t$. An miRNA (or decoy) can unbind with rate $k_b^s s\Delta t$ (or $k_b^d d\Delta t$). A more detailed description of the derivation of the joint pdf is given in Dao Duc and Holcman (2010). The mathematical difficulty and novelty here is to examine the master equation at the reaction boundaries (see Holcman et al. 2014). The subscript $\{s, d\}$ represents that there are s miRNAs and d decoys bound to the mRNA, with $s \in [0, T]$ and $d \in [0, N_b - s]$).

The survival probability of mRNA with s miRNA and d decoys at time t, given its initial position $\boldsymbol{x}_0 \in \Omega$, is given by

$$p^S(s, d, t \,|\, \boldsymbol{x}_0) = \int_\Omega p(\boldsymbol{x}, s, d, t \,|\, \boldsymbol{x}_0)\, d\boldsymbol{x}. \tag{6.35}$$

The conditional probability efflux density $J(s, d, t \,|\, \boldsymbol{x}_0)$ is defined as the instantaneous arrival rate of an mRNA to a target with s miRNAs and d decoys bound,

$$J(s, d, t \,|\, \boldsymbol{x}_0) = -\frac{\partial p^S(s, d, t \,|\, \boldsymbol{x}_0)}{\partial t}. \tag{6.36}$$

Binding to targets is a rare event, because targets occupy only a small fraction of the domain. Therefore, the efflux density can be approximated in the small hole limit as

$$J_{s,d}(t) = \frac{1}{\bar{\tau}} p^S_{s,d}(t), \tag{6.37}$$

where $\bar{\tau}$ is the mean arrival time of an mRNA to a target. This MFPT is independent of the number of bound miRNAs/decoys, but dependent on the diffusion properties of the mRNA and on the number of targets. For constant isotropic diffusion, $\bar{\tau}$ has been calculated for various geometries and binding site configurations (Holcman and Schuss 2013a). The survival probability of a live mRNA in the domain at time t, given by (6.35), satisfies the master equation,

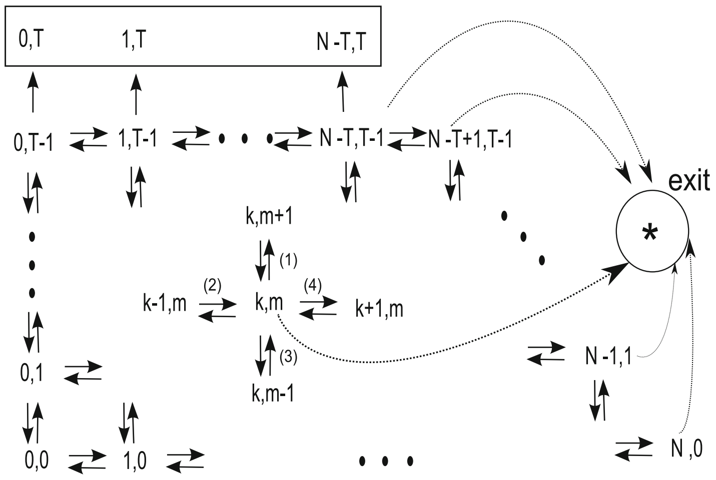

Fig. 6.5 Markov chain diagram for the mRNA state. The general transitions are represented in the inner diagram, while we emphasize the boundary condition. The *rectangle* represents the state where the mRNA is repressed (absorbing state). There is also a probability to exit from each non-absorbing state, represented in the diagram as *asterisk*

$$\begin{aligned}\frac{\partial}{\partial t}p^S_{s,d}(t) =& -\frac{1}{\bar{\tau}}p^S_{s,d}(t) - 2k_f(N_b - s - d)p^S_{s,d}(t) - (k^s_b s + k^d_b d)p^S_{s,d}(t)\\ &+ k^s_b(s+1)p^S_{s+1,d}(t) + k^d_b(d+1)p^S_{s,d+1}(t)\\ &+ k_f(N_b - s - d + 1)p^S_{s-1,d}(t) + k_f(N_b - s - d + 1)p^S_{s,d-1}(t).\end{aligned}$$

The transition diagram for (6.40) is summarized in Fig. 6.5. The boundary terms are obtained in a similar manner (see Holcman et al. 2014) (Fig. 6.6). The first time that the number of bound miRNAs reaches the threshold T is known as the "mean time to threshold" (MTT) and is denoted $\bar{\tau}^T$. It is used to define the escape probability P_a of an mRNA prior to its repression and probability P_d that an mRNA is repressed before it escapes. The probability that an mRNA exits the domain at time t before it is repressed is the sum over all probabilities that there are $s < T$ bound miRNAs when the mRNA reaches a target at time t, that is,

$$P_a(t) = \sum_{s=0}^{T-1}\frac{1}{\bar{\tau}}p^S_{s,d}(t) + \sum_{d=N_b-T+1}^{N_b}\sum_{s=0}^{N_b-d}p^S_{s,d}(t). \tag{6.38}$$

The overall exit probability of a live mRNA is

$$P_a = \int_0^\infty P_a(t)dt. \tag{6.39}$$

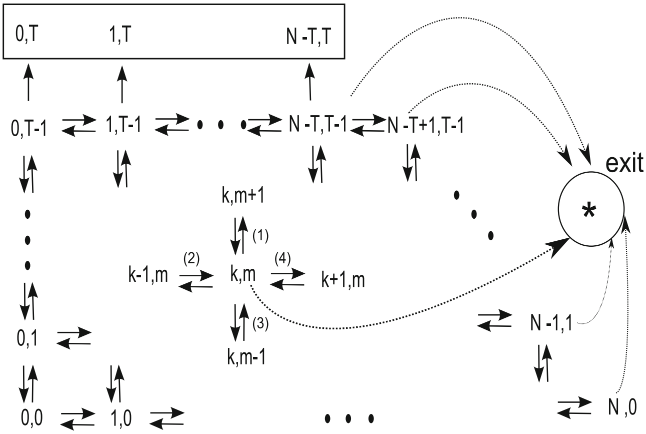

Fig. 6.6 Markov chain diagram for the mRNA state. The general transitions are represented in the inner diagram, while we emphasize the boundary condition. The *rectangle* represents the state where the mRNA is repressed (absorbing state). There is a probability to exit from each non-absorbing state, represented in the diagram as *asterisk*

Similarly, the probability of an mRNA being repressed before it escapes is defined as

$$P_d = \sum_{k=0}^{N_b-T} \sum_{d=0}^{N_b-T} p^S_{T,k}(\infty), \tag{6.40}$$

where

$$p^S_{T,d}(\infty) = \lim_{t\to\infty} p^S_{T,d}(t). \tag{6.41}$$

Combining (6.38) and (6.39) this can be expressed as

$$P_a = \sum_{s=0}^{T-1} \sum_{d=0}^{N_b-T} \int_0^{\infty} J_{s,d}(r)dr + \sum_{d=N_b-T+1}^{N_b} \sum_{s=0}^{N_b-d} \int_0^{\infty} J_{s,d}(r)dr. \tag{6.42}$$

In the small hole approximation the exit time is Poissonian. To estimate the survival probability, we integrate the Markov chain over the domain, Ω, and simplify our results by defining

$$a_{s,d} = \int_0^{\infty} p^S_{s,d}(t)dt, \tag{6.43}$$

which represents the probability of an mRNA being found intact within the domain at any time. From this, (6.42) can be written as

$$P_a = \frac{1}{\bar{\tau}} \sum_{s=0}^{T-1} \sum_{d=0}^{N_b-T} a_{s,d} + \frac{1}{\bar{\tau}} \sum_{d=N_b-T+1}^{N_b} \sum_{s=0}^{N_b-d} a_{s,d}. \tag{6.44}$$

The probability $a_{s,d}$ satisfies

$$\begin{aligned} 0 = & -\frac{1}{\bar{\tau}} a_{s,d} - 2k_f(N_b - s - d)a_{s,d} - (k_b^s s + k_b^d d)a_{s,d} \\ & + k_b^s(s+1)a_{s+1,d} + k_b^d(d+1)a_{s,d+1} \\ & + k_f(N_b - s - d + 1)a_{s-1,d} + k_f(N_b - s - d + 1)a_{s,d-1} \end{aligned} \tag{6.45}$$

for $0 < s < T$ and $0 < d < N_b - T$. This results from

$$\lim_{t \to \infty} p^S_{s,d}(t) = 0 \ \text{ for } s \neq T, \tag{6.46}$$

which means that the probability to find the mRNA inside the cytoplasm is zero, except in the following cases:

$$\begin{aligned} p_{T,d}(\infty) &= k_f(N_b - T - d + 1)a_{T-1,d} \ \text{ for } N_b - T > d \geq 0 \\ p_{T,N_b-T}(\infty) &= k_f a_{T-1,N_b-T}, \end{aligned}$$

which corresponds to mRNA repression at $t = \infty$. The boundary conditions for $s = 0$ and $d = 0$ give the following equations

$$-1 = -\frac{1}{\bar{\tau}} a_{0,0} - 2k_f N_b a_{0,0} + k_b^s a_{1,0} + k_b^d a_{0,1} \tag{6.47}$$

$$0 = -\frac{1}{\bar{\tau}} a_{0,N_b} - k_b^d N_b a_{0,N_b} + k_f a_{0,N_b-1}, \tag{6.48}$$

Finally we recall that the initial condition is

$$p_{0,0}(0) = 1.$$

At this stage,we have the following set of conditions: for $N_b > d > 0$,

$$\begin{aligned} 0 = & -\frac{1}{\bar{\tau}} a_{0,d} - 2k_f(N_b - d)a_{0,d} - k_b^d d a_{0,d} + k_b^s a_{1,d} \\ & + k_b^d(d+1)a_{0,d+1} + k_f(N_b - d + 1)a_{0,d-1}. \end{aligned}$$

For $T-1 > s > 0$,

$$\begin{aligned} 0 = & -\frac{1}{\bar{\tau}} a_{s,0} - 2k_f(N_b - s)a_{s,0} - k_b^s s a_{s,0} + k_b^s(s+1)a_{s+1,0} \\ & + k_b^d a_{s,1} + k_f(N_b - s + 1)a_{s-1,0}. \end{aligned}$$

For $s = T - 1, N_b - T > d > 0$,

$$\begin{aligned}0 = &-\frac{1}{\tau}a_{T-1,d} - 2k_f(N_b - T + 1 - d)a_{T-1,d}\\ &-(k_b^s(T-1) + k_b^d d)a_{T-1,d} + k_b^d(d+1)a_{T-1,d+1}\\ &+k_f(N_b - T - d + 2)a_{T-2,d} + k_f(N_b - T - d + 2)a_{T-1,d-1}.\end{aligned}$$

For $T > s > 0, N_b - s = d$,

$$\begin{aligned}0 = &-\frac{1}{\tau}a_{s,N_b-s} - (k_b^s s + (N_b - s)k_b^d)a_{s,N_b-s} + k_f a_{s-1,N_b-s}\\ &+ k_f a_{s,N_b-s-1}.\end{aligned}$$

Using the SSA, it is possible to simulate, for particular values of the reversible and irreversible binding rates, the number of bound decoys and miRNAs on a single mRNA (see Fig. 6.7). The general system of Eq. (6.40) cannot, in general, be solved analytically. However, in the case of irreversible binding $k_b^s = k_b^d = 0$, we can compute the survival probability by summing probabilities over all trajectories starting from $(0, 0)$ and leading to the repression state (T, m). We start by considering the path σ with n bindings ($T \leq n \leq N_b$), whose probability is

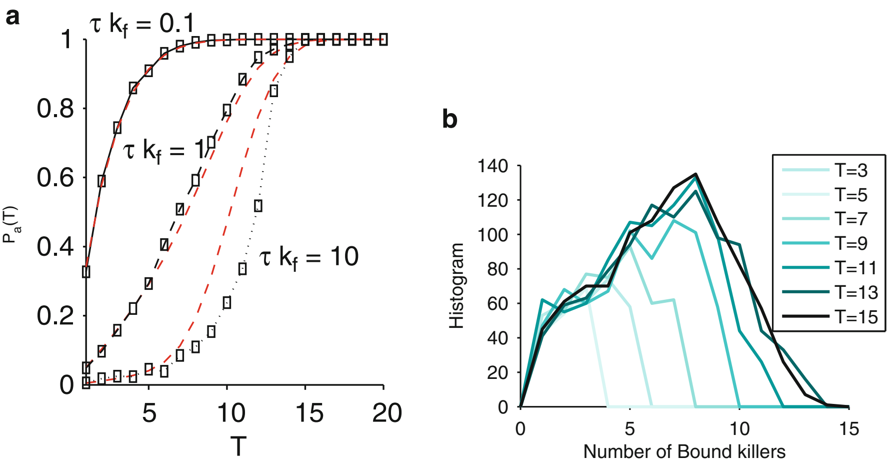

Fig. 6.7 (**a**) The escape probability as a function of the threshold, T, of bound miRNAs. Probability of escape (*squares*) for different values of τ in the reversible PTEN case, compared to the probability of escape in the irreversible PTEN case (*red*) for $N_b = 20$ and $k_f = 1$. (**b**) Histograms of the number of miRNAs bound to an mRNA before exit for different values of the threshold, T. For each value of T, we perform 1000 SSA simulations for $N_b = 20$, $k_f = 1$, $k_b^s = k_b^d = 0.5$

$$P(\sigma) = \left(\frac{1}{2}\right)^n \prod_{i=0}^{n-1} \frac{k_f(N_b - i)}{k_f(N_b - i) + 2/\bar{\tau}}.$$

The number of these paths of length n is then $\binom{n-1}{T-1}$, because there are T bindings with miRNAs, including the last one. Thus, the probability of repression prior to exit, P_d, is given by

$$P_d = \sum_{k=T}^{N_b} \binom{k-1}{T-1} \left(\frac{1}{2}\right)^k \prod_{i=0}^{k-1} \frac{k_f(N_b - i)}{k_f(N_b - i) + 2/\bar{\tau}}. \tag{6.49}$$

When the MFPT is larger than the binding time ($\bar{\tau} \gg 1/k_f$), the approximation

$$\frac{k_f(N_b - i)}{k_f(N_b - i) + 2/\bar{\tau}} = \frac{1}{1 + 2/(\bar{\tau} k_f(N_b - i))} \approx 1$$

can be used in (6.49) to give

$$P_d \approx \sum_{k=T}^{N_b} \binom{k-1}{T-1} \frac{1}{2^k}, \tag{6.50}$$

which can be interpreted as follows. Neglecting the exit probability for large MFPT $\bar{\tau}$, relative to the mean binding time $1/(k_f(N_b - i))$ to either a decoy or miRNA, the Markov chain converges to a steady state, where the number of bound decoys is binomial with parameters $(N_b, 1/2)$. Thus, the probability of repression is given by (6.50). In general, various quantities are computed asymptotically or by the Gillespie SSA (Gillespie 1976). Quantities of interest include the probability that an mRNA escapes to the ER (by locating a ribosome) before it is repressed (see Fig. 6.7a).

As the MFPT $\bar{\tau}$ increases, the rate of unbinding events decreases the escape probability (for intermediate values of T). Dramatic differences appear for a threshold of $T = 11$ and $N_b = 20$ (Fig. 6.7), leading to a twofold increase in the escape probability for the irreversible case ($\approx$0.6) relative to the reversible case ($\approx$0.3). Unbinding of decoys increases the likelihood of reaching the threshold value, and a decrease in the escape probability of escape is observed. This effect is hard to predict, because both decoys and miRNAs can unbind. Irreversible binding reduces the effect of decoys on the escape probability, and so we see an increase in the effect of T on P_a, similar to that is observed in the case of reversible binding alone. The histogram of the number of bound miRNAs before the mRNA exits is given in Fig. 6.7b for different values of T.

To conclude, the MTT is a general methodology for the study of cell activation processes on the molecular level. This framework is applied here to study the effects of elementary parameters, such as the threshold to repression, T, the number of binding sites, N_b, and the various kinetics parameters, on the stochastic repression of mRNA by siRNAs/miRNAs.

6.3 The Spindle Pole Body Activation

The alignment of each pair of chromosomes is a fundamental step in cell division. This process occurs during metaphase, when the center of the chromosomes (centrosome) attached to microtubules interacts with the kinetochores to build the mitotic spindle (Fig. 6.8) (the kinetochore is the protein structure on chromatids where the spindle fibers attach during cell division to pull sister chromatids apart). Only after all chromosomes are aligned and when every kinetochore is properly attached to a bundle of microtubules, the cell enters a new phase, called anaphase. To prevent a premature anaphase, even if all-but-one of the kinetochores have been attached and the chromosomes are aligned, unattached or improperly attached kinetochores generate a signal that inhibits the anaphase activators. This process is called the SAC. Although the exact mechanisms of the SAC and anaphase processes are still unclear, several key steps have been identified. Sister chromatids are initially bound by proteins such as cohesin. However, when the kinetochores are not all properly attached, the SAC enables the ubiquitylation and inhibition of the cell-division cycle protein 20 (Cdc20, which is an essential regulator of cell division in humans, see Wikipedia) to bind another complex of the molecule anaphase-promoting complex (also called the cyclosome or APC/C, see Wikipedia) (Nilsson et al. 2008).

The model proposed here for the study of inhibition followed by fast activation of Cdc20, which is the key activator of the anaphase promoting complex, accounts for the small number of kinetochores in the SAC. Moreover, the forward binding rate of a chemical reaction in the model, which is traditionally assumed in the continuously concentrated limit, is inapplicable here, because the model of chemical reactions in microdomains, described in Sect. 6.1.1, is the one relevant to targets such as kinetochores that have to be reached by the anaphase activators. This is the general framework for the study of the dynamics of activators during the spindle checkpoint and the anaphase transition. The aim of the model is to compute the time-dependent probability that the spindle is not initiated before time t and also to compute the mean time to induce anaphase.

6.3.1 Model of the SAC

In a cell containing N chromosomes, the targets of the Cdc20 molecules are the N associated kinetochores, containing the APC/C complexes. When a Cdc20 molecule reaches a kinetochore, it activates the APC/C complex and this can trigger a cascade of reactions leading to the separation of the sister chromatids.

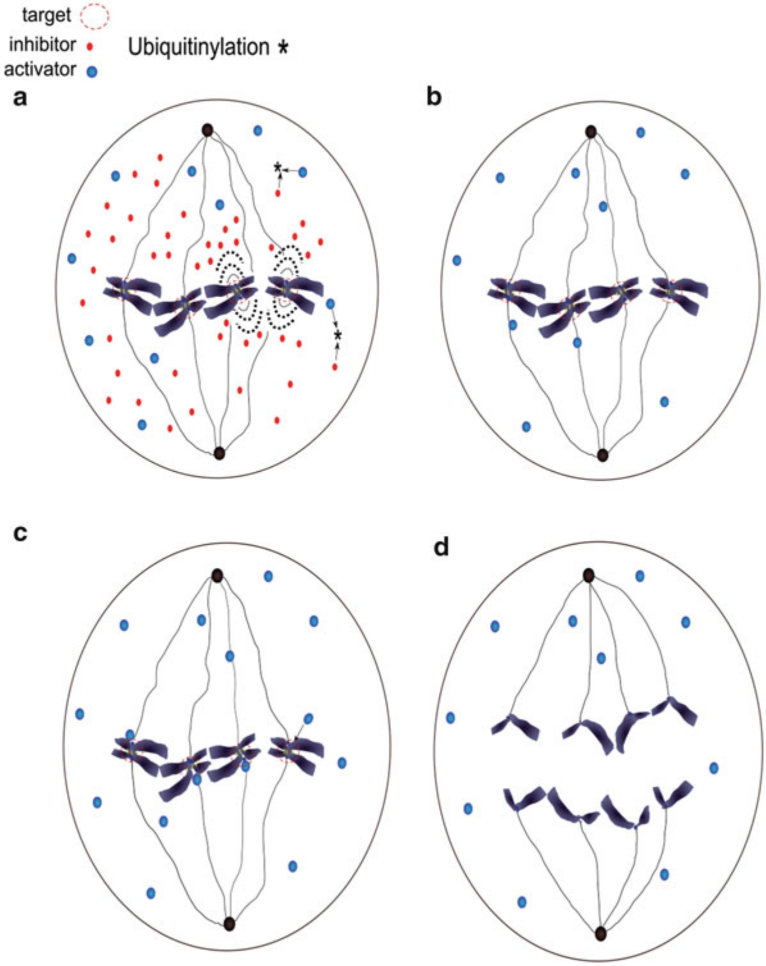

Fig. 6.8 A schematic view of the spindle assembly checkpoint and anaphase. (**a**) Before all chromosomes are attached, the mitotic checkpoint complex inhibits the Cdc20 molecules binding with APC/C to prevent premature separation of sister chromatids. This signal ubiquitylates Cdc20. (**b**) When all chromosomes are properly attached, the inhibiting signal is shut down. (**c**) and (**d**) Activation of APC/C triggers the separation of the chromatids and ultimately the anaphase

A large number of these proteins diffuse in the cell to inhibit the APC/C binding by Cdc20 molecules. Indeed, these proteins form with Cdc20 a complex called mitotic checkpoint complex (MCC). The MCC represents in the proposed model the complex of inhibitory proteins before it binds Cdc20. This contrasts the usual terminology that assumes that MCC includes Cdc20. The chemical reactions of interest are

$$\text{Complex:Cdc20} \xrightarrow{\lambda} \text{Complex} + \text{Cdc20 (production)}$$

$$\text{Cdc20} + \text{MCC} \xrightarrow{k_{-1}} \text{MCC:Cdc20} \quad \text{(ubiquitylation)}$$

$$\text{Cdc20} + \text{APC/C} \xrightarrow{\mu} \text{APC/C:Cdc20} \quad \text{(activation)},$$

where λ is the rate of Cdc20 production and k_{-1} is its degradation rate, whereas μ is the arrival rate of CdC20 to an APC/C site. The joint probability of k Cdc20 molecules and that the APC/C is not activated by any free Cdc20 molecule by time t is denoted

$$p_k(t) = \Pr\{\#\text{Cdc20}(t) = k \quad \text{and no activation has occurred by time } t\}.$$

We define an auxiliary random process $s(t)$ that takes the value 1 if an activation of APC/C by Cdc20 has occurred prior to time t and 0 otherwise. According to the above chemical reactions table, the pair $(\#\text{Cdc20}(t), s(t))$ is a two-dimensional Markov jump process. Starting with k active Cdc20 molecules and no activation, there are three possible transitions (Fig. 6.9):

1. One Cdc20 molecule is inhibited, so that $k-1$ active molecules are left,
2. One Cdc20 molecule activates the APC/C,
3. One Cdc20 molecule is generated, leading to the transition from k to $k+1$ active molecules.

The probability $p^*(t)$ of $s(t)$ satisfies together with the probabilities p_k master (Kolmogorov) equations

$$\begin{aligned}
\dot{p}_0 &= -\lambda S p_0 + k_{-1} p_1 \\
\dot{p}_k &= -(\lambda(S-k) + (\mu N + k_{-1})k)p_k + \lambda(S-k+1)p_{k-1} \\
&\quad + k_{-1}(k+1)p_{k+1}, \quad \text{for } 1 \le k \qquad (6.51) \\
\dot{p}^* &= \sum_k \mu N k p_k.
\end{aligned}$$

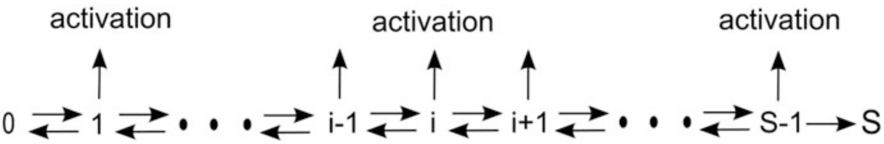

Fig. 6.9 Markov diagram for the probability of number of Cdc20 molecules. Cdc20 at state k is generated and destroyed at rate $\lambda(S-k)$ and $k_{-1}k$, respectively. Diffusing Cdc20 molecules bind to the APC/C complex to trigger the separation of sister chromatids

To understand the derivation of (6.51), we note that the production rate of Cdc20 molecules is proportional to the number of remaining available complex molecule given by $\lambda(S-k)$. Indeed, Cdc20 molecules are produced during metaphase by dissociation from a pool of complexes, which limits the level of Cdc20 to a maximum number of S molecules. When none of the N target kinetochores have been activated, the arrival rate for a Cdc20 molecule to an APC/C is μN, where $\mu = \bar{\tau}^{-1}$ and $\bar{\tau}$ is the mean time for a Cdc20 molecule to reach the APC/C site. The initial condition is $p_k(0) = \delta_{k,0}$. Because there can only be at most S Cdc20 molecules, we have $p_k(t) = 0$ for all times t and $k > S$. In that case, during time t and $t+\delta t$, starting with $k-1$ molecules, the rate of production is $\lambda(S-k+1)$ while when there are $k+1$, the destruction rate is $k_{-1}(k+1)$, leading to the general term in system (6.51).

The Probability of No Activation

To quantify the inhibition capacity of the SAC, we compute the probability $P(t)$ that no APC/C has been activated by time t, so that no chromosomal migration could have been initiated. This probability is given by

$$P(t) = \sum_{k=0}^{\infty} p_k(t). \tag{6.52}$$

Equation (6.51) imply that the generating function

$$f(t,x) = \sum_{k=0}^{\infty} p_k(t) x^k \tag{6.53}$$

satisfies the linear first order PDE

$$\frac{\partial f}{\partial t} = \lambda S(x-1)f + (-\lambda x^2 + (\lambda - \mu N - k_{-1})x + k_{-1})\frac{\partial f}{\partial x}, \tag{6.54}$$

whose characteristics are the solutions of the Riccati equation

$$\dot{X} = \lambda X^2 - (\lambda - \mu N - k_{-1})X - k_{-1}. \tag{6.55}$$

The substitution $X = -\frac{1}{\lambda}\frac{u'}{u}$ reduces (6.55) to the linear second order ODE with constant coefficients

$$u'' + (\lambda - \mu N - k_{-1})\, u' - k_{-1}\lambda u = 0. \tag{6.56}$$

The one-parameter family of solutions of (6.55) is

$$X_C(t) = -\frac{1}{\lambda}\left(\frac{r_1 e^{r_1 t} + r_2 C e^{r_2 t}}{e^{r_1 t} + C e^{r_2 t}}\right), \tag{6.57}$$

where r_1 and r_2 are the two roots of the quadratic polynomial associated with (6.56),

$$\begin{aligned} r_1 &= \frac{1}{2}\left(-\lambda + \mu N + k_{-1} + \sqrt{(-\lambda + \mu N + k_{-1})^2 + 4k_{-1}\lambda}\right) \\ r_2 &= \frac{1}{2}\left(-\lambda + \mu N + k_{-1} - \sqrt{(-\lambda + \mu N + k_{-1})^2 + 4k_{-1}\lambda}\right). \end{aligned}$$

The PDE (6.54) can be written on the characteristics as the linear ODE

$$\frac{df(t, X_C(t))}{dt} = \lambda S(X_C(t) - 1)f(t, X_C(t)), \tag{6.58}$$

whose general solution is

$$f(t, X_C(t), K) = K \exp\left\{\lambda S \int_0^t (X_C(u) - 1)du\right\}, \tag{6.59}$$

where K is a constant. The initial conditions $p_k(0) = \delta_{k0}$ determine $K = 1$. To find the analytical expression for $P(t)$, we use the characteristic for which $X_C(t) = 1$ in the family of solution (6.57). Thus

$$C(t) = -e^{(r_1 - r_2)t}\frac{\lambda + r_1}{\lambda + r_2}, \tag{6.60}$$

and

$$X_{C(t)}(u) = -\frac{1}{\lambda}\left(\frac{r_1 - r_2\left(\dfrac{\lambda + r_1}{\lambda + r_2}\right)\exp[(r_1 - r_2)(t - u)]}{1 - \left(\dfrac{\lambda + r_1}{\lambda + r_2}\right)\exp[(r_1 - r_2)(t - u)]}\right).$$

Thus the probability $P(t)$ of no activation by time t is

$$\begin{aligned} P(t) &= \exp\left\{-\lambda S\left(t + \frac{1}{\lambda}\int_0^t \frac{r_1 - r_2\left(\frac{\lambda + r_1}{\lambda + r_2}\right)e^{(r_1 - r_2)u}}{1 - \left(\frac{\lambda + r_1}{\lambda + r_2}\right)e^{(r_1 - r_2)u}}\,du\right)\right\} \\ &= \exp\left\{-\lambda S\left(t + \frac{1}{\lambda}\left[r_1 u - \ln\left(1 - \left(\frac{\lambda + r_1}{\lambda + r_2}\right)e^{(r_1 - r_2)u}\right)\right]_0^t\right)\right\} \\ &= e^{-\lambda S t - r_1 S t}\left(\frac{-\lambda - r_2 + (\lambda + r_1)e^{(r_1 - r_2)t}}{(r_1 - r_2)}\right)^S \\ &= e^{-\lambda t S}\left(\frac{(\lambda + r_1)e^{-r_2 t} - (\lambda + r_2)e^{-r_1 t}}{\lambda(r_1 - r_2)}\right)^S. \end{aligned}$$

Finally,

$$P(t) = \left(\frac{(\lambda + r_1)e^{-(\lambda+r_2)t} - (\lambda + r_2)e^{-(\lambda+r_1)t}}{r_1 - r_2} \right)^S, \tag{6.61}$$

which is a decreasing function of t. For $\lambda = 0$ and $\mu = 0$ it remains constant. For fixed t the probability $P(t)$ is a decreasing function of λ, that is, increasing the Cdc20 production rate decreases the probability of activation. Similarly, it is a decreasing function of k_{-1}, which means that increasing the inhibition of Cdc20 increases the probability of no activation.

6.3.2 Activation of the APC/C

When all kinetochores are properly attached, the SAC is shut down and the activation of APC/C:Cdc20 complex triggers a cascade of reactions that lead to cohesin ubiquitylation. To study the time to such activation, we assume that production and degradation of MCC are sufficiently fast enough so that the MCC concentration decreases rapidly once all the kinetochores are attached. Neglecting the transient time for the rate k_{-1} to decay to 0, the equilibrium Cdc20 concentrations are taken as the initial conditions for the activation of APC/C. Furthermore, the time for all kinetochores to be attached is not too short on the time scale of degradation and production, so that the CdC20 concentration stays close to equilibrium. When there are k Cdc20 present in the cell and m of them are bound to APC/C, the association rate is $\mu(N-m)(k-m)$. The joint probabilities that there are k Cdc20 molecules and m activated APC/C by Cdc20 are given by

$$p_{k,m}(t) = \Pr\{\#\text{CDC20}(t) = k,\ \text{and } m \text{ APC/C are activated by Cdc20 by time } t\}.$$

Because the transition rate to activation of APC/C on another kinetochore from the state (k, m) is $\mu(k-m)(N-m)$, the master equation is

$$\begin{aligned} \dot{p}_{0,0} &= -\lambda S p_{0,0} \\ \dot{p}_{k,0} &= -(\lambda(S-k) + \mu N k)p_{k,0} + \lambda(S-k+1)p_{k-1,0} \\ \dot{p}_{k,k} &= -\lambda(S-k)p_{k,k} + \mu(N-k+1)p_{k,k-1} \\ \dot{p}_{k,m} &= -(\lambda(S-k) + \mu(N-m)(k-m))p_{k,m} + \lambda(S-k+1)p_{k-1,m} \\ &\quad + \mu(N-m+1)(k-m+1)p_{k,m-1}, \end{aligned} \tag{6.62}$$

with the initial condition

$$p_{k,m}(0) = \frac{\binom{S}{k}\left(\frac{\lambda}{k_{-1}}\right)^k}{\left(1+\frac{\lambda}{k_{-1}}\right)^S}\,\delta_{0,m}. \tag{6.63}$$

In this case, the mean time $\bar{\tau}$ that all APC/C are activated is found from a continuous-time Markov process that reaches a given threshold (see Dao Duc and Holcman 2010). The MFPT to the threshold is expressed as the sum

$$\tau = \sum_{k=0}^{N-1}\sum_{m=0}^{S} a_{k,m}, \tag{6.64}$$

where $a_{k,m} = \int_0^\infty p_{k,m}(t)dt$. Integrating the system (6.62) from 0 to ∞ with the initial conditions (6.63) gives

$$\begin{aligned} -p_{0,0}(0) &= -\lambda S a_{0,0} \\ -p_{k,0}(0) &= -(\lambda+\mu N)(S-k)a_{k,0} + \lambda(S-k+1)a_{k-1,0} \\ 0 &= -\lambda(S-k)a_{k,k} + \mu(N-k+1)a_{k,k-1} \\ 0 &= -(\lambda(S-k)+\mu(N-m)(k-m))a_{k,m} \\ &\quad + \mu(N-m+1)(S-k)a_{k,m-1} + \lambda(S-k+1)a_{k-1,m}. \end{aligned} \tag{6.65}$$

In practice it is easier to solve the system numerically and to use the probability $P(t)$ and the MFPT $\bar{\tau}$ to determine the constraints that define the range of the parameters λ and k_{-1}, as described below.

6.3.3 Determination of the Production and Unbinding Rates

The rates of production and unbinding, λ and k_1, respectively, can be determined from the following principles: a strong inhibition signal keeps the probability for no activation very high during SAC and thus k_{-1} has to be sufficiently high relative to λ to maintain a quasi-steady state. In contrast, fast activation during anaphase keeps the mean time to activate all the kinetochores short, so that λ has to be sufficiently high to maintain a quasi-steady state. These two constraints determine a range for the parameters λ and k_{-1}.

1. First, the probability P of no activation remains sufficiently high for the time τ_1 until all chromosomes get properly attached in the metaphase plate. It has been estimated that $\tau_1 \approx 20\,\text{min}$ (Rieder et al. 1994). Therefore, fixing a threshold of 0.95 for the probability $P(\tau_1)$ of no activation prior to τ_1, we get

$$\Pr\{\tau_1 > 20\,\text{min}\} \geq 0.95. \tag{6.66}$$

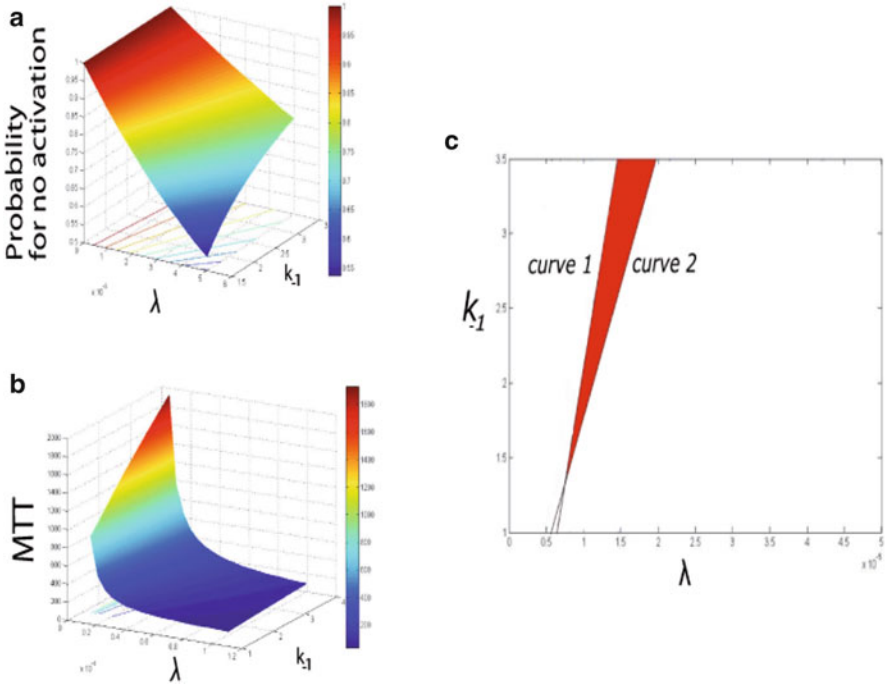

Fig. 6.10 Representation of the domain Ω for the rate constant (*red*). (**a**) The probability for no activation at time $\tau = 10\,\text{min}$ as a function of parameters λ and k_{-1}. (**b**) The mean time to threshold as a function of λ and k_{-1}. (**c**) Line 1 is the level curve $\tau = 10\,\text{min}$ in (**b**). Line 2 is the level curve $P(\tau) = 0.95$ in (**a**). These two curves determine the domain Ω that satisfies (6.66) and (6.67)

2. Second, during the onset of anaphase, the mean time $\bar{\tau}_S$ for all chromosomes to be separated is short. Since APC/C activation triggers the separation of chromosomes, $\bar{\tau}_S$ can be considered to be the time for activation of all APC/C. Indeed, biophysical data (Meraldi et al. 2004) suggest that $\bar{\tau}_S$ should be limited by the time $\tau' \approx 10\,\text{min}$. Thus,

$$\bar{\tau}_S \le \tau'. \tag{6.67}$$

Equation (6.61) for the probability $P(\tau_1)$ and numerical integration of the mean time $\bar{\tau}_S$ from the matrix equation (6.65) determines the range of validity of λ and k_{-1} by the geometrical domain Ω, represented in Fig. 6.10 as the intersection $\Omega = \Omega_1 \cap \Omega_2$, where

$$\Omega_1 = \{(\lambda, k_{-1}) \,:\, \Pr\{\tau_1(\lambda, k_{-1}) > 20\,\text{min}\} \ge 0.95\} \tag{6.68}$$

and

$$\Omega_2 = \left\{(\lambda, k_{-1}) \,:\, \bar{\tau}_S(\lambda, k_{-1}) \le \tau'\right\}. \tag{6.69}$$

6.4 Annotation

Coarse-graining the binding and unbinding reactions on the time scale of the MFPT of the diffusing reactant into and out of binding sites leads to a Markovian jump process description of the stochastic dynamics of the binding and unbinding of molecules is given in Holcman and Schuss (2005b) and applied in Dao Duc and Holcman (2010, 2012).

The Kolmogorov equation (6.2) with the boundary conditions (6.3) were derived in Holcman and Schuss (2005b). Equation (6.4) were used in Holcman and Schuss (2005b) to estimate the fraction of bound receptors in photo-receptor outer segments and also to interpret the variance of channel noise measurements. This analysis was also used in Holcman and Triller (2006) to estimate the number of bound AMPA receptors in the post-synaptic density. A different model was proposed in Bressloff and Earnshaw (2009).

The application of the Markovian approximation to the SAC during cell division is given in Dao Duc and Holcman (2012) and that to the mRNA escaping degradation through binding a number of miRNAs is discussed in Holcman et al. (2014). Formula (6.50) was derived in Dao Duc and Holcman (2010). It is shown in Holcman et al. (2014) that when the siRNA/miRNA bind reversibly, the probability of escape decreases relatively to that of irreversible binding. The SAC has been modeled at the molecular level, however the parameters used in Doncic et al. (2005, 2009) and Mistry et al. (2008) may not necessarily reflect in vivo dynamics. For example, these models do not account for the finite number of binding sites for Cdc20. In addition, the constant flux assumption for molecules reaching a kinetochore impacts the APC/C activation, leading to an overestimate of the catalytic activity (Doncic et al. 2005). The time-dependent probability that the spindle is not initiated before time t and the mean time to induce anaphase was calculated in Dao Duc and Holcman (2012) where also the system (6.65) was solved numerically.

Chapter 7
Random Search with Switching

The NET problem studied so far is essentially that of a Brownian search for a small target. A more complex search is that by a Brownian particle that switches between different states, for example, its diffusion coefficient switches between two values, D_1 and D_2, at exponential waiting times with rates k_{12} and k_{21}, respectively, in search of a small target in a bounded domain Ω (Reingruber and Holcman 2009). When the diffusion coefficient is D_1, the Brownian trajectory is reflected at the boundary $\partial\Omega$, except for a small absorbing part $\partial\Omega_a$. When the diffusion coefficient is D_2, the entire boundary reflects the Brownian trajectory. Thus the target is gated by the state of the searching particle. The gated narrow escape time (GNET) is the time to absorption of the switching Brownian trajectory and the mean time to absorption is the GNET. A generalization is a class of diffusions (Reingruber and Holcman 2010) whose diffusion coefficient can switch between D_i and D_j $(i, j = 1, 2, \ldots, n)$ at exponential waiting times with given rates k_{ij} and are absorbed at a small part $\partial\Omega_a$ of $\partial\Omega$ when in states $D_1, \ldots, D_k$. Otherwise, they are reflected at $\partial\Omega$. The GNET is related to certain intermittent search processes, where switching strategies between different states lead to minimal search time of a target (Bénichou et al. 2005). See Sect. 7.2 for further references.

7.1 Random Switching Between Two Modes of Diffusion

Consider a diffusion process $\boldsymbol{x}(t, i)$ whose diffusion coefficient switches between D_1 and D_2 at exponential waiting times with rates k_{12}. The Euler simulation scheme is given by

D. Holcman, Z. Schuss, *Stochastic Narrow Escape in Molecular and Cellular Biology*, DOI 10.1007/978-1-4939-3103-3_7

$$\boldsymbol{x}(t+\Delta t, i) = \begin{cases} \boldsymbol{x}(t,i) + \sqrt{2D_i}\,\Delta \boldsymbol{w}_i(t) & \text{w.p. } 1 - k_{ij}\Delta t + o(\Delta t) \\ \boldsymbol{x}(t,j) & \text{w.p. } k_{ji}\Delta t + o(\Delta t),\ i \neq j \end{cases} \tag{7.1}$$

for $i, j = 1, 2$, with the randomly chosen initial condition $\boldsymbol{x}(s,i) = \boldsymbol{x}$. Here $\boldsymbol{w}_i(t)$ $(i = 1, 2)$ are independent standard Brownian motions and $\Delta \boldsymbol{w}_i(t) = \boldsymbol{w}_i(t+\Delta t) - \boldsymbol{w}_i(t)$.

The transition probability density $p(\boldsymbol{y}, i, t \,|\, \boldsymbol{x}, s, j)$ of the trajectory $x(t,i)$ in a given domain Ω, given the initial condition $\boldsymbol{x}(s,j) = \boldsymbol{x}$ with probability 1, is the limit as $\Delta t \to 0$ of the solution to the system of integral equations (Schuss 2010b)

$$\begin{aligned} p(\boldsymbol{y}, i, t+\Delta t \,|\, \boldsymbol{x}, s, j) = {} & \frac{1 - k_{ij}\Delta t}{\sqrt{2\pi D_i \Delta t}} \int_\Omega p(\boldsymbol{z}, i, t \,|\, \boldsymbol{x}, s, j) \exp\left\{ -\frac{|\boldsymbol{y} - \boldsymbol{z}|^2}{2D_i \Delta t} \right\} d\boldsymbol{z} \\ & + k_{ji}\Delta t p(\boldsymbol{y}, \ell, t \,|\, s, j) + o(\Delta t) \ \text{ for } i, j, \ell = 1, 2,\ i \neq \ell. \end{aligned}$$

In the limit $\Delta t \to 0$, the system of Kolmogorov (master) equations is obtained

$$\begin{aligned} p_t(\boldsymbol{y}, 1, t \,|\, \boldsymbol{x}, s) &= D_1 \Delta_{\boldsymbol{y}} p\,(\boldsymbol{y}, 1, t \,|\, \boldsymbol{x}, s) - k_{12} p\,(\boldsymbol{y}, 1, t \,|\, \boldsymbol{x}, s) + k_{12} p\,(\boldsymbol{y}, 2, t \,|\, \boldsymbol{x}, s) \\ p_t(\boldsymbol{y}, 2, t \,|\, \boldsymbol{x}, s) &= D_2 \Delta_{\boldsymbol{y}} p\,(\boldsymbol{y}, 2, t \,|\, \boldsymbol{x}, s) + k_{21} p\,(\boldsymbol{y}, 1, t \,|\, \boldsymbol{x}, s) - k_{21} p\,(\boldsymbol{y}, 2, t \,|\, \boldsymbol{x}, s). \end{aligned} \tag{7.2}$$

Setting

$$\boldsymbol{p} = \begin{pmatrix} p\,(\boldsymbol{y}, 1, t \,|\, \boldsymbol{x}, s) \\ p\,(\boldsymbol{y}, 2, t \,|\, \boldsymbol{x}, s) \end{pmatrix}, \quad \boldsymbol{K} = \begin{pmatrix} k_{12} & -k_{12} \\ -k_{21} & k_{21} \end{pmatrix}, \quad \boldsymbol{D_y} = \begin{pmatrix} D_1 & 0 \\ 0 & D_2 \end{pmatrix} \Delta_{\boldsymbol{y}}.$$

The forward master equation (7.2) can be written as

$$\boldsymbol{p}_t(\boldsymbol{y}, t \,|\, \boldsymbol{x}, s) = \boldsymbol{D_y p}\,(\boldsymbol{y}, t \,|\, \boldsymbol{x}, s) - \boldsymbol{Kp}\,(\boldsymbol{y}, t \,|\, \boldsymbol{x}, s). \tag{7.3}$$

The transition probability density $\boldsymbol{p}\,(\boldsymbol{y}, t \,|\, \boldsymbol{x}, s)$ satisfies the backward system of master equations (with respect to $(\boldsymbol{x}, s)$), which is the formal adjoint to (7.3). Upon setting $t - s = \tau$, as we may, we obtain

$$\boldsymbol{p}_\tau(\boldsymbol{y}, \tau \,|\, \boldsymbol{x}, 0) = \boldsymbol{D_x p}\,(\boldsymbol{y}, \tau \,|\, \boldsymbol{x}, 0) - \boldsymbol{K}^T \boldsymbol{p}\,(\boldsymbol{y}, \tau \,|\, \boldsymbol{x}, 0). \tag{7.4}$$

The mean sojourn time $u(i \,|\boldsymbol{x}, 1)$ in state i prior to absorption, of a trajectory of (7.1) that starts at time $\tau = 0$ in state 1 at position $\boldsymbol{x}$ with probability 1, is given by Reingruber and Holcman (2010)

$$u(i \,|\, \boldsymbol{x}, 1) = \int_\Omega d\boldsymbol{y} \int_0^\infty d\tau\, p(\boldsymbol{y}, i, \tau \,|\, \boldsymbol{x}, 1). \tag{7.5}$$

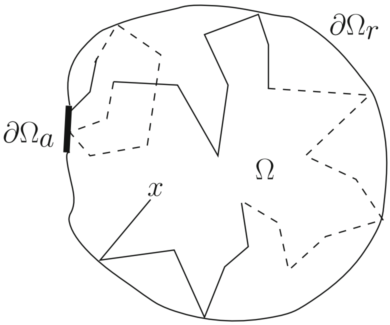

Fig. 7.1 Example of a trajectory of a diffusing Brownian ligand in a confined domain Ω and randomly switching between two states *1* (*continuous line*) and *2* (*dashed line*). The ligand is reflected at the entire boundary when in state *2*, whereas it is absorbed at $\partial\Omega_a$ when in state *1*

To find the differential equations that the times $u(i\,|\boldsymbol{x},j)$ satisfy, the backward equation (7.4) is integrated with respect to $\boldsymbol{y}$ and τ to give

$$\begin{aligned} D_1\,\Delta u(i\,|\,\boldsymbol{x},1) - k_{12}[u(i\,|\,\boldsymbol{x},1) - u(i\,|\,\boldsymbol{x},2)] &= -1 \\ D_2\Delta u(i\,|\,\boldsymbol{x},2) - k_{21}[u(i\,|\,\boldsymbol{x},2) - u(i\,|\,\boldsymbol{x},1)] &= 0. \end{aligned} \tag{7.6}$$

The mean sojourn times $u(2\,|\,\boldsymbol{x},1)$ and $u(2\,|\,\boldsymbol{x},2)$ satisfy equations that are obtained by interchanging $1 \leftrightarrow 2$ in (7.6) (Fig. 7.1).

7.1.1 The GNET for a Particle Switching Between Two States

It suffices to solve the equations only for $i = 1$, because the solutions $u(2\,|\,\boldsymbol{x},j)$ can be obtained from $u(1\,|\,\boldsymbol{x},j)$ by linear transformations. Specifically, averaging $u(i\,|\,\boldsymbol{x},j)$ over a uniform initial spatial distribution of $\boldsymbol{x}$, we define the mean sojourn times prior to absorption as

$$u(i\,|\,j) = \frac{1}{|\Omega|}\int\limits_{\Omega} u(i\,|\,\boldsymbol{x},j)\,d\boldsymbol{x}. \tag{7.7}$$

When the trajectory $\boldsymbol{x}(t,i)$ is absorbed at $\partial\Omega_a$ with $i = 1$ while it is reflected everywhere on the $\partial\Omega$ with $i = 2$, the boundary conditions for the system (7.6) are

$$u(1\,|\,\boldsymbol{x},1) = 0 \text{ for } \boldsymbol{x} \in \partial\Omega_a, \quad \frac{\partial u(1\,|\,\boldsymbol{x},1)}{\partial n} = 0 \text{ for } \boldsymbol{x} \in \partial\Omega_r$$

$$\frac{\partial u(1\,|\,\boldsymbol{x},2)}{\partial n} = 0 \quad \text{for } \boldsymbol{x} \in \partial\Omega.$$

The sojourn times $u(2\,|\,\boldsymbol{x},1)$ and $u(2\,|\,\boldsymbol{x},2)$ are obtained from $u(1\,|\,\boldsymbol{x},1)$ and $u(1\,|\,\boldsymbol{x},2)$ through the linear transformation

$$\begin{pmatrix} u(2\,|\,\boldsymbol{x},1) \\ u(2\,|\,\boldsymbol{x},2) \end{pmatrix} = \frac{k_{12}}{k_{21}} \begin{pmatrix} 1 & 0 \\ 0 & 1 \end{pmatrix} \begin{pmatrix} u(1\,|\,\boldsymbol{x},1) \\ u(1\,|\,\boldsymbol{x},2) \end{pmatrix} + \begin{pmatrix} 0 \\ 1/k_{21} \end{pmatrix}. \tag{7.8}$$

Equations (7.6) and (7.8) show that the spatially averaged sojourn times (7.7) satisfy the relations

$$u(1\,|\,2) = u(1\,|\,1), \quad u(2\,|\,1) = u(1\,|\,1)\frac{k_{12}}{k_{21}}, \quad u(2\,|\,2) = u(2\,|\,1) + \frac{1}{k_{21}}. \tag{7.9}$$

It follows that the mean sojourn times $u(1)$, $u(2)$, and u, conditioned on a uniform initial distribution in states 1, 2, or in 1 and 2 with the equilibrium distribution $(p_1, p_2) = (k_{21}, k_{12})/(k_{12} + k_{21})$, respectively, are

$$\begin{aligned} u(1) &= u(1\,|\,1) + u(2\,|\,1) = u(1\,|\,1)\left(1 + \frac{k_{12}}{k_{21}}\right) \\ u(2) &= u(2\,|\,2) + u(2) = u(1) + \frac{1}{k_{21}} \\ u &= p_1 u(1) + p_2 u(1\,|\,2) = u(1) + \frac{p_2}{k_{21}}. \end{aligned} \tag{7.10}$$

7.1.2 GNET in One Dimension

The GNET for one-dimensional diffusions, though not directly relevant to biological applications, can be calculated explicitly and is quite instructive about the dependence of the NET on switching. Specifically, the system (7.6) in the interval $\Omega = (0, L)$ with absorption at $x = 0$ in state 1 and reflection at $x = L$ is given in the scaled variables

$$\begin{aligned} \hat{x} &= \frac{x}{L}, \quad l_1 = \frac{k_{12}L^2}{D_1}, \quad l_2 = \frac{k_{21}L^2}{D_2} \\ \kappa &= \frac{D_1}{D_2}, \quad v_1(\hat{x}) = \frac{D_1}{L^2}u_1(x,1), \quad v_2(\hat{x}) = \frac{D_1}{L^2}u_1(x,2) \end{aligned} \tag{7.11}$$

by

$$v_1''(\hat{x}) - l_1[v_1(\hat{x}) - v_2(\hat{x})] = -1, \quad v_2''(\hat{x}) + l_2[v_1(\hat{x}) - v_2(\hat{x})] = 0, \tag{7.12}$$

with boundary conditions $v_1(0) = v_1'(1) = v_2'(0) = v_2'(1) = 0$. The system can be solved explicitly and exhibits a nonlinear effect of switching. This can be seen from the explicit expressions

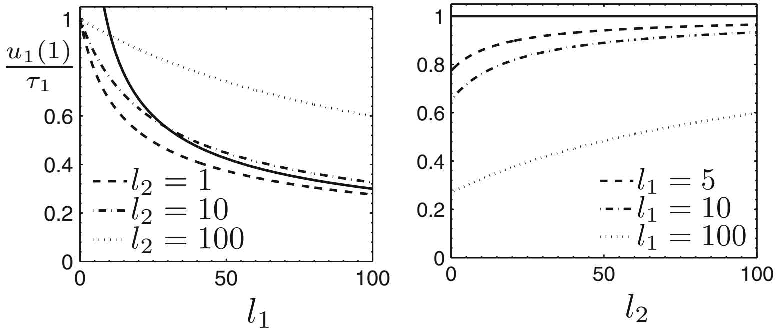

Fig. 7.2 Graph of the sojourn time $u(1\,|\,1)$ obtained from the explicit solution as a function of l_1 (*left*) and l_2 (*right*), scaled by the NET τ_1 with no switching. The *continuous curve* in the *left panel* is the asymptotic approximation $3/\sqrt{l_1}$ for $l_1 \gg 1$ and $\sqrt{l_1} \gg l_2$

$$u(1\,|\,1) = \begin{cases} \dfrac{L^2}{D_1}\left[\dfrac{\coth\sqrt{l_1}}{\sqrt{l_1}} - \dfrac{1}{l_1}\right] + O\left(\dfrac{l_2}{l_1}\right), & \text{for } l_2 \ll l_1 \\[2ex] \dfrac{L^2}{3D_1} + O\left(\dfrac{l_1}{l_2}\right), & \text{for } l_2 \gg l_1, \end{cases} \tag{7.13}$$

while for $l_1 \gg 1$ and $l_2 \ll \sqrt{l_1}$

$$u(1\,|\,1) \approx \frac{L^2}{D_1}\frac{1}{\sqrt{l_1}} = \frac{L}{\sqrt{k_{12}D_1}}, \quad l_1 \gg 1,\ \sqrt{l_1} \gg l_2. \tag{7.14}$$

Figure 7.2 shows the plots of $u(1\,|\,1)$ vs l_1 (left) and vs l_2 (right). The counterintuitive result, that the sojourn time $u(1\,|\,1)$ is always smaller than the mean exit time in state 1 without switching, is remarkable. In addition, when the parameters D_1, D_2, and k_{21} are fixed, Eq. (7.14) shows that $u(1\,|\,1)$ becomes arbitrarily small as k_{12} increases. This counterintuitive behavior can be understood as follows (see also Doering 2000). For a trajectory starting uniformly distributed in state 1, the probability to be in the neighborhood of the absorbing boundary at $x = 0$ decreases quickly as a function of time. However, after switching to state 2, the distribution is re-homogenized and later on, after switching back to state 1, the probability density around $x = 0$ is higher than that in the non-switching case. After switching back to state 1, the ligand starts closer to $x = 0$ with high probability and thus exits in state 1 faster than in the non-switching case. Figure 7.3(left) shows the plot of $u(1)$ vs l_1 for various fixed values of l_2. This situation describes a chemical reaction, where the diffusion constants and the backward rate k_{21} are fixed, but the forward binding rate k_{12} can be adjusted by changing the concentration of a reactant partner. Figure 7.3(right) shows the plot of $u(1)$ vs l_2 for fixed l_1, which demonstrates that also $u(1)$ has a minimum $u(1)_m$ in this case. The minimum $u(1)_m$

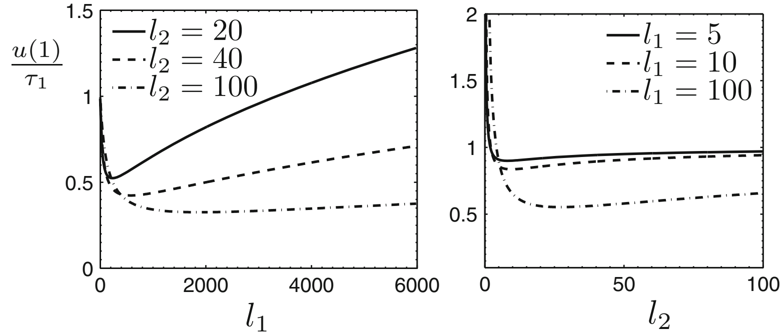

Fig. 7.3 Graph of the exit time $u(1)$ as a function of l_1 (*left*) and l_2 (*right*) for $D_1/D_2 = 0.1$, scaled by NET τ_1 in the absence of switching

decreases as switching becomes faster. A lower bound for $u(1)_m$ can also be found explicitly. The analysis of the one-dimensional case shows that the lower limit of the GNET $u(1)$ corresponds to diffusion with the maximal diffusion constant and for $\kappa = D_1/D_2 \le 1$, the fastest exit is achieved by diffusing most of the time in state 2, with no exits possible. The exit time $u(1)$ has no global or even local minima for $\kappa < 1$ and the best strategy to minimize the GNET needs to be adapted to the given constraints. For example, when k_{21}, k_{12} are the unbinding and the binding rates, respectively, k_{21} usually depends on the local interaction potential while k_{12} can be modulated by changing the concentration of the binding partner.

Furthermore, as shown in Fig. 7.3, the graph of $u(1)$ around and past the minimum is quite flat, and thus increasing switching to attain the minimum may not be necessary, because a similar effect can already by achieved at much slower rates. Moreover, because the graph of $u(1)$ decays steeply for small values l_1 and l_2, this behavior provides an efficient mechanism to modulate the activation time, and thus cellular signaling.

7.1.3 GNET in Three Dimensions

Consider the GNET problem for a three-dimensional domain Ω when the trajectory is absorbed upon hitting $\partial\Omega_a$ in state 1 only. In the scaled variables

$$\hat{\boldsymbol{x}} = \frac{\boldsymbol{x}}{a}, \quad l_1 = \frac{k_{12}a^2}{D_1}, \quad l_2 = \frac{k_{21}a^2}{D_2}$$

$$v_1(\hat{\boldsymbol{x}}) = \frac{aD_1}{|\Omega|}u_1(\boldsymbol{x}, 1), \quad v_2(\hat{\boldsymbol{x}}) = \frac{aD_1}{|\Omega|}u_1(\boldsymbol{x}, 2),$$

the system (7.6) becomes

$$\begin{aligned}\Delta v(i\,|\hat{\boldsymbol{x}},1)-l_1[v(i\,|\,\hat{\boldsymbol{x}},1)-v(i\,|\,\hat{\boldsymbol{x}},2)]&=-\,|\hat{\Omega}|^{-1}\\ \Delta v(i\,|\,\hat{\boldsymbol{x}},2)+l_2[v(i\,|\,\hat{\boldsymbol{x}},1)-v(i\,|\,\hat{\boldsymbol{x}},2)]&=0,\end{aligned}\tag{7.15}$$

where $|\hat{\Omega}| = |\Omega|/a^3 \gg 1$. The boundary condition is absorbing on $\partial\hat{\Omega}_a$ for $v_1(\hat{\boldsymbol{x}})$, and otherwise reflecting. Asymptotic approximations to the solution of (7.15) in the limit of small window and extreme values of the parameters clarify the effect of switching. For $l_1 \ll 1$ or $l_2 \gg l_1$, at leading orders, $v(1\,|\,\hat{\boldsymbol{x}},1)$ is solution of the NET problem $\Delta v(1\,|\,\hat{\boldsymbol{x}},1) = -|\hat{\Omega}|^{-1}$. When $l_2 \ll \sqrt{l_1}$, the leading order approximation for $v(1\,|\,\hat{\boldsymbol{x}},1)$ is found by solving $\Delta v(1\,|\,\hat{\boldsymbol{x}},1)-l_1[v(1\,|\,\hat{\boldsymbol{x}},1)-v_1] = -|\hat{\Omega}|^{-1}$, where v_1 is the spatial average of $v(1\,|\,\hat{\boldsymbol{x}},1)$. The leading order asymptotic approximation to the mean sojourn time is

$$u(1) = \left(1+\frac{k_{12}}{k_{21}}\right)\frac{|\Omega|}{aD_1}v_1 \tag{7.16}$$

$$\sim \left(1+\frac{k_{12}}{k_{21}}\right)\begin{cases}\tau_1 & \text{for } l_1 \ll 1 \text{ or } l_2 \gg l_1\\[2ex] \dfrac{|\Omega|}{|\partial\Omega_a|\sqrt{D_1k_{12}}} & \text{for } l_1 \gg 1,\ \sqrt{l_1} \gg l_2,\end{cases}\tag{7.17}$$

where τ_1 is the NET in state 1 without switching. The asymptotic behavior (7.17) of $u(1)$ and $u(1\,|\,1)$ as functions of l_1 and l_2 (Reingruber and Holcman 2009) is confirmed by Brownian simulations together with the Gillespie-algorithm (Gillespie 1976) to model switching in a sphere of radius $r = 30$ with a circular hole of radius $a = 1$. In the left panel of Fig. 7.4 simulation results are shown for $u(1\,|\,1)$ as a function of l_1 for various values of l_2. Clearly, $u(1\,|\,1) \le \tau_1$, which confirms the asymptotic behavior $u(1\,|\,1)/\tau_1 \approx 4/(\pi\sqrt{l_1})$. The latter follows from (7.17) with the asymptotic approximation $\tau_1 \approx |\Omega|/(4aD_1)$ (see Schuss et al. 2007) and $|\partial\Omega_a| = \pi a^2$. Simulations results for $u(1)$ as a function of l_1 for various values of l_2 and $\kappa = 0.1$ $(D_1 = 1, D_2 = 10)$ are displayed in the left panel of Fig. 7.4. The plot shows that $u(1)$ has a minimum $u(1)_m$ smaller than τ_1, which is attained at some value $l_{1,\min} > 0$.

In the range of parameters such that $u_1(1) \approx \tau_1$ the switching dynamics can be approximated by an effective non-switching diffusion process with diffusion constant $D_{\text{eff}} = D_1/(1 + k_{12}/k_{12})$. However, because $D_{\text{eff}} < D_1$, the effective diffusion approximation cannot give an exit time $u(1)$ smaller than τ_1. Interestingly, (7.17) shows that $u(1)$ in the range $\sqrt{l_1} \gg l_2, l_1 \gg 1$ is smaller than τ_1 and inversely proportional to the surface area of the absorbing window, similarly to the NET to a partially absorbing hole (see Reingruber et al. 2009). In this range, the switching

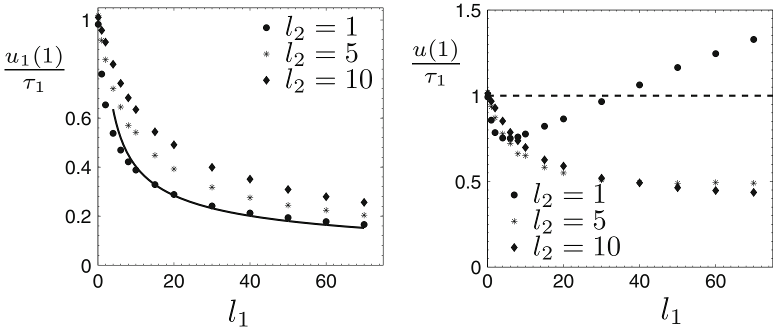

Fig. 7.4 Simulation results for the mean sojourn time $u(1 \mid 1)$ and the mean exit time $u(1)$ as a function of l_1 for different values of l_2 (marked by *various symbols*). The results are scaled by the NET τ_1. The *continuous line* in the *left panel* is the asymptotic value $4/\pi\sqrt{l_1}$, obtained from (7.17) (see text). The results for $u(1)$ in the *right panel* are obtained for $\kappa = 0.1$

dynamics cannot be approximated by the classical diffusion process. If $D_2 > D_1$, then switching can significantly decrease the GNET relative to the non-switching NET. For small values of l_1 and l_2, the GNET is very sensitive to changes in these parameters (see Figs. 7.3 and 7.4).

7.1.4 Application to the Search by a Transcription Factor

The computations of the GNET are relevant to the search time of a transcription factor (TF) for a DNA-promoter site (Fig. 7.5). The search can alternate between three-dimensional diffusion in the nucleus and one-dimensional diffusion along the DNA, as shown in Fig. 7.6 (see for some experimental details Elf et al. 2007; Wang et al. 2006). While diffusing along the DNA, the TF can switch at random between two conformational states: in state 1 the diffusion is slow due to a high affinity of the TF for the DNA and therefore it scans accurately the DNA base pairs. In state 2, diffusion is much faster, but the TF does not scan the DNA molecule accurately. It was shown recently that the search time of such a TF can be significantly reduced relative to that of a TF, which accurately examines all the DNA base pairs. Several recent computations show that the mean time to find the DNA site is several minutes long (see Malherbe and Holcman 2010; Reingruber and Holcman 2011a). The above considerations pose a fundamental question that remains to be addressed: what is the role of DNA conformation, accessibility, and chromatin organization in the search process?

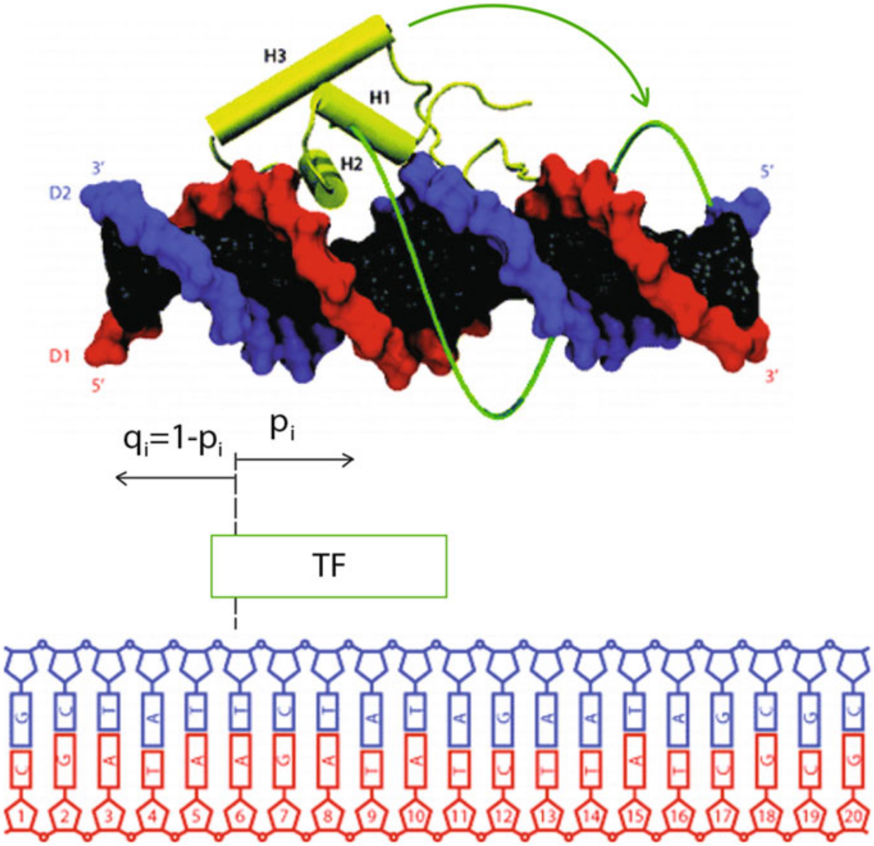

Fig. 7.5 Motion of a transcription factor along the DNA molecule. A TF at position i moves by one base pair to the right with probability p_i and to the left with probability q_i as represented in the lower half of the figure (Malherbe and Holcman 2010). The figure is adapted from Furini et al. (2010)

7.1.5 Search Analysis for a Three State Switching Process

We briefly describe the mean first passage time for a TF to find its promoter site when it freely diffuses in the nucleus, but once bound to the DNA, it alternates between two states: in state 1, it interacts with individual DNA base pairs, while in state 2 it is insensitive. In state 1, the motion occurs in a rough energy landscape described by an effective diffusion with constant D_1, while in state 2, the diffusion is much faster $D_2 \gg D_1$ and occurs in a smooth potential well, generated by interactions with the DNA backbone. The switching dynamics is Poissonian with rates k_{12} and k_{21} that depend on the energy profile (Fig. 7.7b). In state 2, in addition

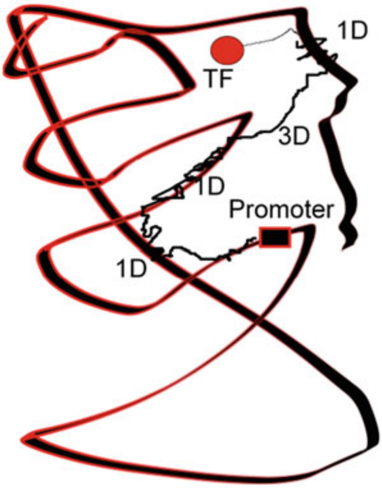

Fig. 7.6 Search scenario for a DNA target by a TF. The TF can attach to the DNA molecule and scan a number of potential binding sites or diffuse freely in the nucleus. The TF alternates periods of one-dimensional random walks along the DNA molecule and free diffusion in the nucleus

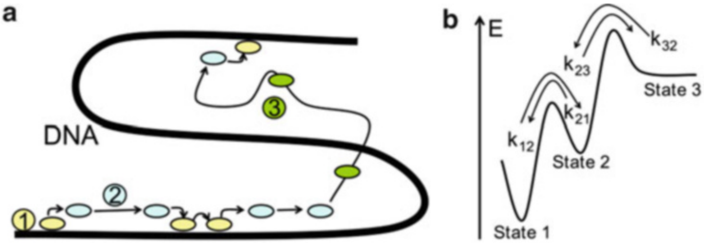

Fig. 7.7 (**a**) Search scenario with three states. (**b**) Energy profile and switching rates between states

to switching to state 1, the TF can detach from the DNA with rate k_{23} and switch to state 3, where it freely diffuses in the nucleus before reattaching in state 2 after an average time k_{32}^{-1}.

The search time can be estimated in a 1D search process in the interval $[0, L]$ with switching between three states. The target (promoter site) is located at $x = 0$ (x is the DNA contour length) and can only be found in state 1. In this approximation, the 3D diffusion in the nucleus (state 3) is described as an effective 1D (diffusion) process in the segment $[0, L]$. In general, this 1D process has to be such that it correctly reproduces the attaching positions in state 2. However, because the attaching positions are random, what only matters is the rate k_{32}.

Using the equations for the sojourn times $t_{nm}(x)$ that a particle spends in state n ($n = 1, 2, 3$), when it starts in state m at position x (Reingruber and Holcman 2010) [see Eq. (7.6)]

$$\begin{aligned} D_1 t_{11}'' - k_{12}(t_{11} - t_{12}) &= -1 \\ D_2 t_{12}'' - k_{21}(t_{12} - \tau_{11}) - k_{23}(t_{12} - t_{13}) &= 0 \\ D_3 t_{13}'' - k_{32}(t_{13} - t_{12}) &= 0 \, , \end{aligned} \tag{7.18}$$

where D_3 is an effective constant that accounts for the complex 3D organization of the nucleus. The boundary conditions are $t_{11}(0) = t'_{11}(L) = t'_{12}(0) = t'_{12}(L) = t'_{13}(0) = t'_{13}(L) = 0$. The remaining sojourn times $t_{2i}(x)$ and $t_{3i}(x)$ are obtained from $t_{1i}(x)$ by $t_{2i}(x) = (k_{12}/k_{21})t_{1i}(x) + k_{21}^{-1}(1-\delta_{i1})$ and $t_{3i}(x) = (k_{23}/k_{32})t_{2i}(x) + k_{32}^{-1}\delta_{i3}$.

By integrating Eq. (7.18), we have that the spatially averaged sojourn times $\tau_{1i} = L^{-1}\int_0^L t_{1i}(x)dx$ satisfy $\tau_{11} = \tau_{13} = \tau_{12}$. Moreover, starting initially uniformly distributed in state m, the MFPT $\tau(m) = \tau_{1m} + \tau_{2m} + \tau_{3m}$ can be expressed in terms of τ_{11} only. Starting in state 1, we have $\tau(1) = \tau_{11}(1 + k_{12}/k_{21} + k_{12}k_{23}/(k_{21}k_{32}))$.

Equation (7.18) can be solved in the limit $D_3 \to \infty$, in which case the sojourn time $t_{13}(x)$ is independent of x and equals the mean, $t_{13}(x) = \tau_{13} = \tau_{12} = \tau_{11}$. In this limit Eq. (7.18) reduces to two equations for $t_{11}(x)$ and $t_{12}(x)$.

Using the dimensionless variables $\hat{x} = x/L$, $l_{12} = k_{12}/(L^2D_1)$, $l_{21} = k_{21}/(L^2D_2)$ and $l_{23} = k_{23}/(L^2D_2)$, and the functions

$$v_1(\hat{x}) = k_{12}\tau_{11}(x)\,, \quad v_2(\hat{x}) = k_{12}\tau_{12}(x)\,, \tag{7.19}$$

($v_1(\hat{x})$ is the mean number of switchings between state 1 and 2), solutions of Eq. (7.18), are given by

$$\begin{aligned}\begin{pmatrix} v_1(\hat{x}) \\ v_2(\hat{x}) \end{pmatrix} &= \frac{l_{21}}{\xi_2}\left(\frac{\cosh(\sqrt{l_{12}}\mu_2(1-\hat{x}))}{\sqrt{l_{12}}\mu_2\sinh(\sqrt{l_{12}}\mu_2)} - \frac{1}{l_{12}\mu_2^2}\right)\boldsymbol{e}_2 \\ &\quad -\frac{l_{21}}{\xi_2}\left(\frac{\cosh(\sqrt{l_{12}}\mu_1(1-\hat{x}))}{\sqrt{l_{12}}\mu_1\sinh(\sqrt{l_{12}}\mu_1)} - \frac{1}{l_{12}\mu_1^2}\right)\boldsymbol{e}_1 + \boldsymbol{v}_1\begin{pmatrix}1\\1\end{pmatrix}\end{aligned} \tag{7.20}$$

where $\xi_2 = \sqrt{(1 + (l_{21} + l_{23})/l_{12})^2 - 4l_{23}/l_{12}}$, $\xi_1 = -1 + (l_{21} + l_{23})/l_{12}$, $\mu_1^2 = 1 + (\xi_1 - \xi_2)/2$, $\mu_2^2 = 1 + (\xi_1 + \xi_2)/2$ and

$$\boldsymbol{e}_1{}^{\top} = (l_{12}(\xi_1 + \xi_2)/(2l_{21}), 1) \tag{7.21}$$

$$\boldsymbol{e}_2{}^{\top} = (l_{12}(\xi_1 - \xi_2)/(2l_{21}), 1). \tag{7.22}$$

The average $v_1 = \int_0^1 v_1(\hat{x})d\hat{x}$ is

$$\begin{aligned} v_1 &= \frac{\xi_2 - \xi_1}{2\xi_2}\left(\sqrt{l_{12}}\frac{\coth(\sqrt{l_{12}}\mu_2)}{\mu_2} - \frac{1}{\mu_2^2}\right) \\ &\quad + \frac{\xi_1 + \xi_2}{2\xi_2}\left(\sqrt{l_{12}}\frac{\coth(\sqrt{l_{12}}\mu_1)}{\mu_1} - \frac{1}{\mu_1^2}\right). \end{aligned} \tag{7.23}$$

Because ξ_1, ξ_2, μ_1, and μ_2 are independent of L, v_1 depends on L only via l_{12}. The relevant physical parameters are L, k_{12}, k_{21}, k_{23}, k_{32}, D_1, and D_2.

The rates k_{12}, k_{21} and k_{23} can be characterized by the probability $p = k_{21}/(k_{21} + k_{23})$ to switch from state 2 to 1 ($q = 1-p$ is the probability to detach and switch from state 2 to 3) and the lengths $l_{s1} = \sqrt{D_1/k_{12}}$ and $l_{s2} = \sqrt{D_2/(k_{21} + k_{23})}$, corresponding to the average sliding distances in state 1 and 2 before switching. The spatially averaged search time $\tau \approx \tau(1)$ is given by

$$\tau = v_1 \left(\frac{l_{s1}^2}{D_1} + \frac{l_{s2}^2}{pD_2} + \frac{1}{k_{32}} \frac{q}{p} \right) . \tag{7.24}$$

Before detaching and switching to state 3, a TF stays bound to the DNA for an average time $\tau_{\mathrm{DNA}} = k_{23}^{-1} + k_{12}^{-1} p/q$, and the overall ratio of the mean time bound to the DNA to the mean time spent in state 3 is

$$r = k_{32} \tau_{\mathrm{DNA}} = \frac{k_{32} l_{s1}^2}{D_2} \left(\frac{p}{q} \frac{D_2}{D_1} + \frac{l_{s2}^2}{q l_{s1}^2} \right) . \tag{7.25}$$

For a fast switching between state 1 and 2 and the diffusion in state 1 is negligible compared to state 2 ($D_1 \ll D_2$), the diffusion constant with which a TF appears to slide along the DNA is

$$D_a \approx \frac{D_2}{1 + k_{21}/k_{12}} = \frac{D_2}{1 + pD_2 l_{s1}^2/(D_1 l_{s2}^2)} . \tag{7.26}$$

The search process depends on l_{s1}, l_{s2}, q, and D_1, when the parameters L, D_2, and k_{32} are given. Modulating these parameters can be a way to regulate gene expression. Because a TF moves in state 2 in a smooth potential, we consider that D_2 is comparable to the 3D diffusion constant. In contrast, in state 1, the TF interacts with individual bp and the effective diffusion constant is much reduced and can be written as $D_1 = D_2 e^{-\chi}$, where $\chi > 0$ depends on the binding energy profile. For a single sliding state, χ is related to the variance of the binding energy. The search is not much sensitive to χ, as long as χ is not too large.

In the regime where $\kappa = l_{sl1}^2/l_{sl2}^2 \ll 1$ and $q \ll 1$, the condition $\kappa \ll 1$ avoids a redundant search in state 1 where diffusion is slow. As long as switching between state 1 and 2 is fast compared to the time k_{32}^{-1} spent in state 3, the limit $q \ll 1$ restricts the frequency of detachment from the DNA that would increase the search time. Under the condition that $\kappa \ll 1$ and $q \ll 1$, we have the asymptotic $\xi_1 \approx -(1-\kappa)$, $\xi_2 \approx 1 + \kappa(1-2q)$, $\mu_1^2 \approx \kappa q$, $\mu_2^2 \approx 1 + \kappa$ and $v_1 \approx L/l_{s1}(1 + \sqrt{\kappa/q})$.

Using these expressions in Eqs. (7.24) and (7.25), we find

$$\tau \approx \sqrt{\frac{L^2}{D_2 k_{32}}} \left(1 + \sqrt{\frac{\kappa}{q}} \right) \left(\frac{e^{\chi}}{\alpha} + \frac{1}{\alpha\kappa} + \alpha q \right) , \tag{7.27}$$

$$r \approx \frac{e^{\chi}}{\alpha^2 q} + \frac{1}{\alpha^2 q \kappa} , \tag{7.28}$$

where $\alpha = \sqrt{D_2/(l_{s1}^2 k_{32})}$. When α and χ are fixed, the minimum of $\tau(q, \kappa)$ as a function of κ and q is achieved for $(\kappa_{\min}, q_{\min}) = (\sqrt{2/(\alpha e^{\chi})}, \alpha^{-2} \kappa_{\min}^{-1})$, and

$$\tau_{\min} = \sqrt{\frac{L^2}{D_2 k_{32}}} \left(1 + \sqrt{\frac{2\alpha}{e^{\chi}}}\right)^2 \frac{e^{\chi}}{\alpha}. \tag{7.29}$$

$$r_{\min} = 1 + \sqrt{2e^{\chi}/\alpha}. \tag{7.30}$$

For $e^{\chi}/\alpha \ll 1$, the asymptotic expansion is $\tau_{\min} \approx 2\sqrt{L^2/(D_2 k_{32})}(1 + \sqrt{2e^{\chi}/\alpha})$, showing that $\tau_{\min}$ does not depend exponentially on χ in that regime. These results can be compared with the ones for a single sliding state: when a TF alternates only between state 1 and 3 with rates k_{13} and k_{31} (the intermediate state 2 is absent), we find from Eq. (7.23) that $\tilde{v}_1 = \sqrt{l_{13}} = \sqrt{L^2/(D_1 k_{13})}$, and for the search time we recover the expression $\tilde{\tau} = \sqrt{L^2/(D_1 k_{13})}(k_{13}^{-1} + k_{31}^{-1})$.

When the rate k_{31} is fixed, the minimum $\tilde{\tau}_{\min} = 2\sqrt{L^2/(D_1 k_{31})}$ is achieved for $k_{13} = k_{31}$, implying that the ratio r is always one at the minimum, which is not the case in the two states sliding model. Increasing the binding strength in state 1, while the motion in state 2 (interaction with DNA backbone) is not affected, affects the search time τ (see Fig. 7.8a, b for $l_{s1} = 0.5$ and various l_{s2} and q that are independent of χ). This is in contrast to cases where $\tau_{\min}$ is achieved for values of $q_{\min}$ and $l_{s2,\min}$ that do depend on χ and l_{s1}. In Fig. 7.8c, we plot the apparent diffusion constant D_a (sliding along the DNA) as a function of χ, with parameters associated with panel a. D_a decreases as χ increases, and for $\chi \sim 7$, we have $D_a \sim 0.4\,\mu\text{m}^2/\text{s}$, which is similar to measurements (Elf et al. 2007). Within a single sliding state model, the 1D diffusion coefficient $D_1 = D_2 \sim -\chi/2$ decreases much faster as function of χ compared to D_a (dashed line in Fig. 7.8c).

Experimental measurements of the apparent diffusion are now compatible with stronger binding energies in a two-state compared to a single state model. Finally, τ is also modulated by varying q or l_{s2} for $\chi = 7.5$ (Fig. 7.8d). The present model, describing the dynamics of a TF that alternates between a slow and a fast state on the DNA molecule, shows that the overall search time is considerably faster and much less sensitive to binding energy fluctuations compared to a scenario, with a single sliding state. Furthermore, performing fast translocations ("hoppings") of the order of 10 bp in state 2 speeds up the search time by reducing a recurrent search in the slow state.

7.2 Annotations

Other switching searches have been investigated, where particles diffuse close to the surface membrane (Tsaneva et al. 2009; Oshanin et al. 2010; Berezhkovskii and Barzykin 2012). The gated narrow escape model is used to calculate the GNET, which requires the solution of a coupled system of mixed Dirichlet–Neumann boundary value problems for Poisson's equations. The system was solved in Reingruber and Holcman (2009, 2010), where (7.3) was generalized in to any number of states and the one-dimensional case was resolved.

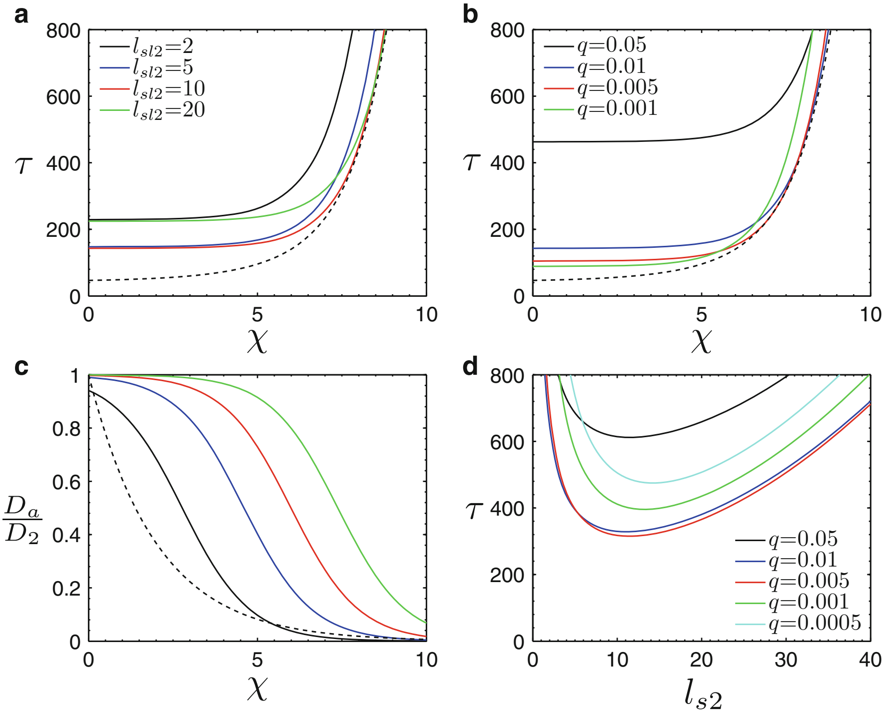

Fig. 7.8 (**a**) Mean search time τ for $l_{sl1} = 0.5$ and $q = 0.01$. The *dashed line* shows the minimum of τ. (**b**) τ for $l_{sl1} = 0.5$ and $l_{s2} = 10$. (**c**) Apparent diffusion constant D_a scaled by D_2 for the situation in (**a**). The *dashed line* is the diffusion constant $D_1/D_2 = e^{-\chi/2}$ for a model with a single sliding state. (**d**) Search time τ for $\chi = 7.5$, showing a minimum

In the absence of switching, the computation of the sojourn time reduces to that of the NET τ_1 (Kolokolnikov et al. 2005; Singer et al. 2006c; Grigoriev et al. 2002), which shows that outside a small boundary layer around the absorbing hole of radius a, where a characterizes the extent of $\partial\Omega_a$, the positional NET is almost independent of the initial ligand position (Singer et al. 2006c). The scaled system (7.15) was derived in Reingruber and Holcman (2009). The model introduced in Sect. 8.1 was proposed in . It is contrary to the early studies in Edelstein-Keshet and Ermentrout (2000), Gennady et al. (2006), Graham et al. (2006), Hammele and Zimmermann (2003), and Miller and Samuels (1997).

Chapter 8
Narrow Escape in Other Cellular Processes

Several applications of the narrow escape theory are considered in this chapter. The first one concerns the process of growth in neurons, which results from the delivery of vesicles to a small initiation place. The second example concerns the rotation of a rigid rod between two layers. This computation provides a time scale in the context of large motion during DNA repair confined in a two-dimensional chromatin structure. The next example is the elucidation of the role of geometry in hiding binding sites that control chemical reactions. The last example concerns the diffusive transfer of molecules in asymmetric dumbbell-shaped domains that are formed during cell division.

8.1 Stochastic Model of Vesicular Trafficking During Neurite Outgrowth

Neurite growth is a fundamental process in the generation of dendritic trees and axons, involved in neuronal wiring during early brain development, learning, and regeneration. Many cellular mechanisms are contributing to axonal and dendritic genesis such as actin cytoskeleton and microtubules (Fig. 8.1) (da Silva and Dotti 2002; Burnette et al. 2007; Bouquet et al. 2007; Dent and Gertler 2003). Indeed membrane is added to the neurite through the delivery of vesicle (exocytosis) during the growth process (Futerman and Banker 1996): by fusing with the cell membrane, these vesicles deliver their membrane, which increases the surface area of the neurite (Alberts et al. 2003, 2006; Futerman and Banker 1996; Pfenninger et al. 2003; Shea and Sapirstein 1988). The cytoskeleton also contribute to the neurite growth process by first being involved in vesicular trafficking, and second by stabilizing the neurite structure (Graham et al. 2006; Zhou et al. 2002). The specific contribution of both vesicle and microtubule dynamics to neurite growth can be examined using

D. Holcman, Z. Schuss, *Stochastic Narrow Escape in Molecular and Cellular Biology*, DOI 10.1007/978-1-4939-3103-3_8

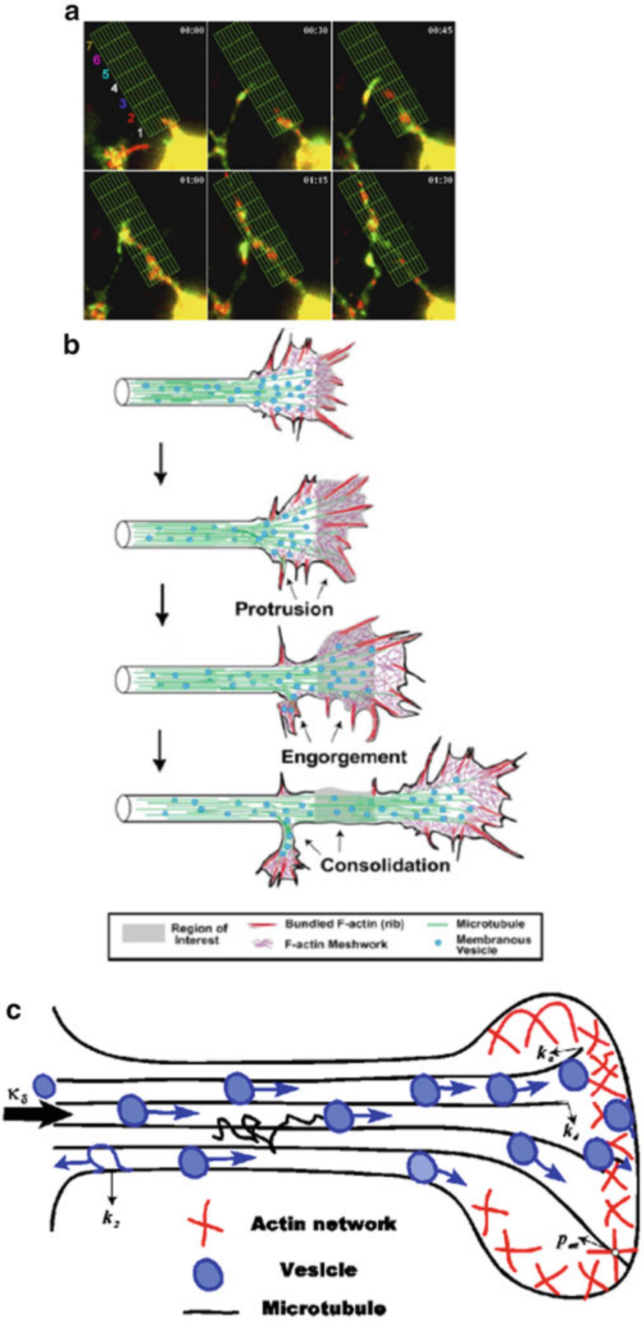

Fig. 8.1 Neuron outgrowth. (**a**) Quantification of fluorescence intensity during neurite outgrowth. The *red* (mRFP-TI-VAMP) and green (EGFP-Syb2) show distribution of vesicles along the growing neurite. To quantify the dynamics of the two FP-tagged proteins, the selected neurite was ideally segmented in seven stages (*colors numbers*), from the cell body limit to the maximal extent of the process. (**b**) Schematic representation of the neurite outgrowth. (**c**) Scheme of microtubules and vesicles dynamics

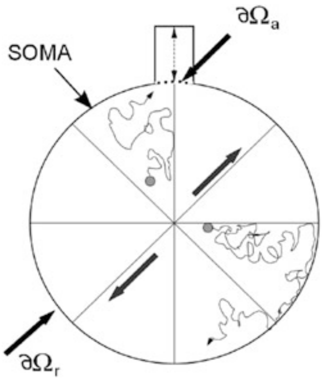

Fig. 8.2 Vesicular motion confined to the soma surface: vesicles enter the neurite when they reach the small part of the soma boundary $\partial\Omega_a$. $L(t)$ is the protrusion length

a modeling approach and the overall neurite outgrowth rate can be computed from vesicular dynamics. We describe here a vesicular stochastic model that accounts for their motion in the cell soma, where the main step is a narrow escape due to the search for the neurite initiation site (Ω_a), that can be described as a two-dimensional diffusion/sequestration/fusion at the cell surface (Tsaneva et al. 2009). The modeling of neurite growth starts with the delivery and insertion of vesicles at a specific boundary location, denoted by Ω_a. It can be, for example, the part where the axon or the dendrite is generated (see Fig. 8.2). Although vesicles may have different sizes, only vesicles of mean radius a are considered. Because there are plenty of vesicles in the cytoplasm (hundreds to thousands), the fluctuations in their number can be neglected and we can assume that after a vesicle fuses, another is generated, resulting in a constant supply of new vesicles. This assumption serves to maintain a constant number of vesicles in the model. The growth is assumed to be initiated by fusion of vesicles with the surface of the membrane (Smith 1994). When this occurs, the vesicular membrane is used to increase the neurite by a quantal length l_0. The dynamics of neurite growth is also controlled by the membrane endocytosis rate k_2. When the neurite radius does not change, the endocytosis rate is proportional to the neurite surface.

The motion of a vesicle toward $\partial\Omega_a$ (Fig. 8.2) consists of intermittent binding and drift along microtubules with deterministic velocity and free diffusion in the cell when the vesicle is detached from any microtubule. The transitions between the two modes of motion are modeled here as a random telegraph process. Thus the dynamics of the motion is described by the switching rule

$$\dot{\boldsymbol{x}}(t) = \begin{cases} \sqrt{2D}\dot{\boldsymbol{w}}(t) & \text{when the particle is free} \\ \\ V(t)\boldsymbol{r} & \text{when the particle is bound,} \end{cases} \tag{8.1}$$

where $\boldsymbol{x}(t)$ represents the position of the particle (the zero of the coordinate system is the center of the soma, approximated as a ball in Fig. 8.2) and $V(t) \geq 0$ is a time-dependent drift velocity along microtubules, directed toward the cell surface,

$\boldsymbol{w}(t)$ is a δ-correlated standard white noise, $\boldsymbol{r} = \frac{\boldsymbol{x}(t)}{|\boldsymbol{x}(t)|}$ is the radial unit vector pointing toward the boundary $\partial\Omega_a$. A simplifying assumption is that the velocity along the microtubules is constant.

8.1.1 Derivation of the Join pdfs for a Coarse-Grained Stochastic Equation

The state of the particle, $S(t)$, is chosen as 1 when the particle is free and -1 when it is bound to a microtubule. We assume $S(t)$ switches from 1 to -1 at exponential waiting times with rate λ_1 and in the opposite direction with rate λ_{-1}. The rates can depend on $\boldsymbol{x}$. The pair $(\boldsymbol{x}(t), S(t))$ is a Markovian jump-diffusion process. We consider, for simplicity, the one-dimensional case. The transition probability densities are

$$\begin{aligned}
&\Pr\{x(t+\Delta t) = y, S(t+\Delta t) = 1\,|\,x(t) = x, S(t) = 1\}\\
&\quad = \frac{(1-\lambda_1\Delta t)}{\sqrt{2\pi D\Delta t}}\exp\left\{-\frac{(x-y)^2}{2D\Delta t}\right\} &(8.2)\\
&\Pr\{x(t+\Delta t) = y, S(t+\Delta t) = -1\,|\,x(t) = x, S(t) = 1\}\\
&\quad = \frac{\lambda_1\Delta t}{\sqrt{2\pi D\Delta t}}\exp\left\{-\frac{(x-y)^2}{2D\Delta t}\right\} &(8.3)\\
&\Pr\{x(t+\Delta t) = y, S(t+\Delta t) = -1\,|\,x(t) = x, S(t) = -1\}\\
&\quad = (1-\lambda_{-1}\Delta t)\delta(y-x-V(t)r\Delta t) &(8.4)\\
&\Pr\{x(t+\Delta t) = y, S(t+\Delta t) = 1\,|\,x(t) = x, S(t) = -1\}\\
&\quad = \lambda_{-1}\Delta t\delta(y-x-V(t)r\Delta t). &(8.5)
\end{aligned}$$

Writing

$$\Pr\{x(t+\Delta t) = y, S(t+\Delta t) = s\,|\,x(\tau) = x, S(\tau) = \sigma\} = p(y, s, t+\Delta t\,|\,x, \sigma, \tau),$$

we can write the Chapman–Kolmogorov equation as (Schuss 2010b)

$$\begin{aligned}
p(y, s, t+\Delta t\,|\,x, \sigma, 0) = &\int p(y, s, t+\Delta t\,|\,z, s, t)p(z, s, t\,|\,x, \sigma, 0)\,dz\\
&+\int p(y, s, t+\Delta t\,|\,z, -s, t)p(z, -s, t\,|\,x, \sigma, 0)\,dz.
\end{aligned}\tag{8.6}$$

Thus, for $s = 1$ Eqs. (8.2) and (8.5) give in (8.6)

$$\begin{aligned} p(y,1,t+\Delta t\,|\,x,\sigma,0) = &\int \frac{(1-\lambda_1\Delta t)}{\sqrt{2\pi D\Delta t}}\exp\left\{-\frac{(z-y)^2}{2D\Delta t}\right\} p(z,1,t\,|\,x,\sigma,0)\,dz \\ &+\int \lambda_{-1}\Delta t\delta(y-z-V(t)r\Delta t)p(z,-1,t\,|\,x,\sigma,0)\,dz. \end{aligned} \tag{8.7}$$

The expansion of the first integral in (8.7) for small Δt gives

$$\begin{aligned} p(y,1,t+\Delta t\,|\,x,\sigma,0) = &\,p(y,1,t\,|\,x,\sigma,0) + D\Delta t\frac{\partial^2 p(y,1,t\,|\,x,\sigma,0)}{\partial y^2} \\ &-\lambda_1\Delta t p(y,1,t\,|\,x,\sigma,0) \\ &+\lambda_{-1}\Delta t p(y-V(t)r\Delta t,-1,t\,|\,x,\sigma,0)+o(\Delta t). \end{aligned}$$

It follows that

$$\begin{aligned} &\frac{\partial p(y,1,t\,|\,x,\sigma,0)}{\partial t} \\ &\quad = D\frac{\partial^2 p(y,1,t\,|\,x,\sigma,0)}{\partial y^2} - \lambda_1 p(y,1,t\,|\,x,\sigma,0) + \lambda_{-1}p(y,-1,t\,|\,x,\sigma,0). \end{aligned} \tag{8.8}$$

For $s = -1$ Eqs. (8.3) and (8.4) give in the Chapman–Kolmogorov equation (8.6)

$$\begin{aligned} p(y,-1,t+\Delta t\,|\,x,\sigma,0) = &\int \frac{\lambda_1\Delta t}{\sqrt{2\pi D\Delta t}}\exp\left\{-\frac{(z-y)^2}{2D\Delta t}\right\} p(z,1,t\,|\,x,\sigma,0)\,dz \\ &+\int (1-\lambda_{-1}\Delta t)\delta(y-z-V(t)r\Delta t)p(z,-1,t\,|\,x,\sigma,0)\,dz, \end{aligned} \tag{8.9}$$

which in the limit $\Delta t \to 0$ reduces to

$$\begin{aligned} \frac{\partial p(y,-1,t\,|\,x,\sigma,0)}{\partial t} = &\,\lambda_1 p(y,1,t\,|\,x,\sigma,0) - \lambda_{-1}p(y,-1,t\,|\,x,\sigma,0) \\ &- V(t)r\frac{\partial p(y,-1,t\,|\,x,\sigma,0)}{\partial y}. \end{aligned} \tag{8.10}$$

Dropping the initial conditions, (8.8) and (8.10) can be written as

$$\begin{aligned} \frac{\partial p_1(y,t)}{\partial t} &= -\lambda_1 p_1(y,t) + \lambda_{-1}p_{-1}(y,t) + D\frac{\partial^2 p_1(y,t)}{\partial y^2} \\ \frac{\partial p_{-1}(y,t)}{\partial t} &= \lambda_1 p_1(y,t) - \lambda_{-1}p_{-1}(y,t) - V(t)r\frac{\partial p_{-1}(y,t)}{\partial y}. \end{aligned} \tag{8.11}$$

Setting

$$\begin{aligned}p_{\pm 1}(t\,|\,\pm 1) &= \Pr\{S(t)=\pm 1\,|\,S(0)=\pm 1\}\\ &= \int_{-\infty}^{\infty} p_0(x)\int_{-\infty}^{\infty} p_{\pm 1}(y,t\,|\,x,0,\pm 1)\,dy\,dx \end{aligned}\tag{8.12}$$

and integrating (8.11) with respect to x and y gives the system

$$\dot{p}_1(t) = -\lambda_1 p_1(t) + \lambda_{-1}p_{-1}(t), \quad \dot{p}_{-1}1(t) = \lambda_1 p_1(t) - \lambda_{-1}p_{-1}(t). \tag{8.13}$$

The normalized stationary solution of (8.13) corresponding to the eigenvalue 0 is

$$p_1 = \frac{\lambda_{-1}}{\lambda_1+\lambda_{-1}}, \quad p_{-1} = \frac{\lambda_1}{\lambda_1+\lambda_{-1}}, \tag{8.14}$$

which is the stationary distribution of the random telegraph process $S(t)$. The other solution decays exponentially in time.

The process $x(t)$ can be approximated by a diffusion process $\tilde{x}(t)$, for example, if the jumps are frequent or small,

$$d\tilde{x}(t) = a(\tilde{x}(t),t)\,dt + \sqrt{2}b(\tilde{x}(t),t)\,dw, \tag{8.15}$$

where

$$\begin{aligned}a(x,t) &= \lim_{\Delta t\to 0}\frac{\mathbb{E}[x(t+\Delta t)-x\,|\,x(t)=x]}{\Delta t},\\ b^2(x,t) &= \lim_{\Delta t\to 0}\frac{\mathbb{E}[(x(t+\Delta t)-x)^2\,|\,x(t)=x]}{\Delta t}.\end{aligned}\tag{8.16}$$

The conditional expectations are calculated by expressing the transition density $p(y,t+\Delta t\,|\,x,t)$ of the process $x(t)$ as the marginal of the joint transition density of the pair $(x(t),S(t))$. That is,

$$\begin{aligned}&\Pr\{x(t+\Delta t)\,|\,x(t)=x\}\\ &\quad= \Pr\{x(t+\Delta t),S(t+\Delta t)=1\,|\,x(t)=x,S(t)=1\}\Pr\{S(t)=1\}\\ &\qquad+ \Pr\{x(t+\Delta t),S(t+\Delta t)=1\,|\,x(t)=x,S(t)=-1\}\Pr\{S(t)=-1\}\\ &\qquad+ \Pr\{x(t+\Delta t),S(t+\Delta t)=-1\,|\,x(t)=x,S(t)=1\}\Pr\{S(t)=1\}\\ &\qquad+ \Pr\{x(t+\Delta t),S(t+\Delta t)=-1\,|\,x(t)=x,S(t)=-1\}\Pr\{S(t)=-1\}.\end{aligned}$$

For sufficiently long time $\Pr\{S(t) = \pm 1\} \approx p_{\pm 1}$, so using (8.2)–(8.5), and (8.14), we obtain the weighted average of the two dynamics in (8.1),

$$a(x,t) = \frac{\lambda_{-1}}{\lambda_1 + \lambda_{-1}} V(t) r, \quad b^2 = \frac{\lambda_1}{\lambda_1 + \lambda_{-1}} D, \tag{8.17}$$

as expected. The generalization to two and three dimensions is pretty straightforward.

The velocity field and diffusion coefficient in (8.17) have to be estimated. Their calibration is found by first solving the Fokker–Planck equation for the transition probability density explicitly in a ball and then fitting it to the vesicles distribution generated by Brownian simulations of (8.1) and (8.15). In these simulations, vesicles move inside a slice domain (Fig. 8.3), where the boundary associated with the dynamics of (8.1) represents the place where the drift occurs, while it reflects trajectories in the case of (8.15). The histogram of vesicles distribution (Fig. 8.3) is generated by Brownian simulations of (8.1) with 1000 vesicles. It is then fit to the explicit solution of the FPE and by optimizing velocity amplitude. Using the same drift amplitude, the histogram of vesicles is generated according to (8.15) and fit to the explicit solution of the FPE, which turns out to be in very good agreement with the given choice of the drift field (Fig. 8.3b). The simulations of vesicular diffusion and velocity along microtubules used the parameter values obtained from experimental studies in PC12 cells (Han et al. 1999) and *Xenopus* embryo neuronal cultures (Zakharenko and Popov 1998) (see details in Tsaneva et al. 2009).

8.1.2 Calibration Procedure to the Explicit Solution of the FPE

The calibration procedure described in the previous section can be made explicit by using for the drift a potential term. Indeed, when the drift field $\boldsymbol{ax}$ is supposed to be radial symmetric in the three-dimensional model (8.17), we chose

$$\boldsymbol{a}(\boldsymbol{x}) = -\nabla \phi(\boldsymbol{x}). \tag{8.18}$$

where

$$\phi(\boldsymbol{x}) = \alpha |\boldsymbol{x}|. \tag{8.19}$$

The parameter α is estimated from a steady distribution, where no neurite can grow. To evaluate the steady state distribution of vesicles inside a cellular domain containing a bundle of microtubules, Brownian trajectories of many vesicles are simulated inside a cell with no-flux (reflection) at the boundary. The simulations are restricted to the case of a repulsive drift, which points towards the cell boundary. For a spherical domain α in (8.19) is a positive constant to be determined. The Brownian simulations of (8.15) are shown in Fig. 8.3. The fitting curve is the steady state solution of the Fokker–Planck equation. Indeed, the probability density function (pdf) $p(\boldsymbol{x}, t)$ of a trajectory is the solution of the FPE

$$\frac{\partial p}{\partial t} = D \triangle p + \nabla \cdot (\nabla \phi p) \tag{8.20}$$

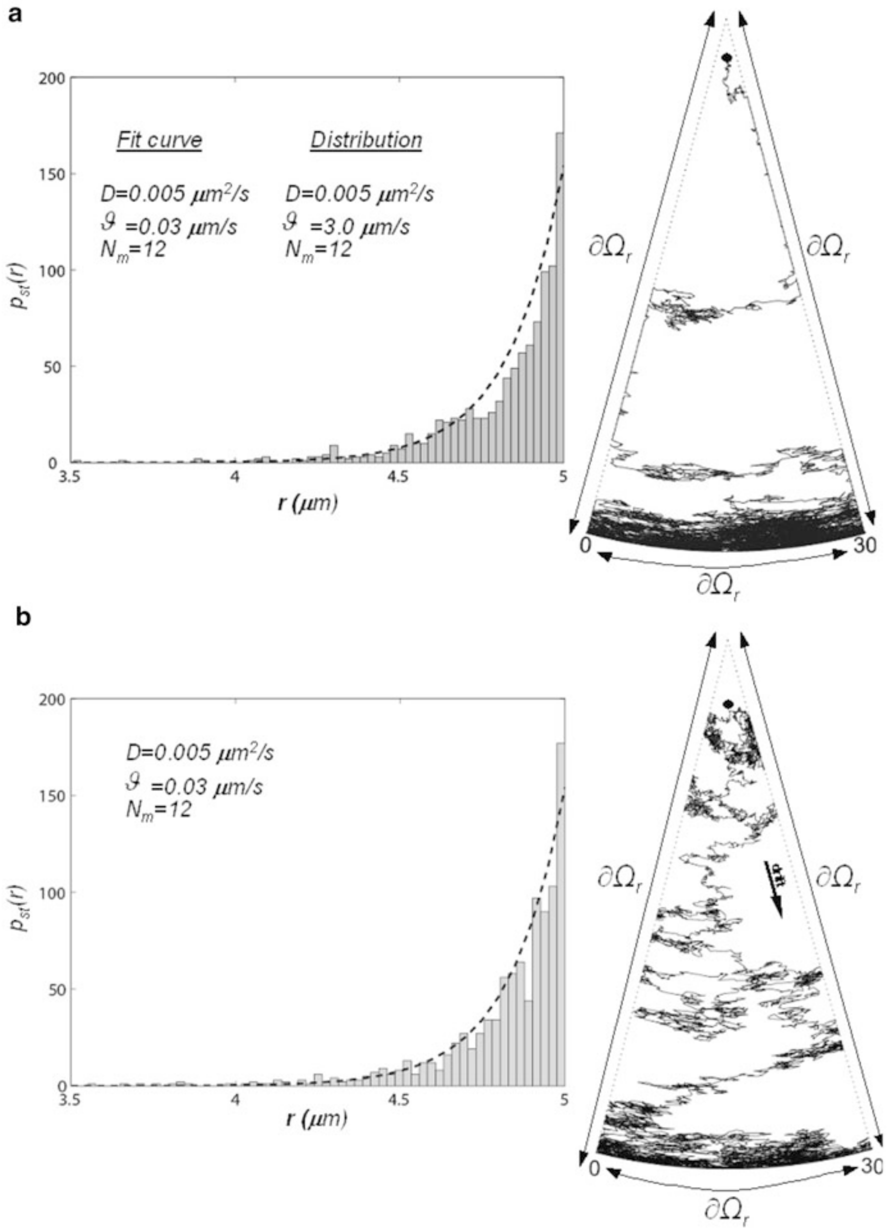

Fig. 8.3 Steady state distribution ($N_0 = 1000$) and probability density function of vesicle in a wedge. (**a**) 2D sample membrane vesicle trajectory obtained by simulating Eq. (8.1); (**b**) 2D sample membrane vesicle trajectory obtained by simulating Eq. (8.15)

with the no-flux boundary condition

$$\boldsymbol{J} \cdot \boldsymbol{n} = -D\frac{\partial p}{\partial n} - p\frac{\partial \phi}{\partial n} = 0. \tag{8.21}$$

The steady state solution of (8.20), (8.21) is given by

$$p(\boldsymbol{x}) = Ce^{-\phi(\boldsymbol{x})/D}, \tag{8.22}$$

where C is determined by the normalization condition

$$\int_{\Omega} p(\boldsymbol{x})\, d\boldsymbol{x} = 1. \tag{8.23}$$

The steady concentration $\rho_{\text{STEADY}}(\boldsymbol{x})$ of N_0 independent vesicles is given by

$$\rho_{\text{STEADY}}(\boldsymbol{x}) = N_0 p(\boldsymbol{x}). \tag{8.24}$$

For a constant drift velocity $\dfrac{\partial \phi}{\partial r} = -\alpha$ in the radial direction (8.22) becomes

$$p_{\text{STEADY}}(\boldsymbol{x}) = Ce^{\alpha|\boldsymbol{x}|/D} \quad \text{for } \ 0 < |\boldsymbol{x}| \leq R. \tag{8.25}$$

In two dimensions it is given by

$$p_{\text{STEADY}}(\boldsymbol{x}) = \frac{\alpha e^{\alpha|\boldsymbol{x}|/D}}{2\pi D\left[Re^{\alpha R/D} - \frac{D}{\alpha}(e^{\alpha R/D} - 1)\right]} \quad \text{for } \ 0 < |\boldsymbol{x}| \leq R \tag{8.26}$$

and in three dimensions

$$p_{\text{STEADY}}(\boldsymbol{x}) = \frac{\alpha e^{\alpha|\boldsymbol{x}|/D}}{4\pi D\left[R^2 e^{\alpha R/D} - \frac{2D}{\alpha}\left(Re^{\alpha R/D} - \frac{D}{\alpha}(e^{\alpha R/D} - 1)\right)\right]} \quad \text{for } \ 0 < |\boldsymbol{x}| \leq R. \tag{8.27}$$

The parameter α is chosen such that the density of vesicle trajectories generated by simulations of (8.15) fits the histogram generated by the model process (8.1) for the same domain in dimension 2.

8.1.3 Arrival Rate of Vesicles to a Small Opening in the Soma

The vesicle motion (Fig. 8.2) is modeled as isotropic diffusion in a spherical domain of radius R. The field of microtubules in this model generates a radial potential

$\phi(\boldsymbol{x}) = -\alpha|\boldsymbol{x}|$, so the homogenized force field is

$$\boldsymbol{F}(\boldsymbol{x}) = -\nabla\phi(\boldsymbol{x}) = \alpha\frac{\boldsymbol{x}}{|\boldsymbol{x}|}. \tag{8.28}$$

The constant radial velocity field points away from the center when $\alpha = v > 0$. This model coarse-grains into effective diffusion the vesicle motion that jumps intermittently between Brownian motion and directed motion along microtubules and actin filaments. The domain Ω for the some is approximated as a ball, where $\partial\Omega_a$ is the absorbing part where vesicles are absorbed upon hitting the boundary (see Fig. 8.2). The switching motion is now replaced by the calibrated homogenized version (8.15).

The arrival rate of vesicles arrival to $\partial\Omega_a$ is the reciprocal of the mean first passage time, which is the sum of the mean time to the boundary plus the mean time to find the small window $\partial\Omega_a$ of radius δ located on the sphere (see Fig. 8.2). This decomposition for the mean times is valid for large α (see relation (8.37) below). To determine the arrival rate of vesicles at $\partial\Omega_a$, we use the narrow escape method with a potential described in Sect. 1.9.1. The probability density function $p_\delta(\boldsymbol{x}, t\,|\,\boldsymbol{x}_0)$ of a vesicle trajectory $\boldsymbol{x}(t)$ that starts anywhere in the entire domain at $\boldsymbol{x}_0 \in \Omega$ is the solution of the FPE in Ω

$$\frac{\partial p_\delta}{\partial t} = D\triangle p_\delta + \nabla\cdot(p_\delta\nabla\phi) \tag{8.29}$$

with the mixed boundary conditions

$$p_\delta(\boldsymbol{x}, t\,|\,\boldsymbol{x}_0) = 0 \quad \text{for } \boldsymbol{x} \in \partial\Omega_a \tag{8.30}$$

$$\boldsymbol{J}\cdot\boldsymbol{n}(\boldsymbol{x}, t\,|\,\boldsymbol{x}_0) = 0 \quad \text{for } \boldsymbol{x} \in \partial\Omega_r, \tag{8.31}$$

and the initial condition

$$p_\delta(\boldsymbol{x}, 0\,|\,\boldsymbol{x}_0) = \delta(\boldsymbol{x} - \boldsymbol{x}_0). \tag{8.32}$$

For an initial density $p_0(\boldsymbol{x}_0)$, the pdf is given by

$$p_\delta(\boldsymbol{x}, t) = \int_\Omega p_\delta(\boldsymbol{x}, t\,|\,\boldsymbol{x}_0)p_0(\boldsymbol{x}_0)\,d\boldsymbol{x}_0, \tag{8.33}$$

so that

$$p_\delta(\boldsymbol{x}, 0) = p_0(\boldsymbol{x}). \tag{8.34}$$

The mean time a trajectory spends at $\boldsymbol{x} \in \Omega$ prior to absorption in $\partial\Omega_a$ is given by Schuss (2010b)

$$u_\delta(\boldsymbol{x}) = \int_0^\infty p_\delta(\boldsymbol{x}, t)\, dt, \tag{8.35}$$

which is exponential $u_\delta(\boldsymbol{x}) = \frac{1}{4D\delta} \exp\left\{\frac{\phi_0 - \phi(\boldsymbol{x})}{D}\right\}$. The MFPT to $\partial\Omega_a$ is given in Sect. 1.9.2 as

$$\bar{\tau}_\delta = \int_\Omega u_\delta(\boldsymbol{x})\, d\boldsymbol{x} \approx \frac{e^{\phi_0/D}}{4D\delta} \int_\Omega \exp\left\{\frac{-\phi(\boldsymbol{x})}{D}\right\} d\boldsymbol{x}, \tag{8.36}$$

where ϕ_0 is the potential at the absorbing window $\partial\Omega_a$. The evaluation of the integral in (8.36) differs from that in Sects. 1.9.1–1.9.2, because the drift here is directed toward the boundary. This compels the trajectories to reach the boundary prior to absorption and search for the absorbing window by surface diffusion. The integral (8.36) can indeed be approximated for sufficiently large drift by the Laplace expansion of the integral,

$$\int_\Omega \exp\left\{-\frac{\phi(\boldsymbol{x})}{D}\right\} d\boldsymbol{x} \approx D \exp\left\{\frac{\phi_m}{D}\right\} \int_{\partial\Omega} \frac{dS_{\boldsymbol{x}}}{\dfrac{\partial\phi(\boldsymbol{x})}{\partial n}} + o(D), \tag{8.37}$$

where the maximum of the potential $\phi_m = \phi(\boldsymbol{x})$ is at $\boldsymbol{x} = R$ achieved on the sphere. Due to the radially symmetric soma, we get

$$\int_\Omega \exp\left\{\frac{-\phi(\boldsymbol{x})}{D}\right\} d\boldsymbol{x} = \frac{4\pi D}{\alpha}\left[R^2 - \frac{RD}{\alpha} + \frac{D^2}{\alpha}\right] \exp\left\{\frac{\phi_m}{D}\right\}, \tag{8.38}$$

where $\alpha = \dfrac{\partial\phi}{\partial r}$ is the constant drift along microtubules. Hence the mean arrival time is

$$\bar{\tau}_\delta = \frac{\pi e^{\frac{\phi_m - \phi_0}{D}}}{\delta\alpha}\left[R^2 - \frac{RD}{\alpha} + \frac{D^2}{\alpha}\right].$$

Thus the arrival rate of vesicles is given by

$$\kappa_\delta = \frac{1}{\bar{\tau}_\delta} = \frac{\delta\alpha}{\pi\left[R^2 - \frac{RD}{\alpha} + \frac{D^2}{\alpha}\right]} e^{-\triangle E/D}, \tag{8.39}$$

where $\triangle E = \phi_m - \phi_0$. Since $\triangle E = 0$ (because ϕ_0 and ϕ_m are both achieved on the cell surface) and neglecting the contribution of the last two terms in the denominator (which is around 1 %) we get

$$\kappa_\delta = \frac{1}{\bar{\tau}_\delta} \approx \frac{\delta\alpha}{\pi R^2}. \tag{8.40}$$

This approximation of the rate assumes that the mean time to find the surface which is R/α is much smaller than the mean time $\bar{\tau}_\delta$. The effective drift α captures the microtubule organization. Furthermore under the spherical cell approximation, the maximum of the potential ϕ is achieved everywhere on the cell surface. Situation where $\triangle E$ is not zero may occur in non-spherical cells where the neurite initiation is located at a distance different from where the maximum of ϕ is achieved.

We conclude that the mean first passage time of a vesicle to a small neurite initiation site of radius a on the cell surface is given (Tsaneva et al. 2009) in the large force limit by

$$\bar{\tau} = \frac{|S|}{av}\left[1 + O\left(\frac{D}{vR}\right)\right], \tag{8.41}$$

where $|S|$ is the entire surface area of the soma. Formula (8.41) reveals that unlike (3.26) for Brownian motion, the search time in this case depends on the boundary surface due to the sequestration at the surface by the strong drift. Simulations show that the Brownian trajectories stay close to the boundary surface in their search for the absorbing window (Tsaneva et al. 2009). The derivation of (8.41) relies on the three-dimensional NET formula for Brownian motion in a potential field in the limit of high velocity v [see (1.166)–(1.168) in Sect. 1.9.1]. In general for small diffusion, the mean arrival time to the small window will be the sum $\frac{R}{v} + \frac{|S|}{av}\left[1 + O\left(\frac{D}{vR}\right)\right]$.

Dynamics of Neurite Outgrowth

Using the vesicular arrival rate at the protrusion, $\partial\Omega_a$, the neurite growth process can be coarse-grained into a Markovian jump process with a simple master equation. The neurite length $L(t)$ increases proportionally to the flux of vesicles and exocytosis, and decreases due to endocytosis, which can occur anywhere on the neurite surface membrane with rate k_2 (see Nishimura et al. 2003). The probabilities $p_q(t) = \Pr\{L(t) = ql_0\}$ that at time t a neurite has exactly length ql_0 satisfy the Kolmogorov (master) equations

$$\begin{aligned}
\dot{p}_q(t) &= -[k_2 q + \kappa_\delta N_0]p_q(t) + k_2(q+1)p_{q+1}(t) + [\kappa_\delta N_0]p_{q-1}(t) \quad \text{for } q \geq 1,\\
\dot{p}_0(t) &= -\kappa_\delta N_0 p_0(t) + k_2 p_1(t) \quad \text{for } q = 0,
\end{aligned}$$

where q is a quantal number, l_0 is quantal length, given by a single vesicle fusion, and the total number of vesicles N_0 is maintained constant inside the soma. The mean and the variance of p_q are given by

$$M(t) = \sum_{q=1}^{\infty} q p_q(t), \quad \sigma^2(t) = \sum_{q=1}^{\infty} q^2 p_q(t) - M^2(t)$$

and in the steady-state,

$$M(\infty) = \frac{\kappa_\delta}{k_2} N_0, \quad \sigma^2(\infty) = \frac{\kappa_\delta}{k_2} N_0.$$

The mean length of the neurite can be shown to satisfy (Tsaneva et al. 2009)

$$\frac{dL}{dt} = l_0 N_0 \kappa_\delta - k_2 L. \tag{8.42}$$

Assuming that initially the neurite length is zero integration of (8.42) gives the time-dependent length

$$L(t) = \frac{l_0 N_0 \kappa_\delta}{k_2} (1 - e^{-k_2 t}). \tag{8.43}$$

and the steady state

$$L_{\text{eq}} = \frac{l_0 N_0 \kappa_\delta}{k_2}.$$

The neurite length with time-dependent vesicles flux $J(t)$ satisfies the equation

$$\frac{dL}{dt} = J(t) - k_2 L. \tag{8.44}$$

In the absence of microtubules, a nascent neurite initiated by vesicular delivery can only reach a small length but by adding the microtubules dynamics to the vesicular dynamics, using stochastic analysis and simulations, the dynamics of neurite growth can be generated, depending on the coupling parameter between the microtubules and the neurite. Indeed, the interactions of vesicles and microtubules can lead to various growing regimes: three types of neurite growth regimes have been identified: axonal, dendritic growth (Prochiantz 1995; da Silva and Dotti 2002) and an oscillatory mode (Tsaneva et al. 2009). Microtubules and neurite growth can be stabilized when they are attached together, preventing collapse or catastrophe microtubule decay. This interaction is measured by the parameter p_a (probability of attachment), p_d (probability of detachment) and k_2 the rate of detachment. The ensemble of stochastic rules for neurite growth are summarized in Tsaneva et al. (2009).

8.1.4 Neurite Outgrowth Modulated by Intermittent Neuronal Activity

The local environment activity can modulate neurite outgrowth. Such activity may represent the modulation by neurotransmitters or any cues involved in growth cone guidance. This modulation influences the growth cone through the mean number of cues released by neighboring neurons. For example, neurotrophins (Pfenninger et al. 2003) can play a key role in regulating neurite growth. To account for this mechanism, this effect can be incorporated by redefining the vesicular fusion rate that should now depend both on the dynamics of external cues and vesicle arrival. Vesicles fusion is now controlled by the presence of external cues at the site vesicular fusion.

Cues arrive at random times, distributed uniformly during a periodic interval of time of length T. During a fraction of time T_a, cues allow vesicles to fuse. The time T_a is chosen uniformly distributed during each period T with a density probability function given by $p(u) = \frac{1}{T}\chi_{[0,T]}$, where χ is the characteristic function (equal to one for $t \in [0, T]$, 0 otherwise). Thus the mean fusing time $T^\star$ is given by

$$T^\star = \int_0^T up(u)du = \frac{1}{T}\int_0^T udu = \frac{T}{2}. \tag{8.45}$$

The rate of vesicle fusion can be computed from the joint event that a vesicle arrives and some cues are located on the neurite tip. The mean of the random time τ^{arrive} that a vesicle is allowed to fuse can be computed from an infinite sum, where a vesicle fuses in the kth time interval kT, when cues are received during a time u_k (distributed according to the uniform probability p). The join probability is for $k = 0, 1, 2, \ldots$

$$p_J(t) = \Pr\{\tau^{\text{arrive}} < t, kT < \tau^{\text{arrive}} < kT + u_k\}. \tag{8.46}$$

Since the arrival time of the vesicles to the small hole is Poissonian,

$$\Pr\{kT < \tau^{\text{arrive}} < kT + u_k\} = \int_{kT}^{kT+u_k} \lambda e^{-\lambda x}dx$$

$$\Pr\{\tau^{\text{arrive}} < t\} = 1 - e^{-\lambda t},$$

where $\lambda = \dfrac{1}{\bar{\tau}_\delta} = \kappa_\delta$, we get for the conditional time

$$E\tau = \int_0^\infty t\frac{d}{dt}p_J(t)dt = \int_0^\infty t\lambda e^{-\lambda t}dt \sum_{k=0}^\infty \int_0^T \int_{kT}^{kT+u} \lambda e^{-\lambda x}dx\frac{1}{T}\chi_{[0,T]}du. \tag{8.47}$$

Consequently,

$$E\tau = \frac{1}{\lambda}\frac{1}{T}\sum_{k=0}^{\infty} e^{-\lambda kT}\left(\int_0^T (1-e^{-\lambda u})\chi_{[0,T]}du\right).$$

Thus the formula for the conditional arrival time of vesicle during the interval where external cues are activated is

$$\overline{\tau} = E\tau = \frac{1}{\lambda}\frac{1}{T}\left(\frac{1}{1-e^{-\lambda T}}\right)\left(T - \frac{1-e^{-\lambda T}}{\lambda}\right). \tag{8.48}$$

This analysis reveals how the neurite growing rate is modified when external cues modulate vesicular fusion.

8.2 DNA Repair in a Two-Dimensional Confined Chromatin Structure

A Brownian needle in a strip can model an mRNA, a transcription factor, or a stiff DNA fragment moving in the very confined chromatin structure (see Sect. 2.2). For example, under severe stress, the DNA of the bacterium *Deinococccus radiodurans*, the most radioresistant organism, undergoes a phase transition in reorganizing the genome into tightly packed toroids (Fig. 8.4a–c), which may facilitate DNA repair (Lieber et al. 2009). Three-dimensional analysis (Minsky 2004) reveals a complex network of double membranes that engulf the condensed DNA, suggesting that two-dimensional domains lying between parallel walls may play a significant role in DNA repair.

The diffusion of the needle is characterized by three diffusion coefficients: longitudinal along the axis D_X, transversal D_Y, and rotational D_r. In the diffusive motion of a needle confined to a planar strip, which is only slightly wider than the length of the needle, its turning around is a rare event (see Fig. 2.4). This is due to the narrow space around the vertical position of the needle in the strip. If the length of the needle l is only slightly smaller than the width of the strip $l_0 > l$, such that $\varepsilon = (l_0 - l)/l_0 \ll 1$, then the mean time for the needle to turn 180° is given in Theorem 2.2 as

$$\bar{\tau} = \frac{\pi\left(\frac{\pi}{2}-1\right)}{D_r\sqrt{l_0(l_0-l)}}\sqrt{\frac{D_X}{D_r}}\left(1+O\left(\sqrt{\frac{l_0-l}{l_0}}\right)\right). \tag{8.49}$$

Formula (8.49) shows that when the free space between two planes decreases, the effective diffusion constant, proportional to the reciprocal of $\bar{\tau}$, experiences a second order phase transition, characterized by a discontinuity of the derivative of the effective diffusion constant for the rotation [reciprocal of the MFPT (8.49)].

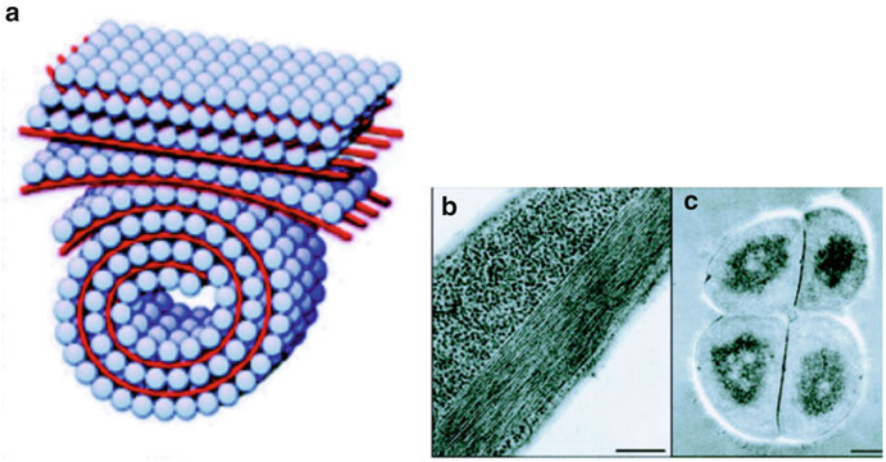

Fig. 8.4 (**a**) Two-dimensional stratification: the model depicts the toroidal morphology that acts as a structural template for growth of the DNA–(DNA-binding protein) co-crystal. The DNA (*red stripe*) is localized in between the pseudohexagonal faces of the dodecameric symmetric proteins (*blue spheres*) (Minsky 2004). Figure 2.4 is a schematic model of the motion of a broken DNA strand in this geometry. (**b**) Two-dimensional arrangement of DNA: formation of DNA-RecA "repairosome" assemblies in *E. coli* cells exposed to DNA-damaging agents. The ordered intracellular assembly is promoted by DNA molecular condensation and the structural features are modulated by the RecA proteins. Scale bar is 200 nm. (**c**) DNA packaging in the radioresistant bacteria *D. radiodurans*. The electron micrograph depicts the toroidal organization of its genome. Within this structure, the tight and ordered packaging of the DNA molecule may facilitate repair of double-stranded DNA breaks. Scale bar is 400 nm. The genomic reorganization in bacterial systems into tightly packed structures is proposed to restrict molecular diffusion

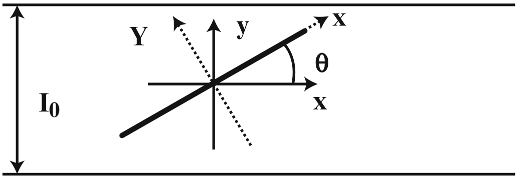

Fig. 8.5 Rod in strip. The strip width is l_0 and the needle length is $l < l_0$. The position of the needle is characterized by the angle θ and the fixed coordinates x, y of the center or in a rotating system of coordinates (X, Y, θ)

Specifically, when the variable l reaches and exceeds the value $l = l_0$ the diffusion constant vanishes (Fig. 8.5). This result explains the crucial role of the chromatin organization in maintaining the genome integrity during heavy radiation stress.

The phase transition indicated by (8.49) was observed experimentally several times and reported in Lieber et al. (2009), Minsky (2004), and Levin-Zaidman et al. (2003). It should be associated with the high probability of DNA repair by preventing the broken DNA strand from drift away or from misaligning by turning over.

8.3 MFPT to a Hidden Binding Site

Active sites of a complex molecule, such as hemoglobin, penicillin-binding proteins, and many others, are often hidden inside the complex organization of α and β-sheet structures. A ligand, such as β-lactam antibiotic, has to bind to a small site hidden inside the molecule and indeed, ligand recognition requires that strands be antiparallel in the active site area. This phenomenon was observed for large antibiotic molecules. In Fig. 8.6(2),(3) the penicillin-binding proteins are in closed (2)(left) and open (2)(right) L-conformations, respectively (Macheboeuf et al. 2005). In the closed conformation the active site is blocked and unavailable for binding, while in the open state the catalytic funnel reveals an elongated binding cleft, where the active site (red arrow) is hidden at the bottom.

The time for changing conformation and molecular activation is thus the mean time for a ligand to hit the active site in the pocket (see arrows in Fig. 8.6). The MFPT in this case is estimated from the asymptotic formula (3.27) for the MFPT from the head of solid of revolution, obtained by rotating a planar symmetric domain about its axis of symmetry, to a small absorbing window at the end of a funnel, given by

$$\bar{\tau} = \frac{1}{\sqrt{2}}\left(\frac{R_c}{a}\right)^{3/2}\frac{|\Omega|}{R_c D}(1+o(1)), \tag{8.50}$$

where D is the diffusion coefficient, R_c is the radius of curvature of the rotated curve at the end of the funnel, and $|\Omega|$ is the volume of the domain explored by the ligand, which contain the volume of the pocket and the immediate accessible volume outside. Thus the mean determinant for complex molecules to be activated is the local geometry near the active site, that contributes significantly to the binding rate.

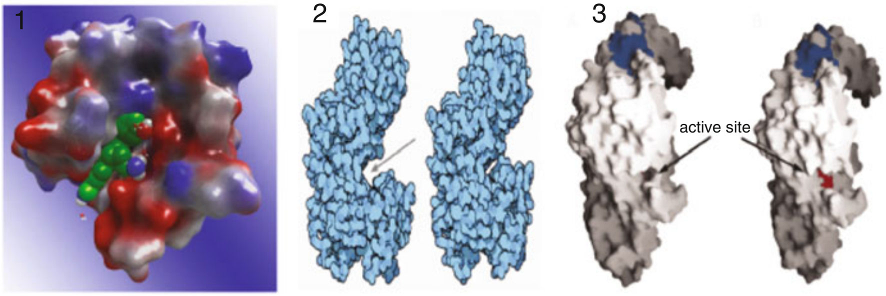

Fig. 8.6 (**1**) Complex molecule containing a hidden site. The domain Ω is the surrounding fluid, the absorbing boundary $\partial\Omega_a$ is the hidden target (marked *green*), and the reflecting boundary $\partial\Omega_r$ is the remaining surface of the molecule. (**2**) Hidden site. (**3**) Hidden active site

8.4 Asymmetric Dumbbell-Shaped Division in Cells

An intermediate stage of a dividing cell consists of an asymmetric dumbbell shape with a relatively long connecting neck (Figs. 3.8 and 8.7). In this stage of the cell division some of the genetic material is delivered from the bigger (mother) to the smaller (daughter) compartment. An open debate in this field is how the genetic material is selected? A recent report Gehlen et al. (2011) proposes that diffusion through the connecting neck is the main determinant of the delivery rate and of the selection of fast-diffusing particles in the transient regime before steady state is reached. Indeed, the analysis below confirms that in the absence of any active mechanism, the delivery process can be controlled by drastic slowdown of the back flow from the daughter to the mother cell, brought about by asymmetry in the curvature of the connecting neck in the smaller compartment, as described in the asymptotic formulas (2.110)–(2.112) for the mean residence times $\bar{\tau}$ in the compartments. Specifically, the mean time to go from mother to daughter is given by $\tau_{M\to D} \sim 2\bar{\tau}_{M\to SS}$ and in the other direction by $\tau_{D\to M} \sim 2\bar{\tau}_{D\to SS}$ in the limit of narrow neck. The transition rates given in (2.110) can differ by orders of magnitude as the geometry changes. This can explain some of the findings reported experimentally in Gehlen et al. (2011).

The rate of equilibration between the two compartments can be found from the estimate of the second eigenvalue μ of the Neumann problem in the dumbbell-shaped domain, given by

$$\frac{1}{\mu} = \frac{1}{\tau_{D\to M}} + \frac{1}{\tau_{M\to D}}.$$

When the time scale of morphological changes in the shape of the dumbbell is slower than diffusion, the protein and genetic material transferred by diffusion from the mother to the daughter cell can be estimated from a reduced system of equations for the mass in the mother and daughter cells, M_M and M_D, respectively, given by

$$\begin{aligned} \dot{M}_D &= -\frac{M_D}{\tau_{M\to D}} + \frac{M_M}{\tau_{D\to M}} \\ \dot{M}_M &= -\frac{M_M}{\tau_{D\to M}} + \frac{M_D}{\tau_{M\to D}} \end{aligned} \tag{8.51}$$

with $M_M(0) = M_0$ and $M_D = 0$. The solution is

$$M_M(t) = M_0 \left(1 - \frac{\mu}{\tau_{D\to M}}\right) e^{-\mu t} + M_0 \frac{\mu}{\tau_{D\to M}}. \tag{8.52}$$

The mean transfer time from the mother to the daughter can be estimated with the following parameters (Gehlen et al. 2011): diffusion coefficient

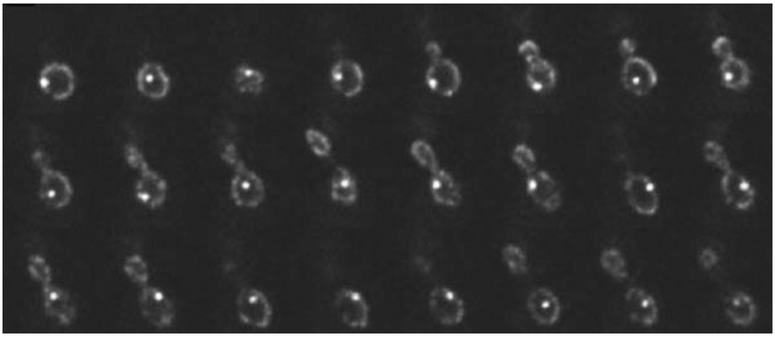

Fig. 8.7 Time-lapse images of mitotic cells: the dumbbell-shaped dividing cell seems to vary with time (Gehlen et al. 2011)

$D = 6.5 \times 10^{-3}\,\mu\text{m}^2/\text{s}$, a neck length $L = 0.1\,\mu\text{m}$, a neck radius $a = 0.2\,\mu\text{m}$, a mother radius of $R = 0.9\,\mu\text{m}$, and a curvature of $R_c = 0.5\,\mu\text{m}$, it is $\tau_{M\to D} = 5626\,\text{s}$, about an hour and a half.

As shown in Fig. 8.7, the connection geometry varies over time, which can change the flux drastically, as formulas (2.112) indicate. The low transfer rate may lead to an early separation between the mother and daughter cells, prior to reaching the steady state in (8.52). If steady state diffusion is reached before separation, the probability density function is uniform in the domain, rendering $M_M(\infty)$ and $M_D(\infty)$ proportional to the respective volumes. In the reduced model (8.51) the steady state masses are proportional to the fractions of the residence times in the two cells. In view of (2.112), these are proportional to the volumes (to leading order in small neck radius). The reduced model can be used before steady state is reached. A simple consequence of (8.52) is that a Brownian simulation of the transferred material (messenger RNA, soluble proteins, and so on) has to be run for times $t \gg 1/\mu$ to reach the steady state. Some transitions $M \to D$ and $D \to M$ have to occur in the simulation in order for steady state to set in.

Chapter 9
Modeling the Early Steps of Viral Infection in Cells

9.1 Introduction

Quantifying the early steps of viral infection in cells is a new area of physical virology. It is dedicated to the analysis of the main pathways used by viruses for reproduction. Most viruses entering cells after binding to specific membrane receptors are enveloped in an endosomal compartment (Fig. 9.1) (see Whittaker et al. 2000; Greber and Way 2006). These viruses entering through the endosome have to escape this compartment later on. Enveloped viruses, such as influenza, contain membrane-associated glycoproteins, which mediate the fusion between the viral and endosomal membranes, from which they have to escape. In particular, acidification of the endosome triggers the conformational change of the influenza hemagglutinins, leading to endosome-virus membranes fusion and release of genes into the cytoplasm. Following the endosomal escape, nuclear replication viruses have to travel through the crowded cytoplasm to reach replication sites such as the nucleus to deliver their genetic material through the nuclear pores. Virus motion into the cytoplasm is composed of periods described as Brownian, while others are directed motion along microtubules. While the cytoplasmic movement of viral particles towards the nucleus is facilitated by the microtubular network and viral proteins, very little is known about the fate of non-viral DNA vectors in the cytoplasm.

The goal of this chapter is to study a recent model of these different steps of viral infection. The model considers viruses as separate diffusers in a random environment. The viral motion is modeled on a coarse scale by a stochastic differential equation. In this model the drift term represents the average velocity along randomly organized microtubules. An important simplification is achieved by separating the random drift into a deterministic component and noise. Note also that the arrival of a virus to a small nuclear pore competes with the killing in the bulk, as described in Sect. 2.7. The mathematical models of viral motion give rise to Brownian dynamics simulations for the study of sensitivity to parameters and,

D. Holcman, Z. Schuss, *Stochastic Narrow Escape in Molecular and Cellular Biology*, DOI 10.1007/978-1-4939-3103-3_9

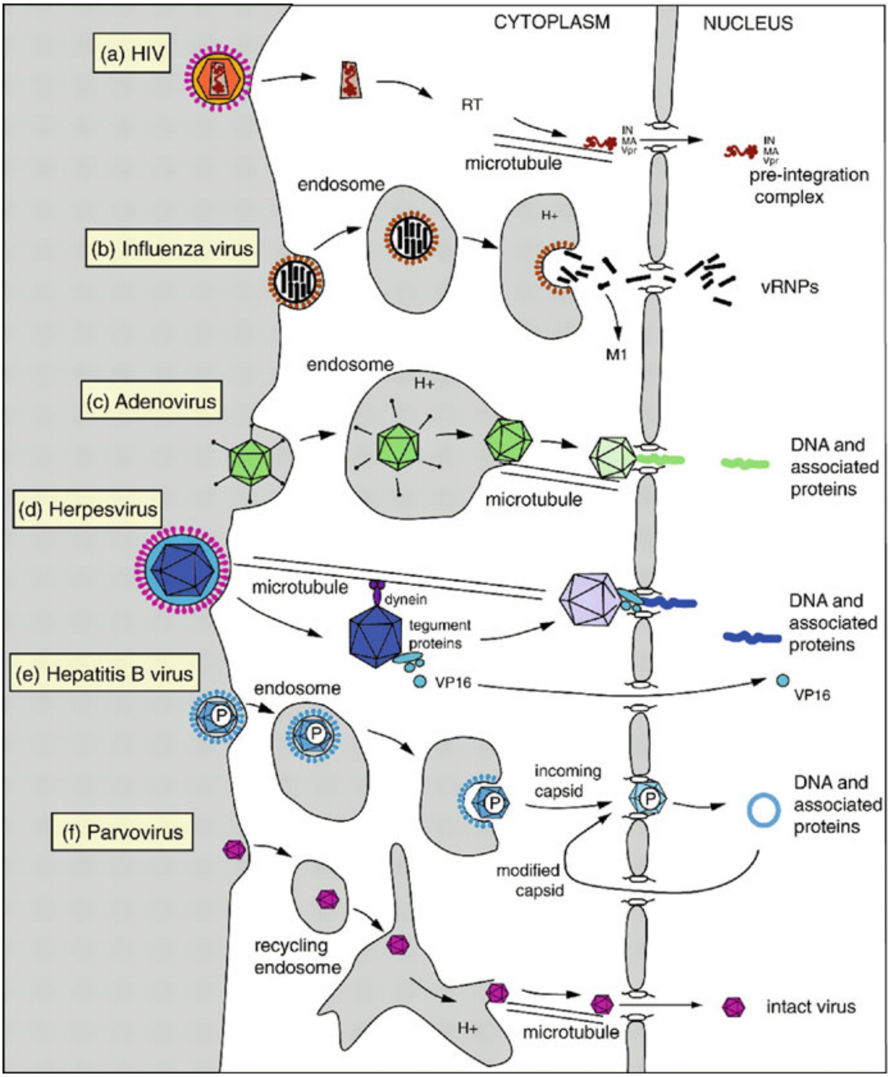

Fig. 9.1 Common Entry and uncoating mechanisms of selected nuclear-replicating viruses. Viruses can undergo substantial uncoating in the cytoplasm before translocating into the nucleus; (**a**) HIV, (**b**) influenza virus. Alternatively, viruses can dock to the NPC and uncoat at the cytoplasmic side of the nuclear membrane; (**c**) adenovirus and (**d**) herpesvirus. They may possibly disassemble within the nuclear pore; (**e**) hepatitis B virus; (**f**) parvovirus (Whittaker et al. 2000)

eventually, for testing the increase or the drop in infectivity by using simultaneously a combination of various drugs. The modeling approach can also be used for designing optimal condition for the delivery considering the high-dimensional parameter space (Lagache et al. 2012). Viral motions alternate intermittently between periods

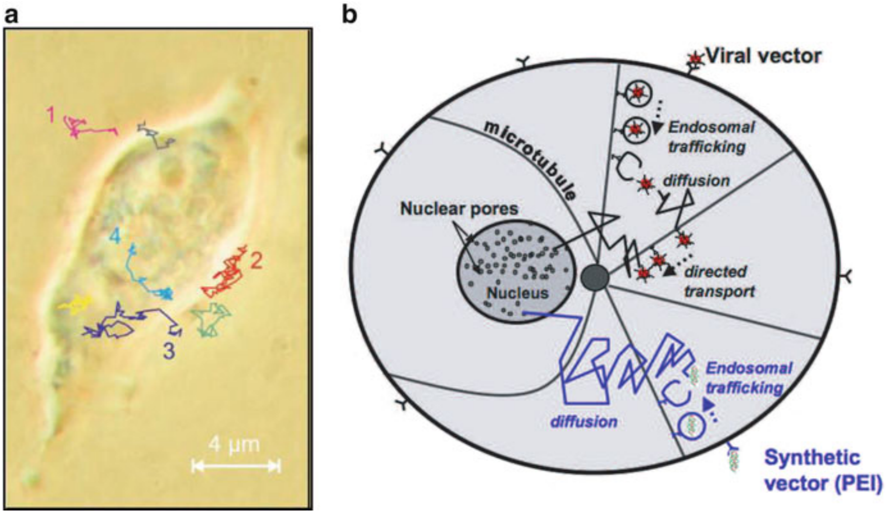

Fig. 9.2 Virus trajectories in cell. (**a**) Trajectories of single AAV-Cy5 particles: the traces showing single diffusing virus particles were recorded at different times. They describe various stages of AAV infection, e.g. diffusion in solution (*1* and *2*), touching at the cell membrane (*2*), penetration of the cell membrane (*3*), diffusion in the cytoplasm (*3* and *4*), penetration of the nuclear envelope (*4*), and diffusion in the nucleoplasm (Seisenberger et al. 2001). (**b**) Schematic description of early steps of infection for viral and synthetic vectors. Synthetic vectors are not assisted by active transport during their cytoplasmic trafficking

of free diffusion and directed motion along microtubules (MTs) (Greber and Way 2006). Such viral trajectories have been recently monitored by using new imaging techniques in vivo (Seisenberger et al. 2001).

The trajectory of a viral particle $\boldsymbol{x}(t)$ (Fig. 9.2a) can be modeled as a randomly switching process, much as in Sect. 8.1,

$$d\boldsymbol{x} = \begin{cases} \sqrt{2D}\, d\boldsymbol{w} & \text{when the virus is free} \\ \boldsymbol{V}(\boldsymbol{x})\, dt & \text{when the virus is bound to a MT,} \end{cases} \tag{9.1}$$

where $\boldsymbol{w}(t)$ is the standard Brownian motion, D is the diffusion constant, and $\boldsymbol{V}(\boldsymbol{x})$ is the velocity field of the motion along the microtubule (MT) network. The switching process can be described as in (8.1). The vector field $\boldsymbol{V}(\boldsymbol{x})$ in (9.1) is difficult to estimate. As in Sect. 8.1 the switched process can be coarse-grained into a diffusion process

$$d\boldsymbol{x} = \boldsymbol{b}(\boldsymbol{x})\, dt + \sqrt{2D}\, d\boldsymbol{w}, \tag{9.2}$$

where $\boldsymbol{b}(\boldsymbol{x})$ is a coarse-grained steady drift field. The expression for $\boldsymbol{b}(\boldsymbol{x})$ depends on the MT organization and on the viral dynamical properties, such as the diffusion constant D, affinity with microtubules, and net velocity along MTs. Finally, the crowded cytoplasm is a risky environment for viruses that can be trapped or degraded by the cellular defense machinery. Thus cytoplasmic trafficking is rate-limiting and to analyze quantitatively that step, an asymptotic expression will be derived for the probability P_N that a virus arrives at a nuclear pore alive, as described in Sect. 9.3.1 below.

9.2 Viral Trafficking in the Cell Cytoplasm

Several steps are necessary before a viral particle can undergo cytoplasmic or nuclear replication. One step is to successfully escape the endosome and thus to avoid degradation in acidic lysosomes. Enveloped viruses, such as influenza, contain membrane-associated glycoproteins, which mediate the fusion between the viral and endosomal membranes. In particular, acidification of the endosome triggers the conformational change of the influenza hemagglutinins (HA) into a fusogenic state, leading to endosome-virus membranes fusion and release of genes into the cytoplasm. Other non-enveloped viruses, such as the adeno-associated-virus (AAV), have to escape the endosome, a process that requires one of the (less than 10) capsid proteins to change conformation. In Sect. 9.5part of this chapter, we will present model for the endosomal escape based on Markov jump processes.

Following the endosomal escape, viruses have to travel through the crowded cytoplasm to reach the nucleus and deliver their genetic material through the nuclear pores. While the cytoplasmic movement of viral particles towards the nucleus is facilitated by the microtubular network and viral proteins, very little is known about the fate of non-viral DNA vectors in the cytoplasm. However, trapping of large DNA particles ($>$500 kDa) in the crowded cytoplasm drastically hinders their cytoplasmic diffusion (Dauty and Verkman 2005) and subsequently diminishes the transfection rate of synthetic gene vectors (see Fig. 9.2). Mathematical and physical models of this process are constructed for the purpose of predicting and quantifying infectivity and the success of gene delivery.

9.2.1 The Steady State Drift for a Two-Dimensional Radial Cell

The motion described by Eq. (9.1) and its coarse-grained version (9.2) is shown in Fig. 9.3. An idealized two-dimensional model of a cell is a circular annulus Ω, representing the cell cytoplasm, with outer radius R and inner radius δ. An abstract model of the cytoplasm contains N MTs radially oriented with equally spaced angles $\Theta = 2\pi/N$ apart. They emanate from the inner circle of radius r, which represents the nucleus, and end at outer circle of radius R, which represents the external membrane. The two-dimensional model can represent flat culture cells,

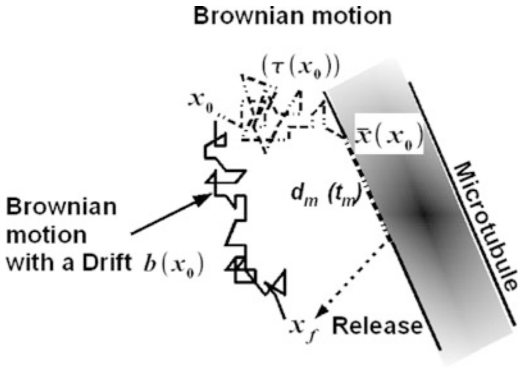

Fig. 9.3 A fundamental step of motion: diffusion and directed motion. A virus (*dotted line*) starts at a position $\boldsymbol{x}_0$ and diffuses freely until it binds to an MT and moves an average distance d_m. It is finally released at $\boldsymbol{x}_f$. This result is compared to a trajectory generated by the steady state Eq. (9.2) (*solid line*)

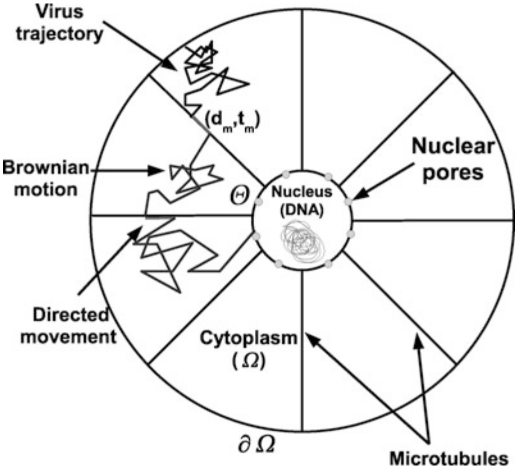

Fig. 9.4 A two-dimensional radial cell with radially equidistributed MTs. A viral trajectory alternates intermittently between directed motion when bound to an MT and free diffusion in the cytoplasm

which stay flat due to adhesion to the substrate. The thickness can be neglected in this model. Before reaching a small nuclear pore, the dynamics of the virus alternates intermittently between free diffusion and directed motion along an MT, as described in Sect. 8.1 (Fig. 9.4). It is enough to study the intermittent dynamics in a single sector $\tilde{\Omega}$ of central angle Θ. The viral motion described in Fig. 9.3 begins at a radius r_0 with an angle uniformly distributed in $[0;\Theta]$. The virus binds to a MT at time $\tau(r_0)$ and radius $\bar{r}(r_0)$ and while moving on the MT, it has a radially directed movement towards the nucleus for an exponentially distributed random time, whose average is t_m, and travels an average distance $d_m = ||\mathbf{V}||t_m$. The virus is released with a uniformly distributed angle at a final radius $r_f = \bar{r}(r_0) - ||\mathbf{V}||t_m$ (Fig. 9.5). In most eukaryotic cell large asters, there are from 600 to 1000 MTs (Nedelec et al. 2001). The average number N of MTs per cell cross section can be estimated as follows: for a cell thickness $h \approx 9\,\mu\text{m}$, an interaction range $\gamma \approx 50\,\text{nm}$ between the MTs and the molecular motors (Coy et al. 1999), and diameter $d = 30\,\text{nm}$ for a virus such as AAV (Seisenberger et al. 2001), the range of N is found for a radial MT organization in a thin cylindrical cell to be between

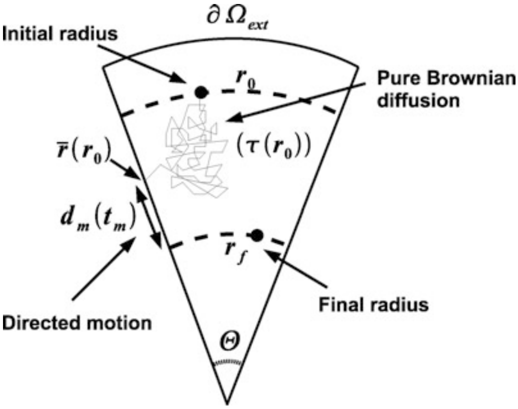

Fig. 9.5 Homogenization of motion in a sector $\tilde{\Omega}$. A virus starts at radius r_0, with an angle uniformly distributed in $[0;\Theta]$, it diffuses freely for time $\tau(r_0)$ until it binds to an MT at an average radius $\bar{r}(r_0)$; after a directed motion over a distance $d_m = ||\boldsymbol{V}||t_m$ it is released randomly at a final radius r_f

$600(2\gamma + d)/h$ and $1000(2\gamma + d)/h$, that is 9–15. In this range $\Theta << 1$. If the reflecting boundary at $r = R$ is neglected, the domain $\tilde{\Omega}$ becomes an open-ended wedge.

9.2.2 MFPT of a Brownian Motion to the Boundary of a Circular Sector

We consider here a Brownian motion in a circular sector Ω^R of radius R and central angle $\Theta \ll 1$. Brownian trajectories are reflected at the arc $\partial\Omega_r^R = \{r = R, -\Theta/2 < \theta < \Theta/2\}$ and absorbed at $\partial\Omega_a^R = \{\theta = -\Theta/2, \Theta/2,\ 0 \le r < R\}$. The MFPT to the absorbing boundary $\partial\Omega_a^R$ (which represents a microtubule) $u = u(r,\theta)$ of a Brownian trajectory to $\partial\Omega_a^R$, given the initial point (r,θ), is the solution of the boundary value problem (Schuss 2010b)

$$D\Delta u(\boldsymbol{x}) = -1 \ \text{ for } \boldsymbol{x} \in \Omega^R,\ u(\boldsymbol{x}) = 0 \ \text{ for } \boldsymbol{x} \in \partial\Omega_a^R,\ \frac{\partial u}{\partial \boldsymbol{n}} = 0 \ \text{ for } \boldsymbol{x} \in \partial\Omega_r^R. \tag{9.3}$$

In polar coordinates (9.3) takes the form

$$\begin{aligned} \frac{\partial^2 u}{\partial r^2} + \frac{1}{r}\frac{\partial u}{\partial r} + \frac{1}{r^2}\frac{\partial^2 u}{\partial \theta^2} &= -1 \ \text{ for } (r,\theta) \in \Omega^R \\ u(r,\theta) &= \ \text{ for } (r,\theta) \in \partial\Omega_a^R \\ \frac{\partial u(r,\theta)}{\partial r} &= 0 \ \text{ for } (r,\theta) \in \partial\Omega_r^R. \end{aligned}$$

The solution is found by separation of variables as Redner (2001)

$$u\left(r,\theta\right)=\frac{r^2}{4D}\left(\frac{\cos 2\theta}{\cos\Theta}-1\right)+\sum_{n=0}^{\infty}A_n r^{\lambda_n}\cos\lambda_n\theta\ \text{ for }-\frac{\Theta}{2}\le\theta\le\frac{\Theta}{2}.\qquad(9.4)$$

The right hand of (9.4) is the general solution of the homogeneous problem $\Delta u=0$ in Ω^R. The boundary condition on $\partial\Omega_a^R$ determines the eigenvalues as

$$\lambda_n=\left(2n+1\right)\frac{\pi}{\Theta},\qquad(9.5)$$

while the reflecting condition at $\partial\Omega_r^R$ is

$$\frac{\partial u\left(R,\theta\right)}{\partial r}=0\ \text{ for }-\frac{\Theta}{2}<\theta<\frac{\Theta}{2}.\qquad(9.6)$$

This determined

$$A_n=\frac{\left(-1\right)^{n+1}8R^{2-\lambda_n}}{D\Theta\lambda_n^2\left(\lambda_n^2-4\right)}.\qquad(9.7)$$

Averaging (9.4) with respect to a uniform initial distribution gives the MFPT to $\partial\Omega_a^R$ as

$$\bar{u}\left(r\right)=\frac{1}{\Theta}\int_{-\Theta/2}^{\Theta/2}u\left(r,\theta\right)\,d\theta=\frac{r^2}{4D}\left(\frac{\tan\left(\Theta\right)}{\Theta}-1\right)-\sum_{n=0}^{\infty}\frac{16R^{2-\lambda_n}r^{\lambda_n}}{D\Theta^2\lambda_n^3\left(\lambda_n^2-4\right)},\qquad(9.8)$$

For small Θ (9.4) can be approximated by

$$\bar{u}\left(r\right)\approx\frac{r^2}{4D}\left(\frac{\tan\left(\Theta\right)}{\Theta}-1\right)-\frac{16\Theta R^2\left(\frac{r}{R}\right)^{\pi/\Theta}}{\left(D\pi^3\left(\frac{\pi}{\Theta}\right)^2-4\right)}.\qquad(9.9)$$

For $\Theta\ll 1$ (9.9) reduces to

$$\tau(r_0)\approx r_0^2\frac{\Theta^2}{12D}+o(\Theta^2).\qquad(9.10)$$

9.2.3 *Distribution of Exit Points on $\partial\Omega_a$*

The probability density of exit points on $\partial\Omega_a$ is the density of points at which a virus attaches to a microtubule. This probability density is the normal flux density on $\partial\Omega_a$ of the solution of the transition probability density $p\left(\boldsymbol{x},t\,|\boldsymbol{x}_0\right)$ of Brownian trajectories that are absorbed in $\partial\Omega_a$ and reflected in $\partial\Omega_r^R$. It is the solution of the initial and boundary value problem for the Fokker–Planck equation

$$\begin{aligned}\frac{\partial p\left(\boldsymbol{x},t\,|\,\boldsymbol{x}_0\right)}{\partial t} &= D\Delta p\left(\boldsymbol{x},t\,|\,\boldsymbol{x}_0\right) \quad \text{for}\, \boldsymbol{x} \in \Omega^R \\ p\left(\boldsymbol{x},0\,|\,\boldsymbol{x}_0\right) &= \delta\left(\boldsymbol{x}-\boldsymbol{x}_0\right) \quad \text{for}\, \boldsymbol{x},\boldsymbol{x}_0 \in \Omega^R \\ p\left(\boldsymbol{x},t\,|\,\boldsymbol{x}_0\right) &= 0 \quad \text{for}\, \boldsymbol{x} \in \partial\Omega_a^R \\ \frac{\partial p\left(\boldsymbol{x},t\,|\,\boldsymbol{x}_0\right)}{\partial n} &= \quad \text{for}\, \boldsymbol{x} \in \partial\Omega_r^R,\end{aligned}$$

The distribution of exit points $\epsilon\left(\boldsymbol{y}\right)$ is given by

$$\epsilon\left(\boldsymbol{y}\right) = \int_0^\infty j\left(\boldsymbol{y},t\right)dt, \tag{9.11}$$

where the flux j is defined by

$$j\left(\boldsymbol{y},t\right) = -D\frac{\partial p\left(\mathbf{r},t\right)}{\partial \boldsymbol{n}}_{|\mathbf{r}=\boldsymbol{y}}.$$

If we denote $C\left(\mathbf{r_0},\mathbf{r}\right) = \int_0^\infty p\left(\mathbf{r},t|\mathbf{r_0}\right)dt$, then C is the solution of

$$-D\Delta C\left(\mathbf{r_0},\mathbf{r}\right) = \delta\left(\mathbf{r}-\mathbf{r_0}\right), \tag{9.12}$$

and

$$\epsilon\left(\mathbf{y}\right) = -D\frac{\partial C}{\partial n}\left(\mathbf{r_0},\mathbf{y}\right) \text{ for } \mathbf{y} \in \Omega_a^R. \tag{9.13}$$

Consequently, to obtain the pdf $\epsilon(\boldsymbol{y})$ of exit points $\boldsymbol{y}$, we use the Green function in the wedge domain Ω^R. By using a conformal transformation, we hereafter solve a simplified case of an open wedge (i.e., without a reflecting boundary at $r = R$). This computation could be compared with the general one that will be derived in the next section.

To compute the exit points distribution, we compute the solution of Eq. (9.12), obtained by the image method and a conformal transformation from the open wedge to the upper complex half-plane. The Green function, solution of Eq. (9.12) in the upper complex half-plane is given by

$$C\left(z\right) = \frac{1}{2\pi D}\ln\frac{z-z_0}{z-z_0^*}, \tag{9.14}$$

where z_0^* the complex conjugate of z_0. Using the conformal transformation $\omega = f\left(z\right) = z^{\frac{\pi}{\Theta}}$, that maps the interior of the wedge of opening angle Θ to the upper half plane, the Green function in the wedge is given by

$$C(z) = \frac{1}{2\pi D} \ln \left(\frac{z^{\frac{\pi}{\Theta}} - z_0^{\frac{\pi}{\Theta}}}{z^{\frac{\pi}{\Theta}} - \left(z_0^*\right)^{\frac{\pi}{\Theta}}} \right). \tag{9.15}$$

The flux to the line θ is given by

$$\begin{aligned}\epsilon_\theta(r) = -\frac{D}{r}\frac{\partial C}{\partial \theta}\left(re^{i\theta}\right) &= \frac{1}{2\pi r}\frac{i\nu\left(re^{i\theta}\right)^\nu . \left(k_0 - k_0^*\right)}{\left(\left(re^{i\theta}\right)^\nu - k_0\right)\left(\left(re^{i\theta}\right)^\nu - k_0^*\right)} \\ &= \frac{1}{2\pi r}\frac{-2\nu\left(re^{i\theta}\right)^\nu r_0^\nu \sin(\nu\theta_0)}{\left(re^{i\theta}\right)^{2\nu} + r_0^{2\nu} - 2\left(re^{i\theta}\right)^\nu r_0^\nu \cos(\nu\theta_0)},\end{aligned}$$

where $\nu = \frac{\pi}{\Theta}$, $k_0 = z_0^\nu = \left(r_0 e^{i\theta_0}\right)^\nu$. Finally, the exit point distribution for $\theta = \Theta$ is given by

$$\epsilon_\Theta(r) = \frac{r_0}{\Theta}\frac{(rr_0)^{(\nu-1)}\sin(\nu\theta_0)}{r^{2\nu} + r_0^{2\nu} + 2(rr_0)^\nu\cos(\nu\theta_0)}, \tag{9.16}$$

while for $\theta = 0$ it is given by

$$\epsilon_0(r) = \frac{r_0}{\Theta}\frac{(rr_0)^{(\nu-1)}\sin(\nu\theta_0)}{r^{2\nu} + r_0^{2\nu} - 2(rr_0)^\nu\cos(\nu\theta_0)}. \tag{9.17}$$

A matlab check guarantees that

$$\int_0^\infty \{\epsilon_\Theta(r) + \epsilon_0(r)\} dr = 1. \tag{9.18}$$

This computation gives the leading order term. The full computation for a closed wedge is given in Lagache and Holcman (2008a).

9.2.4 *The Mean Exit Radius*

To determine the mean exit distribution radius $\bar{\epsilon}(r|r_0)$ for a Brownian particle starting initially at position r_0, θ_0 where θ_0 is uniformly distributed between 0 and Θ, we consider $\epsilon(r|r_0,\theta_0) = \epsilon^0(r|r_0,\theta_0) + \epsilon^\Theta(r|r_0,\theta_0)$ and estimate the integral

$$\bar{\epsilon}(r|r_0) = \frac{1}{\Theta}\int_{\Theta_0=0}^{\Theta} \epsilon(r|r_0,\theta_0)\, d\theta_0. \tag{9.19}$$

We obtain from 9.17

$$\bar{\epsilon}(r|r_0) = \frac{2}{\Theta\pi r}\log\left(\frac{r^\nu + r_0^\nu}{|r^\nu - r_0^\nu|}\right) + \ln\left(\frac{R^{2\nu} + (rr_0)^\nu}{R^{2\nu} - (rr_0)^\nu}\right). \tag{9.20}$$

We define the mean exit point as $r_m(r_0) = \mathbb{E}(r|r_0)$ conditioned on the initial radius r_0. Thus,

$$r_m(r_0) = \mathbb{E}(r|r_0) = \int_0^R r\bar{\epsilon}(r|r_0)\,dr. \tag{9.21}$$

Using the expansion $\log(1+x) = \sum_{n\geq 1}(-1)^{n+1}\frac{x^n}{n}$ for $x < 1$, we obtain by a direct integration that

$$r_m(r_0) = \frac{8}{\pi^2} r_0 \left(\sum_{n=0}^{\infty} \frac{1}{(2n+1)^2} \left(\frac{1}{1 - \frac{1}{(2n+1)^2 \left(\frac{\pi}{\Theta}\right)^2}} \right) \right) \tag{9.22}$$

using the expansion in the first part,

$$\frac{1}{1 - \frac{1}{(2n+1)^2 \left(\frac{\pi}{\Theta}\right)^2}} = \sum_{p=0}^{\infty} \left(\frac{\Theta}{(2n+1)\pi} \right)^{2p} \tag{9.23}$$

and the approximation $\Theta << 1$, we obtain using the value of the Riemann ζ-function, $\zeta(2) = \frac{\pi^2}{6}$ and $\zeta(4) = \frac{\pi^4}{90}$, $r_0 \leq R$, that

$$r_m(r_0) \approx r_0 \left(1 + \frac{\Theta^2}{12}\right) - \frac{8R}{\pi^2} \left(\frac{r_0}{R}\right)^{\pi/\Theta} \frac{\pi/\Theta}{(\pi/\Theta)^2 - 1}. \tag{9.24}$$

For Θ small, the second term in the right-hand side of (9.24) is exponentially small. We conclude that

$$\bar{r}(r_0) \approx r_0 \left(1 + \frac{\Theta^2}{12}\right). \tag{9.25}$$

We can now use relation (9.25) and (9.10) to finalize the homogenization procedure of the drift.

9.2.5 Homogenization Procedure to a Constant Drift

In radial geometry, with a drift $\mathbf{b}(\mathbf{x}) = b(r)\frac{\mathbf{r}}{||\mathbf{r}||}$, the MFPT $u(r_0)$ of a virus starting at r_0 and ending at position $r = r_f$ is described by Eq. (9.2) and it satisfies

$$\begin{aligned} D\Delta u - b(r_0)\nabla u &= -1 \\ \frac{du}{dr}(R) = 0 \text{ and } u(r_f) &= 0, \end{aligned} \tag{9.26}$$

where we approximated $b(r)$ by $b(r_0)$. The solution of Eq. (9.26) is

$$u(r_0) = \int_{r_f}^{r_0} \left(\int_v^R \frac{ue^{-\frac{b(r_0)}{D}(u-v)}}{Dv} du \right) dv. \tag{9.27}$$

For $D << 1$, using the Laplace's method,

$$\int_v^R \frac{ue^{-\frac{b(r_0)}{D}(u-v)}}{Dv} du \approx \frac{1}{b(r_0)}. \tag{9.28}$$

Thus, in the first approximation, $u(r_0) \approx \frac{r_0 - r_f}{b(r_0)}$. We can now obtain the value for the homogenized drift $b(r_0)$, by equalizing the MFPT $u(r_0)$ from r_0 to r_f computed from Eq. (9.2) with the one obtained from an intermittent dynamic: $\tau(r_0) + t_m$. Consequently, we get:

$$b(r_0) = \frac{r_0 - r_f}{\tau(r_0) + t_m} = \frac{d_m - r_0 \frac{\Theta^2}{12}}{t_m + r_0^2 \frac{\Theta^2}{12D}}. \tag{9.29}$$

9.2.6 Asymptotic Solution Versus Brownian Simulations

We impose reflecting boundaries at the external membrane $r = R$ and we shall now compare the steady state distribution (Eq. (9.31)) against Brownian simulations generated by empirical intermittent Brownian trajectories in the pie wedge domain. For a potential field **b**, the steady state distribution satisfies the Fokker–Planck equation

$$D\Delta p - \nabla[\mathbf{b}p] = 0 \text{ in } \Omega \tag{9.30}$$

with reflecting boundary condition $\mathbf{J}(\boldsymbol{x}, t).\mathbf{n}_{\boldsymbol{x}} = 0$ on $\partial\Omega$. The distribution p in a two-dimensional radial geometry is:

$$p(r) = \frac{e^{-\frac{\Phi(r)}{D}}}{\int_0^R e^{-\frac{\Phi(r)D}{2}} \pi r dr}, \tag{9.31}$$

The potential Φ of $b = -\nabla\Phi$ is obtained by integrating Eq. (9.29) with respect to r_0,

$$\Phi(r) = \frac{d_m\sqrt{12Dt_m}}{t_m\Theta} \arctan\left(\frac{\Theta r}{\sqrt{12Dt_m}} \right) - \frac{D}{2} \ln\left(12Dt_m + r^2\Theta^2\right). \tag{9.32}$$

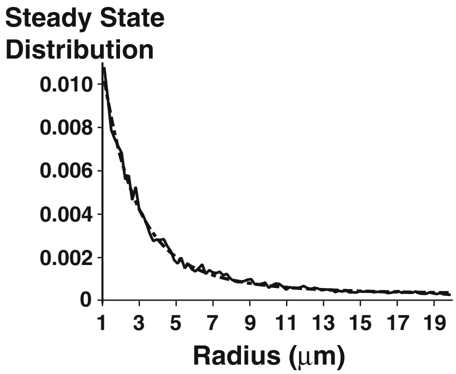

Fig. 9.6 Steady state distributions for the homogenized and switching dynamics. Particle distribution (*dashed line*) generated from (9.31) with the effective drift $b(r)$ (Eq. (9.29)) compared to the empirical steady state distribution (*solid line*) obtained by running 10,000 intermittent Brownian trajectories. The cell radius is $R = 20\,\mu\text{m}$ and $\Theta = \frac{\pi}{6}$

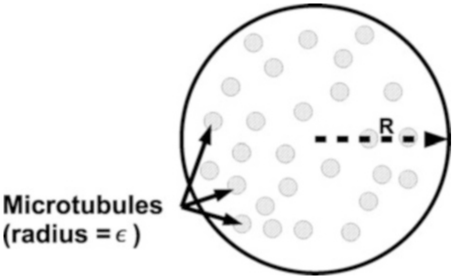

Fig. 9.7 Dendrite cross-section with N MTs, which are thin cylinders uniformly distributed inside the dendrite

In Fig. 9.6, we plotted the steady state distribution given in (9.31) against the distribution of intermittent empirical trajectories generated from (3.2).

The parameters are chosen such that the viruses move towards the nucleus observed in vitro, loaded dynein moves during 1 s over a distance of 0.7 μm (King and Schroer 2000), we thus take $t_m = 1$ s and $d_m = 0.7\,\mu\text{m}$; furthermore, the diffusion constant is $D = 1.3\,\mu\text{m}^2/\text{s}$ as observed for the AAV (Seisenberger et al. 2001). The agreement between the curves in Fig. 9.6 validates that the switch system (9.1) can be coarse-grained into the stochastic Eq. (9.2).

9.2.7 The Cylindrical Geometry

Many transport mechanisms such as viral [herpes virus (Smith et al. 2004)] and vesicular occur in long axons or dendrites, which can be approximated as thin cylinders (radius R and length L). To derive a quantitative analysis of viral infection in that case, we follow the method described above for the case of a disk and compute the steady state drift that accounts for the directed motion along MTs. We model the N MTs parallel to the dendrite principal axis as cylinders (radius $\epsilon \ll R$, Length L). The cross-section Ω of the dendrite is shown in Fig. 9.7. The cylindrical symmetry imposes that the steady state drift $\mathbf{b}(\mathbf{x})$ is independent of z and can be written as $B\mathbf{z}$, where B is a constant and $\mathbf{z}$ the principal axis unit vector along the dendrite. In a small diffusion approximation, the leading order term of B is equal to the effective velocity (Ajdari 1995; Lipowsky et al. 2001): $B = \frac{d_m}{t_m + \tau_m}$, where t_m is the mean time the virus binds to an MT, $d_m = ||\mathbf{V}||t_m$ the mean distance of a run and τ_m the MFPT to find an MT.

To derive an expression for τ, we consider the cross-section Ω and impose reflecting boundary condition at the external membrane of the dendrite ($r = R$) and absorbing ones at the MTs surfaces. In the long time asymptotic, for an MTs radius $\epsilon << 1$, the mean time to a microtubule τ_m is asymptotically equal to $\frac{1}{\lambda D}$ where λ is the first eigenvalue of the Laplace operator in Ω with the boundary conditions described above (Schuss 2010b, p. 175). The leading order term of λ as a function of ϵ is (Ozawa 1980)

$$\lambda = \frac{2\pi N}{|\Omega| \ln\left(\frac{1}{\epsilon}\right)}, \tag{9.33}$$

where $|\Omega| = \pi R^2$. Thus, the MFPT to an MT is

$$\tau_m = \frac{1}{\lambda D} = \frac{R^2 \ln\left(\frac{1}{\epsilon}\right)}{2ND}, \tag{9.34}$$

and the steady state drift amplitude B is given by

$$B = \frac{d_m}{t_m + \tau} = \frac{2NDd_m}{2NDt_m + R^2 \ln\left(\frac{1}{\epsilon}\right)}. \tag{9.35}$$

We conclude that in the limit $t_m \ll \tau_m$, the effective velocity is proportional to the number of MTs: $B \approx N\frac{2Dd_m}{R^2 \ln\left(\frac{1}{\epsilon}\right)}$, as already observed in Nedelec et al. (2001).

9.2.8 Conclusion About Homogenization of Stochastic Equations

The intermittent dynamics (9.1) with random periods of free diffusion and directed motion along MTs characterizes several transport processes. The homogenization of a switching process into a steady state stochastic equation allows explicit expression for the drift in two-dimensional radial cell and in a cylindrical dendrite or axon that depends on some cellular elements such as MTs organization.

The steady state description of the movement can be used to estimate the probability that a virus reaches a small nuclear pore alive and the conditional mean time for it, given that it does. Because viruses are very efficient DNA carriers, understanding and quantifying their movement in the cell cytoplasm is potentially helpful for designing synthetic vectors.

9.3 Probability that a Viral Particle Arrives Alive at a Nuclear Pore

The viral path to the nuclear pore can be computed from the stochastic equation described in Sect. 9.1 and the effective diffusional dynamics of the virus is derived for various geometries in the previous sections. In particular, the expression for the effective drift $\boldsymbol{b}(\boldsymbol{x})$ depends on the organization of the microtubules and on the properties of the viral dynamics, such as the diffusion constant D, affinity with MTs and net velocity along them. The coarse-grained path $\boldsymbol{x}(t)$ of the virus in a domain Ω is modeled as the output of the stochastic differential equation

$$d\boldsymbol{x} = \boldsymbol{b}(\boldsymbol{x})\,dt + \sqrt{2}\boldsymbol{B}(\boldsymbol{x})\,d\boldsymbol{w}(t), \tag{9.36}$$

where $\boldsymbol{b}(\boldsymbol{x})$ is a smooth drift vector, $\boldsymbol{B}(\boldsymbol{x})$ is a diffusion tensor, and $\boldsymbol{w}(t)$ is a vector of independent standard Brownian motions.

The viral trajectory $\boldsymbol{x}(t)$, however, can be terminated at any point $\boldsymbol{x} \in \Omega$ and any time t with probability at rate $k(\boldsymbol{x}, t)$, that is, with probability $k(\boldsymbol{x}, t)\,\Delta t + o(\Delta t)$. The instantaneous rate $k(\boldsymbol{x}, t)$ is called killing measure (see Sect. 2.7). When the boundary $\partial\Omega$ (here the cytoplasmic domain) admits no absorption flux, except for a small absorbing window $\partial\Omega_a$, the NET problem is to find the absorption flux of trajectories that survive the killing. Thus there are two random termination times defined on the trajectories $\boldsymbol{x}(t)$, the time τ^k to killing and the time τ^a to absorption in $\partial\Omega_a$. The virus is said to reach the nucleus alive if $\tau^a < \tau^k$.

9.3.1 *The Probability P_N and Mean Time $\bar{\tau}_N$ to Reach the Nucleus*

We consider the effective viral motion in a cell, whose external boundary is $\partial\Omega_{\text{ext}}$ and the boundary of the nucleus is divided into absorbing and an reflecting parts, ∂N_a and ∂N_r, respectively. The absorbing part ∂N_a is the union of well-separated small pores. The entire boundary is thus $\partial\Omega = \partial\Omega_{\text{ext}} \cup \partial N_a \cup \partial N_r$.

The probability $P_N(\boldsymbol{x}) = \Pr\{\tau^a < \tau^k \,|\, \boldsymbol{x}\}$ that a particle, such as a virus, that starts at $\boldsymbol{x}$ in the cell domain Ω reaches the nucleus, which is modeled as a ball $B(a)$ of radius a before degradation, depends on the cell geometry. Keeping the notation of Sect. 2.7.1, the probability P_N, averaged over the initial density $p_i(\boldsymbol{x})$, is given by

$$\begin{aligned} P_N &= \int_\Omega \Pr\{\tau^a < \tau^k|\boldsymbol{x}(0) = \boldsymbol{y}\}p_i(\boldsymbol{y})\,d\boldsymbol{y} \\ &= 1 - \int_\Omega k(\boldsymbol{x})\tilde{p}(\boldsymbol{x})\,d\boldsymbol{x}. \end{aligned} \tag{9.37}$$

The mean time $\bar{\tau}_N$ to reach the nucleus alive is the conditional average of τ^a, given that $\tau^a < \tau^k$. The probability distribution function (PDF) of the time τ^k that a viral trajectory is killed before reaching an absorbing pore, ∂N_a, is studied in Sect. 2.5. In the notation of that section, the mean time to reach a nuclear pore, averaged over an initial density $p_i(\boldsymbol{x})$,

$$q(\boldsymbol{x}) = \int_0^\infty s\tilde{p}(\boldsymbol{x}, s)\, ds, \tag{9.38}$$

is the solution of the boundary value problem

$$\begin{cases} -\tilde{p}(\boldsymbol{x}) = D\Delta q(\boldsymbol{x}) - \nabla \cdot \boldsymbol{b}(\boldsymbol{x})q(\boldsymbol{x}) - k(\boldsymbol{x})q(\boldsymbol{x}) \ \text{ for } \boldsymbol{x} \in \Omega \\ q(\boldsymbol{x}) = 0 \text{ for } \boldsymbol{x} \in \partial N_a \\ \boldsymbol{J}(\boldsymbol{x}) \cdot \boldsymbol{n}(\boldsymbol{x}) = 0 \ \text{ for } \boldsymbol{x} \in \partial N_r \cup \partial\Omega_{\text{ext}}, \end{cases} \tag{9.39}$$

where

$$\boldsymbol{J}(\boldsymbol{x}) \cdot \boldsymbol{n}(\boldsymbol{x}) = -D\nabla q(\boldsymbol{x}) \cdot \boldsymbol{n}(\boldsymbol{x}) + \boldsymbol{b}(\boldsymbol{x}) \cdot \boldsymbol{n}(\boldsymbol{x})q(\boldsymbol{x}).$$

The mean time to absorption is given by [see formula (2.178) of Sect. 2.7]

$$\bar{\tau}_N = \mathbb{E}[\tau^a \mid \tau^a < \tau^k, p_i] = \frac{\displaystyle\int_\Omega \tilde{p}(\boldsymbol{x})\, d\boldsymbol{x} - \int_\Omega k(\boldsymbol{x})q(\boldsymbol{x})\, d\boldsymbol{x}}{1 - \displaystyle\int_\Omega k(\boldsymbol{x})\tilde{p}(\boldsymbol{x})\, d\boldsymbol{x}}. \tag{9.40}$$

9.3.2 *Probability and MFPT for a Diffusion Process to Reach a Small Nuclear Pore*

A viral particle can enter the nucleus through a small opening ∂N_a in the nucleus surface that may consist of any number of holes. Thus reflecting boundary conditions for the Fokker–Planck equation are imposed on the surface $\partial\Omega$ of the cell, except for ∂N_a, where absorbing boundary conditions are imposed. We may assume that in two dimensions ∂N_a consists of an arc of length $\varepsilon \ll |\partial\Omega|$ and in three dimensions, of a disk B_ε of radius $\varepsilon \ll |\partial\Omega|^{1/2}$. Thus in the two-dimensional case $\eta = \varepsilon/|\partial\Omega| \ll 1$ and in the three-dimensional case $\eta = \varepsilon/|\partial\Omega|^{1/2} \ll 1$. We assume henceforward that all variables are scaled with respect to $|\partial\Omega|$ in dimension $n = 2$ and with respect to $|\partial\Omega|^{1/2}$ in dimension $n = 3$. The probability P_N that a virus arrives alive at the nucleus is the splitting probability between absorption and killing.

When the drift is set to zero, the boundary value problem (2.176) for the density of the time spent at $\boldsymbol{x}$ prior to termination becomes

$$\begin{aligned} D\Delta\tilde{p}(\boldsymbol{x}) - k(\boldsymbol{x})\tilde{p}(\boldsymbol{x}) &= -p_i(\boldsymbol{x}) \ \text{ for } \boldsymbol{x},\boldsymbol{y} \in \Omega \\ \tilde{p}(\boldsymbol{x}) &= 0 \ \text{ for } \boldsymbol{x} \in \partial N_a \\ \frac{\partial \tilde{p}(\boldsymbol{x})}{\partial n} &= 0 \ \text{ for } \boldsymbol{x} \in \partial N_r \cup \partial\Omega_{\text{ext}}. \end{aligned} \tag{9.41}$$

Green's function $G(\boldsymbol{x},\boldsymbol{y})$, which is the solution of the boundary value problem

$$\begin{aligned} D\Delta_{\boldsymbol{x}} G(\boldsymbol{x},\boldsymbol{y}) &= -\delta(\boldsymbol{x}-\boldsymbol{y}) \ \text{ for } \boldsymbol{x},\boldsymbol{y} \in \Omega, \\ D\frac{\partial G(\boldsymbol{x},\boldsymbol{y})}{\partial n(\boldsymbol{x})} &= \frac{-1}{|\partial\Omega|} \ \text{ for } \boldsymbol{x} \in \partial\Omega,\ \boldsymbol{y} \in \Omega, \end{aligned} \tag{9.42}$$

is defined to an additive constant. It is given by (see Garabedian 1964),

$$DG(\boldsymbol{x},\boldsymbol{y}) = \begin{cases} -\dfrac{1}{2\pi} \ln|\boldsymbol{x}-\boldsymbol{y}| + w(\boldsymbol{x},\boldsymbol{y}) & \text{for } n = 2 \\ \dfrac{1}{4\pi|\boldsymbol{x}-\boldsymbol{y}|} + W(\boldsymbol{x},\boldsymbol{y}) & \text{for } n = 3, \end{cases} \tag{9.43}$$

where $w(\boldsymbol{x},\boldsymbol{y})$ and $W(\boldsymbol{x},\boldsymbol{y})$ are bounded harmonic functions. Recall that due to the image source, the singularity of the Green function on the regular boundary ∂N_a is multiplied by a factor of 2, as discussed in Sect. 1.5.1.

9.3.3 Asymptotics of P_N for Small Killing Rate $k(\boldsymbol{x}) \ll 1$

To estimate P_N asymptotically for small absorbing boundary, we note P_N converges to a constant, due to killing. Therefore a regular Taylor expansion gives the leading term. The integral representation of the solution $\tilde{p}$ is obtained by substituting Eqs. (9.41) and (9.42) in Green's formula. We get from

$$\int_{\Omega} \left(G_Q\Delta\tilde{p} - \tilde{p}\Delta G_Q\right)(\boldsymbol{x})d\boldsymbol{x} = \int_{\partial\Omega} \left(G_Q\frac{\partial\tilde{p}}{\partial n} - \tilde{p}\frac{\partial G_Q}{\partial n}\right)(\boldsymbol{x}(S))dS \tag{9.44}$$

that

$$\int_{\Omega} G_Q(\boldsymbol{x})\left(-p_i(\boldsymbol{x}) + k(\boldsymbol{x})\tilde{p}(\boldsymbol{x})\right)d\boldsymbol{x} + \tilde{p}(Q) = D\int_{\partial N_a} G_Q\frac{\partial\tilde{p}}{\partial n}dS + \frac{1}{|\partial\Omega|}\int_{\partial\Omega}\tilde{p}dS.$$

We assumed that the absorbing boundary is a small ball B_η (in dimension 3) or a small arclength (in dimension 2) $\partial N_a = B_\eta$, where $\eta << 1$. Under this assumption the leading order term $\tilde{p}(\boldsymbol{x})$ outside a boundary layer of the absorbing boundary is approximated by a constant (see Holcman and Schuss 2004), $\tilde{p}(\boldsymbol{x}) \approx P_\eta$. We get

$$\begin{aligned}\tilde{p}(Q) = D\int_{\partial N_a} G_Q \frac{\partial \tilde{p}}{\partial n} dS + P_\eta \left(1 - \int_\Omega k(\boldsymbol{x}) G_Q(\boldsymbol{x}) d\boldsymbol{x}\right)\\ + \int_\Omega G_Q(\boldsymbol{y}) p_i(\boldsymbol{y}) d\boldsymbol{y}.\end{aligned} \tag{9.45}$$

In order to estimate the constant P_η, we use that at the absorbing boundary ∂N_a, the function $\tilde{p}$ has to vanish. The unknown flux is

$$g(S) = \frac{\partial \tilde{p}}{\partial n}(\boldsymbol{x}(S)), \tag{9.46}$$

and at a point $Q \in \partial N_a$ where $\tilde{p}(Q) = 0$, we have the relation

$$\begin{aligned}0 = D\int_{\partial N_a} G_Q(\boldsymbol{x}(S)) g(S) dS + P_\eta \left(1 - \int_\Omega k(\boldsymbol{x}) G_Q(\boldsymbol{x}) d\boldsymbol{x}\right)\\ + \int_\Omega G_Q(\boldsymbol{y}) p_i(\boldsymbol{y}) d\boldsymbol{y}.\end{aligned} \tag{9.47}$$

To compute $g(s)$, we integrate (9.41) over the domain Ω, using that $\int_\Omega p_i(\boldsymbol{x}) d\boldsymbol{x} = 1$,

$$\begin{aligned}D\int_{\partial N_a} g(S) dS &= -1 + \int_\Omega k(\boldsymbol{x}) \tilde{p}(\boldsymbol{x}) d\boldsymbol{x}\\ &= -1 + P_\eta \int_\Omega k(\boldsymbol{x}) d\boldsymbol{x}.\end{aligned} \tag{9.48}$$

To estimate the left-hand side of expression (9.48), we use a Taylor expansion of the flux $g(S)$ at a fixed point in the interior of the absorbing boundary far from the edges (Holcman and Schuss 2004), we get

$$\int_{\partial N_a} g(S) dS = \int_{-\eta}^{\eta} g(S) dS = 2\eta g_0 + o(\eta), \tag{9.49}$$

where g_0 is the first term of the expansion of $g(S)$. Thus, we obtain from relation (9.48) that

$$g_0 = \frac{-1 + P_\eta \int_\Omega k(\boldsymbol{x}) d\boldsymbol{x}}{2D\eta}. \tag{9.50}$$

To estimate the constant P_η, we use the expansion of the Green function in dimensions 2 and 3 in expression (9.47),

$$DG_Q(\boldsymbol{x}) = \begin{cases} -\frac{1}{2\pi}\ln|\boldsymbol{x}-Q| + C_0 + h_Q(\boldsymbol{x}), & \text{for} \quad n=2 \\ \frac{1}{4\pi}|\boldsymbol{x}-Q|^{-1} + C_0 + h_Q(\boldsymbol{x}), & \text{for} \quad n=3, \end{cases} \tag{9.51}$$

where C_0 is a constant and h_Q a harmonic function, then in dimension 2, we get (for the details of the computations see Holcman (2007))

$$\begin{aligned} 0 &= D\int_{\partial N_a} G_Q(\boldsymbol{x}(S))g(S)dS + P_\eta\left(1 - \int_\Omega k(\boldsymbol{x})G_Q(\boldsymbol{x})d\boldsymbol{x}\right) \\ &\quad + \int_\Omega G_Q(\boldsymbol{y})p_i(\boldsymbol{y})d\boldsymbol{y} \\ &\approx -\frac{1}{\pi}\int_{-\eta}^{\eta}\ln|s|g_0 dS + 2(C_0-1)g_0\eta + P_\eta\left(1 - \int_\Omega k(\boldsymbol{x})G_Q(\boldsymbol{x})d\boldsymbol{x}\right) \\ &\quad + \int_\Omega G_Q(\boldsymbol{y})p_i(\boldsymbol{y})d\boldsymbol{y} \\ &\approx 2g_0\eta\left(-\frac{\ln\eta}{\pi} + (C_0-1)\right) + P_\eta\left(1 - \int_\Omega k(\boldsymbol{x})G_Q(\boldsymbol{x})d\boldsymbol{x}\right) \\ &\quad + \int_\Omega G_Q(\boldsymbol{y})p_i(\boldsymbol{y})d\boldsymbol{y} \\ &\approx \frac{1}{D}\left(-1 + P_\eta\int_\Omega k(\boldsymbol{x})d\boldsymbol{x}\right)\left(-\frac{\ln\eta}{\pi} + (C_0-1)\right) \\ &\quad + P_\eta\left(1 - \int_\Omega k(\boldsymbol{x})G_Q(\boldsymbol{x})d\boldsymbol{x}\right) + \int_\Omega G_Q(\boldsymbol{y})p_i(\boldsymbol{y})d\boldsymbol{y}. \end{aligned}$$

It is easy to check that this identity does not depend on the Green function. Finally, far enough from the boundary layer near the window $\partial\Omega_a$, the solution $\tilde{p}(\boldsymbol{x})$ is approximated by,

$$\tilde{p}(\boldsymbol{x}) \approx P_\eta \approx \frac{\dfrac{\ln\frac{1}{\eta}}{D\pi} + C_0 - 1 - \displaystyle\int_\Omega G_Q(\boldsymbol{y})p_i(\boldsymbol{y})d\boldsymbol{y}}{\dfrac{\ln\frac{1}{\eta}}{D\pi}\displaystyle\int_\Omega k(\boldsymbol{x})d\boldsymbol{x} + (C_0-1)\int_\Omega k(\boldsymbol{x})d\boldsymbol{x} + \left(1 - \int_\Omega k(\boldsymbol{x})G_Q(\boldsymbol{x})d\boldsymbol{x}\right)} \tag{9.52}$$

In the two-dimensional case, formulas (9.37) and (9.43) give for $\boldsymbol{y} \in \partial N_a$

$$P_N \approx P_N(\boldsymbol{y}) = 1 - \int\limits_{\Omega} k(\boldsymbol{x})\tilde{p}(\boldsymbol{x})d\boldsymbol{x}$$

$$\approx \frac{1 + \int_{\Omega} k(\boldsymbol{x})\,d\boldsymbol{x} \int_{\Omega} G(\boldsymbol{x},\boldsymbol{y})p_i(\boldsymbol{x})\,d\boldsymbol{x} - \int_{\Omega} k(\boldsymbol{x})G(\boldsymbol{x},\boldsymbol{y})\,d\boldsymbol{x}}{\frac{\ln\frac{1}{\eta}}{D\pi}\int_{\Omega} k(\boldsymbol{x})d\boldsymbol{x} + (C_0 - 1)\int_{\Omega} k(\boldsymbol{x})d\boldsymbol{x} + \left(1 - \int_{\Omega} k(\boldsymbol{x})G(\boldsymbol{x},\boldsymbol{y})d\boldsymbol{x}\right)},$$

where C_0 is a constant that fixes the Green function. In the limit of $k(\boldsymbol{x}) \ll 1$, whatever is the choice of C_0, terms of order $O(1)$ in $k(\boldsymbol{x})$ can be neglected, except the term in the denominator, which is multiplied by a large flux. Thus the leading order term in the expansion of P_N in the two-dimensional case is

$$P_N \approx \frac{1}{1 + \frac{\ln\frac{1}{\eta}}{D\pi}\int_{\Omega} k(\boldsymbol{x})\,d\boldsymbol{x}} \quad \text{for } k(\boldsymbol{x}) \ll 1. \tag{9.53}$$

In the three-dimensional case the calculation of P_N follows that in Sect. 1.5. Although similar to that for the two-dimensional case, there are some significant differences. Specifically, the flux through ∂N_a, which can be assumed a small disk of radius ε, is given by

$$\frac{\partial\tilde{p}(\boldsymbol{x}(s))}{\partial n} = g(s) = \frac{g_0}{\sqrt{\eta^2 - s^2}} + o(\eta). \tag{9.54}$$

The leading order term in the expansion of $g(s)$ for small η is computed by integrating Eq. (9.41),

$$D\int\limits_{\partial N_a} g(s)\,ds = -1 + P_\eta \int\limits_{\Omega} k(\boldsymbol{x})\,d\boldsymbol{x}. \tag{9.55}$$

Because

$$\int\limits_{\partial N_a} g(s)\,ds = \int\limits_0^{\eta} \frac{2\pi g_0 s}{\sqrt{\eta^2 - s^2}}\,ds = 2\pi\eta g_0, \tag{9.56}$$

the approximation

$$g_0 = \frac{-1 + P_\eta \int\limits_{\Omega} k(\boldsymbol{x})d\boldsymbol{x}}{2\pi D\eta} \tag{9.57}$$

holds. As in the two-dimensional case, expanding the three-dimensional Green function (9.43) at a point $\boldsymbol{y} \in \partial N_a$, we get

$$D \int\limits_{\partial N_a} G(\boldsymbol{x}(s), \boldsymbol{y}) g(s)\, ds = \int\limits_0^\eta \left(\frac{1}{2\pi |s|} + C_0 \right) \frac{2\pi g_0 s\, ds}{\sqrt{\eta^2 - s^2}}. \tag{9.58}$$

Instead of (9.53) the small $k(\boldsymbol{x})$ approximation becomes

$$P_N = 1 - \int\limits_\Omega k(\boldsymbol{x}) \tilde{p}(\boldsymbol{x})\, d\boldsymbol{x} \approx \frac{1}{1 + \dfrac{1}{4D\eta} \displaystyle\int_\Omega k(\boldsymbol{x})\, d\boldsymbol{x}} \quad \text{for } k(\boldsymbol{x}) \le 1. \tag{9.59}$$

Recall that in the three-dimensional case $\eta = (|\partial N_a| / |\partial \Omega|)^{1/2}$ represents the ratio of the absorbing part to that of the nucleus. When there are N well-separated small holes on the surface of the nucleus Eq. (9.53) is generalized, as in Chap. 1, to

$$P_N = \begin{cases} \dfrac{1}{1 + \dfrac{\ln \frac{1}{\eta}}{ND\pi} \displaystyle\int_\Omega k(\boldsymbol{x})\, d\boldsymbol{x}} & \text{for } n = 2. \\[2ex] \dfrac{1}{1 + \dfrac{1}{4ND\eta} \displaystyle\int_\Omega k(\boldsymbol{x})\, d\boldsymbol{x}} & \text{for } n = 3. \end{cases} \tag{9.60}$$

9.3.4 Asymptotics of $\bar{\tau}_N$ for Small Killing Rate $k(\boldsymbol{x}) \ll 1$

The mean time $\bar{\tau}_N$ to reach a nuclear pore alive is conditioned on $\tau^a < \tau^k$. Its regular expansion for small $k(\boldsymbol{x})$ is given asymptotically for small η by

$$\bar{\tau}_N \approx \begin{cases} |\Omega| \dfrac{\dfrac{\ln(\frac{1}{\eta})}{D\pi} - \displaystyle\int_\Omega G(\boldsymbol{x}, \boldsymbol{y}) p_i(\boldsymbol{x})\, d\boldsymbol{x}}{1 + \dfrac{\ln(\frac{1}{\eta})}{D\pi} \displaystyle\int_\Omega k(\boldsymbol{x})\, d\boldsymbol{x}} & \text{for } n = 2,\ C_0 = 1 \\[3ex] |\Omega| \dfrac{\dfrac{1}{4D\eta} - \displaystyle\int_\Omega G(\boldsymbol{x}, \boldsymbol{y}) p_i(\boldsymbol{x})\, d\boldsymbol{x}}{1 + \dfrac{\int_\Omega k(\boldsymbol{x})\, d\boldsymbol{x}}{4D\eta}} & \text{for } n = 3,\ C_0 = 0, \end{cases} \tag{9.61}$$

where $\boldsymbol{y}$ is any point in ∂N_a. The detailed calculations are given in Holcman (2007). If there are N well-separated small holes on the surface of the nucleus, Eq. (9.58) is generalized, as in Chap. 1, to

$$\bar{\tau}_N \approx \begin{cases} \dfrac{\dfrac{|\Omega| \ln(\frac{1}{\eta})}{ND\pi}}{1 + \dfrac{\ln(\frac{1}{\eta})}{ND\pi} \displaystyle\int_\Omega k(\boldsymbol{x})\, d\boldsymbol{x}} & \text{for } n = 2 \\[2ex] \dfrac{\dfrac{|\Omega|}{4D\eta N}}{1 + \dfrac{\int_\Omega k(\boldsymbol{x}) d\boldsymbol{x}}{4ND\eta}} & \text{for } n = 3. \end{cases} \tag{9.62}$$

where we neglected the first order terms in (9.61). As N tends to infinity (9.62) breaks down. It is necessary in this case to introduce a new term, which is the geometrical capacity of the nucleus with respect to the cellular domain (see Sect. 1.7.1), to account for the time to travel from the cell surface to the nuclear envelop.

It is informative to estimate the probability and the mean time a Brownian particle (like a small plasmid) to reach a small nuclear pore. The typical diffusion coefficient for a cytosolic plasmid DNA of 5500 base pairs (average size of a gene) is about $D \approx 0.02\,\mu\text{m}^2/\text{s}$. Consider, for example, a spherical cell of radius $R = 5\,\mu\text{m}$, with 10 % of its nucleus surface covered by nuclear pores. This gives about $n = 160$ nuclear pores in dimension three and $n = 25$ in dimension two. The lifespan of the cytoplasmic DNA is about 1 h (see Lagache and Holcman 2008b). Thus, choosing $k = 1/3600\,\text{s}^{-1}$ in (9.60), the resulting delivery probability is

$$P_N \approx 0.9371 \ \text{ for } n = 2, \quad P_N \approx 0.6875 \ \text{ for } n = 3, \tag{9.63}$$

while the conditional mean arrival time (9.62) is given by

$$\tau_N \approx 226\,\text{s} \ \text{ for } n = 2, \quad \tau_N \approx 1125\,\text{s} \ \text{ for } n = 3. \tag{9.64}$$

The results in two dimensions can be applied to flat cells, while those in three dimensions are relevant to bulky cells. The difference in the numerical values of P_N can be understood intuitively by noting that the mean time to absorption in the three-dimensional case is of a different order of magnitude than in the two-dimensional case, which gives the killing process a chance to terminate the trajectory prior to absorption.

9.4 The Case of Non-zero Drift

Adding a drift to the Brownian motion changes the probability P_N and the mean reaching time $\bar{\tau}_N$ relative to those for pure Brownian motion. We consider for simplicity the case of a gradient drift, given by $\boldsymbol{b}(\boldsymbol{x}) = -\nabla\phi(\boldsymbol{x})$, with a potential

$\phi(\boldsymbol{x})$ that has a minimum at the origin, inside the nucleus and that $\boldsymbol{b}(\boldsymbol{x})$ is directed into the cell at its external surface, that is, $\boldsymbol{b}(\boldsymbol{x}) \cdot \boldsymbol{n}(\boldsymbol{x}) < 0$ for all $\boldsymbol{x} \in \partial\Omega_{\text{ext}}$. For example,

$$\phi(\boldsymbol{x}) = B|\boldsymbol{x}| \quad \text{for } \boldsymbol{x} \in \Omega, \tag{9.65}$$

see Fig. 9.4.

9.4.1 Probability to Reach Alive the Nucleus Surface

To estimate the probability P_N, we now estimate asymptotically the solution $\tilde{p}$ of Eq. (2.176). According to Sect. 1.9.1, the equilibrium solution of (2.176) in the limit of vanishing Dirichlet boundary is the principal eigenfunction (1.159), which is thus the outer solution of (2.176) outside a boundary layer near $\partial\Omega_a$. It is given by

$$\tilde{p}(\boldsymbol{x}) = C_\eta e^{-\phi(\boldsymbol{x})/D}. \tag{9.66}$$

To determine the constant C_η, we proceed as above. Integrating (2.176) and using the no flux boundary conditions, we get

$$D \int\limits_{\partial N_a} g(s)\, ds = -1 + \int\limits_{\Omega} k(\boldsymbol{x})\tilde{p}(\boldsymbol{x}) d\boldsymbol{x}, \tag{9.67}$$

where the absorption flux at $\partial\Omega_a$ is given by $g(s) = \dfrac{\partial\tilde{p}(\boldsymbol{x}(s))}{\partial n}$. As in Sect. 1.9.1, $g(s)$ in (9.67) can be approximated for s in $\partial\Omega_a$ as

$$g(s) = \begin{cases} g_0 e^{-\phi(\boldsymbol{x}_0)/D} + o(\eta) \ \text{ for } n = 2, \\[2ex] \dfrac{g_0 e^{-\phi(\boldsymbol{x}_0)/D}}{\sqrt{\eta^2 - s^2}} + o(\eta) \text{ for } n = 3, \end{cases} \tag{9.68}$$

where $\phi(\boldsymbol{x}_0)$ is the practically constant value of ϕ in $\partial\Omega_a$ for small η. Thus,

$$g_0 = \begin{cases} e^{\phi(\boldsymbol{x}_0)/D} \dfrac{-1 + C_\eta \displaystyle\int_\Omega k(\boldsymbol{x}) e^{-\phi(\boldsymbol{x})/D} d\boldsymbol{x}}{2D\eta} \ \text{ for } n = 2 \\[4ex] e^{\phi(\boldsymbol{x}_0)/D} \dfrac{-1 + C_\eta \displaystyle\int_\Omega k(\boldsymbol{x}) e^{-\phi(\boldsymbol{x})/D} d\boldsymbol{x}}{2\pi D\eta} \ \text{ for } n = 3. \end{cases} \tag{9.69}$$

The function $\tilde{p}(\boldsymbol{y})$ can be represented in terms of Green's function as

$$\begin{aligned}&\int\limits_{\Omega} G(\boldsymbol{x},\boldsymbol{y})\left[-p_i(\boldsymbol{x}) + k(\boldsymbol{x})\tilde{p}(\boldsymbol{x})\right]\,d\boldsymbol{x}\\ &\quad -\int\limits_{\Omega} \nabla_{\boldsymbol{x}} G(\boldsymbol{x},\boldsymbol{y})\cdot\nabla\phi(\boldsymbol{x})\tilde{p}(\boldsymbol{x})\,d\boldsymbol{x} + \tilde{p}(\boldsymbol{y})\\ &= D\int\limits_{\partial\Omega_a} G(\boldsymbol{x}(s),\boldsymbol{y})\frac{\partial\tilde{p}(\boldsymbol{x}(s))}{\partial n}\,ds + \frac{1}{|\partial\Omega_a|}\int\limits_{\partial\Omega_a}\tilde{p}(\boldsymbol{x}(s))\,ds,\end{aligned} \tag{9.70}$$

which reduces by the absorbing boundary condition $\tilde{p}(\boldsymbol{y}) = 0$ for $\boldsymbol{y} \in \partial\Omega_a$ and by (9.66) to

$$\begin{aligned}&D\int\limits_{\partial\Omega_a} G(\boldsymbol{x}(s),\boldsymbol{y})\,g(s)\,ds + \frac{1}{|\partial\Omega|}\int\limits_{\partial\Omega} C_\eta e^{-\phi(\boldsymbol{x}(s))/D}\,ds\\ &\quad= \int\limits_{\Omega} G(\boldsymbol{x},\boldsymbol{y})\left[-p_i(\boldsymbol{x}) + k(\boldsymbol{x})C_\eta e^{-\phi(\boldsymbol{x})/D}\right]\,d\boldsymbol{x}\\ &\quad -\int\limits_{\Omega}\nabla_{\boldsymbol{x}} G(\boldsymbol{x},\boldsymbol{y})\cdot\nabla\phi(\boldsymbol{x})C_\eta e^{-\phi(\boldsymbol{x})/D}\,d\boldsymbol{x}.\end{aligned} \tag{9.71}$$

The flux condition (9.69) gives for $\boldsymbol{y} \in \partial\Omega_a$

$$D\int\limits_{\partial\Omega_a} G(\boldsymbol{x}(s),\boldsymbol{y})g(s)\,ds \tag{9.72}$$

$$= \begin{cases} 2D\eta g_0 e^{-\phi(\boldsymbol{x}_0)/D}\left(-\dfrac{\ln\eta}{\pi} + C_0 - 1\right) & \text{for } n = 2\\[2ex] \pi D g_0 e^{-\phi(\boldsymbol{x}_0)/D}\left(\dfrac{1}{2} + 2\eta C_0\right) & \text{for } n = 3.\end{cases}$$

Choosing $C_0 = 1$ for $n = 2$ and $C_0 = 0$ for $n = 3$, we get from (9.71) that for $n = 2$ and $\boldsymbol{y} \in \partial\Omega_a$

$$C_\eta \approx$$

$$\frac{\dfrac{\ln\frac{1}{\eta}}{D\pi} - \displaystyle\int_\Omega G(\boldsymbol{x},\boldsymbol{y})p_i(\boldsymbol{x})\,d\boldsymbol{x}}{\dfrac{\ln\frac{1}{\eta}}{D\pi}\displaystyle\int_\Omega e^{-\phi(\boldsymbol{x})/D}k(\boldsymbol{x})\,d\boldsymbol{x} + \frac{1}{|\partial\Omega_a|}\int_{\partial\Omega_a} e^{-\phi(\boldsymbol{x}(s))/D}\,ds - \int_\Omega e^{-\phi(\boldsymbol{x})/D}k(\boldsymbol{x})G(\boldsymbol{x},\boldsymbol{y})\,d\boldsymbol{x}} \tag{9.73}$$

and for $n = 3$ and $\boldsymbol{y} \in \partial\Omega_a$

$$C_\eta \approx \frac{\dfrac{1}{4D\eta} - \displaystyle\int_\Omega G(\boldsymbol{x},\boldsymbol{y})p_i(\boldsymbol{x})\,d\boldsymbol{x}}{\dfrac{1}{4D\eta}\displaystyle\int_\Omega e^{-\phi(\boldsymbol{x})/D}k(\boldsymbol{x})\,d\boldsymbol{x} + \dfrac{1}{|\partial\Omega_a|}\displaystyle\int_{\partial\Omega_a} e^{-\phi(\boldsymbol{x}(s))/D}\,ds - \displaystyle\int_\Omega e^{-\phi(\boldsymbol{x}(s))/D}k(\boldsymbol{x})G(\boldsymbol{x},\boldsymbol{y})\,d\boldsymbol{x}}. \tag{9.74}$$

For small $k(\boldsymbol{x})$ this gives

$$P_N = 1 - \int\limits_\Omega k(\boldsymbol{x})\tilde{p}(\boldsymbol{x})\,d\boldsymbol{x} = 1 - C_\eta \int\limits_\Omega k(\boldsymbol{x})e^{-\phi(\boldsymbol{x})/D}\,d\boldsymbol{x}, \tag{9.75}$$

which can be written as

$$P_N \approx \begin{cases} \dfrac{\dfrac{1}{|\partial\Omega_a|}\displaystyle\int_{\partial\Omega_a} e^{-\phi(\boldsymbol{x})/D}dS_{\boldsymbol{x}}}{\dfrac{\ln\frac{1}{\eta}}{D\pi}\displaystyle\int_\Omega e^{-\phi(\boldsymbol{x})/D}k(\boldsymbol{x})\,d\boldsymbol{x} + \dfrac{1}{|\partial\Omega_a|}\displaystyle\int_{\partial\Omega_a} e^{-\phi(\boldsymbol{x})/D}\,dS_{\boldsymbol{x}}} & \text{for } n = 2 \\[2ex] \dfrac{\dfrac{1}{|\partial\Omega_a|}\displaystyle\int_{\partial\Omega_a} e^{-\phi(\boldsymbol{x})/D}dS_{\boldsymbol{x}}}{\dfrac{1}{4D\eta}\displaystyle\int_\Omega e^{-\phi(\boldsymbol{x})/D}k(\boldsymbol{x})\,d\boldsymbol{x} + \dfrac{1}{|\partial\Omega_a|}\displaystyle\int_{\partial\Omega_a} e^{-\phi(\boldsymbol{x})/D}dS_{\boldsymbol{x}}} & \text{for } n = 3. \end{cases} \tag{9.76}$$

9.4.2 The Arrival Probability P_N with the Potential $\phi(x) = B|x|$

When the (dimensionless) potential $\phi(\boldsymbol{x})$ is an increasing function of the distance from the nucleus, its minimum is achieved on the surface of the nucleus. For simplicity, we assume that the nucleus is a ball of radius δ, centered at the origin. We consider two extreme cases, that $\phi(\boldsymbol{x})$ achieves its minimum uniformly on the nucleus surface and that the minimum is achieved at a finite number of isolated points on the surface.

In the first case, assuming $\phi(\boldsymbol{x}) = B|\boldsymbol{x}|$, we obtain

$$\frac{1}{|\partial\Omega_a|}\int\limits_{\partial\Omega_a} e^{-\phi(\boldsymbol{x})/D}\,dS_{\boldsymbol{x}} = e^{-\delta B/D}. \tag{9.77}$$

Setting

$$\tilde{k}(r) = \int\limits_{|\boldsymbol{x}|=r} k(\boldsymbol{x})\, dS_{\boldsymbol{x}}, \tag{9.78}$$

we obtain for $1 \ll B\delta/D \ll BR/D$ the asymptotic expansion

$$\begin{aligned}\int\limits_{\Omega} e^{-\phi(\boldsymbol{x})/D} k(\boldsymbol{x})\, d\boldsymbol{x} &= \int\limits_{\delta}^{R} \tilde{k}(r) e^{-Br/D} r^{n-1} dr \\ &= \left(\frac{B\delta}{D}\right)^{n-1} e^{-B\delta/D} \left(\tilde{k}(\delta) + \frac{B\delta}{D}\tilde{k}'(\delta) + \cdots\right)\end{aligned}$$

which reduces for a locally constant $k(\boldsymbol{x}) = k(\delta)$ in a neighborhood of the nucleus $|\boldsymbol{x}| = \delta$ to

$$\int\limits_{\Omega} e^{-\phi(\boldsymbol{x})/D} k(\boldsymbol{x})\, d\boldsymbol{x} = \left(\frac{B\delta}{D}\right)^{n-1} e^{-B\delta/D} |\partial\Omega_a| k(\delta), \tag{9.79}$$

with

$$|\partial\Omega_a| = \begin{cases} 2\pi\delta & \text{for } n = 2, \\ 4\pi\delta^2 & \text{for } n = 3. \end{cases} \tag{9.80}$$

With this approximation (9.76) reduces to

$$P_N \approx \begin{cases} \dfrac{1}{\dfrac{2\ln\frac{1}{\eta}}{D}\left(\dfrac{B\delta^2}{D}\right)k(\delta) + 1} & \text{for } n = 2 \\[2ex] \dfrac{1}{\dfrac{\pi}{D\eta}\left(\dfrac{B}{D}\right)^2 \delta^4 k(\delta) + 1} & \text{for } n = 3. \end{cases} \tag{9.81}$$

For a general potential $\phi(\boldsymbol{x})$ that achieves its absolute minimum ϕ_m in the cells at isolated points $(\boldsymbol{x}_1, \boldsymbol{x}_2, \ldots, \boldsymbol{x}_M)$ on the surface of the nucleus the Laplace expansion of the integrals in (9.76) gives

$$\int\limits_{\partial\Omega} e^{-\phi(\boldsymbol{x})/D}\,dS = \begin{cases} e^{-\dfrac{\phi_m}{D}} \displaystyle\sum_{k=1}^{M} \sqrt{\frac{2D\pi}{\operatorname{Hess}(\phi(\boldsymbol{x}_k))}} & \text{for } n=2 \\ e^{-\dfrac{\phi_m}{D}} \displaystyle\sum_{k=1}^{M} \frac{2D\pi}{\sqrt{\operatorname{Hess}(\phi(\boldsymbol{x}_k))}} & \text{for } n=3, \end{cases} \tag{9.82}$$

where $\operatorname{Hess}(\phi(\boldsymbol{x}_k))$ is the $n-1$-dimensional Hessian determinant of the restriction of ϕ to $\partial\Omega_a$ at $\boldsymbol{x}_k \in \partial\Omega_a$. Also the integral

$$\int_{\Omega} e^{-\phi(\boldsymbol{x})/D} k(\boldsymbol{x})\,d\boldsymbol{x}$$

can be evaluated asymptotically by the Laplace method for $1 \ll B\delta/D \ll BR/D$ (Schuss 2010b).

In the reverse limit $B\delta/D \ll 1$ the exponential function in the above integrals can be expanded in Taylor's series to obtain the approximation

$$\frac{1}{|\partial\Omega|}\int\limits_{\partial\Omega} e^{-\phi(\boldsymbol{x})/D}\,dS = 1 - \frac{\bar{\phi}}{D} + o\left(\frac{\phi}{D}\right)^2, \tag{9.83}$$

where $\bar{\phi}$ is the average of ϕ over $\partial\Omega$. For the potential $\phi(\boldsymbol{x}) = B|\boldsymbol{x}|$ in the annular domain $\delta < |\boldsymbol{x}| < R$ with $R >> \delta$,

$$\bar{\phi} \approx BR. \tag{9.84}$$

Thus,

$$P_N \approx \begin{cases} \dfrac{1 - \frac{BR}{D}}{\dfrac{\ln\frac{1}{\eta}}{D\pi}\left(\displaystyle\int_{\Omega} k(\boldsymbol{x})\,d\boldsymbol{x} - \int_{\Omega} k(\boldsymbol{x})\phi(x)\,d\boldsymbol{x}\right) + 1 - \dfrac{BR}{D}} & \text{for } n=2 \\ \dfrac{1 - \frac{BR}{D}}{\dfrac{1}{4D\eta}\left(\displaystyle\int_{\Omega} k(\boldsymbol{x})\,d\boldsymbol{x} - \int_{\Omega} k(\boldsymbol{x})\phi(x)\,d\boldsymbol{x}\right) + 1 - \dfrac{BR}{D}} & \text{for } n=3. \end{cases} \tag{9.85}$$

9.4.3 The Conditional MFPT to the Nucleus

The conditional MFPT to the nucleus, $\bar{\tau}_N$, is computed much like in the no-drift case in Sect. 9.3.2. The detailed computations are given in the references listed in Sect. 9.6. Specifically, keeping the notation of Sect. 9.3.2, the small killing rate result is

$$\bar{\tau}_N \approx \begin{cases} \dfrac{\dfrac{\ln\frac{1}{\eta}}{D\pi}\displaystyle\int_\Omega e^{-\phi(\boldsymbol{x})/D}\,d\boldsymbol{x}}{\dfrac{\ln\frac{1}{\eta}}{D\pi}\displaystyle\int_\Omega e^{-\phi(\boldsymbol{x})/D}k(\boldsymbol{x})\,d\boldsymbol{x} + \dfrac{1}{|\partial\Omega|}\displaystyle\int_{\partial\Omega} e^{-\phi(\boldsymbol{x})/D}\,dS_{\boldsymbol{x}}} & \text{for } n=2 \\ \\ \dfrac{\dfrac{1}{4D\eta}\displaystyle\int_\Omega e^{-\phi(\boldsymbol{x})/D}\,d\boldsymbol{x}}{\dfrac{1}{4D\eta}\displaystyle\int_\Omega e^{-\phi(\boldsymbol{x})/D}k(\boldsymbol{x})\,d\boldsymbol{x} + \dfrac{1}{|\partial\Omega|}\displaystyle\int_{\partial\Omega} e^{-\phi(\boldsymbol{x})/D}\,dS_{\boldsymbol{x}}} & \text{for } n=3. \end{cases} \tag{9.86}$$

If the diffusion coefficient D is small, the potential ϕ achieves its minimum uniformly on the nucleus surface boundary, and the killing rate k is locally constant near the surface,

$$\bar{\tau}_N \approx \begin{cases} \dfrac{\dfrac{2\ln\frac{1}{\eta}}{D}\dfrac{D\delta}{B}}{1 + k\dfrac{2\ln\frac{1}{\eta}}{D}\dfrac{D\delta}{B}} & \text{for } n=2 \\ \\ \dfrac{\dfrac{\pi}{\eta D}\dfrac{D\delta^2}{B}}{1 + \dfrac{\pi}{D\eta}\dfrac{D\delta^2}{B}k} & \text{for } n=3. \end{cases} \tag{9.87}$$

Note that when the diffusion constant is small, the conditional MFPT depends mainly on the time spent in a small region around the nucleus. If $B\delta/D \ll 1$, other limit formulas can be obtained, such as (9.73) and (9.74), with $\bar{\tau}_N = C_\eta$. In the case of n well-separated small holes, formulas (9.81) and (9.87) are modified by replacing η with $n\eta$ in dimension 3 and $\ln\eta$ with $(\ln\eta)/n$ in dimension 2.

The asymptotic formulas can be applied to data concerning the AAV. The diffusion constant is $D \approx 1.3\,\mu\text{m}^2/\text{s}$ and the mean drift is in the range 1.8–3.7 μm/s (Seisenberger et al. 2001). Because the effective drift of a virus toward the nucleus is about 5–10 % of the mean drift on a microtubule, close to the nucleus, the effective drift value can be taken as $B = 2.5/20 = 0.12\,\mu\text{m/s}$ (Lagache et al. 2009b). The killing rate is about $k = 1/3600\,\text{s}^{-1}$. The cell characteristics are identical to the case of a plasmid. For these values the absorption probability of a live virus is

$$P_N = 0.98 \quad \text{for } n=2, \qquad P_N = 0.70 \quad \text{for } n=3, \tag{9.88}$$

while the conditional MFPT is

$$\bar{\tau}_N = 66\,\text{s} \quad \text{for } n=2, \qquad \bar{\tau}_N = 1056\,\text{s} \quad \text{for } n=3. \tag{9.89}$$

Thus the probability to reach the nucleus alive is higher for viruses than for plasmids, which is a consequence here of the drift effect. However, the conditional MFPT in dimension two and three is very different for both plasmids and viruses. For viruses, the difference between dimensions 2 and 3 is observed mainly for the conditional MFPT $\bar{\tau}_N$, which is about 16 times longer [see Lagache and Holcman (2015) for generalizations]. The case of large degradation rate $k \gg 1$ is relevant to plasmid trafficking in the cell cytoplasm, where the killing rate due to the protease can be much larger than absorption rate. A full study of this case is given in Lagache et al. (2009a).

9.4.4 The Large Degradation Rate Limit $k \gg 1$

The previous analysis (Holcman 2007) does not give any results for the probability and the mean time to reach a nuclear pore when the degradation rate is large $k \gg 1$. In some cases such plasmid trafficking in the cell cytoplasm, the killing activity due to the protease could be much larger than the diffusion time scale. Hereafter, we present an asymptotic estimation in the large degradation rate limit. We start with a constant degradation rate $k(\boldsymbol{x}) = k$ [the computations for a general radial degradation rate are given in Lagache et al. (2009a)]. We consider a uniform initial plasmid distribution over the cytoplasm $p_i(\boldsymbol{x}) = p_0 = \frac{1}{|\Omega|}$. To compute the probability P_N, we shall solve Eq. (2.174) (there is no drift)

$$D\Delta\tilde{p}(\boldsymbol{x}) - k(\boldsymbol{x})\tilde{p}(\boldsymbol{x}) = -p_0 = -\frac{1}{|\Omega|}, \tag{9.90}$$

with boundary conditions

$$\begin{aligned} \tilde{p}(\boldsymbol{x}) &= 0 \quad \text{for } \boldsymbol{x} \in \partial N_a \\ \frac{\partial \tilde{p}(\boldsymbol{x})}{\partial n} &= 0 \quad \text{for } \boldsymbol{x} \in \partial N_r \cup \partial\Omega_{\text{ext}}. \end{aligned} \tag{9.91}$$

When $\frac{D}{|\Omega|} \ll k$ and for a particle starting far away from nuclear pores, we approximated the solution of Eq. (9.90) by

$$p_{\text{outer}}(\boldsymbol{x}) = \frac{1}{k|\Omega|} + O(D). \tag{9.92}$$

However, this outer solution does not match the absorbing condition. Thus, we construct an inner solution $p_{\text{inner}}(\boldsymbol{x})$ near nuclear pores, that satisfies the absorbing conditions and match the outer solution.

In local coordinates (ρ, s) near ∂N_a, where ρ is the distance from ∂N_a, measured positively into the domain Ω, and s is the tangential variable in the plane $\rho = 0$.

Projecting Eq. (9.90) on the ρ-coordinate (the variation of $\tilde{p}$ with respect to s is small compared to the one in ρ), we obtain for the leading order term p_{inner}:

$$\frac{d^2 p_{\text{inner}}(\rho)}{d\rho^2} - \frac{k}{D} p_{\text{inner}}(\rho) = -\frac{1}{D|\Omega|}, \tag{9.93}$$

with

$$p_{\text{inner}}(0) = 0. \tag{9.94}$$

Far from the boundary layer, the matching condition is

$$\lim_{\frac{\rho}{\sqrt{D}} \to \infty} p_{\text{inner}}(\rho) = p_{\text{outer}} = \frac{1}{|\Omega| k}. \tag{9.95}$$

Consequently, near the boundary we get

$$p_{\text{inner}}(\rho, s) = \frac{1}{|\Omega| k} \left(1 - e^{-\sqrt{\frac{k}{D}}\rho} \right). \tag{9.96}$$

To compute P_N, we use formula (6.61)

$$P_N = 1 - \int_{\Omega} k(\boldsymbol{x}) \tilde{p}(\boldsymbol{x}) d\boldsymbol{x}, \tag{9.97}$$

which can be rewritten as

$$P_N = 1 - \left(\int_{\Omega \setminus BL} k p_{\text{outer}}(\boldsymbol{x}) d\boldsymbol{x} + \int_{BL} k p_{\text{inner}}(\rho) d\rho \right), \tag{9.98}$$

where BL is the boundary layer. Using expression (9.92) for p_{outer}, we get

$$\int_{\Omega \setminus BL} k p_{\text{outer}}(\boldsymbol{x}) d\boldsymbol{x} = \frac{|\Omega \setminus BL|}{|\Omega|} \tag{9.99}$$

and finally

$$\begin{aligned} \int_{BL} k p_{\text{inner}}(\rho) d\rho &= \frac{1}{|\Omega|} \left(|BL| + |\partial N_a| \int_0^{\rho_0} -e^{-\sqrt{\frac{k}{D}}\rho} d\rho \right) \\ &= \frac{1}{|\Omega|} \left(|BL| - |\partial N_a| \sqrt{\frac{D}{k}} \left(1 - e^{-\sqrt{\frac{k}{D}}\rho_0} \right) \right), \end{aligned} \tag{9.100}$$

where $\rho_0 >> \sqrt{\frac{D}{k}}$ is the thickness of the boundary layer. Finally,

$$P_N = \frac{|\partial N_a|}{|\Omega|}\sqrt{\frac{D}{k}} + O\left(e^{-\sqrt{\frac{k}{D}}\rho_0}\right). \tag{9.101}$$

In a three-dimensional cell, when the boundary consists of n well-separated small holes of radius η, we obtain that

$$P_N = \frac{n\pi\eta^2}{|\Omega|}\sqrt{\frac{D}{k}} + O\left(e^{-\sqrt{\frac{k}{D}}\rho_0}\right). \tag{9.102}$$

Because our analysis is local, it can be extended to any degradation rate, large compared to the exploring rate. In that case, when for n well-separated narrow pores of size η_q, $1 \le q \le n$, located at position $x_1, \ldots, x_n$, the asymptotic formula is

$$P_N \approx \sum_{q=1}^{n} \frac{\pi\eta_q^2}{|\Omega|}\sqrt{\frac{D}{k(x_q)}} + O\left(e^{-\sqrt{\frac{k_0}{D}}\rho_0}\right), \tag{9.103}$$

where k_0 is the minimum value of $k(\boldsymbol{x})$ among the pores. In Fig. 9.8, we show the comparison of Brownian simulations with the analytical formula (9.101): we conclude that the matching occurs for large degradation rate (more than 200 times the normal rate) and thus the large $k \gg 1$ case might be useful to characterize gene delivery for abnormal cells, where the degradation rate is large. We now compute the MFPT τ_N to a small pore for a live virus in the case $k \gg 1$. We recall that from formula (9.40) that

$$\tau_N = \frac{\int_\Omega \tilde{p}(\boldsymbol{x})d\boldsymbol{x} - \int_\Omega kq(\boldsymbol{x})d\boldsymbol{x}}{P_N}. \tag{9.104}$$

where $q(\boldsymbol{x}) = \int_0^\infty s\tilde{p}(\boldsymbol{x}, s)\, ds$ satisfies (9.39). To estimate τ_N, in a small diffusion regime, the outer approximation of q is

$$q_{\text{outer}} = \frac{p_{\text{outer}}}{k} = \frac{1}{|\Omega|k^2}. \tag{9.105}$$

The inner solution q_{inner} in the boundary layer expansion satisfies :

$$\begin{aligned}
\frac{d^2 q_{\text{inner}}(\rho)}{d\rho^2} - \frac{k}{D} q_{\text{inner}}(\rho) &= -\frac{p_{\text{inner}}}{D} = -\frac{1}{D|\Omega|k}\left(1 - e^{-\rho\sqrt{\frac{k}{D}}}\right) \\
q_{\text{inner}}(0) &= 0 \\
\lim_{\frac{\rho}{\sqrt{D}}\to\infty} q_{\text{inner}}(\rho) &= q_{\text{outer}} = \frac{1}{|\Omega|k^2}.
\end{aligned}$$

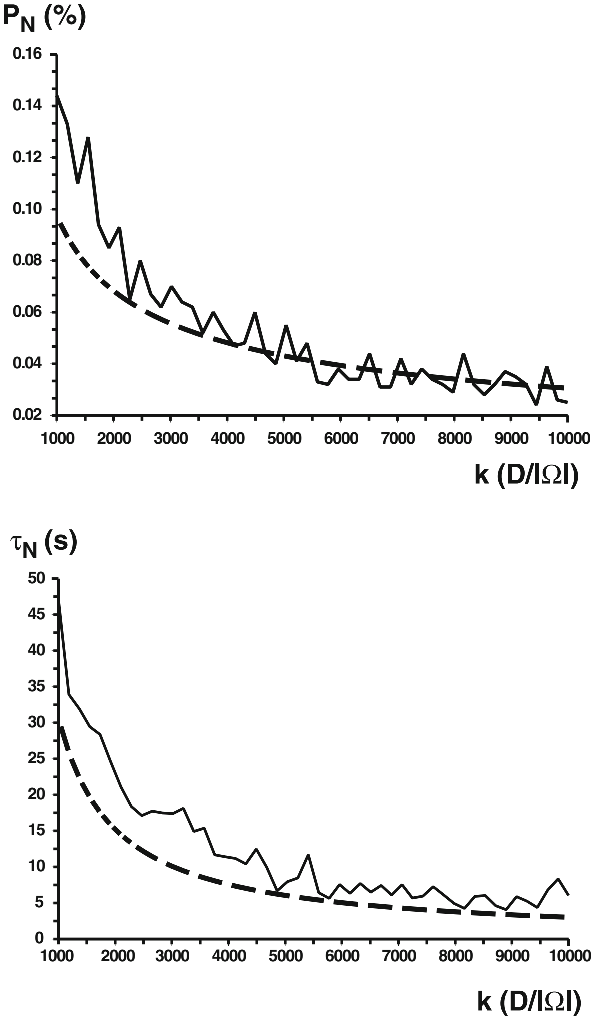

Fig. 9.8 The probability and mean time for a plasmid to reach a small nuclear pore, plotted as a function of the constant degradation rate for a two-dimensional flat cell. The Brownian simulations match the analytic solutions (9.101) and (9.107) only after a rate of $3000\frac{D}{|\Omega|} = 3000\frac{D}{\pi(R^2-\delta^2)} \approx 0.05\,\mathrm{s}^{-1}$, around 200 higher than the normal rate $1/3600 \approx 2.8 \times 10^{-4}\,\mathrm{s}^{-1}$

Consequently, we get :

$$q_{\text{inner}}(\rho) = \frac{1}{|\Omega|k^2}\left(1 - e^{-\sqrt{\frac{k}{D}}\rho}\right) - \frac{\rho}{2\sqrt{D}k^{\frac{3}{2}}|\Omega|}e^{-\sqrt{\frac{k}{D}}\rho}.$$

Finally, we obtain in Eq. (9.40)

$$\int_\Omega \tilde{p}(\boldsymbol{x})d\boldsymbol{x} - \int_\Omega kq(\boldsymbol{x})d\boldsymbol{x} = |\partial N_a|\frac{\sqrt{D}}{2|\Omega|k^{\frac{3}{2}}} + O\left(e^{-\sqrt{\frac{k}{D}}\rho_0}\right). \tag{9.106}$$

Finally,

$$\tau_N = |\partial N_a|\frac{\sqrt{D}}{2|\Omega|k^{\frac{3}{2}}P_N} + O\left(e^{-\sqrt{\frac{k}{D}}\rho_0}\right) = \frac{1}{2k} + O\left(e^{-\sqrt{\frac{k}{D}}\rho_0}\right). \tag{9.107}$$

For a large degradation rate, the analytical results match Brownian simulations (see Fig. 9.8). Moreover, this analysis is local and can be extended to any $\boldsymbol{x}$-dependent degradation rate and for n well separated narrow pores, located at position $x_1, \ldots, x_n$. The general asymptotic formula is

$$\tau_N \approx \frac{1}{n}\sum_{q=1}^{n}\frac{1}{2k(x_q)} + O\left(e^{-\sqrt{\frac{k_0}{D}}\rho_0}\right), \tag{9.108}$$

where $k_0 = \min_q k(x_q)$ is the minimum value of $k(\boldsymbol{x})$ among the pores. k_0 is the minimum concentration of killing factors among nuclear pores.

9.4.5 MFPT of the First DNA Carrier to Reach a Nuclear Pore

When multiple copies of stochastic particle (DNA carries) enter the cytoplasm, the conditional MFPT $\bar{\tau}_{\mathrm{FIRST}}(M)$ of the first carrier (virus or DNA) to reach a nuclear pore alive is also a quantity of interest. The M-DNA carriers' trajectories are assumed independent. The conditional MFPT of the jth carrier to reach the nuclear pore is denoted $\bar{\tau}_N^j$. Two random times are to be considered, the absorbing time $\tau_{\mathrm{FIRST}}(M)$ of the first carrier that reaches the absorbing boundary ∂N_a and the first time $\tau^k_{\mathrm{FIRST}}(M)$ it is degraded. The conditional probability that the first carrier, with initial density p_i, arrives alive at the absorbing boundary prior to time t is given by

$$P(t) = \Pr\{\tau^a_{\mathrm{FIRST}}(M) < t \mid \tau^a_{\mathrm{FIRST}}(M) < \tau^k_{\mathrm{FIRST}}(M), p_i\}. \tag{9.109}$$

The conditional MFPT $\bar{\tau}_{\mathrm{FIRST}}(M)$is defined by

$$\bar{\tau}_{\mathrm{FIRST}}(M) = \int_0^\infty t\frac{dP(t)}{dt}\,dt = \int_0^\infty [P(\infty) - P(t)]\,dt. \tag{9.110}$$

Bayes' law gives

$$P(t) = \frac{\Pr\{\tau^a_{\mathrm{FIRST}}(M) < t, \tau^a_{\mathrm{FIRST}}(M) < \tau^k_{\mathrm{FIRST}}(M), p_i\}}{\Pr\{\tau^a_{\mathrm{FIRST}}(M) < \tau^k_{\mathrm{FIRST}}(M), p_i\}} = \frac{N(t)}{D(t)}, \tag{9.111}$$

where $N(t)$ and $D(t)$ are the numerator and denominator, respectively, to be computed. The event $\{\tau^a_{\text{FIRST}}(M) > t \text{ or } \tau^a_{\text{FIRST}}(M) > \tau^k_{\text{FIRST}}(M)\}$ is that none of the M-carriers have reached a nuclear pore alive by time t. Because the particles are independent, we obtain

$$\begin{aligned}&\Pr\{\tau^a_{\text{FIRST}}(M) > t \text{ or } \tau^a_{\text{FIRST}}(M) > \tau^k_{\text{FIRST}}(M), p_i\}\\ &= \prod_{j=1}^{M}\left[1 - \Pr\{\tau^a_j < t, \tau^a_j < \tau^k_j, p_i\}\right],\end{aligned}$$

where τ^a_j (reps. τ^k_j) is the first time the jth particle is absorbed (resp. killed). Because the normal flux density at the boundary is the pdf of the exit point (Schuss 2010b), we get that for any of the particles

$$\Pr\{\tau^a_j < t, \tau^a_j < \tau^k_j, p_i\} = \int_0^t \oint_{\partial\Omega} \boldsymbol{J}(\boldsymbol{x},t)\cdot\boldsymbol{n}(\boldsymbol{x})\,dS_{\boldsymbol{x}} = \int_0^t J(s)\,ds, \tag{9.112}$$

where the flux $J(s)$ is defined in (2.178). Therefore the numerator in (9.111) is

$$\begin{aligned}N(t) &= \Pr\{\tau^a_{\text{FIRST}}(M) < t, \tau^a_{\text{FIRST}}(M) < \tau^k_{\text{FIRST}}(M), p_i\}\\ &= 1 - \left(1 - \int_0^t J(s)ds\right)^M\end{aligned}$$

and the denominator is

$$D(t) = \Pr\{\tau^a_{\text{FIRST}}(M) < \tau^k_{\text{FIRST}}(M), p_i\} = 1 - \Pr\{\tau^a_{\text{FIRST}}(M) > \tau^k_{\text{FIRST}}(M), p_i\}.$$

Because the particles are independent

$$D(t) = 1 - \prod_{j=1}^{M}\Pr\{\tau^a_j > \tau^k_j, p_i\},$$

which can be written as

$$D(t) = 1 - (1 - P_N)^M\,, \tag{9.113}$$

where P_N is the probability that a particle is killed before reaching the nucleus (Sect. 9.3.1). Thus the conditional probability that the first carrier, with initial density p_i, arrives alive at the absorbing boundary prior to time t is given by

$$P(t) = \frac{N(t)}{D(t)} = \frac{1 - \left(1 - \int_0^t J(s)\,ds\right)^M}{1 - (1 - P_N)^M} \tag{9.114}$$

and the conditional MFPT $\bar{\tau}_{\text{FIRST}}(M)$ of the first particle to reach the nucleus alive [see (9.110)] is

$$\bar{\tau}_{\text{FIRST}}(M) = \int_0^\infty \frac{\left(1 - \int_0^t J(s)\,ds\right)^M - \left(1 - \int_0^\infty J(s)\,ds\right)^M}{1 - (1 - P_N)^M}\,dt. \tag{9.115}$$

The leading term in a small k expansion of $\bar{\tau}_{\text{FIRST}}(M)$ can be found from the long-time tail of the density $p(\boldsymbol{x}, t)$,

$$p(\boldsymbol{x}, t) \approx p_0(\boldsymbol{x})e^{-\lambda_0 t}, \tag{9.116}$$

where $p_0(x)$ is the normalized first eigenfunction of the Fokker–Planck operator and λ_0 is its principal eigenvalue,

$$-\lambda_0 p_0(\boldsymbol{x}) = D\Delta p_0(\boldsymbol{x}) - \nabla[b(\boldsymbol{x})p_0(\boldsymbol{x})] - k(\boldsymbol{x})p_0(\boldsymbol{x}). \tag{9.117}$$

Integrating (9.117) over Ω, we find the flux of the normalized principal eigenfunction

$$J(t) = e^{-\lambda_0 t}\left(\lambda_0 - \int_\Omega k(\boldsymbol{x})p_0(\boldsymbol{x})\,d\boldsymbol{x}\right),$$

which in view of $\lambda_0 = \bar{\tau}_N^{-1}$ for $k \ll 1$ (see Schuss et al. 2007) and (6.61), can be written as

$$J(t) \approx \frac{e^{-t/\bar{\tau}_N}}{\bar{\tau}_N}\left(1 - \int_\Omega k(\boldsymbol{x})\tilde{p}(\boldsymbol{x})\,d\boldsymbol{x}\right) = \frac{P_N}{\bar{\tau}_N}e^{-t/\bar{\tau}_N}. \tag{9.118}$$

Equation (9.118) gives in (9.115) the small $k(\boldsymbol{x})$ approximation

$$\begin{aligned}\bar{\tau}_{\text{FIRST}}(M) &\approx \int_0^\infty \frac{\left(1 - P_N\left(1 - e^{-t/\bar{\tau}_N}\right)\right)^M - (1 - P_N)^M}{1 - (1 - P_N)^M}\,dt\\ &= \frac{\bar{\tau}_N(\xi)}{1 - (1 - P_N)}\sum_{k=0}^{M-1}\left[(1 - P_N)^k - (1 - P_N)^M\right]\frac{1}{M - k}.\end{aligned}$$

Figure 9.9(upper) compares the time decay with Brownian simulations and confirms the validity of the long time asymptotic approximation. Figure 9.9(lower) shows the plot of $\bar{\tau}_{\text{FIRST}}(M)/\bar{\tau}_N$ vs $\xi = 1 - P_N$, which is an increasing function of ξ. As the number of carriers that reach a nuclear pore alive decreases, the MFPT of the first survivor increases. Furthermore, for small ξ, the leading order term of the expansion of $\bar{\tau}_{\text{FIRST}}(M)$ for large M is given by

$$\bar{\tau}_{\text{FIRST}}(M) = \frac{\bar{\tau}_N}{M}(1 + o(1)) \quad \text{for } M \gg 1, \tag{9.119}$$

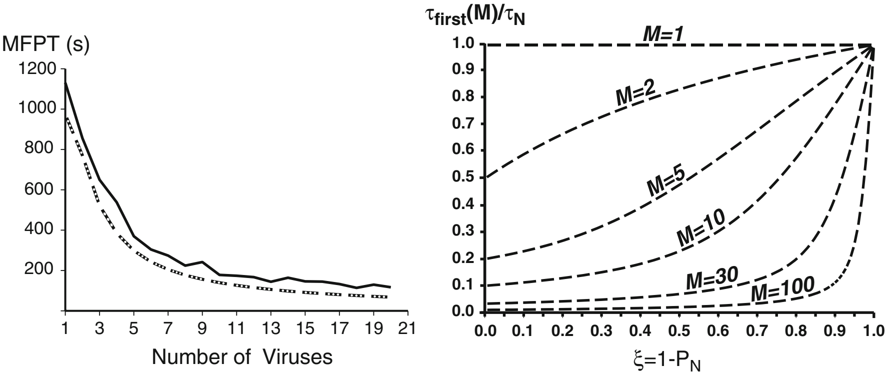

Fig. 9.9 *Left*: MFPT of the first virus to a nuclear pore for 300 simulated Brownian trajectories (*solid line*). The geometry is given by $R = 20\,\mu\text{m}$; $\delta = 4\,\mu\text{m}$; $\eta = \pi\delta/12 = 1.05\,\mu\text{m}$; $D = 1.3\,\mu\text{m}^2\text{s}^{-1}$; $n = 1$ and $B = 0.2\,\mu\text{m}\,\text{s}^{-1}$. *Right*: normalized MFPT of the first virus to the MFPT of a single virus, as a function of the probability $\xi = 1 - P_{300}$ to be killed before reaching the nucleus. Here $\bar{\tau}_{\text{FIRST}} = \bar{\tau}_{300}/300$ for $\xi \to 0$ with $\bar{\tau}_{300} = 974\,\text{s}$. When almost all DNA carriers are degraded $\bar{\tau}_{\text{FIRST}} \to \bar{\tau}_{300}$

whereas when ξ tends to 1, that is, when almost all carriers are killed before reaching nuclear pores, the following approximation holds,

$$\bar{\tau}_{\text{FIRST}}(M) \approx \bar{\tau}_N. \tag{9.120}$$

Note that $\bar{\tau}_N$ is a function of ξ. The general expression for $\bar{\tau}_{\text{FIRST}}(M)$ as a function of ξ and M is still unknown [see a general discussion in Lagache et al. (2009b)].

9.5 Model of the Endosomal Step of Viral Infection

Another step of viral trafficking inside the cytoplasm is that of endosomal trafficking. Indeed, once a virus enters an endosome, it has to escape into the cytoplasm before to be degraded by lysosomes. Although the exact pathways leading to endosomal escape are not fully elucidated, they are a limiting step. Most viruses possess efficient endosomolytic proteins that allow them to disrupt the endosomal membrane. This is the case for VP1 penetration protein of the AAV or the influenza HA. The biophysical mechanism leading to endosomal membrane destabilization and concomitant release for synthetic vectors is still poorly understood. However, in both cases, acidification of the endosome is needed for triggering endosomal escape. For viruses, protons or low pH-activated proteases bind viral endosomolytic proteins, triggering their conformational change into a fusogenic state.

Models aimed at estimating the residence time of a viral particle inside an endosomal compartment are based on the evaluation of the accumulated discrete proton binding events, leading to the conformational change of hemagglutinin proteins (HAs). These models, for both enveloped and non-enveloped viruses, consist of two steps. In the first step, the concentration of protons is fixed and the mean time for protons to bind to fundamental protein-binding sites until a threshold is reached is calculated from a Markovian jump process model by asymptotic methods. After the threshold is reached, a conformational change into a fusogenic state is triggered. In the second step, the dynamics of endosomal escape is modeled by coupling the pH-dependent conformational change of glycoproteins with proton influx rate. The impact of the size of the endosome on the escape kinetics and pH can be mathematically predicted. This approach reconciles different experimental observations: while a virus can escape a small endosome (radius of 80 nm) in the cell periphery at a pH of about 6 in about 10 min, it can also be routed towards the nuclear periphery, where the escape from larger endosomes (radius of 400 nm) is rapid (less than 1 min) at pH = 5 (Lagache et al. 2012).

9.5.1 *Model of the Conformational Change of Hemagglutinin Proteins for the Influenza Virus*

The underlying assumption in the Markovian model of the conformational rate of change of a single HA glycoprotein for a given proton concentration c and n_s HA binding sites is that the protein changes conformation instantaneously when the number of bound sites reaches a critical threshold $n_{\mathrm{crit}} \leq n_s$ (Lagache et al. 2012).

The number of protonated sites $X(t)$ at time t is modeled as a Markovian jump processes (Schuss 2010b) that can increase by 1 with probability $r(X)\Delta t + o(\Delta t)$ when a proton binds to a free site in the time interval $(t, t + \Delta t)$, decreases with probability $l(X)\Delta t + o(\Delta t)$ when a proton unbinds, or remain unchanged with probability $1 - l(X)\Delta t - r(X)\Delta t + ø(\Delta t)$. Setting $\varepsilon = 1/n_s$ and scaling $x(t) = \varepsilon X(t)$, the scaled jump size becomes $\Delta x(t) = x(t + \Delta t) - x(t)$ and the transition probabilities are given by

$$
\begin{aligned}
\Pr\{\Delta x(t) = \varepsilon \,|\, x(t) = x\} &= r(x)\Delta t + o(\Delta t),\\
\Pr\{\Delta x(t) = -\varepsilon \,|\, x(t) = x\} &= l(x)\Delta t + o(\Delta t),\\
\Pr\{\Delta x(t) = 0 \,|\, x(t) = x\} &= [1 - r(x) - l(x)]\,\Delta t + o(\Delta t).
\end{aligned}
$$

For a fixed proton concentration c, the transition probability density function $p(y, t \,|\, x)$ is the solution of the master equation

$$
\begin{aligned}
p(y, t + \Delta t \,|\, x) = & \, p(y - \varepsilon, t \,|\, x) r(y - \varepsilon)\Delta t + p(y + \varepsilon, t \,|\, x) l(y + \varepsilon)\Delta t\\
& + p(y, t \,|\, x)[1 - r(y)\Delta t - l(y)\Delta t] + o(\Delta t),
\end{aligned}
$$

which reduces in the limit $\Delta t \to 0$ to the forward Kolmogorov equation

$$\begin{aligned}\frac{\partial p(y,t\,|\,x)}{\partial t} =& \, p(y-\varepsilon,t\,|\,x)r(y-\varepsilon)+p(y+\varepsilon,t\,|\,x)l(y+\varepsilon)\\ &-p(y,t\,|\,x)[r(y)+l(y)] = L_y p(y,t\,|\,x).\end{aligned} \tag{9.121}$$

The jump moments are given by

$$m_n(y) = \varepsilon^n[r(y)+(-1)^n l(y)]. \tag{9.122}$$

Assume that there is a point $0 < x_0 < x_{\text{crit}} = n_{\text{crit}}/n_s$ such that

$$(y-x_0)m_1(y) < 0 \quad \text{for } y \neq x_0. \tag{9.123}$$

The first time τ (a protein is lysed) is quantified by filling up the number of bound to a critical threshold $x_{\text{crit}} = n_{\text{crit}}/n_s$. It is the first passage time of the (scaled) number of bound protons $x(t)$ to reach the level x_{crit}. The MFPT $\bar{\tau}(x)$ is defined as the conditional expectation

$$\bar{\tau}(x) = \mathbb{E}[\tau\,|\,x(0)=x], \tag{9.124}$$

which is the solution of the boundary value problem

$$\begin{aligned}&L_x\bar{\tau}(x) = -1 \quad \text{for } 0 < x < x_{\text{crit}}\\ &\bar{\tau}(x_{\text{crit}}) = 0, \qquad \frac{\partial \bar{\tau}(0)}{\partial x} = 0,\end{aligned}$$

where L_x is the backward Kolmogorov operator, adjoint to L_y.

An asymptotic expansion of $\bar{\tau}(x)$ for $\varepsilon \ll 1$ is given in Schuss (2010b, Example 9.1) with the leading term

$$\begin{aligned}\bar{\tau}(x) &\approx C(\varepsilon)\left(1-\exp\left\{-\alpha\frac{x_{\text{crit}}-x}{\varepsilon}\right\}\right)\\ &= C(\varepsilon)\left(1-\left(\frac{l(x_{\text{crit}})}{r(x_{\text{crit}})}\right)^{-(x_{\text{crit}}-x)/\varepsilon}\right),\end{aligned} \tag{9.125}$$

where

$$\alpha = \log\left(\frac{l(x_{\text{crit}})}{r(x_{\text{crit}})}\right)$$

is the positive solution of the eikonal equation (Knessl et al. 1984a, Eq. (3.22))

$$e^{\alpha} + \left(\frac{l(x_{\text{crit}})}{r(x_{\text{crit}})}\right)e^{-\alpha} = 1 + \left(\frac{l(x_{\text{crit}})}{r(x_{\text{crit}})}\right). \tag{9.126}$$

Note that outside a boundary layer of width $O(\varepsilon)$ near x_{crit} the expected activation time is the constant $C(\varepsilon)$. We abbreviate therefore $\bar{\tau}(x) = \bar{\tau}$. The constant $C(\varepsilon)$, which increases to infinity as $\varepsilon \to 0$ to 0, is given by

$$C(\varepsilon) \approx \frac{\pi K(\varepsilon)}{\sqrt{\varepsilon r(x_0)[l'(x_0) - r'(x_0)]}}$$

where

$$K(\varepsilon) = \frac{1}{\frac{l(0) - r(0)}{\sqrt{r(0)l(0)}}\phi(0) + \frac{l\,(x_{\text{crit}}, c) - r\,(x_{\text{crit}}, c)}{\sqrt{r(x_{\text{crit}})l(x_{\text{crit}})}}\phi(x_{\text{crit}})}$$

and

$$\phi(x) = \exp\left\{-\frac{1}{\varepsilon}\int_{x_0}^{x} \log\left(\frac{l(s)}{r(s)}\right) ds\right\}. \tag{9.127}$$

When all binding sites are identical and in the absence of any molecular cooperativity, the forward rate $r(x)$ is proportional to the number of free binding sites and to the glycoprotein concentration c in the endosome and the backward rate $l(x)$ is proportional to the number of bound sites, leading to

$$r(x) = k_1(1-x)n_s c, \quad l(x) = k_{-1}xn_s, \tag{9.128}$$

where k_1 and k_{-1} are the forward and backward rate constants, respectively. In this case, the expected number of bound proteases for a given concentration c is

$$x_0 = \frac{1}{1+\alpha_c}, \tag{9.129}$$

where

$$\alpha_c = \frac{k_{-1}}{ck_1}. \tag{9.130}$$

An explicit expression for $\phi(x)$ is given in this case by

$$\begin{aligned}\int_{x_0}^{x} \log\left(\frac{l(s)}{r(s)}\right) ds &= \int_{x_0}^{x} \log\left(\frac{\alpha_c s}{1-s}\right) ds = F\,(x) - F(x_0)\\ &= F\,(x) - F\left(\frac{1}{1+\alpha_c}\right),\end{aligned} \tag{9.131}$$

where

$$F(x) = x\log(\alpha_c) + x\log\left(\frac{x}{1-x}\right) + \log(1-x) \ \text{ for } \ 0 < x < 1. \tag{9.132}$$

Substituting (9.131) in (9.127), we obtain

$$\phi(x_{\text{crit}}) = \exp\left\{-\frac{1}{\varepsilon}\left(F(x_{\text{crit}}) - F\left(\frac{1}{1+\alpha_c}\right)\right)\right\} \frac{\sqrt{\dfrac{\alpha_c x_{\text{crit}}}{1-x_{\text{crit}}}}}{\left(\dfrac{\alpha_c x_{\text{crit}}}{1-x_{\text{crit}}}-1\right)}. \tag{9.133}$$

Using all the above in (9.125), we obtain the explicit formula for the mean activation time (9.128)

$$\begin{aligned}\bar{\tau} \sim {} & \frac{\sqrt{2\pi\varepsilon}\left(1-\dfrac{k_{-1}}{ck_1}\right)\sqrt{1-x_{\text{crit}}}}{k_1 c\sqrt{x_{\text{crit}}}\left(1+\dfrac{k_{-1}}{ck_1}\right)}\left(\frac{\dfrac{k_{-1}}{ck_1}x_{\text{crit}}}{1-x_{\text{crit}}}-1\right) \\ & \times \exp\left\{\frac{1}{\varepsilon}\left[F\left(x_{\text{crit}}\right) - F\left(\frac{1}{1+\dfrac{k_{-1}}{ck_1}}\right)\right]\right\},\end{aligned} \tag{9.134}$$

where

$$F(x) = x\log\left(\frac{k_{-1}}{ck_1}\right) + x\log\left(\frac{x}{1-x}\right) + \log(1-x) \quad \text{for} \quad 0 < x < 1. \tag{9.135}$$

The explicit formula (9.134) expresses the dependence of the expected time for conformational change $\bar{\tau}$ on the protease concentration c and the binding number of binding sites of a single penetration protein. The reciprocal of (9.134) is the rate of conformational change, which has been measured experimentally for several viruses, such as influenza (Krumbiegel et al. 1994).

Specializing the above analysis to the case of influenza the parameters used in Lagache and Holcman (2015) are

$$r(x) = Kcn_s(1-x), \quad l(x) = Kn_s(1-x)10^{-(3(1-x)+4)}, \tag{9.136}$$

the number of binding sites is $n_s = 9$ (Krumbiegel et al. 1994) at concentration c of free protons in the endosome, and K is the binding rate of protons to free binding sites. Here X_0 is the mean number of hemagglutinin (HA1) sites that are additionally protonated for concentrations $c > 10^{-7}\,\text{mol}\,\text{L}^{-1}$, and $0 < x_0 = \varepsilon X_0 < x_{\text{crit}}$ has been obtained by a fitting procedure as (Lagache and Holcman 2015)

$$x_0 = \frac{7}{3} + \frac{\log(c)}{3\log(10)}. \tag{9.137}$$

With the parameters $\varepsilon = 1/n_s$ and $x_{\text{crit}} = n_{\text{crit}}/n_s$ formula (9.134) reduces to

$$\bar{\tau} = \frac{\sqrt{6\pi}\exp\left\{n_s\left[F\left(\frac{n_{\text{crit}}}{n_s}\right) - F\left(\frac{7+\log_{10} c}{3}\right)\right]\right\}}{K\sqrt{cn_s \ln 10}\,(4+\log_{10} c)\left(c10^{7/2-3n}\mathbf{crit}^{/2n_s} - 10^{3n}\mathbf{crit}^{/2n_s-7/2}\right)}, \quad (9.138)$$

where F is given in (9.135). The rate of conformational change $\kappa(\text{pH}) = \bar{\tau}^{-1}$ has been measured for various pH values, $\kappa(4.9) = 5.78\,\text{s}^{-1}$, $\kappa(5.1) = 0.12\,\text{s}^{-1}$, $\ldots$, $\kappa(5.6) = 0.017\,\text{s}^{-1}$ (Krumbiegel et al. 1994). Using a least square method to approximate the data, the value of the critical threshold according to Lagache and Holcman (2015) is $n_{\text{crit}} \approx 6$ and the forward rate is $K \approx 7.5 \times 10^3\,\text{L}\,\text{mol}^{-1}\text{s}^{-1}$. For these values (9.138) gives the theoretical mean time to conformational change $\bar{\tau}$ that in comparison with the experimental data of Krumbiegel et al. (1994) gives $K \approx 7.5 \times 10^3\,\text{L}\,\text{mol}^{-1}\text{s}^{-1}$ and $x_{\text{crit}} \approx 0.7$ (Lagache and Holcman 2015). The theoretical curve $\bar{\tau}$ vs c describes the entire range of the experimental data set of the influenza hemagglutinin, confirming the validity of the present approach. Furthermore, comparing the mean proton binding time $\bar{\tau} = 1/(Kc)$ with the mean time $\bar{\tau}_d$ for a proton to find a binding site by diffusion, the value $\bar{\tau}_d/\bar{\tau} \approx 10^{-4}$ is obtained, suggesting that the HA binding time is dominated by a high activation barrier, which guarantees the stability of the conformational change. That is, it cannot be easily triggered randomly (see Krumbiegel et al. 1994, Table 2). The theory predicts that the HA conformational changes occurs when about $x_{\text{crit}} n_s \approx 6$ HA binding sites are protonated.

Modeling the Endosomal Acidification Escape of the Influenza Virus

In this final section, we present a model of endosomal acidification for the influenza virus based on protons entering through V-ATPase pumps located in the endosomal membrane. This proton entry leads to a pH decrease and the conformational change of HAs into a fusogenic state (Huang et al. 2002). This process characterizes endosomal maturation. After fusion of the viral and endosomal membrane, the influenza genes can be released inside the cytoplasm during a certain time that depends on the proton influx λt, where the rate λ is proportional to the number of pumps and thus to the endosomal surface (Lagache and Holcman 2015). The rate λ may, however, increase as the endosome matures and increases its size by fusion of early endocytic vesicles into larger compartments. As protons accumulate into an endosome, they can bind to influenza HAs, triggering their change of conformation when exactly 6 sites are protonated.

Another step of endosomal escape consists in the enlargement of the fusion pore, that should rely on the activation of additional HA located nearby the contact zone, between the virus and the endosome membranes. In previous models (Lagache et al. 2012), this cooperative mechanism between activated HAs nearby the contact zone was accounted for by considering that genes are released in the cytoplasm when the total number of activated HAs among the viral envelope reaches a threshold $0 \leq T \leq N_{\mathrm{HA}}$, where $N_{\mathrm{HA}} = 400$ is the total number of HAs covering a single virus. Consequently, the escape release time τ_e is defined by

$$\tau_e = \inf\{t | \mathrm{HA}_6(t) \geq T\}, \tag{9.139}$$

where $\mathrm{HA}_0(t), \mathrm{HA}_1(t), \ldots, \mathrm{HA}_6(t)$ are the number of HAs that have bound $0, 1, \ldots, 6$ protons at time t. The acidification time course of an endosome containing an influenza virus is related to the number of free protons located in the endosome by $P(t) = \mathcal{N} V_0 c(t)$, where $c(t)$ is the associated endosomal concentration at time t. Using the on-rate of a proton to a HA free binding site,

$$\tilde{r}(x) = r(x, P(t)) / P(t) = K n_s (1 - x)/(\mathcal{N} V) \tag{9.140}$$

and the off-rate $l(x)$ (9.136), the kinetics equations are

$$\begin{aligned}
\mathrm{HA}_0 + P &\underset{l(1/n_s)}{\overset{\tilde{r}(0/n_s)}{\rightleftharpoons}} \mathrm{HA}_1 \\
\mathrm{HA}_1 + P &\underset{l(2/n_s)}{\overset{\tilde{r}(1/n_s)}{\rightleftharpoons}} \mathrm{HA}_2 \\
& \qquad \cdots \\
\mathrm{HA}_5 + P &\xrightarrow{\tilde{r}(5/n_s)} \mathrm{HA}_6
\end{aligned} \tag{9.141}$$

and the associated mass action law leads to the following reduced differential equations

$$\begin{aligned}
\frac{dP(t)}{dt} &= \lambda - \sum_{i=0}^{5} \tilde{r}\left(\frac{i}{n_s}\right) P(t)\mathrm{HA}_i(t) + \sum_{i=1}^{5} l\left(\frac{i}{n_s}\right) \mathrm{HA}_i(t) \\
\frac{d\mathrm{HA}_0(t)}{dt} &= -\tilde{r}\left(\frac{0}{n_s}\right) P(t)\mathrm{HA}_0(t) + l\left(\frac{1}{n_s}\right) \mathrm{HA}_1(t) \\
\frac{d\mathrm{HA}_1(t)}{dt} &= \left(\tilde{r}\left(\frac{0}{n_s}\right) \mathrm{HA}_0(t) - \tilde{r}\left(\frac{1}{n_s}\right) \mathrm{HA}_1(t)\right) P(t) + l\left(\frac{2}{n_s}\right) \mathrm{HA}_2(t) \\
&\quad - l\left(\frac{1}{n_s}\right) \mathrm{HA}_1(t) \\
\cdots \\
\frac{d\mathrm{HA}_6(t)}{dt} &= \tilde{r}\left(\frac{5}{n_s}\right) \mathrm{HA}_5(t) P(t),
\end{aligned} \tag{9.142}$$

where the proton influx rate in the endosome is a linear function of time λt. The initial conditions ($t = 0$) are a neutral medium pH = 7 and $P_0 = \mathcal{N} V_0 10^{-7} \approx 1$, $\mathrm{HA}_0(t = 0) = N_{\mathrm{HA}}$ and $\mathrm{HA}_i(t = 0) = 0$ for $1 \leq i \leq 6$.

The two critical unknown parameters of the model are the protons influx rate λ and the mean number T of activated HAs, needed for the large fusion pore formation allowing gene release inside the cytoplasm. These parameters can be obtained by solving numerically the system of Eq. (9.142), and by comparing the time τ_e (formula (9.139)) with the experimental mean escape time ($\approx$10 min) obtained for the virus-endosome fusion in Hela cells (Sakai et al. 2006): it was found in Lagache and Holcman (2015) that

$$T \approx 50\,\% N_{\mathrm{HA}} = 200, \text{ and } \lambda \approx 3\,\mathrm{s}^{-1}. \tag{9.143}$$

The details modeling of these two steps were reviewed in Amoruso et al. (2011). It should be noted, in conclusion, that much of the field of physical virology remains to be explored and open questions abound. They include the following questions: what is the mode of vesicular delivery to final locations? Is this search random, as in the NET theory, or are vesicles delivered to specific locations using a Zip-address that needs to be identified? How do viral DNA find their destination site inside the nucleus? Many of these questions do not have at this time any answers that are based on classical physical principles. Answering these questions requires more advanced modeling, analysis, and simulations combined with data analysis.

9.6 Annotations

Mathematical and physical models of the early steps of viral infection are constructed for the purpose of predicting and quantifying infectivity and the success of gene delivery (Holcman 2007; Lagache and Holcman 2008a,b; Amoruso et al. 2011; Lagache et al. 2009a). Principles toward optimization of delivery of virus and exploring the high-dimensional parameter space are discussed in Lagache et al. (2012). Tuning of the pH-sensitivity of fusogenic glycoproteins is discussed in Rachakonda et al. (2007). Escape efficacy of the vector is discussed in Sodeik (2000).

Vesicular and viral motions that alternate intermittently between periods of free diffusion and directed motion along microtubules (MTs) are discussed in Greber and Way (2006). Such viral trajectories have been recently monitored by using new imaging techniques in vivo (Seisenberger et al. 2001). The MFPT of a virus to a nuclear pore was calculated in Holcman (2007). The effective drifts of viral motion have been derived for various geometries in Lagache and Holcman (2008a,b). The adeno-associated virus and the influenza hemagglutinin (HA) have been discussed in Farr et al. (2005) and Huang et al. (2002). Models aimed at estimating the residence time of a viral particle inside an endosomal compartment are considered in Lagache et al. (2012). The key to the calculation of the MFPT of the Markovian jump process model is the method of Knessl et al. (1984a,b). The details modeling of two key steps in the viral release were reviewed in Amoruso et al. (2011).

Asymptotic expressions for the probability of trajectories that are terminated at $\partial\Omega_a$, given in (9.37), and the mean arrival time $\mathbb{E}\tau$ of a virus vector to one of the n small nuclear pores $\partial\Omega_a$, were derived in Holcman (2007) and Lagache et al. (2009b) by the narrow escape methodology.

The endosomal step of viral infection studied in Lagache et al. (2012) aimed to estimate the residence time of a viral particle inside an endosomal compartment. Conformational change kinetics were estimated in Krumbiegel et al. (1994). In Lagache and Holcman (2015), it was predicted that the size of the endosome drastically impacts both the escape kinetics and pH, which reconciles different experimental observations. Thus, while a virus can escape a small endosome (radius of 80 nm) in the cell periphery at pH about 6 in about 10 min (Sakai et al. 2006), it can also be routed towards the nuclear periphery, where escape from larger endosomes (radius of 400 nm) is rapid (less than 1 min) at pH = 5 (Lakadamyali et al. 2006).

Bibliography

Abe, A., A. Miyanohara, and T. Friedmann (1998), “Enhanced gene transfer with fusogenic liposomes containing vesicular stomatitis virus G glycoprotein,” *J. Virol.* **72** pp.6159–6163.

Abramowitz, M. and I. Stegun (1972), *Handbook of Mathematical Functions with Formulas, Graphs, and Mathematical Tables*, Dover Publications, NY.

Aboud, S., M. Saraniti , and R.S. Eisenberg (2003), “Issues in modeling ion transport in biological channels: self-consistent particle-based simulations,” *Journal of Computational Electronics*, **2**, 239–243.

Adesnik, H., R.A. Nicoll, P.M. England (2005), “Photoinactivation of native AMPA receptors reveals their real-time trafficking.” *Neuron* **48** (6), pp.977–985.

A. Ajdari, *Europhys. Lett.* **31**, 69 (1995).

Alberts, P., R. Rudge, T. Irinopoulou, L. Danglot, C. Gauthier-Rouviere, and T. Galli, 2006. Cdc42 and Actin Control Polarized Expression of TI-VAMP Vesicles to Neuronal Growth Cones and Their Fusion with the Plasma Membrane. *Mol Biol Cell* 17:1194–203.

Alberts, P., R. Rudge, I. Hinners, A. Muzerelle, S. MartinezArca, T. Irinopoulou, V. Marthiens, S. Tooze, F. Rathjen, P. Gaspar, and T. Galli, 2003. “Cross talk between tetanus neurotoxin-insensitive vesicle- associated membrane protein-mediated transport and L1- mediated adhesion.” *Mol Biol Cell* 14:4207–4220.

Amoruso, C., T. Lagache, and D. Holcman (2011), “Modeling the early steps of cytoplasmic trafficking in viral infection and gene delivery,” *SIAM. J. Appl. Math.* **71** (6), pp.2334–2358.

Ashby, M.C., S.R. Maier, A. Nishimune, J.M. Henley (2006), “Lateral diffusion drives constitutive exchange of AMPA receptors at dendritic spines and is regulated by spine morphology.” *J. Neurosci.* **26** 7046.

Aubin, T. *Some Nonlinear Problems in Riemannian Geometry*, Springer Verlag, NY 1998.

Bénichou O., M. Coppey, M. Moreau, P.H. Suet, and R. Voituriez (2005), “A stochastic model for intermittent search strategies,” *J. Phys.-Cond. Mat.* **17** (49), pp.4275–4286.

Bénichou, O. and R. Voituriez (2008), “Narrow-escape time problem: Time needed for a particle to exit a confining domain through a small window,” *Phys. Rev. Lett.*, **100**, 168105.

Berezhkovskii, A. M. and Makhnovskii, Y. A. and Monine, M. I. and Zitserman, V. Yu. and Shvartsman, S. Y., Boundary homogenization for trapping by patchy surfaces, *J. Chem. Phys.* 2004, **121**,22, 11390–94

Berezhkovskii, A.M., A.V. Barzykin, and V.Yu. Zitserman (2009), “Escape from cavity through narrow tunnel,” *J. Chem. Phys.*, **130**, 245104.

Berezhkovskii, A.M. and A.V. Barzykin (2012), “Search for a small hole in a cavity wall by intermittent bulk and surface diffusion,” *J. Chem. Phys.* **136** (5):054115.

Berg, H.C. and E.M. Purcell (1977), “Physics of chemoreception”, *Biophys. J.* **20**, pp.193–219.

D. Holcman, Z. Schuss, *Stochastic Narrow Escape in Molecular and Cellular Biology*, DOI 10.1007/978-1-4939-3103-3

Bloodgood, B.L., B.L. Sabatini (2005), "Neuronal activity regulates diffusion across the neck of dendritic spines." *Science* **310** (5749), pp.866–869.

Biess, A., E. Korkotian, D. Holcman (2007), "Diffusion in a dendritic spine: the role of geometry," *Phys. Rev. E, Stat. Nonlin. Soft Matter Phys.*, **76** (1), 021922.

Biess, A., E. Korkotian, D. Holcman (2011), "Barriers to diffusion in dendrites and estimation of calcium spread following synaptic inputs," *PloS Computational Biology* **7** (10), e1002182.

Boda, D., W. Nonner, M. Valisko, D. Henderson, R.S. Eisenberg, and D. Gillespie (2007), "Steric selectivity in na channels arising from protein polarization and mobile side chains," *Biophysical Journal*, **93**, 1960–1980.

Borgdorff, A.J. and D. Choquet (2002), "Regulation of AMPA receptor lateral movements," *Nature* **417**, pp.649–653.

Bouquet, C., M. Ravaille-Veron, F. Propst, and F. Nothias, (2007). MAP1B coordinate microtubule and actin filament remodeling in adult mouse Schwann cell tips and DRG neuron growth cones. *Mol Cell Neurosci* 36:235–47.

Bourne, J.N., K.M. Harris (2008), "Balancing structure and function at hippocampal dendritic spines," *Annu. Rev. Neurosci.*, **31**, 47–67.

Bredt, D.S., R.A. Nicoll (2003), "AMPA receptor trafficking at excitatory synapses." *Neuron* **40** (2), pp.361–379.

Bressloff, P.C. and B.A. Earnshaw (2009), "A dynamical corral model of protein trafficking in spines." *Biophys. J.* **96**, 1786–1802.

Bressloff, P.C. and J. Newby (2013), "Stochastic models of intracellular transport," *Rev. Mod. Phys.* **85**, pp.135–196.

Burger, M., R.S. Eisenberg, and H.W. Engl (2007), "Inverse problems related to ion channel selectivity," *SIAM J. Appl. Math.*, **67** (4), 960–989.

Burnette, D. T., A. W. Schaefer, L. Ji, G. Danuser, and P. Forscher, (2007). Filopodial actin bundles are not necessary for microtubule advance into the peripheral domain of Aplysia neuronal growth cones. *Nat Cell Biol* 9:1360–9.

Chen, L., D.M. Chetkovich, R.S. Petralia, N.T. Sweeney, Y. Kawasaki, R.J. Wenthold, D.S. Bredt, R.A. Nicoll (2000), "Stargazin regulates synaptic targeting of AMPA receptors by two distinct mechanisms." *Nature* **408** (6815), pp.936–943.

Chen, D., J. Lear, and R.S. Eisenberg (1997), "Permeation through an open channel: Poisson-Nernst-Planck theory of a synthetic ionic channel," *Biophysical Journal*, **72**, 97–116.

Chen, D.P., L. Xu, A. Tripathy, G. Meissner, and R.S. Eisenberg (1999), "Selectivity and permeation in calcium release channel of cardiac muscle: alkali metal ions," *Biophys. J.*, **76**, 1346–1366.

Cheviakov, A., M.J. Ward, and R. Straube (2010), "An asymptotic analysis of the mean first passage time for narrow escape problems: Part II: The sphere," *SIAM Multiscale Modeling and Simulation*, **8** (3), 836–870.

Choquet, D. (2010), "Fast AMPAR trafficking for a high-frequency synaptic transmission," *Eur. J. Neurosci.* **32**, pp.250–260.

D. Coy, M. Vagenbach and J.J. Howard, *Biol. Chem.* **274**, 3667 (1999).

Collin, C., K. Miyaguchi, M. Segal (1997), "Dendritic spine density and LTP induction in cultured hippocampal slices." *J. Neurophysiol.* **77** (3), pp.1614–1623.

Coombs, D., R. Straube, and M. Ward, (2009), "Diffusion on a sphere with localized traps: Mean first passage time, eigenvalue asymptotics, and Fekete points," *SIAM J. Appl. Math.*, **70** (1), pp. 302–332.

Crank, J. (1980), *The Mathematics of Diffusion,* Oxford University Press, 2nd edition.

Dalva, M.B., A.C. McClelland, M.S. Kayser (2007), "Cell adhesion molecules: signalling functions at the synapse." *Nat. Rev. Neurosci.* **8** (3), pp.206–220.

Dao Duc, K. and D. Holcman (2010), "Threshold activation for stochastic chemical reactions in microdomains," *Phys Rev E Stat Nonlin Soft Matter Phys.* **81** (4 Pt 1): 041107.

Dao Duc, K. and D. Holcman (2012), "Using default constraints of the spindle assembly checkpoints to estimate the associate chemical rates," *BMC Biophysics* **5** (1), p.1.

da Silva, J. S., and C. G. Dotti, 2002. Breaking the neuronal sphere: regulation of the actin cytoskeleton in neuritogenesis. Nat Rev Neurosci 3:694–704.

Dauty E. and A.S. Verkman (2005), “Actin cytoskeleton as the principal determinant of size-dependent DNA mobility in cytoplasm: a new barrier for non-viral gene delivery,” *J. Biol. Chem.* **280** pp.7823–7828.

Delgado, M.J., M. Ward, D. Coombs, (2015), “Conditional Mean First Passage Times to Small Traps in a 3-D Domain with a Sticky Boundary: Applications to T Cell Searching Behaviour in Lymph Nodes, *SIAM J. Multiscale Analysis and Simulation* (in press).

Dent, E. W., and F. B. Gertler, 2003. Cytoskeletal dynamics and transport in growth cone motility and axon guidance.Neuron 40:209–27.

Doering, C. (2000), “Stochastic Processes in Physics, Chemistry, and Biology,” *Lecture Notes in Physics*. **557**, p.316.

Doncic, A., E. Ben-Jacob, and E. Barkai (2005), “Evaluating putative mechanisms of the mitotic spindle checkpoint,” *PNAS* **102** (18), pp.6332–6337.

Doncic A., Ben-Jacob E., Einav S., Barkai1N., 2009, Reverse Engineering of the Spindle Assembly Checkpoint *PLoS One* 4(8).

Durand, C.M., J. Perroy, F. Loll, D. Perrais, L. Fagni, T. Bourgeron, M. Montcouquiol, N. Sans (2011), “SHANK3 mutations identified in autism lead to modification of dendritic spine morphology via an actin-dependent mechanism.” *Mol. Psychiatry* **17** (1), pp.71–84.

Dudko. O. K., A. M. Berezhkovskii, and G. H. Weiss. 2004 Rate constant for diffusion-influenced ligand binding to receptors of arbitrary shape on a cell surface. *J. Chem. Phys.* 121: 1562–1565.

Earnshaw, B.A. and P.C. Bressloff (2006), “A biophysical model of AMPA receptor trafficking and its regulation during LTP/LTD.” *J. Neurosci.* **26**, pp.12362–12373.

Edelstein-Keshet, L., and G. B. Ermentrout, 2000. Models for spatial polymerization dynamics of rod-like polymers. J Math Biol 40:64–96.

Edidin, M., S.C. Kuo and M.P. Sheetz (1991), “Lateral movements of membrane glycoproteins restricted by dynamic cytoplasmic barriers,” *Science* **254**, pp.1379–1382.

Eisenberg, R.S. and D. Chen (1993), “Charges, currents, and potentials in ionic channels of one conformation,” *Biophysical Journal*, **64**, 1405–1421.

Eisinger, J., J. Flores and W.P. Petersen (1986), “A milling crowd model for local and long-range obstructed lateral diffusion. Mobility of excimeric probes in the membrane of intact erythrocytes,” *Biophys J.* **49**, pp.987–1001.

Elf, J., G. Li, and X. Xie (2007), “Probing transcription factor dynamics at the single-molecule level in a living cell,” *Science* **316**, 1191.

Fabrikant, V.I. (1989), *Applications of Potential Theory in Mechanics*, Kluwer, Dodrecht.

Fabrikant, V.I. (1991), *Mixed Boundary Value Problems of Potential Theory and Their Applications in Engineering*, Kluwer, Dodrecht.

Farr, G.A., L.G. Zhang, and P. Tattersall (2005), “Parvoviral virions deploy a capsid-tethered lipolytic enzyme to breach the endosomal membrane during cell entry,” *Proc. Natl. Acad. Sci. USA* **102**, pp.17148–17153.

Freche, D., U. Pannasch, N. Rouach, and D. Holcman (2011), “Synapse geometry and receptor dynamics modulate synaptic strength.” *PLoS One* **6** (10): e25122.

D. Fresche, C.Y. Lee N. Rouach, D. Holcman, Synaptic transmission in neurological disorders dissected by a quantitative approach, 5:5, 1–5; Communicative and Integrative Biology (2012).

friedman, A. (2008), *Partial Differential Equations*, Dover Publications, NY.

S. Furini, C. Domene, S. Cavalcanti, “Insights into the sliding movement of the lac repressor nonspecifically bound to DNA”, *J Phys Chem B*, **114** (6): 2238–45. (2010)

Futai, K., M.J. Kim, T. Hashikawa, P. Scheiffele, M. Sheng, and Y. Hayashi, (2007), “Retrograde modulation of presynaptic release probability through signaling mediated by PSD-95-neuroligin.” *Nat. Neurosci.* **10**, pp.186–195.

Futerman, A., and G. Banker, 1996. The economics of neurite outgrowth–the addition of new membrane to growing axons.Trends.Neurosci. 19:144–149.

Gandolfi, A., A. Gerardi, and F. Marchetti (1985), “Diffusion-controlled reactions in two dimensions,” *Acta Applicandae Mathematicae*, **4**, pp.139–159.

Garabedian, P.R. (1964), *Partial Differential Equations*, Wiley, NY.

Gehlen, L.R., S. Nagai, K. Shimada, P. Meister, A. Taddei, S.M. Gasser (2011), "Nuclear geometry and rapid mitosis ensure asymmetric episome segregation in yeast." *Biol.* **21** (1), pp.25–33.

Gebhardt, C. and Cull-Candy, S.G. (2006) Influence of agonist concentration on AMPA and kainate channels in CA1 pyramidal cells in rat hippocampal slices.*J. Physiol. 573*, pp.371–394.

Gennady, M., V. G. Ivan, V. G. Holly, and S. A. Mark, (2006). Analysis of a mesoscopic stochastic model of microtubule dynamic instability.

Gilbarg, D. and N.S. Trudinger, *Elliptic Partial Differential Equations of Second Order*, Springer Verlag, NY 2001.

Gillespie, D.T. (1976). "A General Method for Numerically Simulating the Stochastic Time Evolution of Coupled Chemical Reactions". *J. Comput. Phys.* **22** (4), pp.403–434.

Graham, B. P., K. Lauchlan, and D. R. McLean, (2006). Dynamics of outgrowth in a continuum model of neurite elongation. J Comput Neurosci 20:43–60.

Greber, U.F. and M. Way (2006), "A superhighway to virus infection," *Cell* **124** (4), pp.741–754.

C. Guerrier D. Holcman, The search time to a Ribbon and applications to calcium diffusion near a vesicle at synapses (pre-print).

Grigoriev, I.V., Y.A. Makhnovskii, A.M. Berezhkovskii, and V.Y. Zitserman (2002), "Kinetics of escape through a small hole," *J. Chem. Phys.*, **116**, (22), pp.9574–9577.

Hammele, M., and W. Zimmermann, 2003.Modeling oscillatory microtubule polymerization. Phys Rev E Stat Nonlin Soft Matter Phys 67:021903.

Han, W., Y. K. Ng, D. Axelrod, and E. S. Levitan, 1999. Neuropeptide release by efficient recruitment of diffusing cytoplasmic secretory vesicles. Proc Natl Acad Sci U S A 96:14577–82.

Hänggi, P., P. Talkner, and M. Borkovec (1990), "50 years after Kramers," *Rev. Mod. Phys.*, **62**, pp.251–341.

Harris, K.M., J.K. Stevens (1988), "Dendritic spines of rat cerebellar Purkinje cells: serial electron microscopy with reference to their biophysical characteristics," *J. Neurosci.*, **12**, pp.4455–4469.

Helmholtz, H.L.F. von (1860), "Theorie der Luftschwingungen in Röhren mit offenen Enden", *Crelle Bn.*, **57**, pp.1–72.

Hentschel, H. G., and A. Fine, 1994. Instabilities in Cellular Dendritic Morphogenesis. Physical Review Letters 73:3592–3595.

Hille, B. (2001), *Ionic Channels of Excitable Membranes*, Sinauer Associates Inc. Sunderland, 3-rd edition.

Hille, E. (1976), *Analytic Function Theory*, volume 1. Chelsea Publishing Company, NY.

Holcman, D. and Z. Schuss (2004), "Escape through a small opening: receptor trafficking in a synaptic membrane," *J. Stat. Phys.*, **117** (5/6), 191–230.

Holcman, D., Z. Schuss, and E. Korkotian (2004), "Calcium dynamics in dendritic spines and spine motility," *Biophys J.*, **87**, 81–91.

Holcman, D. and Z. Schuss (2005a), "Stochastic Chemical Reactions in Micro-domains." *Journal of Chemical Physics* **122**, 1.

Holcman, D. and Z. Schuss (2005b), "Stochastic chemical reactions in microdomains", *J. Chem. Phys.* **122**, 11470.

Holcman, D., A. Marchewka and Z. Schuss (2005a), "Survival probability of diffusion with trapping in cellular neurobiology." *Phys. Rev. E, Stat. Nonlin. Soft Matter Phys.* **72** (3) 031910.

Holcman, D. and Z. Schuss (2005c), "Stochastic chemical reactions in microdomains," *J. Chem. Phys.*, **122**, 114710.

Holcman, D., E. Korkotian, and M. Segal (2005b), "Calcium dynamics in dendritic spines, modeling and experiments," *Cell Calcium*, **37**, pp.467–475.

Holcman, D., A. Triller (2006), "Modeling synaptic dynamics and receptor trafficking," *Biophys. J.*, **91** (7), pp.2405–2415.

Holcman, D. (2007), "Modeling viral and DNA trafficking in the cytoplasm of a cell," *J. Stat. Phys.* **127**, pp.471–494.

Holcman, D. and Z. Schuss (2008a), "Diffusion escape through a cluster of small absorbing windows," *J. Phys. A: Math. and Theoretical*, **41**, 155001.

Holcman, D. and Z. Schuss (2008b), “Diffusion through a cluster of small windows and flux regulation in microdomains,” *Phys. Lett. A*, **372**, 3768–3772.

Holcman, D., I. Kupka (2010), “Some questions in computational cellular biology,” *Journal of Fixed Point Theory and Applications*, **7** (1), 67–83.

Holcman, D., N. Hoze, Z. Schuss (2011), “Narrow escape through a funnel and effective diffusion on a crowded membrane,” *Phys. Rev. E*, **84**, 021906.

Holcman, D. and Z. Schuss (2011), “Diffusion laws in dendritic spines,” *The Journal of Mathematical Neuroscience*, **1** (10), pp.1–14.

Holcman, D. and Z. Schuss (2012a), “Brownian motion in dire straits.” *SIAM. J. on Multiscale Modeling and Simulation* **10**(4), pp.1204–1231.

Holcman, D. and Z. Schuss, “Brownian needle in dire straits: Stochastic motion of a rod in very confined narrow domains.” *Phys. Rev. E* **85** 010103(R) (2012b).

Holcman, D. and Z. Schuss (2013a), “The narrow escape problem,” *SIAM Rev.* **56** (2), pp.213–257.

D. Holcman and Z. Schuss, Control of flux by narrow passages and hidden targets in cellular biology, Phys Progr. Report **76** (2013b), no. 7.

D Holcman, Z Schuss, Time scale of diffusion in molecular and cellular biology, Journal of Physics A: Mathematical and Theoretical 47 (17), 173001 (2014).

D Holcman, K. Dao Duc, E. Byrne A. Jones K. Burrage, “Successful delivery of PTEN in the cytoplasm escaping from micro RNA degradation. J. Math Bio., 70 (4), 805–828 (2014).

Hotulainen, P., C.C. Hoogenraad (2010), “Actin in dendritic spines: connecting dynamics to function,” *J. Cell Biol.*, **189** (4), 619–629.

Hoze, N., D. Nair, E. Hosy, C. Sieben, S. Manley, A. Herrmann, J.B. Sibarita, D. Choquet, D. Holcman, (2012) *Proc Natl Acad Sci USA* **109**, pp.17052–17057 (2012)

Hoze, N., D. Holcman, Residence Times of Receptors in Dendritic Spines Analyzed by Stochastic Simulations in Empirical Domains, *Biophys. Journ.* 107 (12), 2999–3008 (2014) (in press).

Huang, Q., R. Opitz, E.W. Knapp, A. Herrmann, “Protonation and stability of the globular domain of influenza virus hemagglutinin.” *Biophys J.*, **82** (2), 1050–1058 (2002).

Huang, B., H. Babcock, X. Zhuang (2010), “Breaking the diffraction barrier: Super-resolution imaging of cells”, *Cell* **143**, pp.1047–1058.

Jackson, J.D. (1975), *Classical Electrodynamics*, 2nd Ed., Wiley, NY.

John, F. *Partial Differential Equations*, Applied Mathematical Sciences, v.1,. Springer, NY, 4th edition 1982.

Kandel, E.R., J.H. Schwartz, T.M. Jessell (2000), *Principles of Neural Science*, McGraw-Hill, New York, 4th edition.

Karlin, S. and H. Taylor, *A Second Course in Stochastic Processes*, Academic Press, New York-London, 1981.

Kellog, O.D. (1954), *Foundations of Potential Theory*, Dover Publications, NY.

Kerchner, G.A. and R.A. Nicoll (2008), “Silent synapses and the emergence of a postsynaptic mechanism for LTP.” *Nat. Rev. Neurosci.* **9** (11), pp.813–825.

S. J. KING AND T. A SCHROER, *Dynactin Increases the Processivity of the Cytoplasmic Dynein Motor*, Nat. Cell Biol., 2 (2000), pp. 20–24.

Knessl, C., M. Mangel, B.J. Matkowsky, and Z. Schuss (1984a), “Solution of Kramers-Moyal equations for problems in chemical physics,” *J. Chem. Phys.* **81**, pp.1285–1293.

Matkowsky, B.J., Z. Schuss, C. Knessl, C. Tier, and M. Mangel (1984), “Asymptotic solution of the Kramers-Moyal equation and first-passage times for Markov jump processes,” *Phys. Rev. A* **29**, pp.3359–3369.

Knessl, C., B.J. Matkowsky, Z. Schuss, and C. Tier (1984b), “An asymptotic theory of large deviations for Markov jump processes,” *SIAM J. Appl. Math.* **45**, pp.1006–1102.

Kochubey, O., X. Lou, and R. Schneggenburger (2011), “Regulation of transmitter release by Ca^{2+} and synaptotagmin: insights from a large cns synapse,” *Trends in Neuroscience* **34** (5).

Korkotian, E., M. Segal (1999), “Release of calcium from stores alters the morphology of dendritic spines in cultured hippocampal neurons.” *Proc. Natl. Acad. Sci. USA.* **96** (21), pp.12068–12072.

Kolokolnikov, T., M. Titcombe and M.J. Ward (2005), “Optimizing the fundamental Neumann eigenvalue for the Laplacian in a domain with small traps,” *European J. Appl. Math.*, **16**, 161–200.

Korkotian, E., D. Holcman and M. Segal (2004), “Dynamic regulation of spine-dendrite coupling in cultured hippocampal neurons,” *Euro. J. of Neuroscience*, **20** (10), pp.2649–2663.

Krumbiegel M., A. Herrmann, R. Blumenthal (1994) Kinetics of the low pH-induced conformational changes and fusogenic activity of influenza hemagglutinin. *Biophys J* 67:2355–2360.

Kusumi, A., C. Nakada, K. Ritchie, K. Murase, K. Suzuki, H. Murakoshi, R.S. Kasai, J. Kondo, T. Fujiwara (2005), “Paradigm shift of the plasma membrane concept from the two-dimensional continuum fluid to the partitioned fluid: high-speed single-molecule tracking of membrane molecules,” *Annu Rev Biophys Biomol Struct.* **34**, pp.351–378.

Kusumi, A., Y. Sako and M. Yamamoto (1993), “Confined lateral diffusion of membrane receptors as studied by single particle tracking (nanovid microscopy). Effects of calcium-induced differentiation in cultured epithelial cells,” *Biophys J.* **65**, pp.2021–2040.

Lagache, T. and D. Holcman (2008a), “Effective motion of a virus trafficking inside a biological cell,” *SIAM. J. Appl. Math.* **68**, pp.1146–1167.

Lagache, T. and D. Holcman (2008b), “Quantifying intermittent transport in cell cytoplasm,” *Phys. Rev. E* **77**, 030901.

Lagache, T., E. Dauty, and D. Holcman (2009a), “Physical principles and models describing intracellular virus particle dynamics,” *Curr. Opin. Microbiol.* **12** (4), pp.439–445.

Lagache, T., E. Dauty, and D. Holcman (2009b), “Quantitative analysis of virus and plasmid trafficking in cells,” *Phys. Rev. E, Stat. Nonlin. Soft Matter Phys.* **79**:011921

Lagache, T., O. Danos, D. Holcman (2012), “Modeling the step of endosomal escape during cell infection by a nonenveloped virus,” *Biophys. J.* **102** (5), pp.980–989.

Lagache, T., D. Holcman, pre-print (2015).

Levin-Zaidman, S., J. Englander, E. Shimoni, A.K. Sharma, K.W. Minton, A. Minsky (2003), *Science* **299** (5604), pp.254–256.

Lieber, A., A. Leis, A. Kushmaro, A. Minsky, O. Medalia (2009), “Chromatin organization and radio resistance in the bacterium gemmata obscuriglobus,” *J. Bacteriol.*, **191** (5), pp.1439–1445.

R. Lipowsky, S. Klumpp and T.M. Nieuwenhuizen, *Phys. Rev. Lett.* **87**, 108101 (2001).

Lurie, A.I. (1964), *Three-Dimensional Problems of the Theory of Elasticity*, Interscience Publishers, NY.

Macheboeuf, P., A.M. Di Guilmi, V. Job, T. Vernet, O. Dideberg, A. Dessen (2005), “Active site restructuring regulates ligand recognition in class A penicillin-binding proteins.” *Proc. Natl. Acad. Sci. U.S.A.* **102** (3), pp.577–582.

MacKinnon, R. (2003), “Potassium channels and the atomic basis of selective ion conduction,” *Nobel Lecture 2003*, http://www.nobelprize.org/nobel_prizes/chemistry/laureates/2003/mackinnon-lecture.html.

G. Malherbe and D.Holcman, “Stochastic modeling of gene activation and application to cell regulation.,” J Theor Biol., vol.271, no.1, p.51;63, 2010.

Malinow, R., R.C. Malenka (2002), “AMPA receptor trafficking and synaptic plasticity.” *Annu. Rev. Neurosci.*

Malinow, R. (2003),“AMPA receptor trafficking and long-term potentiation.” *Philos. Trans. R. Soc. London B, Biol Sci.* **358** (1432), pp.707–714. Review.

Manley, S., J.M. Gillette, G.H. Patterson, H. Shroff, H.F. Hess, E. Betzig, and J. Lippincott-Schwartz (2008), “High-density mapping of single-molecule trajectories with photoactivated localization microscopy.” *Nature Methods* **5**, pp.155–157.

McLean, D. R., and B. P. Graham, 2006. Stability in a mathematical model of neurite elongation. Math Med Biol 23:101–17.

Meraldi, P., V.M. Draviam , P.K. Sorger (2004), “Timing and Checkpoints in the Regulation of Mitotic Progression,” *Developmental Cell*, **7**, pp.45–60.

Miller, K. E., and D. C. Samuels, (1997). The axon as a metabolic compartment: protein degradation, transport, and maximum length of an axon. J Theor Biol 186:373–9.

Milstein AD, Zhou W, Karimzadegan S, Bredt DS, Nicoll RA., TARP subtypes differentially and dose-dependently control synaptic AMPA receptor gating. Neuron. 2007 Sep 20;55(6):905–18.

Minsky, A. (2004), "Information content and complexity in the high-order organization of DNA," *Annu. Rev. Biophys. Biomol. Struct.* **33**, pp.317–342.

Mistry H., D. MacCallum, R. Jackson, M. Chaplain, F. Davidson (2008), "Modeling the temporal evolution of the spindle assembly checkpoint and role of Aurora B kinase." *PNAS* **105** (51).

Nadler, B., T. Naeh, and Z. Schuss (2002), "The stationary arrival process of diffusing particles from a continuum to an absorbing boundary is Poissonian," *SIAM J. Appl. Math.*, **62** (2), pp.433–447.

F. Nedelec, T. Surrey and A.C. Maggs, Phys Rev Lett. **86**, 3192 (2001).

Newpher, T.M., M.D. Ehlers (2009), "Spine microdomains for postsynaptic signaling and plasticity," *Trends Cell Biol.*, **5**, pp.218–227.

Nilsson, J., M. Yekezare, J. Minshull, J. Pines (2008), "The APC/C maintains the spindle assembly checkpoint by targeting Cdc20 for destruction," *Nature Cell Biology* **10** (12), pp.1411–1420.

Nishimura, T., Y. Fukata, K. Kato, T. Yamaguchi, Y. Matsuura, H. Kamiguchi, and K. Kaibuchi, 2003. "CRMP-2 regulates polarized Numb-mediated endocytosis for axon growth." *Nat. Cell Biol.* **5**, pp.819–826.

S. Ozawa, Proc. Japan. Acad. **56**, 459 (1980).

Oshanin G, Tamm M, Vasilyev O., Narrow-escape times for diffusion in microdomains with a particle-surface affinity: mean-field results. J Chem Phys. 2010 Jun 21;132(23):235101

Papa, M., M. Segal (1996), "Morphological plasticity in dendritic spines of cultured hippocampal neurons." *Neuroscience* **71** (4), pp.1005–1011.

Pfenninger, K. H., L. Laurino, D. Peretti, X. Wang, S. Rosso, G. Morfini, A. Caceres, and S. Quiroga, 2003. Regulation of membrane expansion at the nerve growth cone. J Cell Sci 116:1209–17.

Pontryagin, L.S., A.A. Andronov, and A.A. Vitt (1933), "On the statistical treatment of dynamical systems," *J. Theor. Exper. Phys. (Russian)* **3**, pp.165–180. English translation in *Noise in Nonlinear Dynamics* **1**, pp.329–340.

Popov, I.Yu. (1992), "Extension theory and localization of resonances for domains of trap type," *Math. USSR Sbornik*, **71** (1), pp.209–234.

Prochiantz, A., 1995. Neuronal polarity: giving neurons heads and tails. Neuron 15:743–746.

Rachakonda, P.S., M. Veit, T. Korte, K. Ludwig, C. Böttcher, Q. Huang, M.F.G. Schmidt, and A. Herrmann (2007), "The relevance of salt bridges for the stability of the influenza virus hemagglutinin," *FASEB J.* **21**, pp.995–1002.

Ramón y Cajal, S. (1909), "Les nouvelles idées sur la structure du système nerveux chez l'homme et chez les vertébrés," Transl. L. Azouly, Malaine, Paris, France. "New ideas on the structure of the nervous system of man and vertebrates," Transl. N. & N.L. Swanson, MIT Press, Cambridge, MA 1991.

Rayleigh, J.W.S. (1945), *The Theory of Sound*, volume 2. Dover, NY, 2nd edition.

S. REDNER, *A Guide to First Passage Processes*, Cambridge University Press, Cambridge, Massachussets, 2001.

Reingruber, J. and D. Holcman (2009), "The Gated Narrow Escape Time for Molecular Signaling," *Phys. Rev. Lett.* **103**, 148102.

Reingruber, J., E. Abad, and D. Holcman (2009), "Narrow escape time to a structured target located at the boundary of a microdomain," *J. Chem. Phys.* **130**, 094909.

Reingruber, J. and D. Holcman (2010), "Narrow escape for a stochastically gated Brownian ligand," *J. Phys. Condens. Matter* **22** (6):065103.

Reingruber, J. and D. Holcman (2011a), "Transcription factor search for a DNA promoter in a three-state model," *Physical Review E* **84** (2), 020901.

Reingruber, J. and D. Holcman (2011b), "The narrow escape problem in a flat cylindrical microdomain with application to diffusion in the synaptic cleft." *Multiscale Model. Simul.* **9** (2), pp.793–816.

Renner, M., D. Choquet and A. Triller (2009), "Control of the postsynaptic membrane viscosity," *J. Neurosci.* **29** (9), pp.2926–2637.

Rieder C.L., Schultz A., Cole R., Sluder G. "Anaphase onset in vertebrate somatic cells is controlled by a checkpoint that monitors sister kinetochore attachment to the spindle." *J Cell Biol.* 1994, 127(5):1301–1310.

Lakadamyali M, M. J. Rust, X. Zhuang (2006) Ligands for clathrin-mediated endocytosis are differentially sorted into distinct populations of early endosomes. *Cell* 124: 997–1009.

Saffman, P.G. and M. Delbrück (1975), "Brownian motion in biological membranes." *Proc. Natl Acad. Sci.* **72**, pp.3111–3113.

Saffman, P.G. (1976), "Brownian motion in thin sheets of viscous fluid," *J . Fluid Mech.* **73** (4), pp.593–602.

Sakai et al. Dual wavelength imaging allows analysis of membrane fusion of influenza virus inside cells, *J. of Virology.* **4** 2006.

Saxton, M.J. (1993), "Lateral diffusion in an archipelago. Single-particle diffusion," *Biophys. J.* **64**, p.1766–1780.

Saxton, M.J. (1995), "Single-particle tracking: effects of corrals," *Biophys. J.* **69**, pp.389–398.

Saxton, M.J. and K. Jacobson (1997), "Single-particle tracking: applications to membrane dynamics," *Annu. Rev. Biophys. Biomol. Struct.* **26**, pp.373–399.

Schuss, Z. (1980), *Theory and Applications of Stochastic Differential Equations.* John Wiley & Sons, NY.

Schuss, Z., A. Singer, and D. Holcman (2007), "The narrow escape problem for diffusion in cellular microdomains," *Proc. Natl. Acad. Sci. USA*, **104**, 16098–16103.

Schuss, Z. (2010a), "Equilibrium and recrossings of the transition state: what can be learned from diffusion?" *J. Phys. Chem. C*, **114** (48), pp.20320–20334.

Schuss, Z. (2010b), *Theory and Applications of Stochastic Processes, and Analytical Approach*, Springer series on Applied Mathematical Sciences 170, NY.

Schuss, Z. (2012), *Nonlinear Filtering and Optimal Phase Tracking*, Springer series on Applied Mathematical Sciences 180, NY.

Schuss, Z.(2013) *Brownian Dynamics at Boundaries and Interfaces in Physics, Chemistry, and Biology*, Springer series on Applied Mathematical Sciences, NY.

Shea, T. B., and V. S. Sapirstein, 1988. Vesicle-mediated delivery of membrane to growth cones during neuritogenesis in embryonic rat primary neuronal cultures. Exp Cell Biol 56:67–73.

Seisenberger, G., M.U. Ried, T. Endress, H. Brüning, M. Hallek, Bräuchle (2001), "Real-time single-molecule imaging of the infection pathway of an adeno-associated virus," *Science* **294** (5548), pp.1929–1932.

Sheetz, M.P. (1993), "Glycoprotein motility and dynamic domains in fluid plasma membranes," *Ann. Rev. Biophys. Biomol. Struct.* **22**, pp.417–431.

Sheng, M., B. Sabatini, T. Sudhof (editors) (2012), *The Synapse*, Cold Spring Harbor Laboratory Press.

Smith, C. L., 1994. The initiation of neurite outgrowth by sympathetic neurons grown in vitro does not depend on assembly of microtubules. *J Cell Biol* 127:1407–18.

G.A. Smith et al., *Proc. Natl. Acad. Sci. U.S.A.* **45**, 16034 (2004).

Shi, S.H., Y. Hayashi, R.S. Petralia, S.H. Zaman, R.J. Wenthold, K. Svoboda, R. Malinow (1999), "Rapid spine delivery and redistribution of AMPA receptors after synaptic NMDA receptor activation." *Science* **284** (5421), pp.1811–1816.

Silbergleit, A., I. Mandel, I. Nemenman (2003), "Potential and field singularity at a surface point charge," *J. Math. Phys.*, **44** (10), pp.4460–4466.

Singer, A., Z. Schuss, D. Holcman, and R.S. Eisenberg (2006a), "Narrow escape, Part I," *J. Stat. Phys.*, **122** (3), pp.437–463.

Singer, A., Z. Schuss, and D. Holcman (2006b), "Narrow escape, Part II: The circular disk," *J. Stat. Phys.*, **122** (3), pp.465–489.

Singer, A., Z. Schuss, and D. Holcman (2006c), "Narrow escape, Part III: Non-smooth domains and Riemann surfaces," *J. Stat. Phys.*, **122** (3), pp.491–509.

Singer, A. and Z. Schuss (2006), "Activation through a narrow opening," *Phys. Rev. E (Rapid Comm.)*, **74**, 020103(R).

Singer, A. and Z. Schuss (2007), "Activation through a narrow opening". *SIAM J. Appl. Math.* **68** (1), pp.98–108.

Singer, A., Z. Schuss and D. Holcman (2008a), "Narrow escape and leakage of Brownian particles." *Physical Review E* **78**, 051111.

Singer, A. Z. Schuss, A. Osipov, and D. Holcman (2008b), "Partially Reflected Diffusion" *SIAM J. Appl. Math.* **68**, pp.844–868.

Smith, T.C. and J.R. Howe (2000), "Concentration-dependent substate behavior of native AMPA receptors," *Nat. Neurosci.* **3**, pp.922–927.

Sneddon, I.N. (1966), *Mixed Boundary Value Problems in Potential Theory*, Wiley, NY.

Südhof, T.C. (2008), "Neuroligins and neurexins link synaptic function to cognitive disease." *Nature* **455** (7215), pp.903–911.

Sodeik, B. (2000), "Mechanisms of viral transport in the cytoplasm," *Trends Microbiol.* **8** pp.465–472.

Svoboda, K., D.W. Tank, W. Denk (1996), "Direct measurement of coupling between dendritic spines and shafts," *Science*, **272** (5262), pp.716–719.

Suzuki, K. and M.P. Sheetz (2001), "Binding of cross-linked glycosylphosphatidylinositol-anchored proteins to discrete actin-associated sites and cholesterol-dependent domains," *Biophys. J.* **81**, pp.2181–2189.

Taflia, A. and D. Holcman (2007), "Dwell time of a molecule in a microdomain," *J. Chem. Phys.* **126**, (23) 234107.

Taflia, A. and D. Holcman (2011), "Estimating the synaptic current in a multiconductance AMPA receptor model." *Biophys. J.* **101** (4), pp.781–792.

Tardin, C., L. Cognet, C. Bats, B. Lounis, and D. Choquet (2003), "Direct imaging of lateral movements of AMPA receptors inside synapses," *Embo J.* **22**, pp.4656–4665.

Triller, A. and D. Choquet (2003), "The role of receptor diffusion in the organization of the postsynaptic membrane," *Nat. Rev. Neurosci.*, **4**, pp.1251–1265.

Tsaneva, K., A. Burgo, T. Galli, D. Holcman (2009), "Quantifying neurite growth mediated by interactions between secretory vesicles, microtubules and actin networks," *Biophys. J.* **96** (3), pp.840–857.

Usmani, RA. (1994) Inversion of a tridiagonal jacobi matrix. Linear Algebra and its Applications, **212–213** pp 413–414.

Whittaker, G.R., M. Kann, A. Helenius (2000), "Viral entry into the nucleus," *Annu. Rev. Cell Dev. Biol.* **16**, pp.627–651.

Wang, Y., R. Austin, and E. Cox (2006), "Single Molecule Measurements of Repressor Protein 1D Diffusion on DNA," *Phys. Rev. Lett.* **97**, 048302.

Ward, M.J. and E. Van De Velde (1992), "The onset of thermal runaway in partially insulated or cooled reactors," *IMA J. Appl. Math.*, **48**, 53–85.

Ward, M.J. and J.B. Keller (1993), "Strong localized perturbations of eigenvalue problems," *SIAM J. Appl. Math.*, **53**, pp.770–798.

Ward, M.J., W.D. Henshaw, and J.B. Keller (1993), "Summing logarithmic expansions for singularly perturbed eigenvalue problems," *SIAM J. Appl. Math.*, **53**, pp.799–828.

Ward, M.J., S. Pillay, A. Peirce, and T. Kolokolnikov (2010), "An Asymptotic Analysis of the Mean First Passage Time for Narrow Escape Problems: Part I: Two-Dimensional Domains," *SIAM J. on Multiscale Modelling and Simulation* **8** (3), pp.803–835.

Zakharenko, S., and S. Popov, 1998. Dynamics of axonal microtubules regulate the topology of new membrane insertion into the growing neurites. J Cell Biol 143:1077–86.

Zhou, F. Q., C. M. Waterman-Storer, and C. S. Cohan, 2002. Focal loss of actin bundles causes microtubule redistribution and growth cone turning. J Cell Biol 157:839–49.

Zwanzig, R. (1990), "Diffusion-controlled ligand binding to spheres covered by receptors: An effective medium treatment," *Proc. Natl. Acad. Sci. USA.* **87**, pp.5856–5857.

Zwanzig, R., and A. Szabo (1991), "Time dependent rate of diffusion-influenced ligand binding to receptors on cell surfaces," *Biophys. J.* **60**, pp.671–678.

Index

D. Holcman, Z. Schuss, *Stochastic Narrow Escape in Molecular and Cellular Biology*, DOI 10.1007/978-1-4939-3103-3